UC San Diego

UC San Diego Electronic Theses and Dissertations

Title

Thermal and Mechanical Properties of Semiconductor and Polymer Nanostructures

Permalink

https://escholarship.org/uc/item/8qz2132v

Author

Wingert, Matthew

Publication Date

2016

Peer reviewed|Thesis/dissertation

eScholarship.org Powered by the California Digital Library
University of California

UNIVERSTIY OF CALIFORNIA, SAN DIEGO

Thermal and Mechanical Properties of Semiconductor and Polymer Nanostructures

A dissertation submitted in partial satisfaction of the requirements for the degree Doctor of Philosophy

in

Doctor of Philosophy in Engineering Sciences (Mechanical Engineering)

by

Matthew C. Wingert

Committee in charge:

Professor Renkun Chen, Chair
Professor Prabhakar Bandaru
Professor Shengqiang Cai
Professor Massimiliano Di Ventra
Professor Kalyanasundaram Seshadri

2016

Copyright

Matthew C. Wingert, 2016

All rights reserved

The Dissertation of Matthew C. Wingert is approved, and it is acceptable in quality and form for publication on microfilm and electronically:

_____

_____

_____

_____

_____

Chair

University of California, San Diego

2016

Dedication

Dedicated to Parisa Sarkarati, whose patience, support, and love helped me through the hard times.

Table of Contents

Signature Page iii
Dedication iv
Table of Contents v
List of Figures viii
List of Tables xiv
Acknowledgements xv
Vita xix
Abstract of the Dissertation xxi
Chapter 1: Introduction 1
1.1 Introduction to thermal properties of solids 1
1.2 Phonon transport in nanostructures 8
1.3 Thermal conductivity of thin Si and Ge films 11
1.4 Sub-30 nm Si and Ge films 14
1.5 Thermal conductivities of thin Si and Ge nanowires 16
1.6 Thermal transport in polymers 19
1.7 Organization of the thesis 23
References 25
Chapter 2: High-resolution thermal conductance measurement of nanostructures enhanced by differential bridge 30
2.1 Introduction 30
2.2 Bridge measurement: setup and verification 33
2.3 Bridge measurement sensitivity 41
2.4 Demonstration of the bridge method on a thin germanium nanowire 45
2.5 Characterization of heat loss from heating beams 49
2.6 Modeling heat loss in variable length beams 49
2.7 Verification of negligible heat loss in short-beam devices 53
2.8 Effects of heat loss from long-beam suspended devices 55
2.9 Background conductance and cancellation 60
2.10 Calculation of background conductance due to blackbody radiation 64
2.11 Conclusion 65
Acknowledgments 66
References 66

Chapter 3: Thermal conductivity of Ge and Ge-Si core-shell nanowires in the phonon confinement regime 70
3.1 Introduction 70
3.2 Nanowire fabrication 74
3.3 Nanowire thermal conductivity measurement 76
3.4 Thermal conductivity of Ge nanowires 81
3.5 Thermal conductivity modeling of Ge nanowires 83
3.6 Thermal conductivity of Ge-Si core-shell nanowires 87
3.7 Conclusion 89
Acknowledgments 90
References 90
Chapter 4: Sub-amorphous thermal conductivity in ultra-thin crystalline Silicon nanotubes 93
4.1 Introduction 93
4.2 Thermal conductivity of crystalline and amorphous Si nanotubes 96
4.3 Mechanical testing of crystalline and amorphous Si nanotubes 104
4.4 Molecular dynamics simulation of thermal and mechanical properties 108
4.5 Estimation of Thermal Contact Resistance 111
4.6 Further Equilibrium Molecular Dynamics (EMD) Simulation Details 112
4.7 Growth of Silicon Nanotubes and Nanowires 114
4.8 Preparation of Nanotube Thermal Measurement Samples 115
4.9 Thermal Conductivity Measurement 118
4.10 AFM Cantilever Calibration for Tensile Measurements 120
4.11 Elastic Modulus Measurement Details 121
4.12 Conclusion 124
Acknowledgments 125
References 125
Chapter 5: Fluid-like surface layer and its dynamics in glassy nanotubes 130
5.1 Introduction 130
5.2 Nanotube fabrication and characterization 131
5.3 Tensile setup and measurement 135
5.4 Creep measurement 137
5.5 Creep activation energy 144
5.6 Electron beam exposure 147

5.7 Conclusion 148
Acknowledgments 148
References 148
Chapter 6: Structure-induced enhancement of thermal conductivities in electrospun polymer nanofibers 153
6.1 Introduction 153
6.2 Sample preparation 156
6.3 Structure measurement 156
6.4 Structural characterization 157
6.5 Thermal measurement 162
6.6 Size dependence of thermal conductivity 164
6.7 As-spun nanofibers 165
6.8 Hot-stretched nanofibers 166
6.9 Temperature dependence of thermal conductivity 167
6.10 High temperature measurement and annealing effect 169
6.11 Effect of structural defects 171
6.12 Comparison with other nanofibers 172
6.13 Conclusion 173
Acknowledgments 176
References 176
Chapter 7: Strong size-dependent stress relaxation in polymer nanofibers 181
7.1 Introduction 181
7.2 Mechanics measurement 183
7.3 Measured modulus and stress relaxation 187
7.4 Size-dependent relaxation in other polymers 189
7.5 Viscoelastic model of stress relaxation 190
7.6 Size-dependent stiffness and damping 193
7.7 Conclusion 195
Acknowledgements 196
References 197
Chapter 8: Conclusions and future work 200
Appendix A 204

List of Figures

Figure 1.1: Infinite one-dimensional line of atoms of mass m, distance a apart, connected together by springs with spring constant g. 1

Figure 1.2: Dispersion relation for the infinite one-dimensional chain of atoms..... 3

Figure 1.3: Schematic of kinetic theory formulation of phonon transport. 6

Figure 1.4: Phonon mean-free paths (MFPs) associated with phonon-phonon or *Umklapp* (Λ_U), boundary (Λ_D), and impurity/defect (Λ_I) scattering. As the characteristic size of the nanostructure shrinks and approaches 9

Figure 1.5: Phonon mean-free path (MFP) and wavelength (λ) distribution in crystalline Si at 277 K based on molecular dynamics 11

Figure 1.6: Thickness/diameter dependence of thermal conductivity for Si and Ge films 13

Figure 1.7: Temperature dependent thermal conductivity of Si nanowires (NWs) 14

Figure 1.8: Angle-resolved Brillouin light scattering measurement on suspended Si films showing a steep drop in the phonon velocities 16

Figure 1.9: Temperature power law relations compared to experimental measurements on 22, 37, 56, and 115 nm diameter crystalline 18

Figure 1.10: (A) Thermal conductivity versus Young's modulus of micron-sized polyethylene fibers are strongly correlated and 21

Figure 2.1: Experimental setup. (A) A SEM images of the suspended microdevice used for single nanowire κ measurement; (B) Electrical 31

Figure 2.2: (A) Changes in sensing side temperature as a function of heating power passed through the heating membrane using bridge circuit and standard steady-state 4-point method. The enhanced sensitivity 38

Figure 2.3: Thermal conductivity of a ~62nm Ge nanowire calculated using the bridge and four-point measurement methods. 40

Figure 2.4: Temperature rise of the sensing membrane as measured by the bridge circuit for different lock-in time constants (0.3 s, 1 s, 3 s, and 10 s) with (A) 20mV, (B) 70mV, (C) 100mV applied to the 44

Figure 2.5: Suspended 15 nm Germanium nanowire bridging the gap between the heating and sensing membranes. Thermal conductance of a 15 nm diameter Ge nanowire with the background signal, the 47

Figure 2.6: Thermal conductivity (κ) and heat transfer coefficient (h) determination of the SiNx beams. (a) Schematic of the thermal fin model. (b) A suspended beam of total length L self-heated by applying a current I 50

Figure 2.7: Heating power over average temperature rise vs. width over length for suspended beams with and without heat loss, solid and dashed lines, respectively. Three microfabricated beams of different 51

Figure 2.8: Measured (dots) and calculated (dash line, Eq. 2.22) heat transfer coefficient for the 400-μm-long beam from 300 to 450 K. 53

Figure 2.9: SEM image of microfabricated short-beam ($Lb = 50\,\mu m$) suspended device with pads containing serpentine Pt lines. 54

Figure 2.10: Average measured temperature rise of suspended pad and suspending beams for two cases, self-heating (green square) and 55

Figure 2.11: (a) Heat loss factor versus temperature. The upper limit of the heat loss factor is 0.5 for no or negligible heat loss (blue dashed line). (b) Percent change in γ versus temperature. (c) Percent 60

Figure 2.12: Characterization of background conductance. (a) Schematic of the canceling scheme for directly measuring the conductance of a nanowire. (b) Measurement results based on 400-μm-long devices. 62

Figure 2.13: Measured background conductance vs. chamber pressure. At high vacuum, the background conductance was measured consecutively over a 4-hour period on separate days after removing 63

Figure 3.1: Ge and Ge-Si core-shell nanowires synthesized by the CVD method. (A) Schematic illustration of a Ge-core Si-shell NW. (B) A SEM image of the side view of Ge-Si core shell NWs grown on a Si substrate 75

Figure 3.2: Experimental setup of the Wheatstone bridge circuit for NW thermal measurement. (A) A SEM image of a micro-fabricated device used for single nanowire κ measurement. The device 77

Figure 3.3: (A) Measured temperature rise on the heating and sensing sides as a function of the heating power. The bridge method has a Ts sensitivity of ~1 mK, leading to a G sensitivity of ~10 pW/K 80

Figure 3.4: Measured thermal conductivity of pristine Ge NWs (green and blue triangles) and Ge-Si core-shell NWs (red and black circles) with diameters ranging from 15-20 nm. The error bars shown are 83

Figure 3.5: Comparisons between modeling and experimental results. (A) The calculated κ of the 62-nm Ge NW using bulk dispersions (black solid line) agree well with the experimental data (circles), ... 86

Figure 4.1: TEM images of silicon NTs: Crystalline 5 nm Si shell thickness, a, and diffraction pattern (inset a) as well as 95

Figure 4.2: Fracture strength of crystalline silicon nanowires and nanotubes versus nanowire diameter or nanotube shell 96

Figure 4.3: Thermal conductivity of silicon NTs: a, ~5, 7, and 10 nm c-Si NTs versus temperature and b, ~5 nm amorphous and 98

Figure 4.4: Thermal conductivity of crystalline and amorphous nanotubes versus (a) outer diameter, (b) suspended sample 100

Figure 4.5: TEM EDX on Si NTs. (a) Elemental concentrations in c-Si and a-Si NTs. The Si shell (~5 nm thick) and outer/inner 102

Figure 4.6: Elastic tensile tests: a, Elastic modulus tensile measurement using manipulator probe to pull NW attached to 106

Figure 4.7: Correlation between thermal conductivity (κ) and elastic modulus (E) in crystalline NTs and NWs. κ, D, and E 108

Figure 4.8: (a) EMD simulation of thermal conductivity and elastic modulus with different NT thickness. The interface 110

Figure 4.9: Comparison of vibrational density of states from EMD simulation in crystalline and amorphous layers in a thin 111

Figure 4.10: Nanotube thermal device fabrication procedure. The nanotube thermal conductivity samples are fabricated via a pick-and-place procedure 117

Figure 4.11: TEM of nanotube sample for thermal measurement (a) before and (b) after device fabrication. Nanotube samples 118

Figure 4.12: SEM of elastic tensile testing. (a) AFM cantilever deflection measurements for applied stress. The nanotube 123

Figure 4.13: Stress-strain curve from nanotube tensile test. Applied stress to nanotubes during tensile tests is calculated from the nanotube geometry 124

Figure 5.1: TEM images of individual ultrathin (a) amorphous SiO2, (b) amorphous Si, and (c) crystalline Si nanotube (NT) samples and (d) SEM of tensile creep experimental setup. Scale bars are (a) 10 nm, (b) 50 nm, and (c) 5 nm. 133

Figure 5.2: TEM images of (a) 14 and (b) 25 nm thick a-SiO2 and (c) 12, (d) 20, and (e) 150 nm thick a-Si NTs, and (f) representative c-Si NW. Scale bars are (a) 10, (b) 20, (c) 10, (d) 10, (e) 50, and (f) 5 nm. 134

Figure 5.3: Nanotube stress-strain measurement exhibiting linear elastic regime up to 8% strain. 136

Figure 5.4: Measured fracture strength of a-Si NTs versus suspended NT length..... 137

Figure 5.5: Creep strain measured for (a) amorphous SiO2 (a-SiO2), (b) amorphous Si, and (c) crystalline Si nanotubes (NTs), and (d) viscoelastic 138

Figure 5.6: (a) Core-shell model describing the dynamic and size-dependent behavior of the amorphous nanotubes and (b) the experimental (circles and squares) and modeled (dashed line) size-dependent normalized saturated creep..... 140

Figure 5.7: Size-dependent (a) instantaneous and (b) relaxed moduli of a-SiO2, a-Si, c-Si NTs, and c-Si NWs measured by us and also by Zhu et al.38. 142

Figure 5.8: Dependence of normalized maximum creep strain increase versus (a) initial applied stress and (b) initial applied strain. 143

Figure 5.9: (a) Creep strain observed for 20 nm shell amorphous SiO2 nanotubes at various temperatures. (b) Creep viscosity versus temperature, fitted to an Arrhenius temperature dependence (red dashed line). 145

Figure 6.1: (a) Schematic of the molecular arrangement in Nylon-11 nanofibers. WAXS patterns from uniaxially aligned 158

Figure 6.2: Structural data of the crystalline domains as a function of diameter for nanofibers as-spun at room temperature (blue circles) and hot-stretched at 120 °C to a 1.5× draw ratio (red squares). (a) and (b) are 161

Figure 6.3: (a) Thermal conductivity versus nanofiber diameter at 300 K. Black circles represent as-spun nanofibers and red triangles 163

Figure 6.4: Thermal conductivity versus temperature for all measured nanofiber samples. Nanofiber diameters ranged from 168

Figure 6.5: Thermal conductivity versus temperature for annealed nanofiber sample NF2 (196 nm diameter as-spun). Nanofiber 171

Figure 6.6: Thermal conductivity of a beaded nanofiber. Bulk Nylon-1110 (blue dashed line) shown for comparison purposes. 172

Figure 7.1: (a) Single nanofiber tensile relaxation measurement setup and (b) diameter dependence of instantaneous and relaxed 184

Figure 7.2: (a) Nanofiber strain measurement. During each loading, in addition to the cantilever deflection, the fiber length is 185

Figure 7.3: Stress-strain curve for single ~200 nm diameter nanofiber. The measured cantilever deflection and fiber length are 186

Figure 7.4: Stress relaxation in individual Nylon-11 nanofibers. The time-dependent stress normalized by the initial stress, ... 188

Figure 7.5: Diameter dependent (a) stress relaxation and (b) relaxation time constant. The relaxation and time constants were 191

Figure 7.6: Full stress relaxation versus initial applied stress. The amount of relaxation is strongly dependent on the diameter of the nanofiber and not on the initial applied stress or induced strain. Data points are labeled by fiber diameter. 192

Figure 7.7: Specific modulus versus maximum dissipation capacity. The specific modulus and dissipation capacity of the 195

Figure A1: TEM and SEM images of measured ~5 nm thick crystalline nanotube (sample ID: C5-1): (a) shell thickness 204

Figure A2: TEM and SEM images of measured ~5 nm thick crystalline nanotube sample (sample ID: C5-2): (a) shell thickness 204

Figure A3: TEM and SEM images of measured ~5 nm thick crystalline nanotube sample (sample ID: C5-3): (a) shell thickness 205

Figure A4: TEM and SEM images of measured ~5 nm thick crystalline nanotube sample (sample ID: C5-4): (a) shell thickness 205

Figure A5: TEM and SEM images of measured ~5 nm thick crystalline nanotube sample (sample ID: C5-5): (a) shell thickness 205

Figure A6: TEM and SEM images of measured ~7 nm thick crystalline nanotube sample (sample ID: C7-1): (a) shell thickness 206

Figure A7: TEM and SEM images of measured ~7 nm thick crystalline nanotube sample (sample ID: C7-2): (a) shell thickness 206

Figure A8: TEM and SEM images of measured ~10 nm thick crystalline nanotube sample (sample ID: C10-1): (a) shell thickness 206

Figure A9: TEM and SEM images of measured ~10 nm thick crystalline nanotube sample (sample ID: C10-2): (a) shell thickness 207

Figure A10: TEM and SEM images of measured ~10 nm thick crystalline nanotube sample (sample ID: C10-3): (a) shell thickness 207

Figure A11: TEM and SEM images of measured ~5 nm thick amorphous nanotube sample (sample ID: A5-1): (a) shell thickness 207

Figure A12: TEM and SEM images of measured ~5 nm thick amorphous nanotube sample (sample ID: A5-2): (a) shell thickness 208

Figure A13: TEM and SEM images of measured ~5 nm thick amorphous nanotube sample (sample ID: A5-3): (a) shell thickness 208

List of Tables

Table 4.1: Geometry and thermal conductivity of measured Si nanotube samples. 99

Table 5.1: Nanotube information for samples used in creep tests. 136

Acknowledgements

When I first arrived at UC San Diego, I knew that I would find the warm weather, ocean breezes, and beautiful towns and coastlines enjoyable for a great many years. Ultimately, however, I conclude my doctoral studies here finding that, more than anything else, it is the great people I have met and worked with that define and give substance to this chapter in my life. Chiefly I am grateful to my advisor, Prof. Renkun Chen, without whom I would not have had the opportunity to work on the great many interesting projects I have. His support and guidance allowed me to grow and flourish during my studies and overcome many of the hurdles inherent in scientific study. He continues to exemplify the importance of hard work, curiosity, and excitement in the scientific and academic process, setting a high bar for which we must always strive to reach.

I would also like to thank my close collaborators and dissertation committee members Prof. Jie Xiang and Prof. Shengqiang Cai. Without Prof. Jie Xiang's insights and ideas, a great many of the hurdles in my research would have been taken much longer to resolve. Furthermore, many of the incredible semiconductor nanostructure samples I was able to measure would not have been possible without him and his students Dr. Zack C. Y. Chen and Dr. Soonshin Kwon, who spent months on end fabricating materials for me. During the later period of my studies, Prof. Shengqiang Cai was integral in helping me expand my studies into the mechanics of these nanostructures. Without his ideas and guidance, much of this work would not have occurred and the insights hidden for another to uncover. I also appreciate the time that Prof. Prabhakar Bandaru, Prof. Massimiliano Di Ventra, and Prof. Kalyanasundaram

Seshadri have taken out of their busy schedules to take part in my senate and dissertation committees.

I would like to thank Dr. Zhang Jiang and Dr. Zhenxin Zhong of Argonne National Lab (Dr. Zhenxin Zhong is now at FEI) for bringing polymers to our attention and providing us with many very nice electrospun polymer fibers to measure as well as their expertise in polymers and structure characterization. I would also like to thank Prof. Ming Hu (AWTH Aachen) and Prof. Dimos Poulikakos (ETH Zurich) for discussions and insight into the physics of our silicon nanotubes, as well as molecular modeling expertise.

Additionally, I would like to thank Dr. Mike DiBattista of Qualcomm, Inc. for his help in allowing us the use of the excellent facilities at Qualcomm, Inc., specifically their FIB and TEM, especially when we needed them most. I must also acknowledge Ryan Anderson and Dr. Bernd Fruhberger at the UCSD Nano3 facility who allowed me to do important work with our FIB system beyond its normal capabilities and allowing me to get the significant number of hours I required on it.

I also appreciate all the help, company, and friendship of my group mates, Shuang Cui, Sahngki Hong, Qingyang Wang, and Lizzie Caldwell, but specifically Jianlin Zheng, Edward Dechaumphai, and Dr. Soonshin Kwon, whom I worked with closely on nanoscale heat transfer measurements and my office mates for many years: Jaeyun Moon (now a Prof. at UNLV) and Sunmi Shin. Our many discussions during late nights in the lab and office provided respite and grounding as well as fun and levity when they were needed most.

Finally, I must thank my family for their love and support and much calling

back and forth, for both counsel and comfort.

I appreciate my collaborators allowing me to use the following publications in my dissertation:

The majority of chapter 2 is a reprint of (1) M. C. Wingert, Z. C. Y. Chen, S. Kwon, J. Xiang, R. Chen, "Ultra-sensitive Thermal Conductance Measurement of One-dimensional Nanostructures Enhanced by Differential Bridge," *Review of Scientific Instruments*, 83, 024901 (2012), with the rest from portions of (2) J. Zheng*, M. C. Wingert*, E. Dechaumphai*, R. Chen, "Sub-picowatt/Kelvin Resistive Thermometry for Probing Nanoscale Thermal Transport," *Review of Scientific Instruments*, 84, 114901 (2013) and (3) Z. Zhong*, M. C. Wingert*, J. Strzalka, H. H. Wang, T. Sun, J. Wang, R. Chen, Z. Jiang, "Structure-induced Enhancement of Thermal Conductivities in Electrospun Polymer Nanofibers," *Nanoscale*, 6, 8283-8291 (2014). *These authors contributed equally to the respective works. For publication (1), I performed the experimental work and wrote the paper. For the sections of (2) used in this chapter, I did the experimental work and wrote the sections in the publication. In (3), I did the thermal characterization and experimental work and wrote those sections of the paper.

Chapter 3 is a reprint of M. C. Wingert, Z. C. Y. Chen, E. Dechaumphai, J. Moon, J. Kim, J. Xiang, R. Chen, "Thermal Conductivity of Ge and Ge-Si Core-Shell Nanowires in the Phonon Confinement Regime," *Nano Letters*, 11, 5507-5513 (2011). For this publication, I did the experimental work and wrote the paper.

Chapter 4 is a reprint of M. C. Wingert, S. Kwon, M. Hu, D. Poulikakos, J. Xiang, R. Chen, "Sub-Amorphous Thermal Conductivity in Ultra-Thin Crystalline

Silicon Nanotubes," *Nano Letters*, 15, 2605-2611 (2015). For this publication, I did the experimental work and wrote the paper.

Chapter 5 is a reprint of material which has been submitted for publication by Matthew C. Wingert, Soonshin Kwon, Shengqiang Cai, and Renkun Chen. The dissertation author was the primary investigator and author of this material. For this material, I did the experimental work, developed the model, and wrote the paper.

Chapter 6 is a reprint of Z. Zhong*, M. C. Wingert*, J. Strzalka, H. H. Wang, T. Sun, J. Wang, R. Chen, Z. Jiang, "Structure-induced Enhancement of Thermal Conductivities in Electrospun Polymer Nanofibers," *Nanoscale,* 6, 8283-8291 (2014). *These authors contributed equally to this work. For this work I did the thermal characterization and experiments, prepared the polymer thermal conductivity samples, and wrote those sections of the paper.

Chapter 7 is a reprint of material currently being prepared for submission for publication by Matthew C. Wingert, Zhang Jiang, Shengqiang Cai, and Renkun Chen. The dissertation author was the primary investigator and author of this material. For this work, I did the experimental work, prepared the fiber samples, modeled and analyzed the results and wrote the paper.

Vita

2009	Bachelor of Science, University of California, Santa Barbara
2011	Master of Science, University of California, San Diego
2016	Doctor of Philosophy, University of California, San Diego

Publications

1. M. C. Wingert*, Z. C. Y. Chen*, E. Dechaumphai, J. Moon, J. Kim, J. Xiang, R. Chen, "Thermal Conductivity of Ge and Ge-Si Core-Shell Nanowires in the Phonon Confinement Regime," *Nano Letters*, 11, 5507-5513 (2011).
   *These authors contributed equally to this work.

2. M. C. Wingert, Z. C. Y. Chen, S. Kwon, J. Xiang, R. Chen, "Ultra-sensitive Thermal Conductance Measurement of One-dimensional Nanostructures Enhanced by Differential Bridge," *Review of Scientific Instruments*, 83, 024901 (2012).

3. C. L. Hsin*, M. C. Wingert*, C. W. Huang, H. Guo, T. J. Shih, J. Suh, K. Wang, J. Wu, W. W. Wu, R. Chen, "Phase Transformation and Thermoelectric Properties of Bismuth-Telluride Nanowires," *Nanoscale*, 5, 4669-4672 (2013).
   *These authors contributed equally to this work.

4. J. Zheng*, M. C. Wingert*, E. Dechaumphai*, R. Chen, "Sub-picowatt/Kelvin Resistive Thermometry for Probing Nanoscale Thermal Transport," *Review of Scientific Instruments*, 84, 114901 (2013).
   *These authors contributed equally to this work.

5. Z. Zhong*, M. C. Wingert*, J. Strzalka, H. H. Wang, T. Sun, J. Wang, R. Chen, Z. Jiang, "Structure-induced Enhancement of Thermal Conductivities in Electrospun Polymer Nanofibers," *Nanoscale*, 6, 8283-8291 (2014).
   *These authors contributed equally to this work.

6. E. Dechaumphai, J. Moon, M. C. Wingert, R. Chen, "Engineering Phononic and Electronic Transport in Nanowires for Enhanced Thermoelectrics," Book Chapter in 'Semiconductor Nanowires: From Next-Generation Electronics to Sustainable Energy', Royal Society of Chemistry, 400-437 (2015).

7. M. C. Wingert*, S. Kwon*, M. Hu, D. Poulikakos, J. Xiang, R. Chen, "Sub-Amorphous Thermal Conductivity in Ultra-Thin Crystalline Silicon Nanotubes," *Nano Letters*, 15, 2605-2611 (2015).
   *These authors contributed equally to this work.

8. S. Cui, H. Ahn, M. C. Wingert, D. Leung, S. Cai, R. Chen, "Bio-inspired Effective and Regenerable Cooling Using Tough Hydrogels," *Applied Energy*, 168, 332-339 (2016).

9. M. C. Wingert, S. Kwon, S. Cai, R. Chen, "Fluid-like Surface Layer and Its Dynamics in Glassy Nanotubes," *Physical Review Letters*, (Under review).

10. J. Zheng, M. C. Wingert, R. Chen, "Simultaneous Specific Heat and Thermal Conductivity Measurement of Individual Nanostructures," *Semiconductor Science and Technology*, (Submitted).

11. M. C. Wingert, Z. Jiang, S. Cai, R. Chen, "Strong Size-dependent Stress Relaxation in Polymer Nanofibers," (To be submitted).

12. M. C. Wingert, S. Kwon, S. Cui, J. Xiang, R. Chen, "Size-dependent Thermal Conductivity of Amorphous Silicon," (To be submitted).

Abstract of the Dissertation

Thermal and Mechanical Properties of Semiconductor and Polymer Nanostructures

by

Matthew C. Wingert

Doctor of Philosophy in Engineering Sciences (Mechanical Engineering)

University of California, San Diego, 2016

Professor Renkun Chen, Chair

Thermal conductivity of one dimensional nanostructures, such as nanowires, nanotubes, and polymer fibers, is of significant interests for understanding nanoscale thermal transport processes as well as for technological applications in nanoelectronics, energy conversion and thermal management. This has fueled a significant body of research aiming to identify causes and enable rational engineering of thermal conductivity, which has predominantly been achieved by limiting the phonon mean-free-path by the characteristic size of the nanostructure. Thermal conductivity in such small nanostructures could be further altered by way of phonon confinement as the

structure approaches the phonon wavelength and reduction of the phonon velocity, signified *via* change in the elastic constants.

An enhanced experimental technique with 100-fold increase in calorimetric sensitivity has been developed to characterize the thermal properties of one-dimensional nanostructures such as semiconductor nanowires, nanotubes, and polymer fibers. Thermal conductivity and mechanical properties of semiconductor nanostructures were measured using the developed calorimetry setup and an *in-situ* FIB tensile testing setup. The thermal conductivities of sub-20 nm Ge and Ge-Si core-shell nanowires were measured and found to be significantly lower than bulk SiGe alloys or smooth Si NWs due to phonon confinement. Meanwhile, ~5 nm thick shell crystalline Si nanotubes were found to exhibit thermal conductivity lower than the apparent boundary scattering limit and even lower than ~5 nm thick amorphous Si nanotubes. This apparently surprising result is understood by elastic softening measured *via* tensile testing. Next, further mechanical characterization of crystalline and amorphous nanotubes was performed, and strong size-dependent viscoelastic behavior was observed in amorphous nanotubes due to a fluid-like surface, with room temperature viscosity equivalent to that of bulk glass above 1000 °C. Finally, thermal conductivity and mechanical properties of polymer nanofibers with diameters down to sub-100 nm were measured and analyzed. The axial thermal conductivity of individual nanofibers is strongly correlated with the crystalline morphology of these semi-crystalline nanofibers, while the elastic modulus stress relaxation is found to be highly size-dependent, enabling the smallest diameter fibers to break the stiffness-toughness tradeoff present in most material systems.

Chapter 1: Introduction

1.1 Introduction to thermal properties of solids

An important focus of nanoscale physics research has been thermal energy transport since it was discovered that nano-structuring can be used to engineer the thermal properties of many materials. In particular, studies of heat transport in structures with at least one nanoscale dimension, specifically in the form of thin films, nanowires, or nanotubes, have found that the thermal conductivity is highly dependent on the structure size.[1-3] Heat transport in non-conducting solids, such as the materials studied in this thesis, is dominated by quantized atomic vibrations, called phonons, which propagate through the atomic structure of the material. A brief discussion regarding the mechanics of phonons is helpful for understanding the nature of phonon thermal transport.

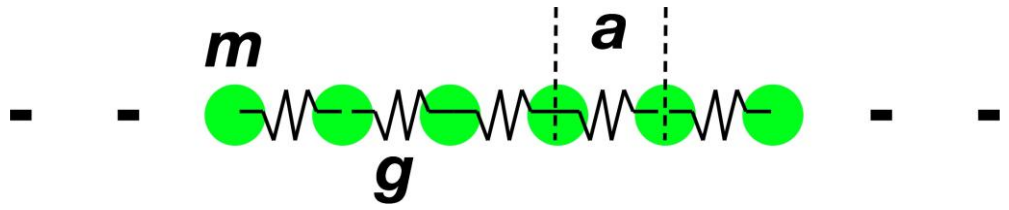


Figure 1.1: Infinite one-dimensional line of atoms of mass m, distance a apart, connected together by springs with spring constant g.

In a crystalline dielectric solid, thermal energy is transmitted through atoms, which are held together by chemical bonds in a regular periodic order. At a finite temperature, the atoms vibrate about their equilibrium positions. The chemical bonds

holding the atoms to one another is similar in effect to that of springs connecting many small masses to each other in a very large system. Motion transmits from one mass (atom) to another through these springs (chemical bonds), such that the displacement of one or more atoms propagates through the system in the form of a wave. These propagating microscopic vibrations, or phonons, dictate many of the macroscopic properties of solids, such as the specific heat and thermal conductivity. In a simple model, where we have an infinite one-dimensional chain of atoms of mass m connected together by springs with spring constant g (Fig. 1.1), the harmonic potential is:

$$P = \frac{1}{2} g \sum_n (x_n - x_{n+a})^2, \quad (1.1)$$

where x_n is the displacement of the n^{th} atom from its equilibrium position and a is the spacing between atoms. The force on a single atom is then:

$$m \frac{d^2 x_n}{dt^2} = -g(2x_n - x_{n-1} - x_{n+1}). \quad (1.2)$$

The plane-wave solution for the atomic displacement at location *n* is:

$$x_n(t) = U_K \exp[i(Kna - \omega t)], \quad (1.3)$$

where K is the wave vector and ω is the frequency of the plane wave. Here we can define the wavelength as $\lambda_n = \frac{aN}{n}$. From this we can tell that the minimum possible wavelength is $\lambda_{min} = 2a$, since there are not enough atoms below this length to support the waveform. Furthermore, the maximum wave-vector is $K_{max} = \frac{\pi}{a}$ and a corresponding $-K_{max} = -\frac{\pi}{a}$, which correspond to the edges of the first Brillouin zone.

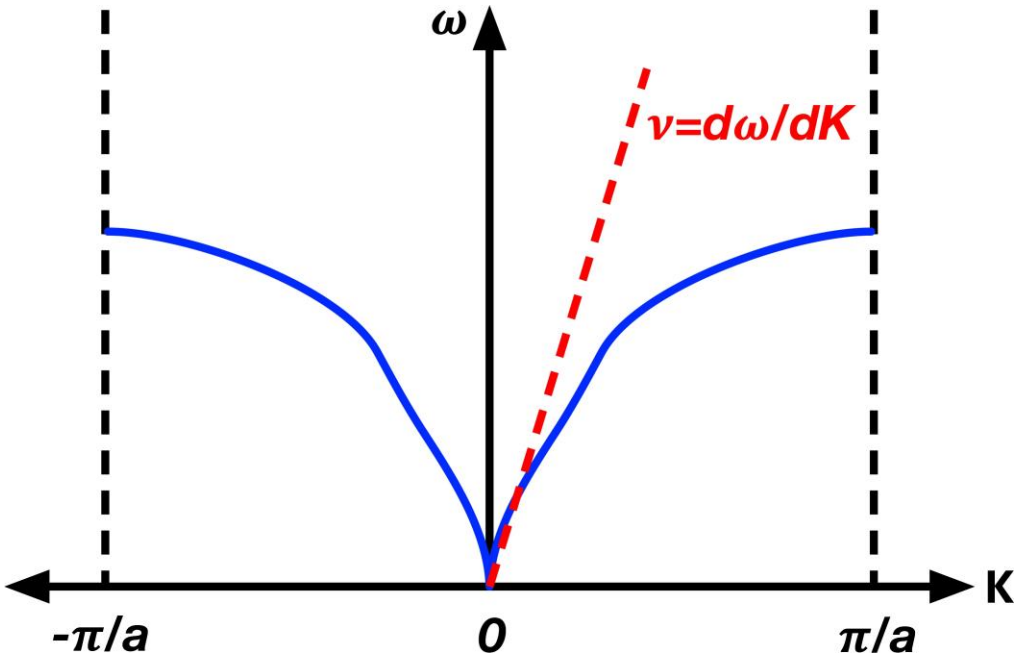


Figure 1.2: Dispersion relation for the infinite one-dimensional chain of atoms.

Substituting the plane-wave solutions Eq. 1.3 into Eq. 1.2 allows us to define the relationship between the frequency, ω, and wave vector, K, otherwise known as the dispersion relation for the lattice (Fig. 1.2):

$$\omega_K = 2\sqrt{\frac{g}{m}}\sin\left(\frac{Ka}{2}\right), \tag{1.4}$$

where the maximum frequency is $\omega_{max} = 2\sqrt{\frac{g}{m}}$ and $v_g = \frac{\partial\omega}{\partial K}$ is the group velocity. The group velocity, which is the slope of the dispersion curve, is of primary interest throughout the following discussions of phonons as it directly relates to energy transport in the system. At the zero frequency limit, the group velocity is equal to the speed of sound, hence, they are called 'acoustic' phonons.

Since phonons are actually quantum mechanical descriptions of atomic vibrations, the energy of each vibrational mode is quantized:

$$E_K = \left(N_K + \frac{1}{2}\right)\hbar\omega_K, \quad (1.5)$$

where ½ is due to the zero-point energy and the number of excited modes, N_K, is given by the Bose-Einstein distribution:

$$N_K = \frac{1}{\exp\left(\frac{\hbar\omega_K}{k_B T}\right)-1}. \quad (1.6)$$

The total energy of all the lattice vibrations (phonons) per unit volume is the summation of all phonon energies and branches or polarizations (p):

$$u = \sum_p \int \hbar\omega_p N_{K,p} D_p(\omega) d\omega, \quad (1.7)$$

where $D_p(\omega)$ is the phonon density of states for phonons of polarization p.

The number of allowable phonon states per polarization can be represented in a crystal lattice with side length L in one, two, and three dimensions as:

$$N_{1D} = \frac{2K}{\left(\frac{2\pi}{L}\right)}, \quad (1.8)$$

$$N_{2D} = \frac{\pi K^2}{\left(\frac{2\pi}{L}\right)^2}, \quad (1.9)$$

$$N_{3D} = \frac{\frac{4}{3}\pi K^3}{\left(\frac{2\pi}{L}\right)^3}. \quad (1.10)$$

The density of states in one, two, and three dimensions is therefore:

$$D_{1D}(\omega) = \frac{1}{L}\frac{d}{d\omega}N_{1D} = \frac{1}{\pi v_g}, \quad (1.11)$$

$$D_{2D}(\omega) = \frac{1}{L^2}\frac{d}{d\omega}N_{2D} = \frac{K}{2\pi v_g}, \quad (1.12)$$

$$D_{3D}(\omega) = \frac{1}{L^3}\frac{d}{d\omega}N_{3D} = \frac{K^2}{2\pi^2 v_g}. \quad (1.13)$$

The volumetric phonon specific heat is simply the derivative of the total phonon internal energy with respect to temperature:

$$C_v = \frac{du}{dT} = \sum_p \int \hbar\omega_p \frac{dN_{K,p}}{dT} D_p(\omega) d\omega, \quad (1.14)$$

where the dimensionality of $D_p(\omega)$ dictates the dimensionality of C_v. The simplest solution for the phonon specific heat comes by way of the Debye approximation, which assumes a linear dispersion relation $\omega = v_g K$, with an upper bound (cutoff) of ω_D on the frequency. This approximation in three dimensions leads to density of states per polarization of:

$$D_{3D,Debye}(\omega) = \frac{\omega^2}{2\pi^2 v_g^3}, \quad (1.15)$$

where the cutoff frequency is:

$$\omega_D = \frac{k_B \theta_D}{\hbar} = \frac{\pi v_g}{a_D}. \quad (1.16)$$

Here, θ_D is the Debye temperature of the material (which is tabulated for many materials) and a_D is the effective lattice constant under the Debye approximation. Using this simplification, the volumetric phonon specific heat becomes:

$$C_v = \frac{3\hbar^2}{2\pi^2 v_g^3 k_B T^2} \int_0^{\omega_D} \frac{\omega^4 \exp\left(\frac{\hbar\omega}{k_B T}\right)}{\left[\exp\left(\frac{\hbar\omega}{k_B T}\right) - 1\right]^2} d\omega, \quad (1.17)$$

and using the definitions of Eq. 1.18, this can be rewritten as:

$$C_v = \frac{3\pi k_B}{2a_D^3} \left(\frac{T}{\theta_D}\right)^3 \int_0^{\frac{\theta_D}{T}} \frac{x^4 \exp(x)}{[\exp(x) - 1]^2} dx. \quad (1.18)$$

Under the Debye approximation, $C_v \propto T^3$, otherwise known as the Debye T^3 law. At sufficiently low temperature ($T < \theta_D/20$), the phonon specific heat scales as T^3 for a three-dimensional solid, T^2 for a two-dimensional solid, or T for a one-dimensional solid, respectively.

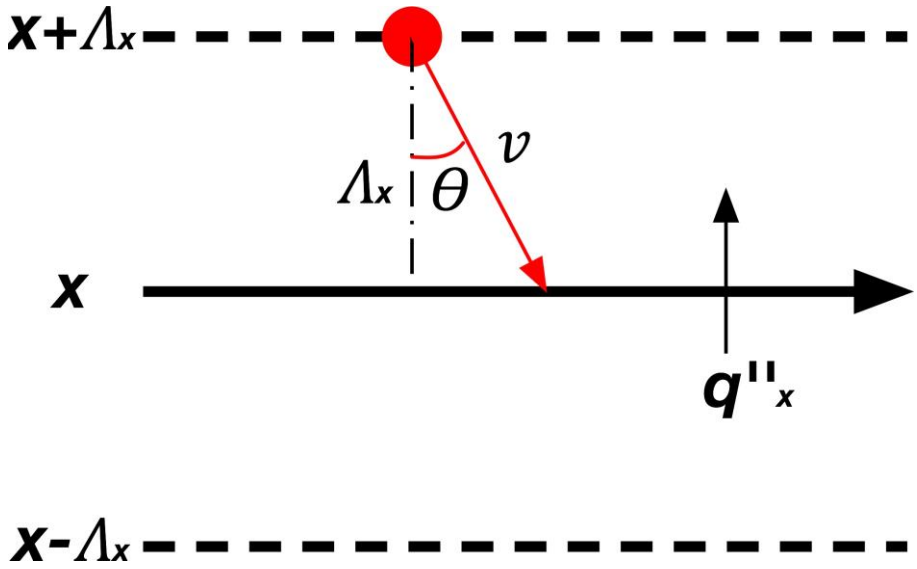


Figure 1.3: Schematic of kinetic theory formulation of phonon transport.

The thermal conductivity of the solid can be derived from the kinetic theory, where a particle (here we will consider phonons) at position $x + \Lambda_x$ travels a distance Λ, after which it experiences a scattering event (Fig. 1.3). The heat flux rate across the plane of travel is then:

$$q_x'' = \frac{1}{2} v_x [u(x - \Lambda_x) - u(x + \Lambda_x)], \tag{1.19}$$

where ½ comes from half the particles coming from a distance Λ_x above or below *x*, u is the internal energy of the particle, and v is the particle's velocity. The internal energy can be expanded in a Taylor series as such:

$$u(x + \Lambda_x) = u(x - \Lambda_x) + \frac{\partial u}{\partial x}\Big|_x (2\Lambda_x) + \mathcal{O}(\Lambda_x^2). \tag{1.20}$$

Substituting Eq. 1.22 into 1.21 and taking $\Lambda_x = \Lambda \cos(\theta)$ and $v_x = v \cos(\theta)$, while truncating the $\mathcal{O}(\Lambda_x^2)$ term gives us:

$$q_x'' \approx -v_x \Lambda_x \frac{\partial u}{\partial x} = -(\cos^2 \theta) v \Lambda \frac{\partial u}{\partial x}. \tag{1.21}$$

Since the actual directions of motion of the particles are random, the average heat flux must be found by integrating over all possible directions through the three-dimensional solid angle, $d\Omega = \sin\theta \, d\theta d\phi$, where ϕ is the azimuthal angle:

$$\langle q_x'' \rangle = -v\Lambda \frac{\partial u}{\partial x}\left[\frac{1}{2\pi}\int_0^{2\pi}\int_0^{\frac{\pi}{2}} \cos^2\theta \sin\theta \, d\theta d\phi\right] = -\frac{1}{3}v\Lambda\frac{\partial u}{\partial x}. \quad (1.22)$$

We can then use the derivative chain rule and the fact that $\frac{\partial u}{\partial T} = C_v$, as derived earlier to simplify as:

$$\langle q_x'' \rangle = -\frac{1}{3}v\Lambda\frac{\partial u}{\partial x} = -\frac{1}{3}v\Lambda\frac{\partial u}{\partial T}\frac{\partial T}{\partial x} = -\frac{1}{3}v\Lambda C_v\frac{\partial T}{\partial x}. \quad (1.23)$$

From Fourier's Law, we know that the heat flux is proportional to the temperature gradient by the thermal conductivity:

$$q'' = -\kappa\frac{\partial T}{\partial x}. \quad (1.24)$$

Seeing that Eq. 1.25 and Eq. 1.26 are the same form, we find that the thermal conductivity is simply:

$$\kappa = \frac{1}{3}C_v v\Lambda. \quad (1.25)$$

Phonon transport at the micro/nano-scale is complicated by the fact that the characteristic length scales of the solids can be much smaller than the phonon mean-free path (MFP), Λ, and even similar in size to the phonon wavelength, λ. Furthermore, Λ and λ are not constant and can have a broad distribution of values for a given material. From these length scales, the effects of size reduction on thermal transport can be categorized into three regimes: diffusive, size limited (or Casimir), and confinement. In the following sections, the diffusive and size-limited regimes will be discussed, as well as the results of previous thermal transport studies in Si and Ge

nanostructures and possible effects as structures are reduced to sizes comparable to the phonon wavelength. Finally, we will conclude the chapter with a discussion of thermal transport in polymers and outline the work covered in Chapters 2 through 7 of this thesis.

1.2 Phonon transport in nanostructures

As discussed earlier, phonon transport in nanostructures can most easily be understood *via* the kinetic theory formulation of thermal conductivity, where phonons are depicted as particles with specific heat *C*, phonon group velocity *v*, and phonon MFP Λ:[4]

$$\kappa = \frac{1}{3}\int_0^\infty C(\omega)v(\omega)\Lambda(\omega)\,d\omega. \quad (1.26)$$

Here the frequency (ω) dependence of each parameter is taken into account. The total phonon MFP (Λ) is found from the Matthiessen's rule, where the individual MFPs due to phonon-phonon or *Umklapp* (Λ_U), boundary (Λ_D), and impurity/defect (Λ_I) scattering (Figure 1.4) are taken in parallel:

$$\frac{1}{\Lambda} = \frac{1}{\Lambda_U} + \frac{1}{\Lambda_D} + \frac{1}{\Lambda_I} \quad (1.27)$$

When the characteristic size of sample, including its length and lateral size, is longer than the phonon MFP ($D>>\Lambda$), heat transport is considered to be diffusive. In the diffusive regime, the MFP (Λ) is dominated by volumetric phonon-phonon (*Umklapp*) or phonon-defect scattering. Heat conduction here is well matched to Fourier's Law and the thermal conductivity generally follows the Debye T^3 power law at low temperature.

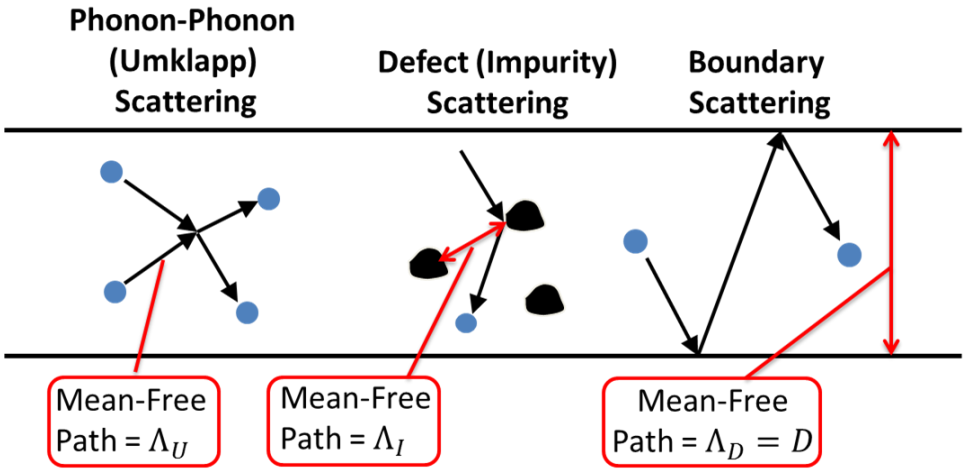


Figure 1.4: Phonon mean-free paths (MFPs) associated with phonon-phonon or *Umklapp* (Λ_U), boundary (Λ_D), and impurity/defect (Λ_I) scattering. As the characteristic size of the nanostructure shrinks and approaches the scale of the phonon MFP (D~Λ), increased diffuse boundary scattering at surfaces and interfaces dominates the thermal conductivity, a regime known as the boundary-limited or Casimir regime.

As the characteristic size of the nanostructure is reduced to the order of the phonon MFP (D~Λ), increased diffuse phonon boundary scattering at nanostructure surfaces and interfaces dominates[5-7] and a strong size dependent thermal conductivity, nearly proportional to the characteristic size, is observed. This is the size limited or Casimir regime and the MFP in the thermal conductivity, as defined in Eq. 1.1, can be replaced with the characteristic size of the nanostructure, D, yielding:

$$\kappa = \frac{1}{3} C v D. \qquad (1.28)$$

To better understand the effect of reduced structure size, it is useful to understand the length scales associated with phonon transport, namely, the MFP and wavelength. Of particular interest are semiconductor materials, specifically Si as it is the most widely used and studied semiconductor. Molecular dynamics (MD) simulations for crystalline silicon have expanded the knowledge of phonon spectrums in such materials, especially towards the engineering of nanostructures to control thermal conductivity.[8] Phonon MFPs in silicon (Figure 1.5) have been found, both computationally and experimentally, to extend up to 10 μm and phonons with MFPs longer than 1 μm contribute to almost half of heat transport at 277 K.[8, 9] Meanwhile, the phonon wavelength (λ) can extend from 0.5 nm up to 6 nm. Optical phonons, which have low propagating speed, have MFPs less than 9 nm[10] and contribute only to ~5% of heat transport.[8]

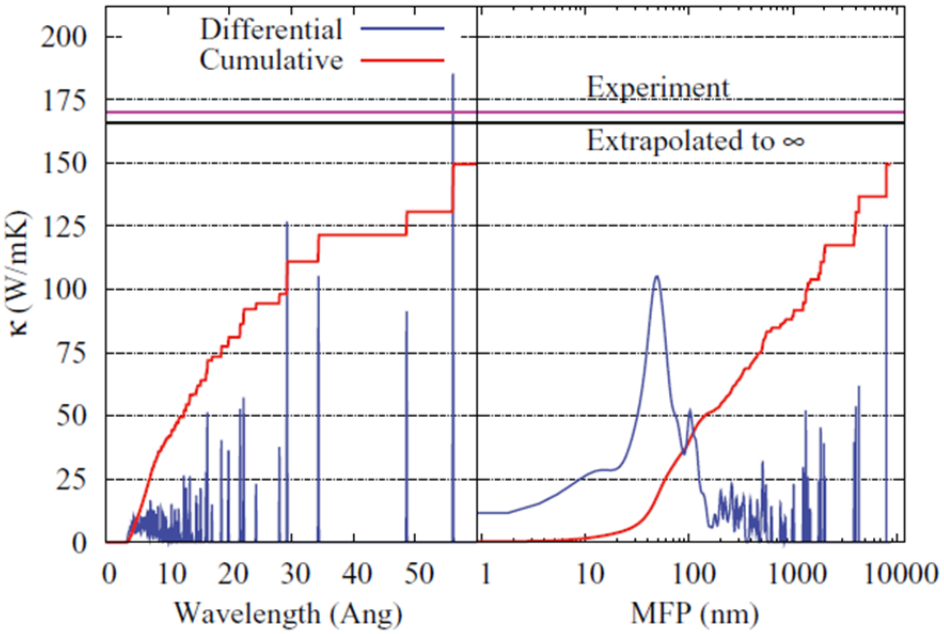


Figure 1.5: Phonon mean-free path (MFP) and wavelength (λ) distribution in crystalline Si at 277 K based on molecular dynamics simulations. Red lines represent the thermal conductivity accumulations as functions of phonon MFPs and wavelengths.[11]

1.3 Thermal conductivity of thin Si and Ge films

Since the MFP in Si ranges from ~10 nm to 10 μm (Fig. 1.5), boundary scattering is expected to have a significant impact the thermal conductivity of micro- and nano- scaled thin films. This strong size dependence has been observed in Si films measured on SOI wafers and in suspended films, all on the order of ~100 nm, with thermal conductivities slightly reduced (~100 W m^{-1} K^{-1}) from the bulk value (~140 W m^{-1} K^{-1}).[12-18] These measurements showed that the average phonon MFP in Si is ~300 nm, much longer than previous estimates based on kinetic theory (~40 nm), as the latter neglects the dispersion of phonons. Measurements on suspended Si bridges have

shown that the thermal conductivity of 30 and 20 nm thick Si films is further reduced by a factor of ~5, to 31 and 22 W m^{-1} K^{-1}, respectively,[19-21] similar to that of an ~18 nm thick single crystal film measured with the suspended micro-device technique[22] (~20 W m^{-1} K^{-1}). A non-contact technique based on two-laser Raman thermometry[23] has also been used to measure suspended films down to a thickness of ~10 nm, which were found to have thermal conductivity of ~10 W m^{-1} K^{-1}, while micron scale films were bulk-like.[24] Figure 1.6 shows the size-dependent thermal conductivity of the various measured films. Similar size-dependence has been observed in ~40, 60, and 100 nm thick Ge films,[25] however, the thermal conductivity is subdued compared to that of Si due to the heavier atomic mass of Ge, which reduces phonon group velocity. The Ge films also exhibit an interesting nearly constant thermal conductivity above 100 K, at least up to the maximum measured temperature of 300 K (Fig. 1.7).

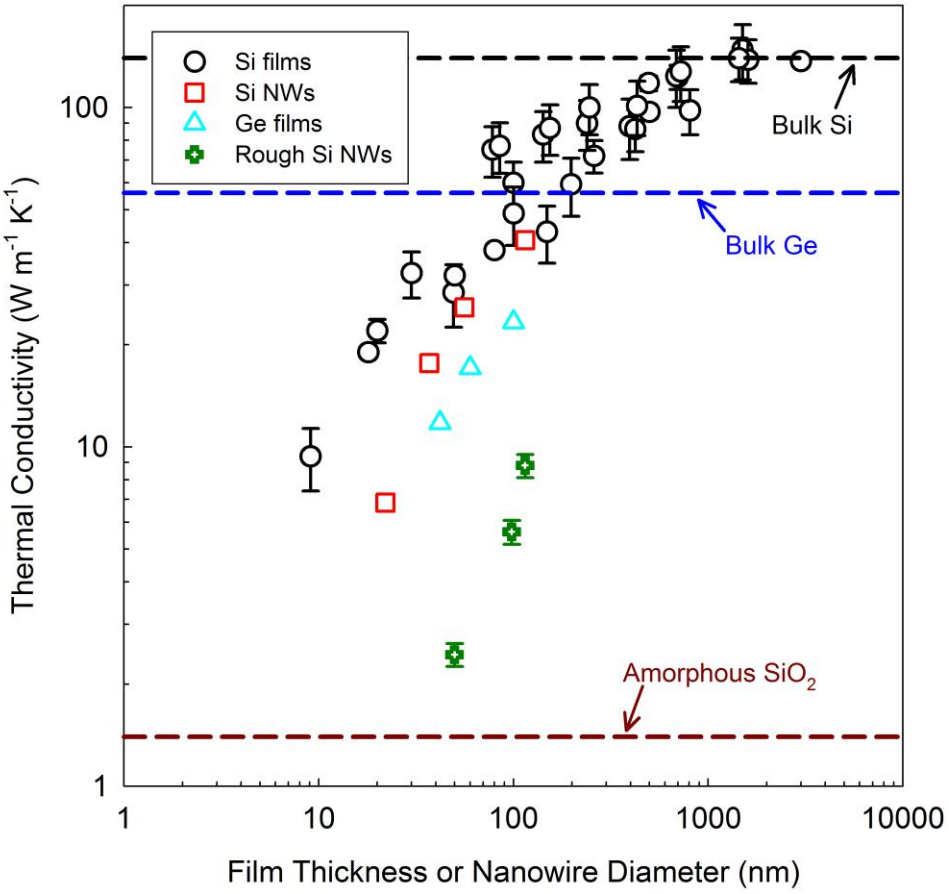


Figure 1.6: Thickness/diameter dependence of thermal conductivity for Si and Ge films[12-25] and nanowires (NWs)[5, 6] at 300 K. Si film thermal conductivity decreases rapidly with film thickness from bulk-like values for micron scale films and ultimately reduced almost twenty-fold in 10 nm thick films. Si NWs experience an even steeper drop in thermal conductivity with size due to increased phonon boundary scattering. Surface roughness has also been found to significantly reduce the thermal conductivity, with large roughness allowing further reductions below size alone, allowing for relatively large nanostructures with low thermal conductivity.

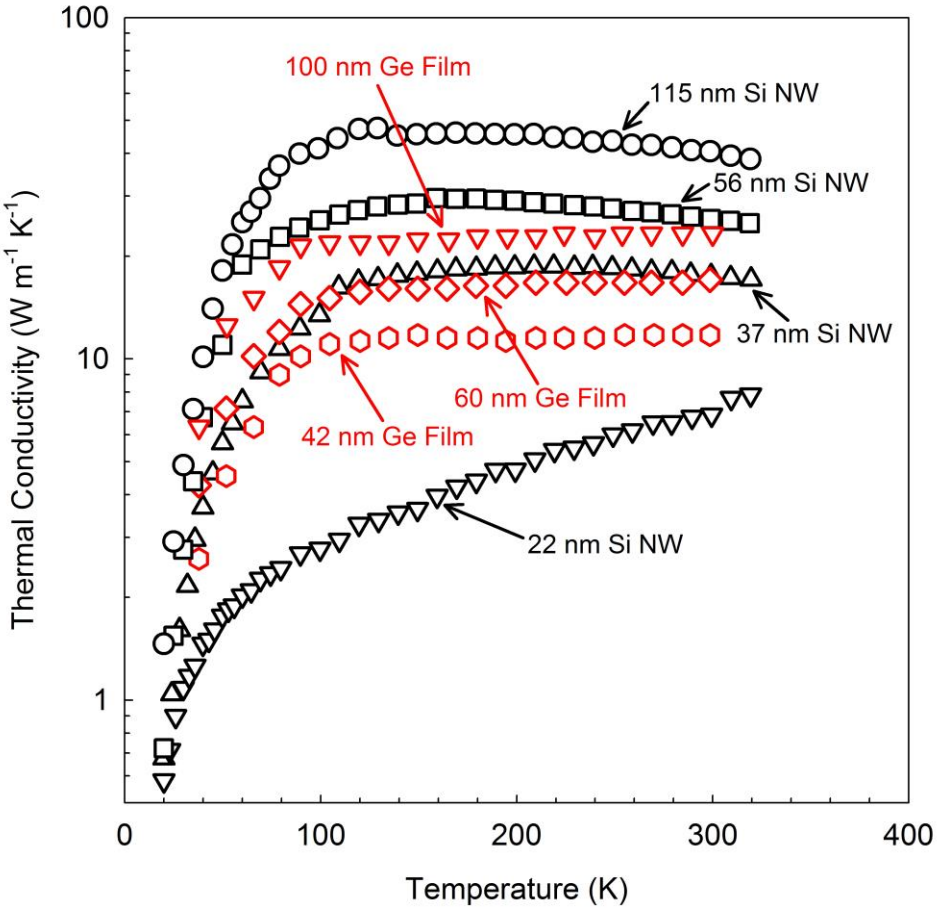


Figure 1.7: Temperature dependent thermal conductivity of Si nanowires (NWs)[6] and Ge films[25]. A clear reduction of thermal conductivity with size can be seen, with labelled sizes indicating the thickness of films and diameter of NWs. A clear change in temperature dependence in Si NWs occurs as the diameter shrinks below 30 nm, as observed in the nearly linear temperature dependence of the 22 nm Si NW.

1.4 Sub-30 nm Si and Ge films

While size limitations on the MFP are the primary mechanism responsible for reductions in thermal conductivity, as the characteristic length scales of structures become comparable to the phonon wavelength (D~λ), Fig. 1.5, further thermal conductivity reductions can be imposed on top of the Casimir limit, primarily by

reducing the phonon group velocity in the material. Angle-resolved Brillouin light scattering studies on suspended Si films have shown a steep drop in the phonon velocities of fundamental flexural modes for membrane thicknesses of ~10-30 nm, indicating a modification of the phonon dispersion (Fig. 1.8).[26] This observation could also indicate that, at these small size scales, the effective elastic constants have been reduced from their bulk values, possibly due to surface effects such as coupling with the native oxide coating or changes in the length of near-surface atomic bonds. Such alterations of the elastic constants (c_{11}, c_{12}, c_{44}), would lead to changes in the elastic modulus (E) of the nanostructure:

$$E = 3c_{44}\frac{c_{11}+2c_{12}}{c_{11}+c_{12}+c_{44}} \tag{1.29}$$

and subsequently, to the speed of sound:

$$v = \sqrt{\frac{E}{\rho}} \tag{1.30}$$

where ρ is mass density. Reduced effective elastic constants on this size scale have been observed *via* measurements of the Young's modulus of sub-30 nm Si NWs[27] and in thicker Si cantilevers[28, 29], as well as in sound velocity measurements on InSb nanowires[30]. Experimental measurements of coherent confined phonons in sub-30 nm Si membranes have also found that phonon relaxation times are dominated by scattering due to surface roughness of about 0.5 nm while thicker films in the range of ~100 nm were dominated by phonon-phonon interactions.[31]

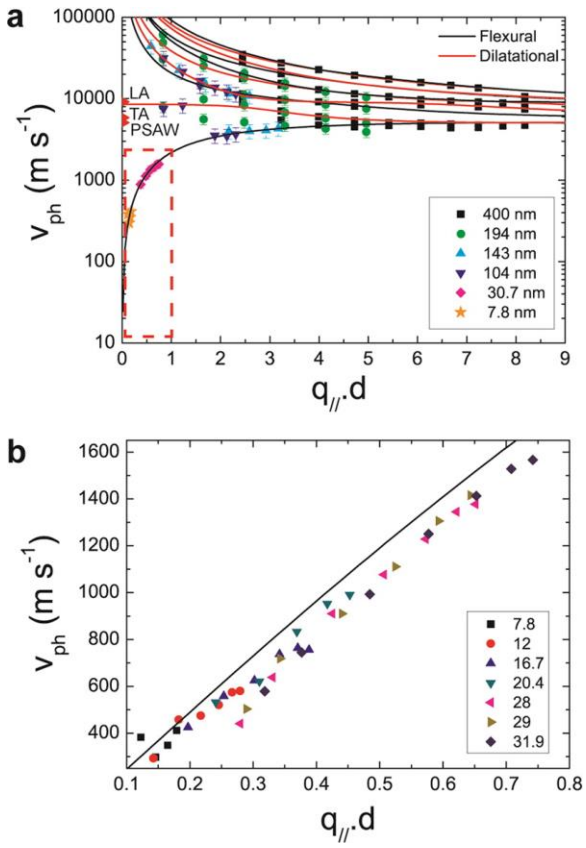


Figure 1.8: Angle-resolved Brillouin light scattering measurement on suspended Si films showing a steep drop in the phonon velocities of fundamental flexural modes for ~10-30 nm thick films.[26]

1.5 Thermal conductivities of thin Si and Ge nanowires

Thermal conductivity of individual crystalline Si NWs[6] with diameters ranging from 22 to 115 nm were measured over a temperature range of 20-320 K and were found to be highly dependent on the wire diameter (Figure 1.6). The reduced thermal conductivity is due to the increase in phonon-boundary scattering as the diameter is reduced. Modeling based on the BTE, using only classical size effects and fully diffuse boundary scattering,[32, 33] was able to accurately predict the thermal conductivity of the larger NWs (37-115 nm), but was unable to replicate the

temperature dependence or thermal conductivity of the 22 nm wire. This thin NW exhibited a unique linear temperature dependence with no peak over the measured temperature range, up to ~300 K, as seen in Figure 1.7. This is in contrast to the behavior of the larger diameter wires where the peak thermal conductivity values occurred at higher temperatures as the diameter was reduced, indicating the growing importance of boundary scattering over phonon-phonon (Umklapp) scattering.

At low temperatures (Fig. 1.9) the thermal conductivity of the relatively larger nanowires, 115 and 56 nm diameter follows the Debye T^3 law, similar to bulk Si. This is due to the temperature dependence of the phonon heat capacity, as phonon boundary scattering is temperature or frequency independent and only scales the thermal conductivity. A transition occurs near ~30 nm, as the 37 nm diameter Si NW shows the beginning of deviations from the cubic trend. Further size reduction leads to the near linear temperature dependence of thermal conductivity observed in the 22 nm Si NW. Further measurements on sub-30 nm diameter Si NWs[34] confirmed the low-temperature (20-100 K) linear behavior.

Several reasons have been posited for the strong change in thermal conductivity behavior for the sub-30 nm wires, including frequency dependent phonon boundary scattering rates (quasi-specular reflection at surface)[34], the presence of high frequency phonon modes not present in bulk Si due to surface oxidation[32] or confinement of phonons and reduced phonon group velocity[35, 36]. It is also noteworthy that studies on the elastic moduli of individual Si NWs show a steep reduction from bulk values for wire diameters thinner than 30 nm,[27] which could mean that the

effective elastic constants soften as wires become thinner, similar to the previously mentioned phenomena softening in sub-30 nm thin films[26] and InSb NWs[30].

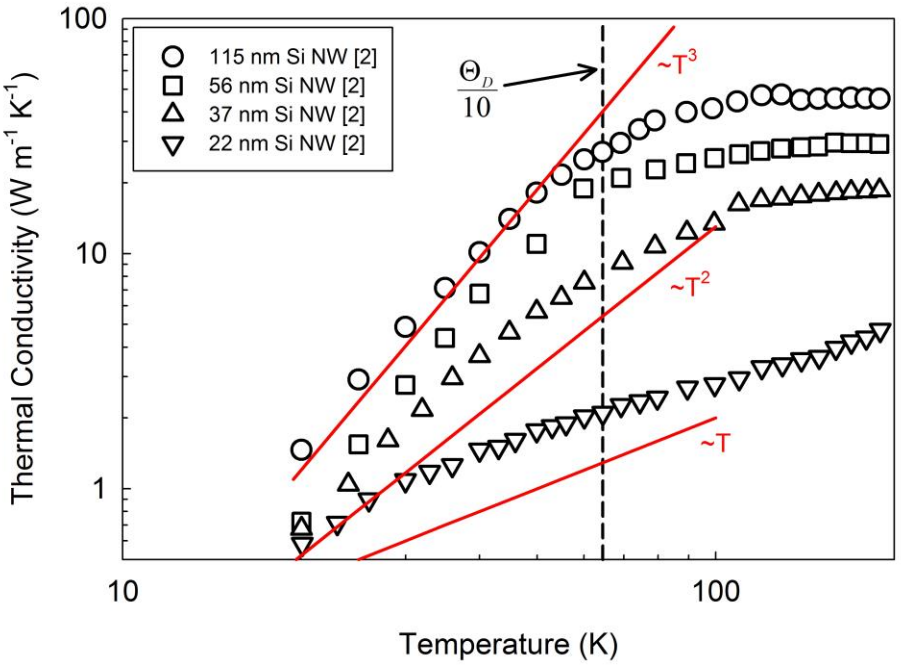


Figure 1.9: Temperature power law relations compared to experimental measurements on 22, 37, 56, and 115 nm diameter crystalline Si nanowires (NWs)[6]. The solid red lines denote the linear (T), quadratic (T^2), and cubic (T^3) temperature power law trends for thermal conductivity. The cubic temperature trend for thermal conductivity is valid at low temperatures, specifically one tenth of the Debye temperature (Θ_D=645 K for Si), where *Umklapp* scattering processes freeze out and the phonon MFP is limited to the characteristic size of the sample.

Molecular dynamics simulations of wires approaching ~20 nm diameter with realistic oxidized surface and roughness have shown that drastic reductions in thermal conductivity can occur and could help explain mechanisms present in sub-30 nm wires.[37-40] One theory regarding the measured linear temperature dependence is based on results of such simulations and concerns the interplay between the reduced dimensions and the presence of non-propagating vibrational phonon modes.[41] Another theoretical framework developed to explain the ~20 nm NW thermal conductance behavior is based on incoherent scattering of short wavelength phonons at surfaces combined with contributions from long wavelength phonons which are quasi-ballistic.[42] These quasi-ballistic modes are only weakly scattered by surface roughness on the scale of the lattice constant (~0.5 nm) and will reflect specularly from the NW surface, leading to a similarly linear low temperature dependence of thermal conductance. This study also concluded that at such small length scales, localization effects become increasingly important. For thick NWs, specularly reflected modes can be neglected, as they do not contribute as much to the thermal conductivity, however they become increasingly important for small structures.[34]

1.6 Thermal transport in polymers

Highly efficient thermal energy transport is a crucial aspect due to its extensive applications in energy dissipation and conversion devices such as solar heat collectors, heat spreaders and exchangers, and electronic packaging. Nowadays, most commercial heat transfer components are made of conventional metallic materials, such as Cu and

Al. Recent progress in polymeric material engineering, especially in the synthesis and processing of materials with structure on nanometer length scales has created very promising opportunities for designing and fabricating nanostructured thermal transport materials with enhanced or entirely new combinations of functions that are very different from the corresponding macroscopic entities. Highly thermally conductive particles such as carbon nanotubes and metal nanoparticles are often incorporated into resins to optimize nanocomposite structures for heat transfer along a continuous path to a heat sink[43]. This approach, however, can only yield very limited enhancement due to the high interfacial thermal resistance between the additive foreign particles and the polymer matrix[44]. Alternatively, it has been discovered that, in addition to enhanced mechanical performance[45, 46], polymer materials under tension also exhibit increased thermal conductivity along the tensile direction[45, 47-51]. Polymeric materials that are nearly insulating in conventional bulk forms[52-54] can increase in thermal conductivity when they are stretched (drawn) to high aspect ratios. For instance, the thermal conductivity (κ) of micron-sized polyethylene fibers were found to increase from 0.2 W m^{-1} K^{-1} in bulk forms to 50 W m^{-1} K^{-1}, accompanied by a drastic increase in Young's modulus[45] (Fig. 1.10a). More recently, Shen et al.[55] observed a κ as high as ~100 W m^{-1} K^{-1} for a single polyethylene (PE) nanofiber with diameter down to ~100 nm (Fig. 1.10b,c), whose thermal performance is above that of most metallic alloys and approximately half of pure metals, including platinum, iron and nickel. Theories suggest that even a very high (~350 W m^{-1} K^{-1}) or possibly divergent thermal conductivity could be possible for isolated individual PE chains, which is competitive with commonly used pure aluminum (237 W m^{-1} K^{-1}) and copper (401 W m^{-1} K^{-1}).[56, 57]

Therefore, polymer nanofibers represent a new class of materials ideally suited to energy applications and related technologies that require good thermal conductivity, electric insulation, chemical stability, high mechanical performance, light weight, controllable cost, and mass producibility.

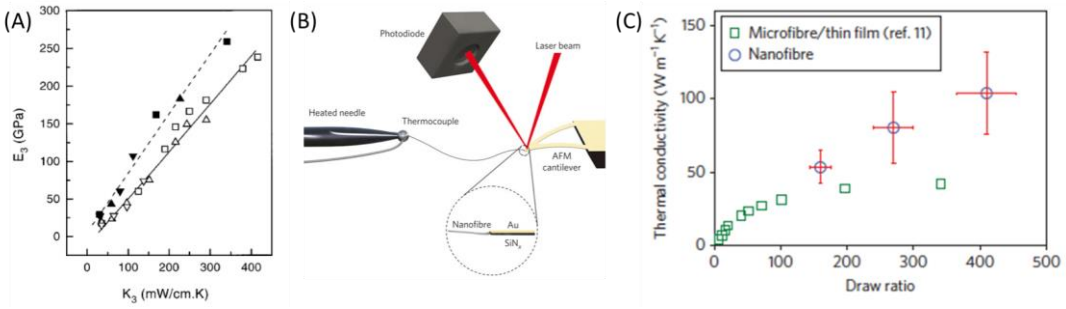


Figure 1.10: (A) Thermal conductivity versus Young's modulus of micron-sized polyethylene fibers are strongly correlated and both increase when the fibers are drawn.[45] (B) Thermal conductivity measurement setup for single polyethylene (PE) nanofiber measurement (with diameter down to ~100 nm).[55] (C) Thermal conductivity versus draw ratio of single polyethylene (PE) nanofiber with near-metallic thermal conductivity.

A number of studies have attempted to explain the heat transport mechanisms in polymer fibers. It has been found that the thermal conductivity often exhibits significant anisotropy when the polymers are under strain. This anisotropy can be related to a statistical distribution of the polymer chain orientations. As an intrinsically low-dimensional system, isolated individual polymer chains can have very high thermal conductivity[58]. However, a macroscopic ensemble of polymers chains is often a thermal insulator because the twisted random orientations of the polymer chains and the weak coupling between the chains, in addition to inherent defects such as voids, impurities, polymer chain ends and entanglements, generate high interfacial thermal

resistance between conducting crystalline domains such that the mean free path of the major energy carriers, phonons, is very short and the energy contained in high-frequency phonon modes must first transfer to low-frequency modes through phonon-phonon coupling in order for the energy to be exchanged across these defect locations. However, in low-dimensional polymeric nanofibers, defects due to fiber fractures are less likely to exist and polymer chains tend to form highly oriented structures because of the axial confinement and large surface aspect ratio. Liu and Yang[59] showed by molecular dynamics simulations that κ of polymer nanofibers is tunable through mechanical strain. They further examined the length dependence of κ in polymer nanofibers and found that the competition between ballistic phonon transport and diffusive phonon transport in a polymer chain leads to a diverging length-dependent thermal conductivity[60]. Henry *et al.*[56, 61] also showed that thermal conductivity increased with polymer chain length, specifically PE, and could be as large as several orders of magnitude greater than bulk PE. Ab-initio calculations performed by Jiang et al.[62] showed that κ of PE nanofibers can be as high as 100 W/m-K at room temperature. Zhang *et al.*[63] further showed that the thermal conductivity of PE nanofibers is tunable through morphology. Pal *et al.*[64] showed that the conductivity is enhanced as adjacent chains become more aligned along the direction of heat conduction but diminishes when they are oriented orthogonally to heat flow.

It is believed that stress imposed during the fiber drawing will re-orient the crystallites along the draw direction. These crystallites are connected by tie-molecules which originate in the unfolding polymer chains. Upon further drawing, increasing numbers of tie-molecules become fully extended, producing extended polymer chains

and leading to increases in average crystal sizes leading to both enhanced mechanical strength and thermal conductivity. Therefore, much effort has gone into developing advanced fabrication techniques to align the polymer chains by uniaxially stretching the bulk polymer into nanofibers for high modulus and high thermal conductivity. This includes direct proximal probe based drawing[55] and nanoporous template wetting.[65]

Despite these recent advancements in drawing techniques, there is still a lack of fundamental and quantitative understanding of the relationship between the structures and the attained thermal transport properties, specifically, how the anisotropic alignment of polymer crystallites in nanofibers is correlated with the heat transport. In Chapters 6 and 7 of this thesis, we cover the relationship between size, structure, and mechanical and thermal properties of individual semi-crystalline Nylon-11 nanofibers, aiming to shed light on the structure-property relationship.

1.7 Organization of the thesis

The first part of this dissertation (Chapter 2) details an enhanced experimental technique capable of measuring thermal conductance of ~10-11 W K^{-1}, ~100X more sensitive than the original method. The improved sensitivity is achieved by using an on-chip Wheatstone bridge circuit that overcomes several instrumentation issues and provides a more effective method of characterizing the thermal properties of smaller and less conductive one-dimensional nanostructures such as sub-30 nm semiconductor nanowires and polymer fibers. Heat losses and parasitic background signals are also discussed and methods to mitigate or remove them are detailed.

The next section (Chapters 3, 4, and 5) details thermal conductivity and mechanical measurements on sub-30 nm semiconductor nanostructures using the developed calorimetry setup. In Chapter 3, the thermal conductivities of pristine Ge and Ge-Si core-shell nanowires with diameters less than 20 nm were measured and found to be significantly lower than bulk SiGe alloys or smooth Si NWs of similar size. Boltzmann transport models reveal that thermal conductivities of the sub-20 nm nanowires are further suppressed beyond the diffusive boundary scattering limit by phonon confinement.

Next (Chapter 4), ~5 nm thick shelled crystalline Si nanotubes were found to have a low thermal conductivity of ~1.1 W m^{-1} K^{-1}, which is lower than the apparent boundary scattering limit, and ~30% lower than that of amorphous Si nanotubes of similar size. This finding diverges from the prevailing general notion that amorphous materials represent the lower limit of thermal transport, but can be explained by elastic softening measured *via* tensile testing for the crystalline Si nanotube. These results illustrate the prospect of using elastic softening to engineer lower than amorphous, or 'sub-amorphous', thermal conductivity in ultra-thin crystalline nanostructures.

Furthermore, in Chapter 5, strong size-dependent viscoelastic mechanical behavior is observed in ~8 nm thick shelled amorphous SiO_2 and Si nanotubes. Modeling shows that a ~1 nm thick fluid-like surface layer, with room temperature viscosity equivalent to that of bulk glass above 1000 °C, leads to the observed mechanical behavior and matches well with our experimental results. Additionally, temperature dependent creep tests indicate that the creep is due to bond motion/switching, as opposed to bond breaking.

The last section deals with thermal (Chapter 6) and mechanical (Chapter 7) properties of polymer nanofibers with diameters ranging from 100s of nanometers down to sub-100 nm. In Chapter 6, the axial thermal conductivity of individual polymer nanofibers fabricated by electrospinning is measured and shown to strongly correlate with the crystalline morphology measured by high-resolution wide-angle X-ray scattering. Meanwhile in Chapter 7, even larger increases in the elastic modulus are measured as the fiber diameter is reduced. Strong size-dependent stress relaxation is, however, also observed, enabling the smallest diameter fibers to break the stiffness-toughness tradeoff present in most material systems.

References

1. A. I. Hochbaum, R. K. Chen, R. D. Delgado, W. J. Liang, E. C. Garnett, M. Najarian, A. Majumdar and P. D. Yang, Nature **451** (7175), 163-167 (2008).

2. D. Y. Li, Y. Y. Wu, P. Kim, L. Shi, P. D. Yang and A. Majumdar, Appl Phys Lett **83** (14), 2934-2936 (2003).

3. A. I. Boukai, Y. Bunimovich, J. Tahir-Kheli, J. K. Yu, W. A. Goddard and J. R. Heath, Nature **451** (7175), 168-171 (2008).

4. G. Chen, *Nanoscale energy transport and conversion: a parallel treatment of electrons, molecules, phonons, and photons*. (Oxford University Press, USA, 2005).

5. A. I. Hochbaum, R. Chen, R. D. Delgado, W. Liang, E. C. Garnett, M. Najarian, A. Majumdar and P. Yang, Nature **451** (7175), 163-167 (2008).

6. D. Li, Y. Wu, P. Kim, L. Shi, P. Yang and A. Majumdar, Appl Phys Lett **83** (14), 2934-2936 (2003).

7. A. I. Boukai, Y. Bunimovich, J. Tahir-Kheli, J.-K. Yu, W. A. Goddard Iii and J. R. Heath, Nature **451** (7175), 168-171 (2008).

8. K. Esfarjani, G. Chen and H. T. Stokes, Phys Rev B **84** (8) (2011).

9. K. T. Regner, D. P. Sellan, Z. H. Su, C. H. Amon, A. J. H. McGaughey and J. A. Malen, Nat Commun **4** (2013).

10. Z. T. Tian, K. Esfarjani, J. Shiomi, A. S. Henry and G. Chen, Appl Phys Lett **99** (5) (2011).

11. K. Esfarjani, G. Chen and H. T. Stokes, Phys Rev B **84** (8), 085204 (2011).

12. M. Asheghi, M. N. Touzelbaev, K. E. Goodson, Y. K. Leung and S. S. Wong, Journal of Heat Transfer **120** (1), 30-36 (1998).

13. M. Asheghi, Y. K. Leung, S. S. Wong and K. E. Goodson, Appl Phys Lett **71** (13), 1798-1800 (1997).

14. Y. S. Ju and K. E. Goodson, Appl Phys Lett **74** (20), 3005-3007 (1999).

15. M. Asheghi, K. Kurabayashi, R. Kasnavi and K. E. Goodson, J Appl Phys **91** (8), 5079-5088 (2002).

16. X. Liu, X. Wu and T. Ren, Appl Phys Lett **98** (17), 174104 (2011).

17. S. Alaie, D. F. Goettler, K. Abbas, M. F. Su, C. M. Reinke, I. El-Kady and Z. C. Leseman, Rev Sci Instrum **84** (10), 105003 (2013).

18. H. Zhang, Z. Lv, L. Tian, Z. Tan, L. Liu and Z. Li, presented at the Solid-State and Integrated Circuit Technology, 2006. ICSICT '06. 8th International Conference on, 2006 (unpublished).

19. W. Liu and M. Asheghi, Journal of Heat Transfer **128** (1), 75-83 (2005).

20. W. Liu and M. Asheghi, Appl Phys Lett **84** (19), 3819-3821 (2004).

21. W. Liu and M. Asheghi, J Appl Phys **98** (12), 123523 (2005).

22. P. Ferrando-Villalba, A. F. Lopeandia, L. Abad, J. Llobet, M. Molina-Ruiz, G. Garcia, M. Gerboles, F. X. Alvarez, A. R. Goni, F. J. Munoz-Pascual and J. Rodriguez-Viejo, Nanotechnology **25** (18), 185402 (2014).

23. J. S. Reparaz, E. Chavez-Angel, M. R. Wagner, B. Graczykowski, J. Gomis-Bresco, F. Alzina and C. M. Sotomayor Torres, Rev Sci Instrum **85** (3), 034901 (2014).

24. E. Chávez-Ángel, J. S. Reparaz, J. Gomis-Bresco, M. R. Wagner, J. Cuffe, B. Graczykowski, A. Shchepetov, H. Jiang, M. Prunnila, J. Ahopelto, F. Alzina and C. M. Sotomayor Torres, APL Materials **2** (1), 012113 (2014).

25. J. Alvarez-Quintana, J. Rodríguez-Viejo, F. X. Alvarez and D. Jou, International Journal of Heat and Mass Transfer **54** (9–10), 1959-1962 (2011).

26. J. Cuffe, E. Chávez, A. Shchepetov, P.-O. Chapuis, E. H. El Boudouti, F. Alzina, T. Kehoe, J. Gomis-Bresco, D. Dudek, Y. Pennec, B. Djafari-Rouhani, M. Prunnila, J. Ahopelto and C. M. Sotomayor Torres, Nano Lett **12** (7), 3569-3573 (2012).

27. Y. Zhu, F. Xu, Q. Q. Qin, W. Y. Fung and W. Lu, Nano Lett **9** (11), 3934-3939 (2009).

28. H. Sadeghian, C. K. Yang, J. F. L. Goosen, E. van der Drift, A. Bossche, P. J. French and F. van Keulen, Appl Phys Lett **94** (22), 221903 (2009).

29. H. Sadeghian, C. K. Yang, J. F. L. Goosen, A. Bossche, U. Staufer, P. J. French and F. van Keulen, J Micromech Microeng **20** (6), 064012 (2010).

30. A. Jurgilaitis, H. Enquist, B. P. Andreasson, A. I. H. Persson, B. M. Borg, P. Caroff, K. A. Dick, M. Harb, H. Linke, R. Nuske, L. E. Wernersson and J. Larsson, Nano Lett **14** (2), 541-546 (2014).

31. J. Cuffe, O. Ristow, E. Chávez, A. Shchepetov, P. O. Chapuis, F. Alzina, M. Hettich, M. Prunnila, J. Ahopelto, T. Dekorsy and C. M. Sotomayor Torres, Phys Rev Lett **110** (9), 095503 (2013).

32. N. Mingo, L. Yang, D. Li and A. Majumdar, Nano Lett **3** (12), 1713-1716 (2003).

33. N. Mingo, Phys Rev B **68** (11), 113308 (2003).

34. R. Chen, A. I. Hochbaum, P. Murphy, J. Moore, P. Yang and A. Majumdar, Phys Rev Lett **101** (10), 105501 (2008).

35. A. Khitun, A. Balandin and K. L. Wang, Superlattices and Microstructures **26** (3), 181-193 (1999).

36. J. Zou and A. Balandin, J Appl Phys **89** (5), 2932-2938 (2001).

37. D. Donadio and G. Galli, Phys Rev Lett **102** (19), 195901 (2009).

38. Y. He and G. Galli, Phys Rev Lett **108** (21), 215901 (2012).

39. T. Zushi, K. Ohmori, K. Yamada and T. Watanabe, Phys Rev B **91** (11), 115308 (2015).

40. Y. Gao, W. Bao, Q. Meng, Y. Jing and X. Song, J Non-Cryst Solids **387** (0), 132-138 (2014).

41. D. Donadio and G. Galli, Nano Lett **10** (3), 847-851 (2010).

42. P. G. Murphy and J. E. Moore, Phys Rev B **76** (15), 155313 (2007).

43. K. I. Winey, T. Kashiwagi and M. F. Mu, Mrs Bull **32** (4), 348-353 (2007).

44. S. T. Huxtable, D. G. Cahill, S. Shenogin, L. P. Xue, R. Ozisik, P. Barone, M. Usrey, M. S. Strano, G. Siddons, M. Shim and P. Keblinski, Nat Mater **2** (11), 731-734 (2003).

45. C. L. Choy, Y. W. Wong, G. W. Yang and T. Kanamoto, J Polym Sci Pol Phys **37** (23), 3359-3367 (1999).

46. C. T. Lim, E. P. S. Tan and S. Y. Ng, Appl Phys Lett **92** (14) (2008).

47. T. Kanamoto, A. Tsuruta, K. Tanaka, M. Takeda and R. S. Porter, Macromolecules **21** (2), 470-477 (1988).

48. D. B. Mergenthaler, M. Pietralla, S. Roy and H. G. Kilian, Macromolecules **25** (13), 3500-3502 (1992).

49. B. Poulaert, J. C. Chielens, C. Vandenhende, J. P. Issi and R. Legras, Polym Commun **31** (4), 148-151 (1990).

50. P. Smith and P. J. Lemstra, J Mater Sci **15** (2), 505-514 (1980).

51. C. L. Choy, Y. Fei and T. G. Xi, J Polym Sci Pol Phys **31** (3), 365-370 (1993).

52. A. L. Moore, A. T. Cummings, J. M. Jensen, L. Shi and J. H. Koo, J Heat Trans-T Asme **131** (9) (2009).

53. C. L. Choy, E. L. Ong and F. C. Chen, J Appl Polym Sci **26** (7), 2325-2336 (1981).

54. G. DeCarvalho, E. Frollini and W. N. DosSantos, J Appl Polym Sci **62** (13), 2281-2285 (1996).

55. S. Shen, A. Henry, J. Tong, R. T. Zheng and G. Chen, Nat Nanotechnol **5** (4), 251-255 (2010).

56. A. Henry and G. Chen, Phys Rev Lett **101** (23) (2008).

57. A. Henry, G. Chen, S. J. Plimpton and A. Thompson, Phys Rev B **82** (14) (2010).

58. S. Lepri, R. Livi and A. Politi, Phys Rep **377** (1), 1-80 (2003).

59. J. Liu and R. G. Yang, Physical Review B **81** (17), 174122 (2010).

60. J. Liu and R. G. Yang, Physical Review B **86** (10), 104307 (2012).

61. A. Henry and G. Chen, Phys Rev B **79** (14) (2009).

62. J. W. Jiang, J. H. Zhao, K. Zhou and T. Rabczuk, Journal of Applied Physics **111** (12), 124304 (2012).

63. T. Zhang and T. Luo, Journal of Applied Physics **112**, 094304 (2012).

64. S. Pal, G. Balasubramanian and I. K. Puri, Journal of Chemical Physics **136** (4), 044901 (2012).

65. B. Y. Cao, Y. W. Li, J. Kong, H. Chen, Y. Xu, K. L. Yung and A. Cai, Polymer **52** (8), 1711-1715 (2011).

Chapter 2: High-resolution thermal conductance measurement of nanostructures enhanced by differential bridge

2.1 Introduction

Thermal conductivity measurements of individual one-dimensional (1D) nanostructures have attracted significant interest in the literature, including semiconductor nanowires,[1-3] single and multi-walled carbon nanotubes,[4-12] polymer nanofibers,[13] and molecular chains,[14] etc. These fundamental measurements not only advance our understanding of nanoscale thermal transport,[15-17] but have also shown broad implications for thermal management of nanostructure based nanoelectronics circuits,[18, 19] thermoelectric refrigeration and power generation[20] as well as the design of thermal interface materials.[21, 22]

Thermal properties of individual one-dimensional nanostructures have been measured quite extensively in the past by a variety of methods, including the commonly suspended micro-fabricated devices,[23] and its variations,[24] as well as the joule heating method.[6 25] Since the joule heating method is only applicable for electrically conducting materials, the direct, suspended device method is more commonly used. The device consists of heating and sensing membranes, separated by a small gap (several μm wide) and are thermally connected to the substrate solely by several long beams,[1, 2, 23, 26] as shown in Fig. 2.1A. The nanowire is located bridging the gap, in contact with both the heating and sensing membranes. A finite temperature difference between the membranes, measured by resistive thermometers, is used to

extract the thermal conductance of the nanowire. This standard, 4-point method has a measurement sensitivity of approximately 1 nW/K, as demonstrated by Shi *et al.*[23] Consequently, measurements are limited to measuring large diameter samples or small diameter samples which exhibit high thermal conductivity such as carbon nanotubes. For example, the thinnest nanowires with κ measured by this method are ~20 nm diameter Si nanowires with κ of approximately 10 W/m-K (thermal conductance G ~1 nW/K).[26]

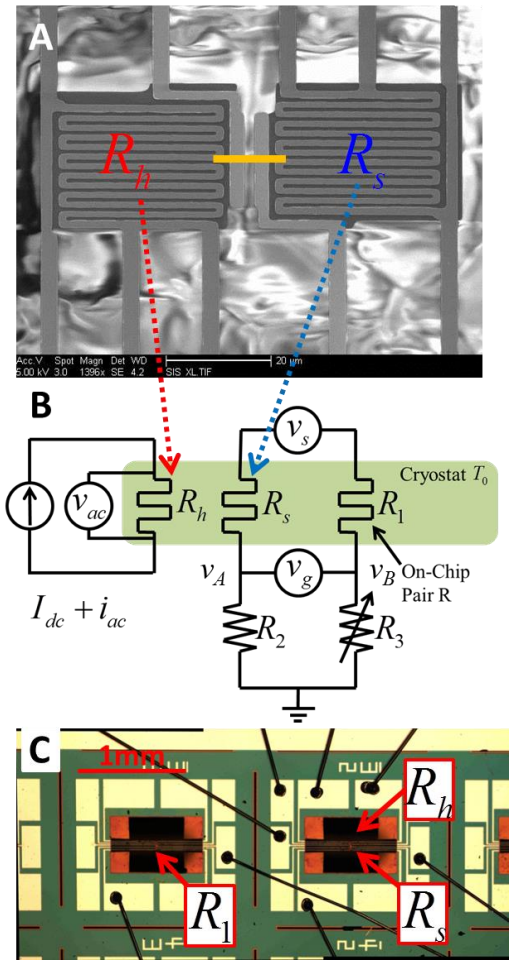


Figure 2.1: Experimental setup. (A) A SEM images of the suspended microdevice used for single nanowire κ measurement; (B) Electrical measurement setup including 4-point measurement of the heater resistance R_h, and bridge measurement of the sensor resistance Rs. (C) Photograph of the on-chip heating, sensing and pair resistors.

However, as the size of 1D nanostructures keeps shrinking, a more sensitive measurement technique is necessary to measure the thermal conductivity of smaller nanowires which would exhibit lower thermal conductivity. Consider the case of a nanowire with κ = 1 W/m-K, D = 10 nm and L = 1 μm, the thermal conductance G is approximately 80 pico-Watt/Kelvin (pW/K), about 10 times lower than the sensitivity of the current measurement technique. In order to overcome this limitation, a measurement system capable of measuring sub-10 pW/K thermal conductance would be extremely desirable as sub-10 nm diameter nanowires may exhibit new phonon transport physics, such as quantum confinement,[27] partial ballistic scattering,[26] ultra-low κ approaching the amorphous limit,[3] as well as providing experimental data to directly compare with atomistic scale simulations.[28] Such a sensitive measurement system could also be used to measure single wall carbon nanotubes,[7] polymer nanofibers,[13] or single strands of DNA.[29]

In this paper, we developed and characterized an ultra-sensitive technique for measuring thermal conductance of 1D nanostructures based on suspended micro-devices integrated into a Wheatstone bridge configuration. The Wheatstone bridge is extremely sensitive to small changes in resistance in one branch of the bridge and is commonly used for sensitive resistance detection, such as in a strain gauge. By using a bridge circuit based differential measurement instead of the absolute four-point I-V measurement, extremely small changes in resistance can be measured to detect temperature changes. This also takes advantage of the ability of the bridge circuit to reject common environmental instabilities such as fluctuations in ambient temperature. The steady-state thermal conductance measurement for nanowires can be significantly

enhanced through the use of a bridge circuit in conjunction with the microfabricated measurement device. In this paper, both the bridge system analysis and sample measurement results show that the measurement sensitivity is enhanced by a factor of nearly 100, with a thermal conductance measurement limit of approximately 10 pW/K. Our study shows that the bridge measurement setup is ideally suited for measuring low thermal conductance samples such as small diameter nanowires and thin materials with low thermal conductivity.

We also show measurements on a 15 nm diameter germanium (Ge) nanowire and the corresponding parasitic device background conductance signal (after the nanowire has been removed). This shows that for very low conductance measurements, the background signal becomes an appreciable portion of the measurement (about ~1/3 in this case) and cannot be neglected.

2.2 Bridge measurement: setup and verification

Similar to the standard 4-point I-V measurement,[23] the bridge based system consists of a micro-fabricated resistive platinum heater (R_h) and a resistive platinum thermometer (R_s). These make up the heating and sensing elements of the system, respectively. Changes in membrane resistance are used to monitor temperature in the systems. Each membrane is suspended by six long (> 400 μm) and narrow (< 2 μm) Si nitride beams (as seen in Figure 2.1A) ensuring heat loss from the sample to the ambient environment is small.[1, 23] In the 4-point configuration (no bridge circuit), κ of a nanowire placed across the gap of the device is measured by passing a direct current

I_{dc} through the Pt heater, thereby heating and raising the resistance of R_h. Both heating and sensing membrane resistances (R_h and R_s) are measured by 4-point *I*-*V* method using a small ac current i_{ac} (< 0.5 μA) and lock-in amplifiers.[1, 23] The 4-point method has a measured sensitivity of approximately 1 nW/K,[1, 23] which is mainly limited by two factors[23]: 1) large temperature fluctuation of the sample stage (> 20 mK); 2) amplifier noise due to the large dynamic range required to measure small voltage changes (μV range)) on top of a large output voltage (mV range).

The new measurement configuration using the Wheatstone bridge is shown schematically in Fig. 2.1B. Here, an additional on-chip pair Pt resistor (R_1), with nominally equal resistance compared to the sensing thermometer R_s, is used. R_1 is located on the same device chip as the heating and sensing membranes, but is comparatively far away from the heater and sensor such that the pair resistor R_1 will not be heated by I_{dc}. A suitable position for R_1 would be close in proximity to R_h and R_s (approximately 0.5 mm) in order to minimize the effects of variation in ambient temperature over the area of the chip.

During the bridge measurement, a DC current coupled to an AC current (I_{dc} + i_{ac}) with $i_{ac} \ll I_{dc}$ is applied to the heating membrane with a heating power of $P = I_{dc}^2 R_h$. A lock-in amplifier (Stanford Research SR830) is used to measure the AC voltage drop across the heater coil at 1ω. The heater coil TCR (temperature coefficient of resistance) is calculated after measuring the coil resistance over a large range of temperatures, similar to the previous method.[23] On the sensing side, however, the sensor resistance is measured using the Wheatstone bridge circuit instead of by 4-point

I-V measurement. The bridge circuit contains the sensing resistor (R_s), a pair resistor (R_1), both inside the cryogenic chamber, and a high precision resistor (R_2) as well as a variable resistor or potentiometer (R_3). For the following experiments, a Vishay/Spectrol model #534B1203JCB10 potentiometer was used. Alternatively, two variable resistor boxes (Extech Instruments model #380400 was used) can be substituted in for R_2 and R_3, which can be tuned to balance the bridge.

A small source voltage to drive the circuit (v_s), is applied using a second lock-in amplifier, which also measures the bridge gate voltage (v_g), defined as the voltage difference between the left and right branches, v_A and v_B respectively:

$$v_A = \frac{R_2}{R_s + R_2} v_s \tag{2.1}$$

$$v_B = \frac{R_3}{R_1 + R_3} v_s \tag{2.2}$$

Thus we can define the following gate voltage in terms of the four resistors and the source voltage:

$$v_g = v_A - v_B = \left(\frac{R_2}{R_s + R_2} - \frac{R_3}{R_1 + R_3} \right) v_s \tag{2.3}$$

Equation (2.3) allows, with trivial rearrangement, for the calculation of the sensor resistance as a function of the gate voltage, where all other quantities are known:

$$R_s = \frac{R_2}{\left(\frac{v_g}{v_s} + \frac{R_3}{R_1 + R_3} \right)} - R_2 \tag{2.4}$$

In the limit where R_3 approaches the resistance of R_2 (which is the case in our measurement), changes in ambient temperature are canceled out of the measurement, thereby guaranteeing that changes in the sensing resistance are the result of heat conducted from the heating membrane. This analysis however calculates the total sensor resistance, which is a sum of the coil resistance, R_c, and the resistance of its two supporting beams, $2R_b$. The temperature is uniform over the coil and membrane (T_s) but varies linearly along the beams from T_s to the ambient cryostat temperature, T_o. The total heated sensor resistance is given by:

$$R_s + \Delta R_s = 2\left[R_b + \frac{dR_b}{dT}\left(\frac{T_s - T_0}{2} \right) \right] + R_c + \frac{dR_c}{dT}\left(T_s - T_0 \right) \tag{2.5}$$

Hence the change in resistance (ΔR_s) is solely due to the temperature difference:

$$\Delta R_s = \left(\frac{dR_b}{dT} + \frac{dR_c}{dT} \right)\left(T_s - T_0 \right) \tag{2.6}$$

By this simple analysis, it is shown that the change in sensing resistance can be equivalently modeled as a uniform temperature change over the membrane and along the length of only one single beam. From this result, an effective dR/dT can be found. Using the $\Delta R_s / \Delta T$ measured from the bridge system, the effective change in resistance per degree change in temperature can be found to be:

$$\frac{\Delta R_{s,eff}}{\Delta T} = \left(\frac{\Delta R_s}{\Delta T} \right)\left(\frac{R_b + R_c}{2R_b + R_c} \right) \tag{2.7}$$

This allows the standard steady-state measurement analysis for suspended micro-fabricated devices to be used with slight modification.

Before starting the measurements, the bridge was first balanced by adjusting the potentiometer (R_3) such that v_g is in the 1-10 μV range. The bridge needs to be balanced manually only once at room temperature. At other temperatures, the bridge becomes self-balanced due to the symmetry of the bridge and because the sensing and pair resistors increase by approximately the same resistance. Strictly speaking, the bridge was not completely balanced as v_g was not zero. However, this would not cause errors in thermal measurement because R_s (which is related to ΔT_s and ultimately to G) is calculated from Eq. 2.4, which is strictly valid for a bridge circuit even when it is not completely balanced.

The bridge measurement shows great improvement in sensitivity compared to the standard 4-point measurement approach. This can obviously be seen in Figure 2.2A, comparing effective temperature changes measured by the bridge and 4-point methods. This shows that the 4-point voltage measurement follows step like behavior, due to digitization noise in the lock-in amplifier at a large output sensitivity range of 2 mV to accommodate the large background voltage on the thermometer. The bridge method effectively nullified the background signal leaving a small output signal at the gate (on the order of 1-10 μV). Using the bridge method, the sensing lock-in amplifier full-scale sensitivity was set to 5 μV, reduced by a factor of 400 compared to the 4-point measurement. Such dramatic increase of signal-background ratio from the bridge circuit eliminates the limitation on the dynamic range of the lock-in amplifier.

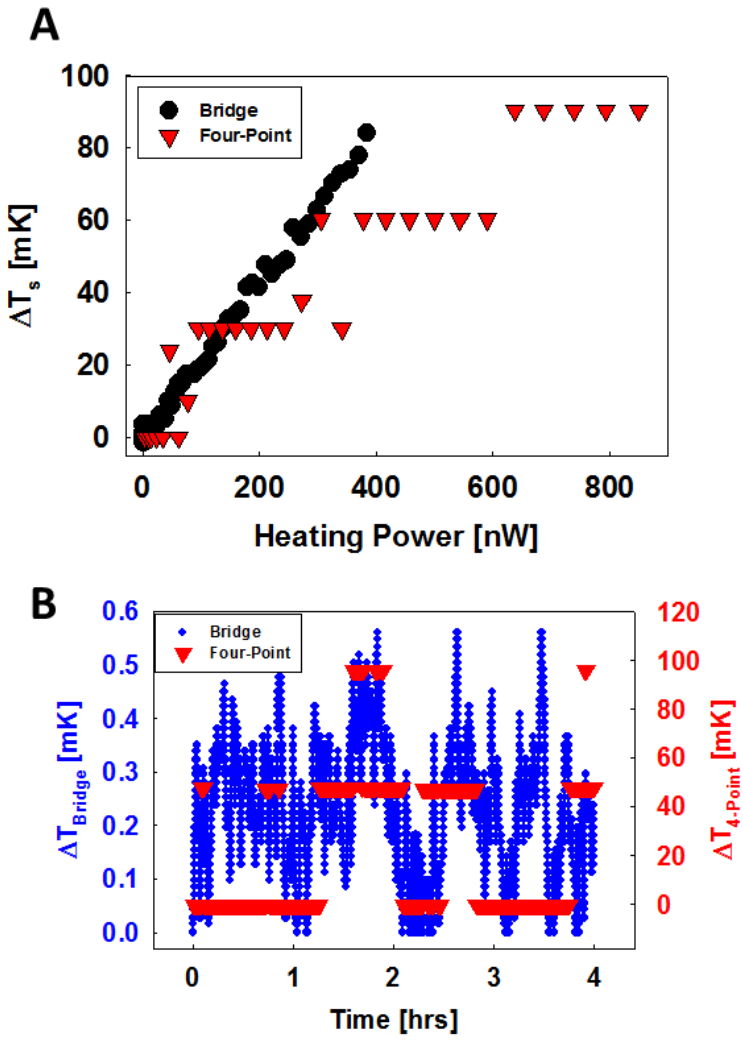


Figure 2.2: (A) Changes in sensing side temperature as a function of heating power passed through the heating membrane using bridge circuit and standard steady-state 4-point method. The enhanced sensitivity of the bridge circuit can be seen by comparing the step-like signal of the 4-point measurement to the smoother bridge signal. (B) The temperature fluctuation in the vacuum chamber as measured by the bridge and 4-point measurement methods.

Not only does the bridge configuration allow for more sensitive measurement of changes in resistance, it also allows for compensation of fluctuations in the ambient temperature of the cryostat. This is due to the sensor and on-chip pair resistors being nominally equal, such that global temperature increases affect both equally. The differential nature of the Wheatstone bridge cancels out such increases in resistance thanks to its symmetric design. Such behavior is shown in Figure 2.2B, where temperature fluctuations in the cryostat were measured over a four-hour time period using both the bridge configuration and 4-point method simultaneously. The 4-point measurement experiences a maximum temperature fluctuation of 100mK, which is within the temperature control range of the cryostat and temperature controller. The bridge measurement shows a very stable signal with an effective maximum temperature fluctuation of only 0.6 mK despite the ~100 mK fluctuation, thus effectively isolating the actual sample temp rise from the change in environment. This is nearly a 180-fold decrease and greatly reduces the limitations on measurable conductance due to specific cryostat and temperature controller capabilities.

In order to validate any results obtained using the bridge measurement setup, comparison between the bridge and traditional four-point methods was necessary. A 62-nm-diameter Ge nanowire was used for the measurement in order to make sure both methods were able to measure the conductance. Both the four-point and bridge measurements took place in the same cryo-chamber on the same suspended microfabricated device. The four-point measurement was run first and then device was re-configured to run as the bridge measurement. Both measurements were run from 300 to 340 K. The measured thermal conductivity of the 62 nm Ge nanowire obtained

using the bridge and four-point methods are shown in Figure 2.3. The thermal conductivity, as measured by the bridge, agrees well with the 4-point measurement. The small discrepancy (less than 10%) between the two measurements is due to the difference in the different values of TCR of the Pt resistive thermometers measured at different times. This indicates that the bridge method results are valid and can be trusted for smaller nanostructures with lower thermal conductance, which cannot be measured using the 4-point measurement.

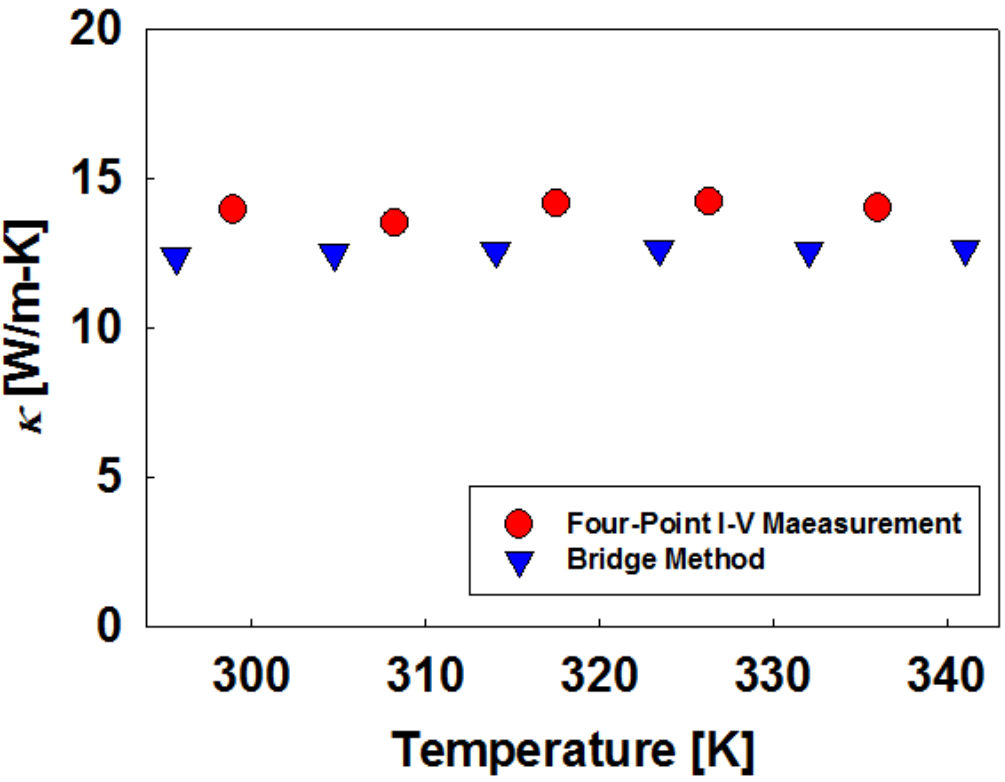


Figure 2.3: Thermal conductivity of a ~62nm Ge nanowire calculated using the bridge and four-point measurement methods.

2.3 Bridge measurement sensitivity

The sensitivity of the bridge measurement overcomes the sensitivity of the lock-in amplifier and is dictated by the voltage noise at the amplifier input. This noise is calculated using the time constant and filter roll-off settings of the amplifier. For the sensing resistor lock-in amplifier measurement, these correspond to 300 ms and 24 dB/oct, respectively. Given the input noise of the SR830 lock in amplifier of $5\,nV/\sqrt{Hz}$ and the equivalent noise bandwidth (ENBW, Δf) of 0.26 Hz ($\Delta f = 5/64\tau$ where τ is the time constant, 300 ms), the noise at the amplifier input is therefore,

$$N_{amp} = (5nV)\sqrt{\Delta f} = 2.6nV \tag{2.8}$$

Additional voltage noise is then caused by the individual resistors used in the bridge circuit itself. This Johnson noise is calculated for each resistor and is given by:

$$N_J = \sqrt{4k_B TR\Delta f} = 7.4nV \tag{2.9}$$

Here, T is the temperature of the resistor (300 K), R is the respective resistance value ($R_s = R_1 = R_2 = R_3 = 3.2k\Omega$), k_B is the Boltzmann constant, and Δf is the equivalent noise bandwidth (0.26Hz). The total voltage noise at the lock-in input is calculated using all of the noise sources in the system:

$$\Delta V_g = \sqrt{\sum_i N_i^2} \approx 8nV \tag{2.10}$$

Using Eq. (2.3), we can define a small change in sensor resistance corresponding to a small change in gate voltage. After setting the gate voltage change equal to the total voltage noise, the limit of the resistance change (noise equivalent

resistance) that can be resolved can be found. Assuming that the resistance values are much larger than the change in resistance, we can calculate the following:

$$\Delta R_s = \left(\frac{\Delta V_g}{V_s} \right) \frac{\left(R_s + R_2 \right)^2}{R_2} \approx 5 m\Omega \tag{2.11}$$

Using the measured temperature coefficient of resistance (TCR) of the platinum coil (0.0018/K), the noise equivalent temperature (NET) can be defined from the noise equivalent resistance calculated above:

$$NET = \frac{\Delta R_s \big/ R_s}{TCR} \approx 0.6 mK \tag{2.12}$$

This NET, 0.6 mK, is consistent with Fig. 2.2B and is much lower than that of the 4-point method using similar micro-devices, 13-27 mK at 300 K (as seen in Figure 2.2A).[23] Tests at lower temperatures show that there is no appreciable change in the sensitivity.

Finally, a noise equivalent conductance (NEG_s) can be defined, representing the resolution of the measured conductance. To calculate the resolution, we used the previously calculated NET, the conductance of the suspending beams measured experimentally (~98 nW/K), and the temperature difference between the heating and sensing membranes (~ 5 K):

$$NEG_s = G_b \frac{NET}{\Delta T_h - \Delta T_s} \approx 12\ pW / K \tag{2.13}$$

This is approximately 100 times more sensitive than the 4-point method ($NEG_s \approx 1 nW / K$).[23]

Experimental validation of the above calculations was performed at 300K. Several lock-in bridge settings were also varied to experimentally fine tune the sensitivity. From the ENBW ($\Delta f = 5/64\tau$) and Eq. (2.11), the two settings that can be easily changed are the lock-in time constant, τ, and the bridge circuit drive voltage, v_s. Figure 2.4 shows temperature rise of the sensing resistor versus applied heating power of the heater for cases of 20, 70, and 100 mV applied to drive the bridge circuit as well as time constants of 0.3, 1, 3, and 10 s. These measurements were taken while measuring the background signal (consisting of radiation, conduction by residual gas molecules, etc.) with no wires or solid materials bridging the two membranes. The output signal from the bridge can easily be measured due to background heat transfer, whereas output from the 4-point measurement of the sensor is not sensitive enough to capture this behavior and only experiences the noise in the system. As can be seen in Figure 2.4A, B and C, for any applied voltage, increasing the time constant allows for a smoother, more accurate measurement, although total measurement time must still be practical. The inset of Figure 2.4A shows that NET falls from 2 mK with a time constant of 0.3 s to 1 mK with a 10 s time constant for 20 mV applied voltage. For 70 mV applied voltage, NET falls from 1mK for τ = 3 s to less than 0.5 mK for τ = 10 s (Figure 2.4B). As the driving voltage is increased to 100 mV (Figure 2.4C), NET is, conservatively, 1 mK for τ = 0.3 s, down to less than 0.5 mK for τ > 3 s. The associated temperature rise in the heating and sensing resistances shows that heat conducted to the sensing side is very small compared to Joule heating of the heater coil. From the approximate NETs in Fig. 2.4, $NEG_s s$ can be calculated using Eq.

(2.13). For a 5 K difference between the heating and sensing membranes, the NEG_s is ~40, ~20 and ~10 pW/K for NET values of 2, 1 and 0.5 mK, respectively. This compares favorably to the previous calculations while also exhibiting better resolution due to slight changes in the measurement settings.

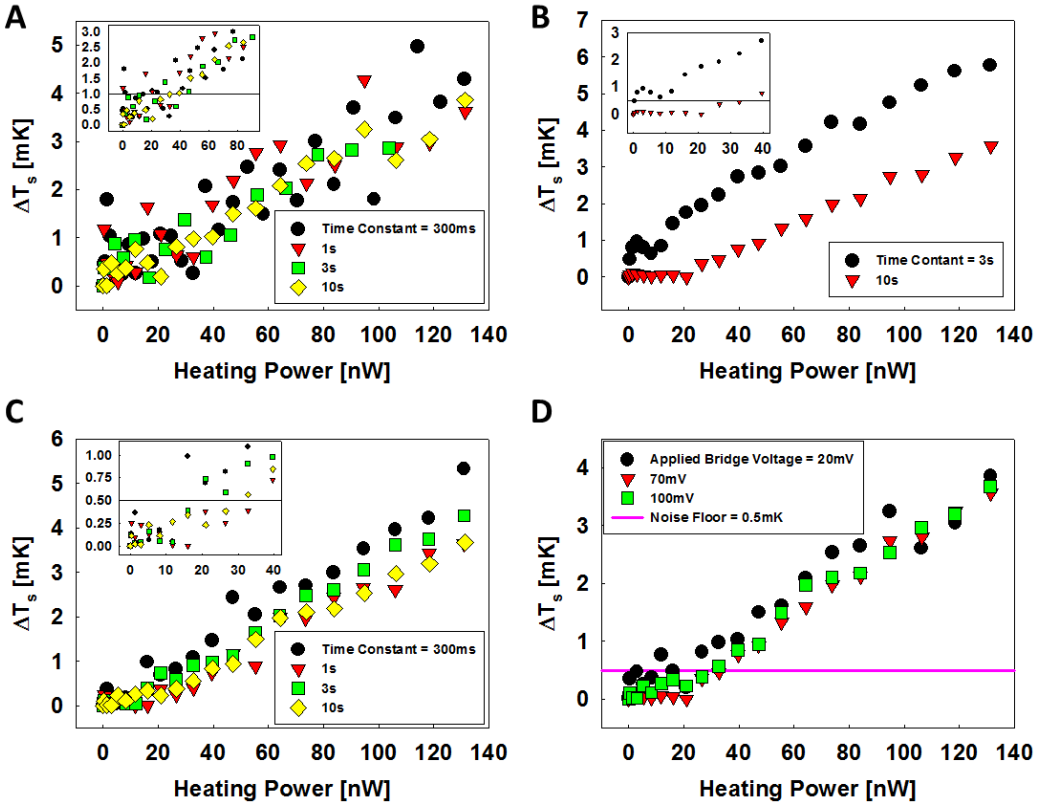


Figure 2.4: Temperature rise of the sensing membrane as measured by the bridge circuit for different lock-in time constants (0.3 s, 1 s, 3 s, and 10 s) with (A) 20mV, (B) 70mV, (C) 100mV applied to the bridge. The insets of (A), (B), and (C) show close up portions of the curves to identify noise equivalent temperature (NET) of the measurement. (D) Compares the 10 s time constant signals for each of the voltages applied to the bridge.

With greatly increased sensitivity to changes in resistance and measurement limitations due to lock-in amplifier mechanisms and temperature control, the bridge setup is ideal for measuring thermal conductance of small diameter nanowires with low thermal conductivity. Consider a nanowire at 30 K with only four acoustic phonon modes filled, the maximum conductance of such a wire is $4g_o = 0.11nW/K$.[27] The case of a 10 nm diameter nanowire with a thermal conductivity of 1 W/m-K can also be considered. Assuming a length equal to the gap between the heating and sensing membranes (1 μm), the wire would have a conductance of 78.5 pW/K. Both cases are comfortably within the measurable range of the bridge measurement system detailed above.

Future improvement of the measurement sensitivity can be attained by reducing the resistances and improving the sensing coil *TCR*, by using a NbN resistance thermometer[30] rather than Pt. Also, if the geometry of the beams is altered to reduce the beam conductance-one can further reduce the heat loss to the environment and improve the *G* measurement sensitivity (Eq. (2.13)).

2.4 Demonstration of the bridge method on a thin germanium nanowire

To demonstrate the superior sensitivity of the new bridge method, the thermal conductance of a ~15 nm diameter Ge nanowire was measured. Ge nanowire is expected to show lower thermal conductance compared to Si nanowires with similar diameters because of the larger atomic mass of Ge. Measurement on ~20 nm diameter

Si nanowires has been done using the 4-point I-V method,[26] but the measurement was performed at the vicinity of the sensitivity limit of this method, and hence is not applicable for thin Ge nanowires or smaller Si nanowires. The suspended device consisting of the thin Ge nanowire is shown in Fig. 2.5A. The measured Ge nanowires were grown by chemical vapor deposition (CVD)[31] and submerged in solutions of organic solvent (isopropanol).[26] These solutions were sonicated to disperse Ge nanowires from the wafer into the solution. Solutions with appropriate concentrations of dispersed nanowires were then drop cast onto the suspended measurement device chips. As the solution evaporated, nanowires migrated to the devices and a very small fraction bridged the gap between the heating and sensing membranes. Devices with suitably located single nanowires were chosen for bridge measurements. Nanowire samples were measured within a cryogenic chamber cooled by a closed cycle liquid helium system. The system was evacuated to ~10^{-5} torr ensuring that heat transfer due to conduction and convection was negligible. A radiation shield placed between the sample and chamber housing was also used to minimize the radiative exchange between the measurement device and the surrounding environment.[32]

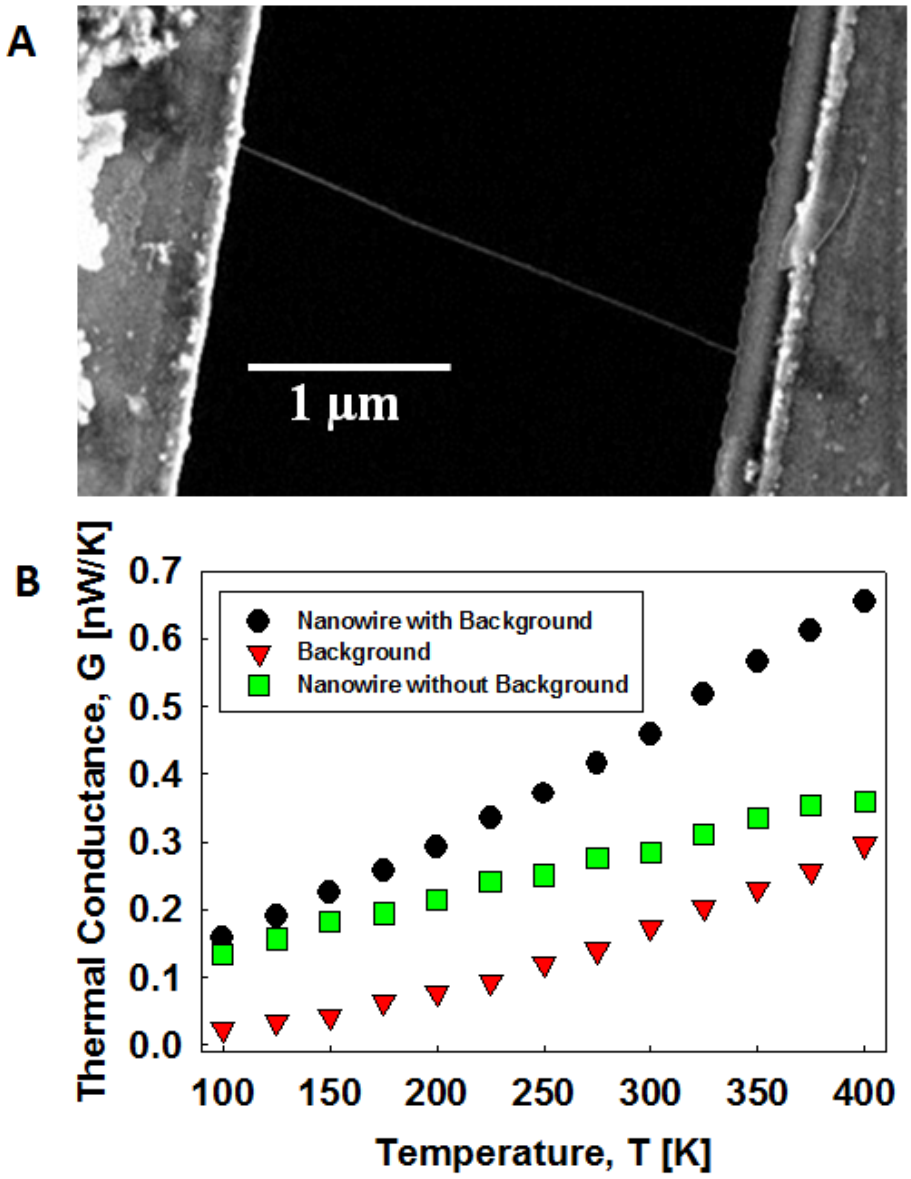


Figure 2.5: Suspended 15 nm Germanium nanowire bridging the gap between the heating and sensing membranes. Thermal conductance of a 15 nm diameter Ge nanowire with the background signal, the background radiation signal (with nanowire removed) and the conductance of the nanowire with the background subtracted, all measured with the bridge measurement setup.

Figure 2.5B shows the thermal conductance of the nanowire compared to the background signal (consisting of radiation, conduction by residual gas molecules, etc.) for the device, over the range of 100-400 K. The background conductance was measured after measuring the conductance of the nanowire and cutting the wire from the membranes using a focused ion beam (FIB). The bridge based conductance measurement was run again without the nanowire, measuring the conductance equivalent of the radiation transfer and residual gas molecules between the heating and sensing membranes. The difference between the two signals represents the thermal conductance of the nanowire. As shown in Fig. 2.5B, the background signal is an appreciable proportion (~1/3) of the conductance measured for the 15-nm diameter nanowire and indicates that when measuring very small conductance values, the heat transfer between device membranes is no longer negligible. The capability to measure the small background conductance represents an important advantage of the bridge method over that of the 4-point for accurately measuring 1D nanostructures with sub nW/K thermal conductance. The measured conductance at 300 K, ~0.5 nW/K for the nanowire with background of ~0.2 nW/K, are well within the measurable conductance range as specified by the $NEG_s \approx 10\,pW/K$. Therefore, smaller wires less than 10 nm in diameter may also be measured using this setup.

2.5 Characterization of heat loss from heating beams

2.6 Modeling heat loss in variable length beams

In the previous sections, we analyzed the thermal models describing the fabricated measurement device, assuming negligible heat loss along the length of the suspending beams. In order to verify the validity of this assumption, we measured average temperature of the self-heated microfabricated beams using the schematic shown in Fig. 2.6(b) and compared to results to a theoretical model that takes the heat loss into account. In this experiment, SiN_x beams of varying lengths (100, 200, 400 μm) coated with Pt for self-heating and temperature sensing were utilized for the comparison (Fig. 2.6).

The heat loss along the beam is modeled by a constant heat transfer coefficient, *h*, from the beam to the ambient. The heat transfer equation along the beam thus follows the fin model (Fig. 2.6(a)):

$$kA\frac{d^2T}{dx^2} - hP(T - T_o) + \frac{Q}{L} = 0 \qquad (2.14)$$

where *A* is the cross sectional area, *L* is the length of the beam (note that $L = 2L_b$), *T* is the temperature along the beam, T_o is the ambient temperature, *h* is the heat transfer coefficient, *P* is the perimeter of the SiN_x surfaces, and *Q* is the electrical power dissipated in the beam.

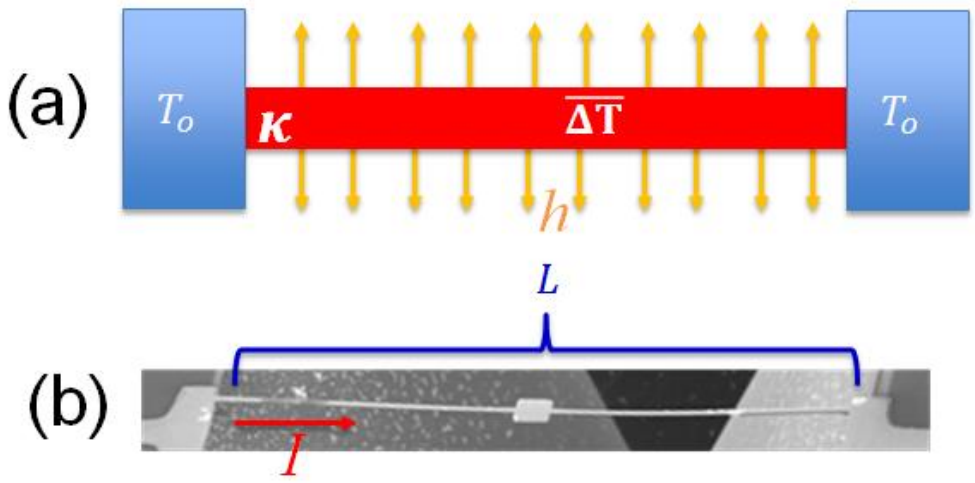


Figure 2.6: Thermal conductivity (κ) and heat transfer coefficient (h) determination of the SiNx beams. (a) Schematic of the thermal fin model. (b) A suspended beam of total length L self-heated by applying a current I.

In the case when the heat loss is negligible (h=0):

$$\Delta T = T - T_o = \frac{Qx}{2kA}\left(1 - \frac{x}{L}\right) \tag{2.15}$$

$$\overline{\Delta T} = \frac{QL}{12kA} \tag{2.16}$$

$$\frac{Q}{\overline{\Delta T}} = \frac{12kA}{L} \tag{2.17}$$

Whereas assuming heat loss is not negligible ($h \neq 0$)[33]:

$$\Delta T = \frac{Q}{hPL}\left[1 - \frac{\sinh(mx)+\sinh(m(L-x))}{\sinh(mL)}\right] \tag{2.18}$$

where

$$m = \sqrt{\frac{hP}{kA}} \tag{2.19}$$

and subsequently,

$$\overline{\Delta T} = \frac{Q}{hPL}\left[1 - \frac{2(\cosh(mL)-1)}{mL\sinh(mL)}\right] \tag{2.20}$$

$$\frac{Q}{\overline{\Delta T}} = \frac{hPL}{\left[1-\frac{2(\cosh(mL)-1)}{mL\sinh(mL)}\right]} \tag{2.21}$$

Figure 2.7 shows heating power over average beam temperature vs. beam width divided by length. For short beam lengths (<200 μm), the negligible and non-negligible heat loss models converge, validating the simplified thermal analysis. For longer beams, however, heat loss becomes increasingly significant, such that neglecting heat loss can lead to an overestimated temperature rise.

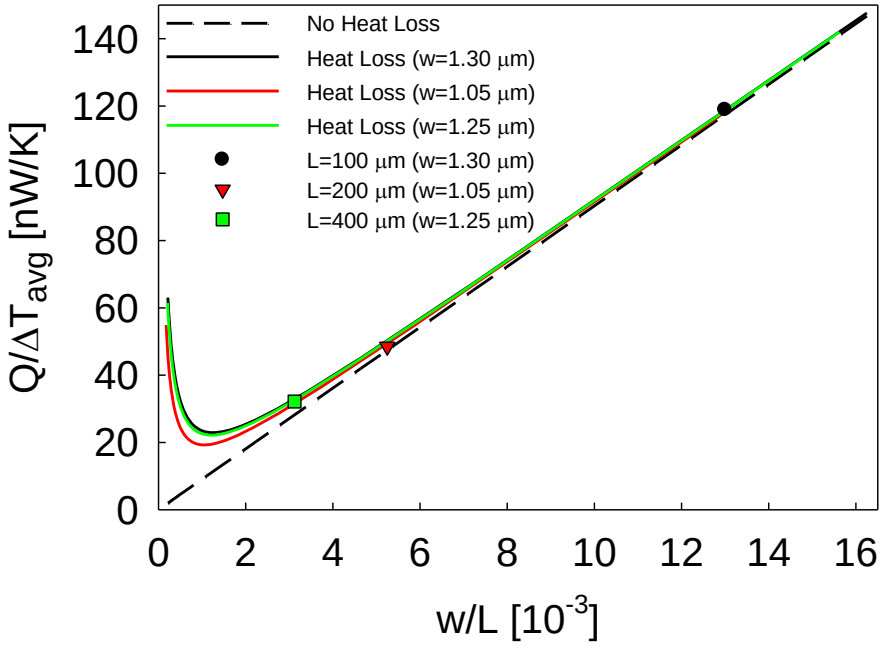


Figure 2.7: Heating power over average temperature rise vs. width over length for suspended beams with and without heat loss, solid and dashed lines, respectively. Three microfabricated beams of different lengths (100, 200, 400 μm) were measured (solid dots) and compared to theoretical curves with fitted thermal conductivity and heat transfer coefficient.

The effective thermal conductivity of the Pt coated SiN_x can be found from fitting the short length beams to the negligible or non-negligible heat loss models. With knowledge of the effective thermal conductivity of the beams, we can calculate the heat transfer coefficient describing the heat loss for longer beams. After calculating the effective thermal conductivity of the beams from 300 to 450 K using the 100-μm-long device, we calculated the heat transfer coefficient at each ambient temperature using the 400-μm-long beam, as shown in Fig. S6. In the limit of small temperature rise due to the self-heating (< 10 K), one can also estimate the heat transfer coefficient due to radiation heat transfer from the SiNx beam to the ambient from:

$$h_r = 4\varepsilon\sigma T^3 \qquad (2.22)$$

where ε and σ are the emissivity (0.88 for SiN_x[34]) and Stefan-Boltzmann constant, respectively. The calculated h_r is also plotted as the dash line in Fig. 2.8. The measured and calculated heat transfer coefficient values are in good agreement with each other, leading us to believe that that heat loss in the suspended structures is primarily due to radiative thermal exchange with the sample surroundings.

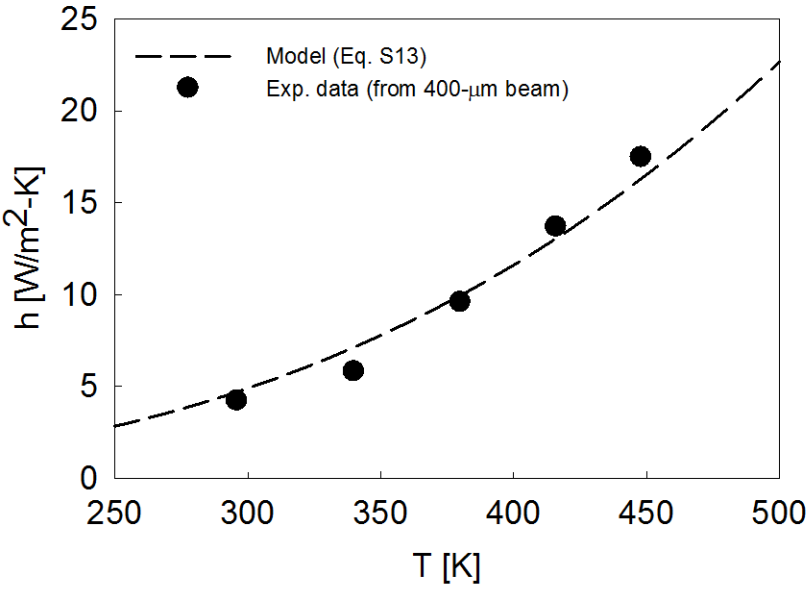


Figure 2.8: Measured (dots) and calculated (dash line, Eq. 2.22) heat transfer coefficient for the 400-μm-long beam from 300 to 450 K.

2.7 Verification of negligible heat loss in short-beam devices

In the previous section, it was shown that the heat loss is negligible in devices with $L = 100\ \mu m$ (or $L_b = 50\ \mu m$). Therefore, these short-beam suspended devices were chosen in this study for thermal measurements in order to ensure accurate thermal analysis (in addition to the fact that the short-beam devices have smaller thermal time constant and higher roll-off frequency). To directly verify negligible heat loss from the beams in the short-beam devices, we fabricated suspended devices with the same beam length ($L_b = 50\ \mu m$) but containing pads with serpentine Pt lines in order to measure temperature of both the beams and the pads (Fig. 2.9).

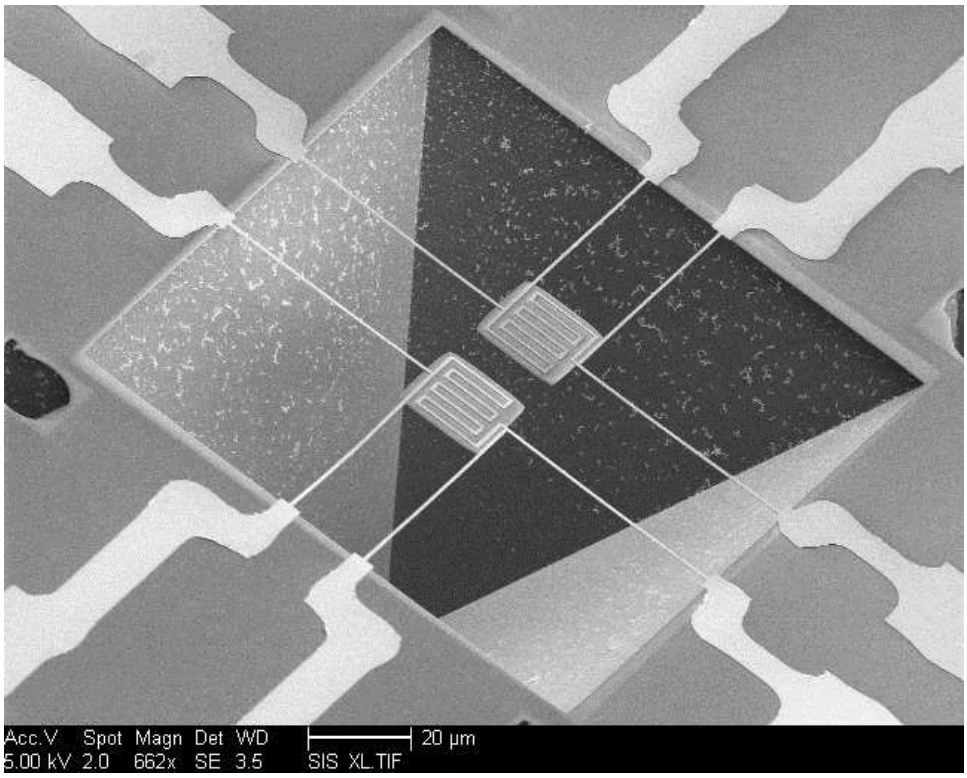


Figure 2.9: SEM image of microfabricated short-beam ($L_b = 50\ \mu m$) suspended device with pads containing serpentine Pt lines.

The average temperature rise of the self-heated beams, non-self-heated beams, and the suspended pads were measured and are plotted in Fig. 2.10. It can be shown that, for beams with negligible heat loss, the average temperature rise for the self-heated and non-self-heated beams is 2/3 and 1/2 of that for the pad, respectively, as we observed experimentally (Fig. 2.10). Therefore, we have verified experimentally that the heat loss from devices with $L_b = 50\ \mu m$ is negligible at room temperature.

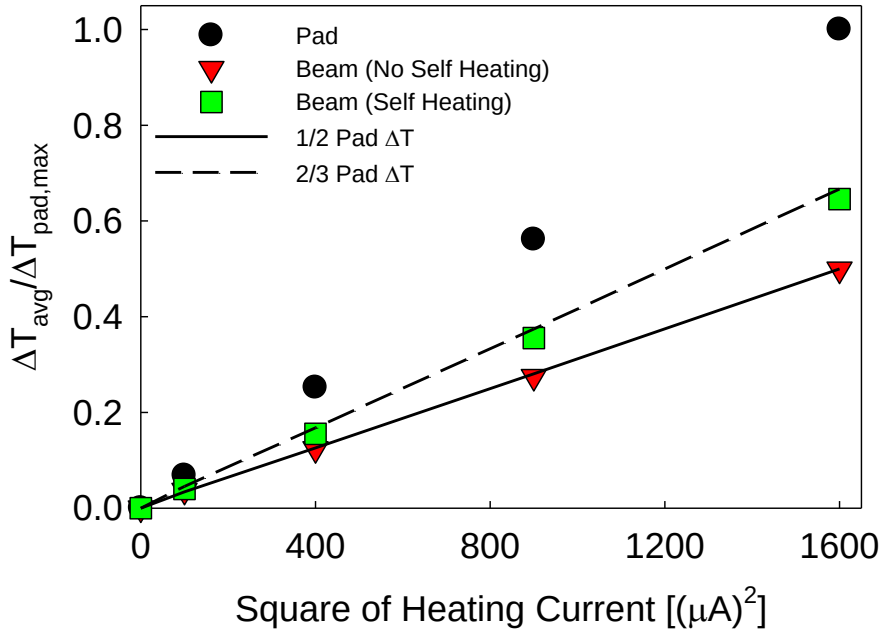


Figure 2.10: Average measured temperature rise of suspended pad and suspending beams for two cases, self-heating (green square) and no self-heating (red triangle). Dashed and solid lines represent 2/3 and 1/2 of the pad temperature rise (black circle), respectively.

2.8 Effects of heat loss from long-beam suspended devices

For devices suspended by long/wide beams, such as those used in this study, heat loss along the length via radiation or conduction by residual gas molecules may not be negligible, and needs to be examined.[35] First, assuming the heat loss from a suspended beam to the ambient is characterized by *h*, the heat transfer coefficient along the beam, the differential temperature distribution along the suspended beam is

$$\Delta T = \frac{\theta_L \sinh(mx) + \theta_b \sinh(m(L-x))}{\sinh(mL)}, \qquad (2.23)$$

and the heat current transferred through that beam from the suspending pad to the environment is

$$Q = \sqrt{hPkA}\,\frac{\theta_b \cosh(mL) - \theta_L}{\sinh(mL)}, \tag{2.24}$$

where P is the perimeter of surfaces undergoing heat loss along the beam, k is the thermal conductivity of the beam, A is the cross sectional area of the beam, L is the length of the beam, $m = \sqrt{hP/(kA)}$, and on the heating pad

$$\theta_L = \begin{cases} \frac{I_h^2 R_b}{hPL}, & heating\ beam \\ 0, & non-heating\ beam \end{cases} \tag{2.25}$$

$$\theta_b = \begin{cases} \Delta T_h - \frac{I_h^2 R_b}{hPL}, & heating\ beam \\ \Delta T_h, & non-heating\ beam \end{cases} \tag{2.26}$$

while on the sensing pad

$$\theta_L = 0 \tag{2.27}$$

$$\theta_b = \Delta T_s \tag{2.28}$$

where ΔT_h is the temperature rise of the heating pad, ΔT_s is the temperature rise of the sensing pad, I_h is the DC heating current applied to the heating pad, and R_b is the resistance of one suspending beam.

Since the total power input to the heating pad ($I_h^2 R_c$) is dissipated through the suspending beams (each with resistance R_b) of both the heating and sensing pads, an energy balance gives us

$$I_h^2 R_c = -4kA \left.\frac{\partial T}{\partial x}\right|_{\substack{x=0,non-heating,\\ heating\ pad}} - 2kA \left.\frac{\partial T}{\partial x}\right|_{\substack{x=0,heating,\\ heating\ pad}} - 6kA \left.\frac{\partial T}{\partial x}\right|_{x=0,sensing\ pad}, \tag{2.29}$$

which becomes

$$I_h^2 R_c = 6\sqrt{hPkA}\coth(mL)\,[\Delta T_h + \Delta T_s] - 2I_h^2 R_b \frac{\cosh(mL) - 1}{mL \sinh(mL)}, \tag{2.30}$$

and can be simplified to

$$I_h^2 R_c + 2f I_h^2 R_b = P_{tot} = G_L(\Delta T_h + \Delta T_s), \quad (2.31)$$

where $G_L = 6\sqrt{hPkA}\coth(mL)$ is the total heat loss conductance from the pad, including the heat conduction along the beams and heat loss from the beams to the environment, and *f* is defined as the heat loss factor

$$f = \frac{\cosh(mL)-1}{mL\sinh(mL)}. \quad (2.32)$$

For simplicity, P_{tot} has been defined as the multiplication factor γ multiplied by the power dissipated in the suspended pad ($P_0 = I_h^2 R_c$), namely,

$$P_{tot} = \gamma P_0 = \gamma I_h^2 R_c, \quad (2.33)$$

and γ is a multiplication factor

$$\gamma = 1 + 2f\frac{R_b}{R_c}. \quad (2.34)$$

Importantly, *f* represents the fraction of heat generated in the supporting beam that conducts into the suspended pad. When heat loss is negligible, $h \to 0$, the heat loss factor f approaches the value 0.5, representing half the heat dissipated in the suspending beams conducting into the heating membrane and the other half conducting to the substrate. In this case, the multiplication factor becomes

$$\gamma = 1 + \frac{R_b}{R_c}, \quad (2.35)$$

which is the definition used for previous analysis[1] of suspended nanowire measurements with negligible heat loss assumed.

The sensing side measurement requires the use of a Wheatstone bridge circuit, which measures the change in resistance of the suspended pad coil and two of the supporting beams. This leads to a non-uniform temperature distribution, which requires a slight change in the TCR used.[36] That definition, however, is based on the

linear temperature distribution in the suspending beams on the sensing side and therefore must also be altered:

$$\Delta R_s = 2\frac{dR_b}{dT}\overline{\Delta T_b} + \frac{dR_c}{dT}\Delta T_p = 2\frac{dR_b}{dT}f\Delta T_p + \frac{dR_c}{dT}\Delta T_p \quad (2.36)$$

$$TCR_{s,eff} = \left(\frac{dR_s}{dT}\right)_{eff} = \left(\frac{dR_s}{dT}\right)\frac{2fR_b+R_c}{2R_b+R_c} \quad (2.37)$$

where ΔR_s is the change in resistance of the sensing side including coil and two beams, R_b is the resistance of a single suspending beam, and R_c is the resistance of the coil on the suspended pad.

It is shown from both eqs. (2.34) and (2.37) that the heat loss factor *f* is an important parameter which dictates the degree of heat loss. The heat transfer coefficient, *h*, has been experimentally measured and was found to be well predicted by radiation heat transfer $h = 4\sigma\varepsilon T^3$, where σ is the Stefan-Boltzmann constant, ε is the emissivity of SiN_x, and T is the absolute temperature of the ambient sample environment.[37] Based on this, we can predict *f* as function of the ambient temperature according to eq. (2.32). As shown in Figure 2.11a, *f* varies from 0.5 at low temperature to approximately 0.46 at room temperature. Furthermore, definitions of γ and $TCR_{s,eff}$ above can be used to see the effect of heat loss on the system. Heat loss reduces the amount of heat generated in the beam being conducted to the pad and has a larger effect at higher ambient temperatures (Figure 2.11b), but its overall impact on γ in the studied system is negligible, as shown by the small change in γ (< 1%) from the no heat loss case. The change in the calculated TCR from ideal (no heat loss) conditions is also small (<2% change) (Figure 2.11c). Since the nanowire sample conductance

G_{nw} is calculated from the measured temperature rises of the heating (ΔT_h) and sensing pads (ΔT_s),[1]

$$\Delta T_h = \Delta R_h \Big/ \left(\frac{dR_h}{dT}\right) = \frac{G_L+G_{nw}}{G_L(G_L+2G_{nw})}\gamma P_0, \quad (2.38)$$

$$\Delta T_s = \Delta R_s \Big/ \left(\frac{dR_s}{dT}\right)_{eff} = \frac{G_{nw}}{G_L(G_L+2G_{nw})}\gamma P_0, \quad (2.39)$$

the parameters affected by the heat loss factor each affect the calculated conductance. Since γ and $TCR_{s,eff}$ are not significantly altered, the cumulative effects on the nanowire conductance are themselves limited, as seen in Figure 2.11(d) (< 1%). Therefore, for the system geometry and temperature range studied herein, the heat loss along the suspended beams has negligible effect compared to the other uncertainties in the measurement.

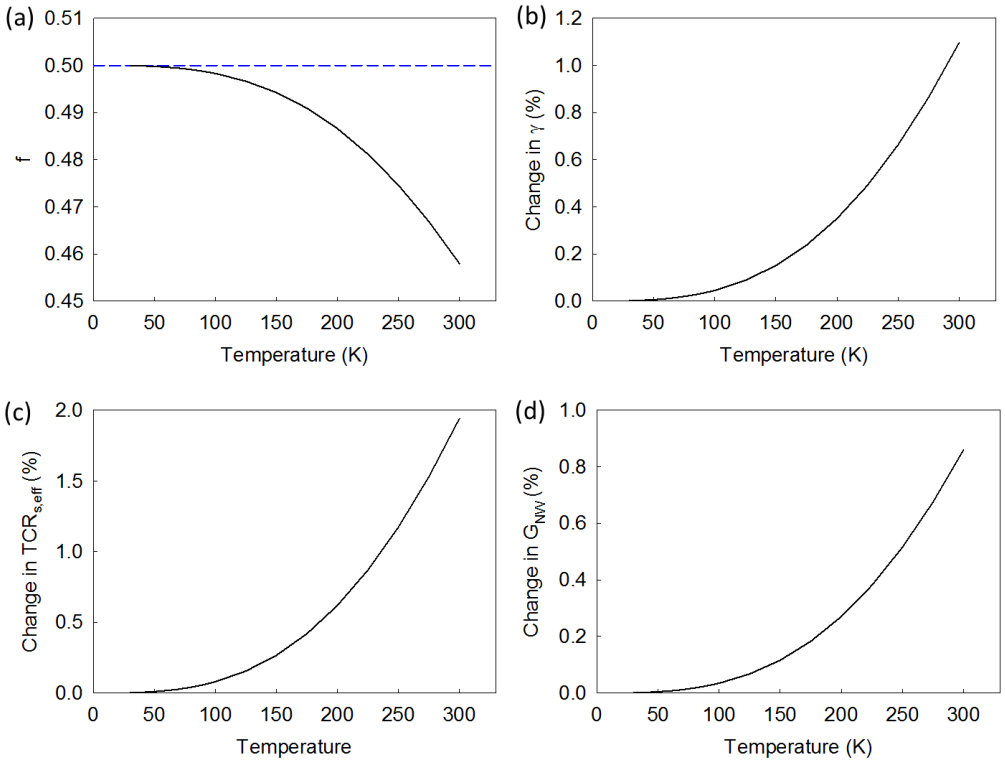


Figure 2.11: (a) Heat loss factor versus temperature. The upper limit of the heat loss factor is 0.5 for no or negligible heat loss (blue dashed line). (b) Percent change in γ versus temperature. (c) Percent change in TCRs,eff versus temperature. (d) Percent change in calculated nanowire conductance versus temperature. All based on average measured values of device parameters such as beam and coil resistance.

2.9 Background conductance and cancellation

The enhanced resolution of bridge-based thermal measurements also captures the background conductance transferred between the suspended beams. While this is always present, we can use the bridge system's inherent symmetry to subtract this signal. As shown in Fig. 2.12 (a), one can construct a 'cancelling' bridge circuit to measure the conductance difference between a device with a nanowire sample (called device 1 hereafter) and a blank pair device without a nanowire (called device 2

hereafter). In this 'cancelling' scheme, an identical heating current (I_h) is applied to the heating sides (R_h and $R_{h,p}$) of both devices, and the difference in the temperature rises (or resistance changes on R_s and $R_{s,p}$) on the sensing sides of the two devices is directly measured using a Wheatstone bridge. Since the devices are almost identical and their background conductance values are about the same (as we will show later), we can directly obtain the nanowire conductance from a single measurement based on this scheme (i.e., $G_{NW} = G_{NW+BG,1} - G_{BG,2}$).

Figure 2.12 (b) shows the measurement results for devices with 400-μm beam length we used previously. The long-beam devices were used here for demonstration purposes because these devices possess G_{BG} values of the same order of magnitude as a nanowire sample (~100 pW/K). First, the total conductance of device 1 containing a nanowire sample ($G_{NW+BG,1}$) was measured without the canceling scheme (shown by the red triangles in Fig. 2.12 (b)), followed by the previously-described canceling scheme, which essentially directly measured G_{NW} ($G_{NW+BG,1} - G_{BG,2}$, shown as black circles). The difference in these two measurements (green squares) yields the background conductance of device 2 ($G_{BG,2}$). Subsequently, the nanowire in device 1 was cut using a FIB, and its background conductance ($G_{BG,1}$) was measured (blue triangles). The difference in $G_{NW+BG,1}$ and ($G_{BG,1}$) yields the intrinsic conductance of the NW (blue hexagons). Finally, another cancelling measurement on the two blank devices (devices 1 & 2) showed essentially negligible conductance (yellow diamonds) within the measurement uncertainty, which proved that the background conductance of the two devices are the same (i.e., $G_{BG,1} = G_{BG,2}$). In effect, the cancelling scheme

shown in Fig. 2.12 (a) is capable of directly measuring the nanowire conductance (i.e., $G_{NW+BG,1} - G_{BG,2} = G_{NW}$).

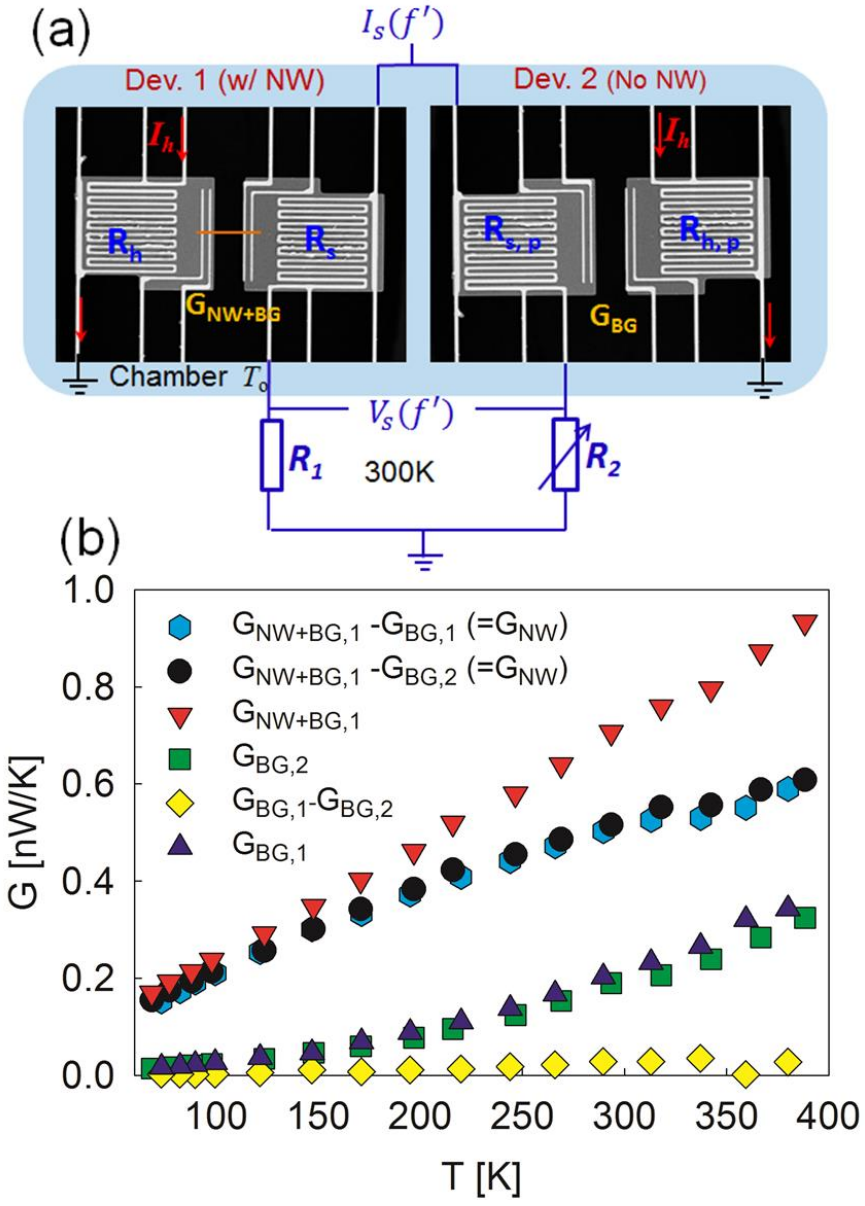


Figure 2.12: Characterization of background conductance. (a) Schematic of the canceling scheme for directly measuring the conductance of a nanowire. (b) Measurement results based on 400-μm-long devices.

Further examination of the background signal of a blank device was conducted through measurements at various chamber pressures (Fig. 2.13). At high-vacuum pressures (~10^{-4} torr) with the turbo pump switched on, the background signal was found to be stable around 215±7 pW/K. This was verified over multiple measurement runs and with multiple devices with the same gap distance between the heating and sending pads (all with gaps of ~4 μm wide and with 400-μm long suspending beams). The background conductance was slightly increased at higher pressures when only the mechanical pump was turned on.

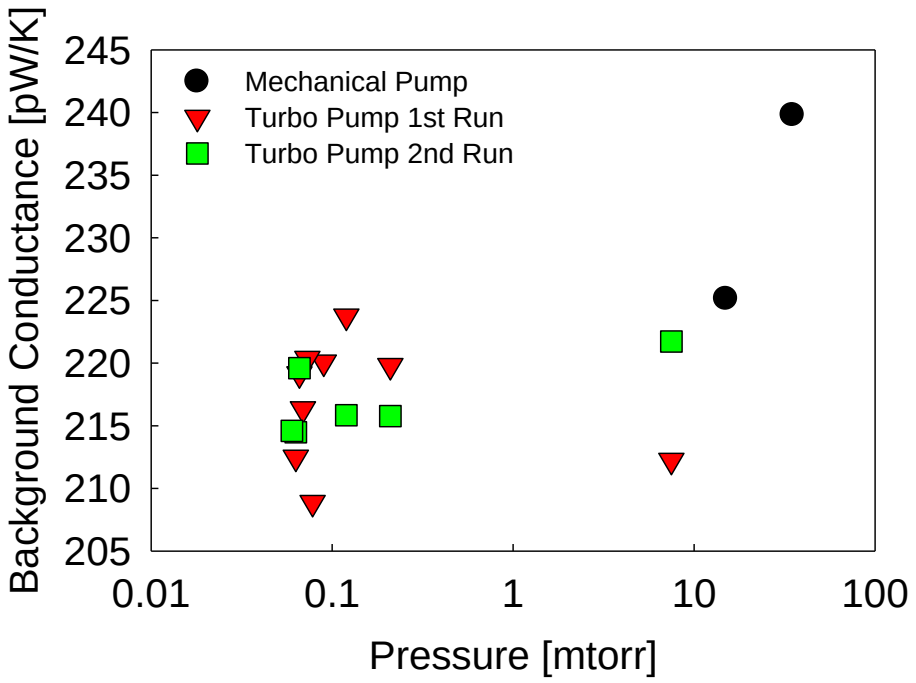


Figure 2.13: Measured background conductance vs. chamber pressure. At high vacuum, the background conductance was measured consecutively over a 4-hour period on separate days after removing and replacing samples (1st and 2nd runs). The measured conductance has little variation (±3%) as long as the pressure is below 10 mtorr.

2.10 Calculation of background conductance due to blackbody radiation

The expected background conductance due to blackbody radiation in the new short-beam devices can be calculated based on the measured radiative heat transfer coefficient, *h*, and the view factor between the suspended beams. The radiative heat transfer coefficient was previously found to be ≈4.2 W/m-K in section 2.5.1, meanwhile, the view factor, *f*, can be calculated by[33]:

$$f = \frac{2}{\pi XY}\left\{\left[\ln\sqrt{\frac{(1+X^2)(1+Y^2)}{1+X^2+Y^2}}\right] + X\sqrt{1+Y^2}\tan^{-1}\left(\frac{X}{\sqrt{1+Y^2}}\right) + Y\sqrt{1+X^2}\tan^{-1}\left(\frac{Y}{\sqrt{1+X^2}}\right) - X\tan^{-1}X - Y\tan^{-1}Y\right\} \quad (2.40)$$

where $X = t/d$ and $Y = L/d$ are the dimensionless beam thickness (t) and length (L), where d is the gap distance between the beams. The calculated view factors for the 100 μm long, 300 nm thick beams were 0.0205, 0.0098, and 0.0019 for gap sizes of 7, 14, and 54 μm, respectively. The corresponding conductance can be calculated as $G_{BG} = fhtL$ and are 2.6, 1.2, and 0.24 pW/K for the 7, 14, and 54 μm gaps, respectively. The calculated values are about one order of magnitude lower than the measured conductance for the corresponding devices (measured at 29.82, 13.70, and 2.45 pW/K at 300 K for gap distance of 7, 14, and 54 μm,). This discrepancy could be caused by near-field radiation effects and/or other experimental factors, which warrants further investigation.

2.11 Conclusion

In summary, we have demonstrated that the steady-state thermal conductance measurement for 1-D nanostructures can be significantly enhanced through the use of a differential bridge circuit in conjunction with the micro-fabricated measurement devices. The differential bridge method is exploited to cancel the common ambient temperature fluctuation and reduce the output signal (hence a greater sensitivity setting in the amplifier can be employed. The measurement sensitivity can be enhanced by more than 100 times, with a thermal conductance measurement limit of ~10 pW/K when appropriate experimental conditions are chosen, as demonstrated in this study. This makes the bridge measurement setup an excellent platform for probing thermal transport of 1D nanostructure with low thermal conductivity.

We have further demonstrated this method by measuring the thermal conductance of a 15 nm diameter Ge nanowire and the corresponding parasitic background conductance signal measured from the blank device. This indicates that for very low conductance measurements, the background signal becomes a significant percentage of the measurement and therefore cannot be neglected as it is in the 4-point measurement. The high sensitivity of this measurement system could allow for the investigation of thermal properties of single wall carbon nanotubes,[7] as well as low conductance signal applications such as polymer nanofibers[13] or single strands of DNA.[29]

Additionally, heat loss in the suspended heating beams was discussed. After analyzing heat loss as a function of the beam length including analytical temperature models, heat loss in short beam length devices was found to have negligible effect on

the measurement. Furthermore, a compensation factor was derived to correct for heat loss in long beam length devices. Finally, the parasitic background conductance present during nanowire measurement can be eliminated *via* the discussed canceling measurement scheme.

Acknowledgments

The majority of this chapter is a reprint of M. C. Wingert, Z. C. Y. Chen, S. Kwon, J. Xiang, R. Chen, "Ultra-sensitive Thermal Conductance Measurement of One-dimensional Nanostructures Enhanced by Differential Bridge," *Review of Scientific Instruments*, 83, 024901 (2012), with the rest from portions of J. Zheng*, M. C. Wingert*, E. Dechaumphai*, R. Chen, "Sub-picowatt/Kelvin Resistive Thermometry for Probing Nanoscale Thermal Transport," *Review of Scientific Instruments*, 84, 114901 (2013) and Z. Zhong*, M. C. Wingert*, J. Strzalka, H. H. Wang, T. Sun, J. Wang, R. Chen, Z. Jiang, "Structure-induced Enhancement of Thermal Conductivities in Electrospun Polymer Nanofibers," *Nanoscale*, 6, 8283-8291 (2014). *These authors contributed equally to the respective works.

References

1. D. Y. Li, Y. Y. Wu, P. Kim, L. Shi, P. D. Yang and A. Majumdar, Appl Phys Lett **83** (14), 2934-2936 (2003).

2. A. I. Hochbaum, R. K. Chen, R. D. Delgado, W. J. Liang, E. C. Garnett, M. Najarian, A. Majumdar and P. D. Yang, Nature **451** (7175), 163-167 (2008).

3. A. I. Boukai, Y. Bunimovich, J. Tahir-Kheli, J. K. Yu, W. A. Goddard and J. R. Heath, Nature **451** (7175), 168-171 (2008).

4. C. H. Yu, L. Shi, Z. Yao, D. Y. Li and A. Majumdar, Nano Lett **5** (9), 1842-1846 (2005).

5. J. K. Yang, Y. Yang, S. W. Waltermire, T. Gutu, A. A. Zinn, T. T. Xu, Y. F. Chen and D. Y. Li, Small **7** (16), 2334-2340 (2011).

6. E. Pop, D. Mann, Q. Wang, K. Goodson and H. J. Dai, Nano Lett **6** (1), 96-100 (2006).

7. M. T. Pettes and L. Shi, Advanced Functional Materials **19** (24), 3918-3925 (2009).

8. P. Kim, L. Shi, A. Majumdar and P. L. McEuen, Phys Rev Lett **87** (21), 215502 (2001).

9. C. W. Chang, D. Okawa, H. Garcia, A. Majumdar and A. Zettl, Phys Rev Lett **101** (7), 075903 (2008).

10. C. W. Chang, D. Okawa, H. Garcia, A. Majumdar and A. Zettl, Phys Rev Lett **99** (4), 045901 (2007).

11. C. W. Chang, D. Okawa, A. Majumdar and A. Zettl, Science **314** (5802), 1121-1124 (2006).

12. C. W. Chang, A. M. Fennimore, A. Afanasiev, D. Okawa, T. Ikuno, H. Garcia, D. Y. Li, A. Majumdar and A. Zettl, Phys Rev Lett **97** (8), 085901 (2006).

13. S. Shen, A. Henry, J. Tong, R. T. Zheng and G. Chen, Nature Nanotechnology **5** (4), 251-255 (2010).

14. T. Kodama, A. Jain and K. E. Goodson, Nano Lett **9** (5), 2005-2009 (2009).

15. D. G. Cahill, W. K. Ford, K. E. Goodson, G. D. Mahan, A. Majumdar, H. J. Maris, R. Merlin and P. Sr, J Appl Phys **93** (2), 793-818 (2003).

16. D. G. Cahill, K. Goodson and A. Majumdar, Journal of Heat Transfer-Transactions of the ASME **124** (2), 223-241 (2002).

17. V. P. Carey, G. Chen, C. Grigoropoulos, M. Kaviany and A. Majumdar, Nanoscale and Microscale Therm Eng **12** (1), 1-60 (2008).

18. P. K. Schelling, L. Shi and K. Goodson, Materials Today **8** (6), 30-35 (2005).

19. E. Pop, Nano Research **3** (3), 147-169 (2010).

20. G. Chen and A. Shakouri, Journal of Heat Transfer-Transactions of the Asme **124** (2), 242-252 (2002).

21. T. Tong, Y. Zhao, L. Delzeit, A. Kashani, M. Meyyappan and A. Majumdar, IEEE Transactions on Components and Packaging Technologies **30** (1), 92-100 (2007).

22. X. J. Hu, A. A. Padilla, J. Xu, T. S. Fisher and K. E. Goodson, Journal of Heat Transfer-Transactions of the ASME **128** (11), 1109-1113 (2006).

23. L. Shi, D. Y. Li, C. H. Yu, W. Y. Jang, D. Kim, Z. Yao, P. Kim and A. Majumdar, Journal of Heat Transfer-Transactions of the Asme **125** (5), 881-888 (2003).

24. M. Fujii, X. Zhang, H. Q. Xie, H. Ago, K. Takahashi, T. Ikuta, H. Abe and T. Shimizu, Phys Rev Lett **95** (6), 065502 (2005).

25. L. Lu, W. Yi and D. L. Zhang, Rev Sci Instrum **72** (7), 2996-3003 (2001).

26. R. Chen, A. I. Hochbaum, P. Murphy, J. Moore, P. D. Yang and A. Majumdar, Phys Rev Lett **101** (10), 105501 (2008).

27. K. Schwab, E. A. Henriksen, J. M. Worlock and M. L. Roukes, Nature **404** (6781), 974-977 (2000).

28. D. Donadio and G. Galli, Phys Rev Lett **102** (19), 195901 (2009).

29. A. V. Savin, M. A. Mazo, I. P. Kikot, L. I. Manevitch and A. V. Onufriev, Physical Review B **83** (24), 245406 (2011).

30. O. Bourgeois, E. Andre, C. Macovei and J. Chaussy, Review of Scientific Instruments **77** (12), 126108 (2006).

31. J. Xiang, W. Lu, Y. J. Hu, Y. Wu, H. Yan and C. M. Lieber, Nature **441** (7092), 489-493 (2006).

32. A. L. Moore and L. Shi, MEAS SCI TECHNOL **22** (1), 015103 (2011).

33. F. P. Incropera, *Fundamentals of heat and mass transfer*, 6th ed. (John Wiley, Hoboken, NJ, 2007).

34. N. M. Ravindra, S. Abedrabbo, W. Chen, F. M. Tong, A. K. Nanda and A. C. Speranza, IEEE Trans. Semicond. Manuf. **11** (1), 30-39 (1998).

35. A. Weathers, K. Bi, M. T. Pettes and L. Shi, Review of Scientific Instruments **84** (8), 084903 (2013).

36. M. C. Wingert, Z. C. Y. Chen, S. Kwon, J. Xiang and R. K. Chen, Review of Scientific Instruments **83** (2), 024901 (2012).

37. J. Zheng, M. C. Wingert, E. Dechaumphai and R. Chen, Rev Sci Instrum **84** (11), 114901 (2013).

Chapter 3: Thermal conductivity of Ge and Ge-Si core-shell nanowires in the phonon confinement regime

3.1 Introduction

Heterostructure semiconductor nanowires (NWs), such as core-shell structures of Ge-Si[1] and III-V materials[2], have become an increasingly important class of nanomaterials because of their remarkable electronic, optical and thermal properties as well as potential applications as building blocks for nanoelectronics[3], nanophotonics[2, 4], photovoltaics[5, 6] and thermoelectrics[7]. For example, Xiang *et al.*[8] found that Ge-Si core shell NW transistors have high hole mobility compared to bulk Ge and strained SiGe heterostructure devices due to the quasi-1D hole transport in the thin NWs (~15 nm diameter). Zhang *et al.*[9] observed an enhanced thermopower and reduced thermal conductivity (κ) in composites consisting of Te-Bi and Te-Bi_2Te_3 core-shell nanorods. Understanding thermal transport in heterostructure NWs is crucial for many of their recently proposed potential applications, such as thermal management of nanoelectronics and nanophotonics and optimization of thermoelectric materials and devices[10, 11]. However, phonon transport in core-shell nanostructures has been relatively less explored compared to homogenous NWs and a complete picture of physical understanding has yet to be established. In the case of homogenous NWs, numerous studies have shown that NW thermal conductivity (κ) can be significantly suppressed due to phonon boundary scattering[12-14] and surface roughness[15-17] when the characteristic size of the NW is smaller than the phonon mean free path (MFP), which

is in the range of 10-1000 nm for Ge and Si at 300 K[18, 19]. When the NW diameter is even smaller and is comparable to the phonon wavelength, it is expected that phonon confinement effects will become important, leading to a modified phonon dispersion, which can be important for Si NWs 20 nm in diameter as studied theoretically by Zou *et al.*[20].

Recently, a few theoretical and numerical studies have shed light on the unique phonon spectra and thermal transport in core-shell NWs[10, 11, 21, 22 23, 24]. Yang *et al.*[11] reported one of the first modeling works by solving the phonon Boltzmann transport equations (BTE) in core-shell and tubular NWs. Prasher[10] obtained a simpler and yet highly effective analytical solution of the BTE. Both reports show that the effective κ changes with the composition and size of the core and shell structures, due to the nature of the ballistic phonon transport. Pokatilov *et al.*[21, 25] have theoretically shown that the acoustically mismatched barriers between the core and the shell dramatically influence the phonon spectra. The key parameter is the acoustic impedance, *Z*, defined as $Z = \rho V_s$, where ρ and V_s are the density and speed of sound of the materials respectively. When the shell is acoustically softer, i.e., with lower *Z*, the modified phonon spectra will lead to a strong phonon depletion effect, where almost all the phonon modes are squeezed due to the redistribution of the elastic deformations in the acoustically mismatched nanowire. Such an effect would have a dramatic influence on phonon transport (e.g., κ) and phonon-carrier interactions (e.g., carrier mobility). Very recently, Hu *et al.*[22, 24] and Chen *et al.*[23] performed molecular dynamics (MD) simulations on κ of Si-Ge and Ge-Si core shell NWs, respectively. Their calculations show that the core-shell structure strongly suppressed κ compared to uncoated Si or

Ge NWs. The reduced κ is attributed to the depression and localization of long-wavelength phonon modes at the Si-Ge interface and also of high frequency non-propagating diffusive modes. In particular, detailed analysis and simulation by Chen *et al.*[23] attributed the origin of the localized modes to a unique coherent resonant coupling between longitudinal modes and quantized transverse modes.

Despite the tremendous theoretical effort, there is currently no experimental study on thermal transport in core shell NWs with small diameters that would possess strong confinement effects as proposed theoretically (e.g., d < 20 nm[20]). The low κ (0.5 – 1 W/m-K) obtained by Zhang *et al.*[9] on composites of Bi-Te (or Bi-Bi_2Te_3) core-shell nanorods suggests promising applications for thermoelectrics. However, the non-uniform size and random arrangement of nanorods preclude a direct comparison with theoretical models on single NWs. Very recently, Kang *et al.*[26] measured κ of single Bi-Te core-shell NWs with large diameters, and observed a significant reduction in κ for NWs with rough core-shell interfaces, which agrees with the prior study on rough Si NWs[15]. However, the diameter of NWs (d >170 nm) is larger than the dominant phonon wavelength and mean free path in Bi and Te, therefore, phonon transport in these NWs probably falls in a regime different from the one concerned in this study.

One of the technical challenges of measuring κ in small diameter core shell NWs lies in the low thermal conductance (G) needed to be measured. Thermal conductivities of various NWs have been previously measured using suspended micro-fabricated devices[12, 13, 15, 27, 28]. This method has a G sensitivity of approximately 1

nW/K [27], therefore it is only applicable for measuring large diameter NWs, or samples with high thermal conductivity (e.g., single wall carbon nanotubes [29]). Previously, thermal conductivities have been measured for single Si NWs with diameters as small as 18-20 nm[12]. However, the wires have a relatively higher effective κ (~10 W/m-K), therefore, their thermal conductance (G > 1 nW/K) is still within the measurement limit. Consider a hypothetical NW of 10-nm-diameter and 2-μm long with κ of 1 W/m-K, the thermal conductance would be less than 0.1 nW/K, which is one order of magnitude lower than the measurement sensitivity of ~1 nW/K in the traditional direct-measurement schemes. It becomes apparent that a more sensitive method is needed in order to measure small diameter core-shell NWs, which are expected to possess low κ. More broadly, such a sensitive technique will also be valuable for probing low dimensional phonon transport physics, such as phonon confinement effects[30], ultra-low κ that approaches the amorphous limit[14], thermal properties of single-wall carbon nanotubes[31], polymer nanofibers[32], and single strands of DNA[33] and could potentially provide experimental data which can be compared directly with atomistic scale simulations[17, 34].

Herein, we report the first experimental study on thermal conductivity of Ge and Ge-Si core-shell NWs with diameters less than 20 nm, by developing a novel setup with drastically improved sensitivity for single NW κ measurement. The Ge and Ge-Si NWs, synthesized by a vapor liquid solid (VLS) process[8, 35, 36], are single crystalline with diameters ranging from 10-20 nm. The improved measurement sensitivity is built upon a Wheatstone bridge circuit by employing an on-chip pair resistance for highly sensitive temperature and conductance measurements (with ~1

mK and ~10 pW/K sensitivities respectively). Contrary to the expectation that coating the Ge core with the higher κ Si shell would lead to an increase in the overall κ, the measurement results show that κ of the of core-shell NWs are comparable to or even lower than that of the pure Ge NWs at higher temperatures. This surprising result, however, is in good qualitative agreement with the recent MD studies on thin core shell NWs[22, 24, 37]. Comparing the experimental data with Boltzmann phonon transport models also elucidate the important role of phonon confinement on further reducing κ of the 15-20 nm diameter NWs in addition to the reduced MFP by phonon boundary scattering. The low measured κ of 1.5-2 W/m-K at 300-400 K also suggests that the core shell NWs are promising for thermoelectric applications[31]

3.2 Nanowire fabrication

Two types of NWs were investigated in this study: pristine Ge NWs and Ge-Si heterostructure core-shell NWs. Both NWs were synthesized by a chemical vapor deposition (CVD) method within the framework of VLS growth, as described in an earlier work by Lu *et al.* [35]. Briefly, colloidal Au nanoparticles of ~2-5-nm diameter were deposited on Si substrates as the growth catalysts and placed in a tube furnace. For growing Ge NWs, 10% GeH_4 in H_2 [30 standard cm^3 per min (sccm)] were introduced as the precursor gases at 300 torr and 280 ^oC for ~15 min. For core shell NW synthesis, the intrinsic Si shell was deposited within the same reactor immediately after Ge core growth at 450 ^oC for 5 minutes by using SiH_4 (5 sccm) at 5 torr. Fig. 3.1(A) shows the schematic illustration of the core-shell structure, while Fig. 3.1(B)

shows a representative SEM image of the side view of as-grown Ge-Si core-shell NWs. As shown in the figure, the NWs have lengths of 10-15 μm. Fig. 3.1 (C) and (D) show the representative high resolution TEM (HRTEM) images of the Ge and Ge-Si core-shell NWs respectively. As shown in the figures and based on extensive TEM observations, the Ge NWs (or Ge cores) have diameters of 10-20 nm while the Si shells are typically 1-3 nm thick, and the Si-Ge interface is epitaxial with no dislocations. Both types of wires typically exhibit a layer of ~1 nm thick amorphous native oxide (either GeO_2 or SiO_2).

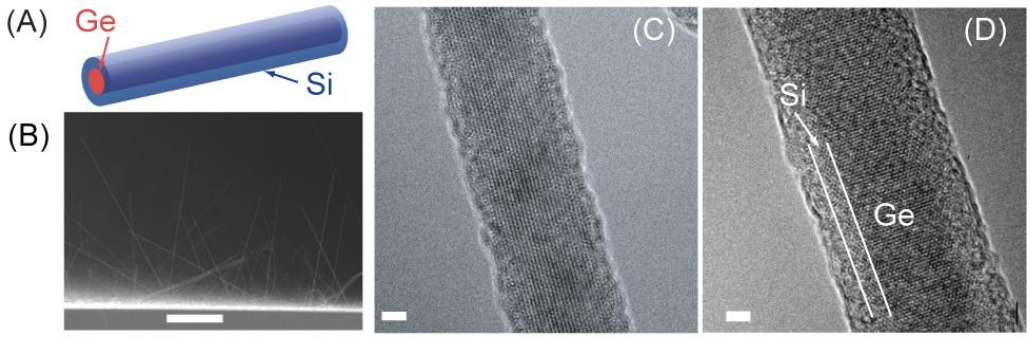


Figure 3.1: Ge and Ge-Si core-shell nanowires synthesized by the CVD method. (A) Schematic illustration of a Ge-core Si-shell NW. (B) A SEM image of the side view of Ge-Si core shell NWs grown on a Si substrate. (C) A high resolution TEM image of a single crystalline Ge NW. The NW growth direction is [110]. (D) A HRTEM image of a single crystalline Ge-Si core-shell NW. The Ge core axial direction is also [110] and the Si shell is epitaxially grown on Ge. The scale bars in B, C, and D are 10 μm, 2 nm and 2 nm, respectively.

The NWs synthesized with this manner are ideally suited for studying the effects of core-shell acoustic interfaces on low dimensional thermal transport. First, both the core and shell materials are high quality single crystalline, hence one can eliminate non-ideal effects such as grain boundaries and porosity. Second, the interface between the core and shell are epitaxial and free of voids or other impurities, since the Si shell was grown in the same vacuum reactor immediately after the Ge core synthesis. More importantly, by comparing the thermal properties of Ge wires with and without the Si shell, we can elucidate the effect of the core-shell interface.

3.3 Nanowire thermal conductivity measurement

In order to perform κ measurement with ultra-high sensitivity, a new setup based on Wheatstone bridge circuit has been developed. The setup employs a similar micro-fabricated device used previously for single NW κ measurements[12, 13, 15, 27], but has been improved substantially in its measurement sensitivity. As shown in Fig. 3.2(A), the device consists of two suspended membranes, each integrated with a serpentine Pt coil, serving both as the heaters and resistive thermometers (R_h and R_s). A Ge or Ge-Si NW is placed between the two membranes [Fig. 3.2(B)] by wet transfer[12]. Temperature changes of each membrane (ΔT_h and ΔT_s) are obtained from the measured R_h and R_s. To convert the resistances to temperatures, the temperature coefficient of the resistances (TCR) of the Pt coils needs to be accurately determined. We have measured R vs. T over a wide temperature range (60-382 K) and use the Bloch-Grüneisen relation to fit the data to obtain the TCR. With the measured

temperature changes of each membrane (ΔT_h and ΔT_s), as well as the heat flux conducted along the NW (Q_s), one can calculate the effective NW thermal conductance ($G = Q_s /(\Delta T_h - \Delta T_s)$) and $\kappa = GL/A$, where L and A are the length and cross sectional area of the NW, respectively. In the previous temperature measurement configuration[12, 13, 15, 27], both the heating and sensing resistances (R_h and R_s) were measured by a standard four-point probe *I-V* method with a small ac current (~0.5 μA) and lock-in amplifiers[13, 27]. The method has a sensitivity of G of approximately 1 nW/K[13, 27].

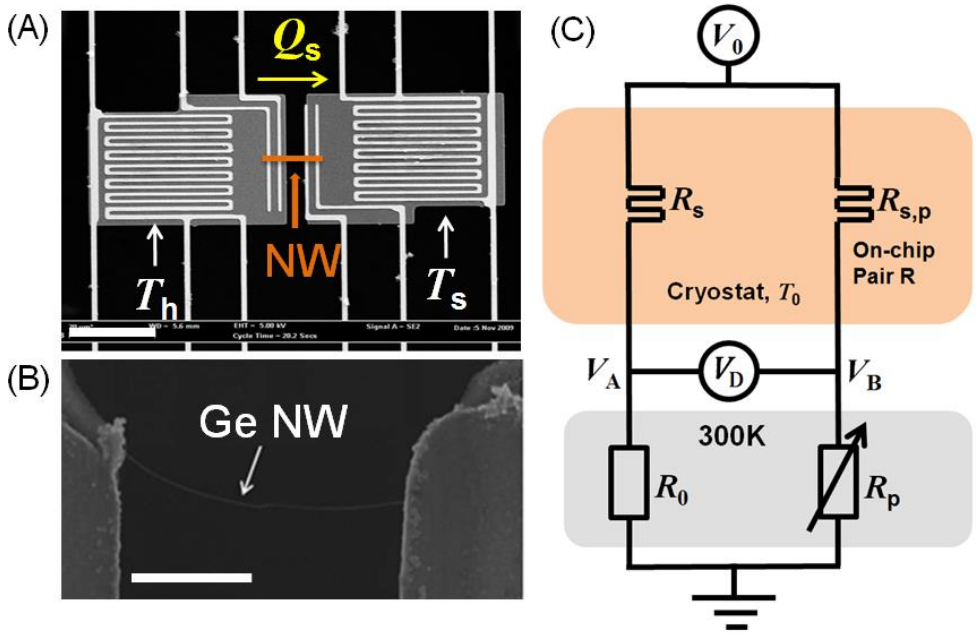


Figure 3.2: Experimental setup of the Wheatstone bridge circuit for NW thermal measurement. (A) A SEM image of a micro-fabricated device used for single nanowire κ measurement. The device consists of two membranes bridged by a single NW. One of the membranes will be heated up (ΔTh), transferring a small amount of heat flux, Qs, through the NW, which in turn raises the temperature of the sensing membrane (ΔTs). Thermal conductance G is calculated as Qs/(Th-Ts). (B) A SEM image of a ~15 nm Ge NW on the suspended device. (C) The Wheatstone bridge setup for measuring the sensing resistance Rs.

The relationship between the temperature and thermal conductance sensitivity can be derived using a standard heat transfer analysis:

$$G_{\min} = G_b \frac{\Delta T_{\min}}{\Delta T_h - \Delta T_s} \tag{3.1}$$

To further reduce G_{min}, the key is then to improve the thermometry sensitivity of the sensing membrane (allowing for smaller ΔT_{min}). The new setup employing the Wheatstone bridge for R_s measurement is shown schematically in Fig. 3.2(C). In this configuration, an additional on-chip pair resistor ($R_{s,p}$) located in close proximity to R_s is used, which has nominally the same resistance as R_s. Both R_s and $R_{s,p}$ are located within the cryostat chamber, therefore any fluctuation in the cryostat ambient temperature can be cancelled out. The other two resistors in the bridge circuit include a high precision resistor (R_0) and a potentiometer (R_p), which are both located outside of the cryostat chamber (~300 K). A radiation heat shield is used in order to minimize radiative heat transfer between the sample and environment[38]. The cryostat is evacuated to ~2-3×10^{-5} torr such that conduction and convection heat transfer are negligible. Before the measurement, the bridge is balanced (V_D = 0) by adjusting R_p. When the heating membrane is heated (T_h), the heat flux conducted along the NW will raise the temperature of the sensing membrane (T_s), thereby increasing R_s and leading to a change in V_D that is measured by a lock-in amplifier (Stanford Research 830). The resistance of the sensing coil, R_s, is related to the measured V_D by the following equation,

$$R_s = R_0 \left(\frac{V_D}{V_0} + \frac{R_p}{R_p + R_{s,p}} \right)^{-1} - R_0 \tag{3.2}$$

where V_0 is the fixed source voltage of the bridge circuit.

Figure 3.3(A) shows the measured ΔT_h and ΔT_s using the new bridge setup. The figure shows that the setup is able to measure ΔT_s with a sensitivity of ~1 mK, which indicates a measurement sensitivity of the conductance (G_{min}) of about 10 pW/K according to Eq. 3.1. The sensitivity achieved by the bridge setup is about two orders of magnitude lower than that of the four-point probe method using similar suspended micro-devices[12, 13, 27].

Fig. 3.3(B) shows the measured G of a ~20-nm diameter Ge-Si NW. Thermal conductance of the NW (G_{NW}) was obtained as the difference between the conductance of the NW device (G_{NW+B}) and the background conductance (G_B) of the *same* device after the NW was cut using a focused ion beam (FIB). Note that the thermal contact resistance between the small diameter NWs and the substrate is negligible because of the extremely large conduction thermal resistance of NWs (see the Supporting Information), so the measured G_{NW} can be interpreted as the intrinsic thermal conductance of the NWs. The insets in Fig. 3.3(B) show the SEM images of the same device, before and after the NW was cut, respectively. Note that the background conductance G_B is not negligible compared to that of G_{NW}, and needs to be carefully measured for NWs with conductance less than 1 nW/K. This background conductance is likely due to near field thermal radiation energy exchange between the two membranes whose gaps (~2-5 μm) are comparable to the dominant photon wavelength (~10 μm at 300 K) as well as conduction by residual gas molecules. We also noticed that G_B varies quite significantly among devices, ranging from 0.15 to 0.4 nW/K, presumably due to the variations in the distance and view factor between the

two membranes of each device. Therefore, it is necessary to measure the background conductance of each individual sample to extract the intrinsic NW conductance.

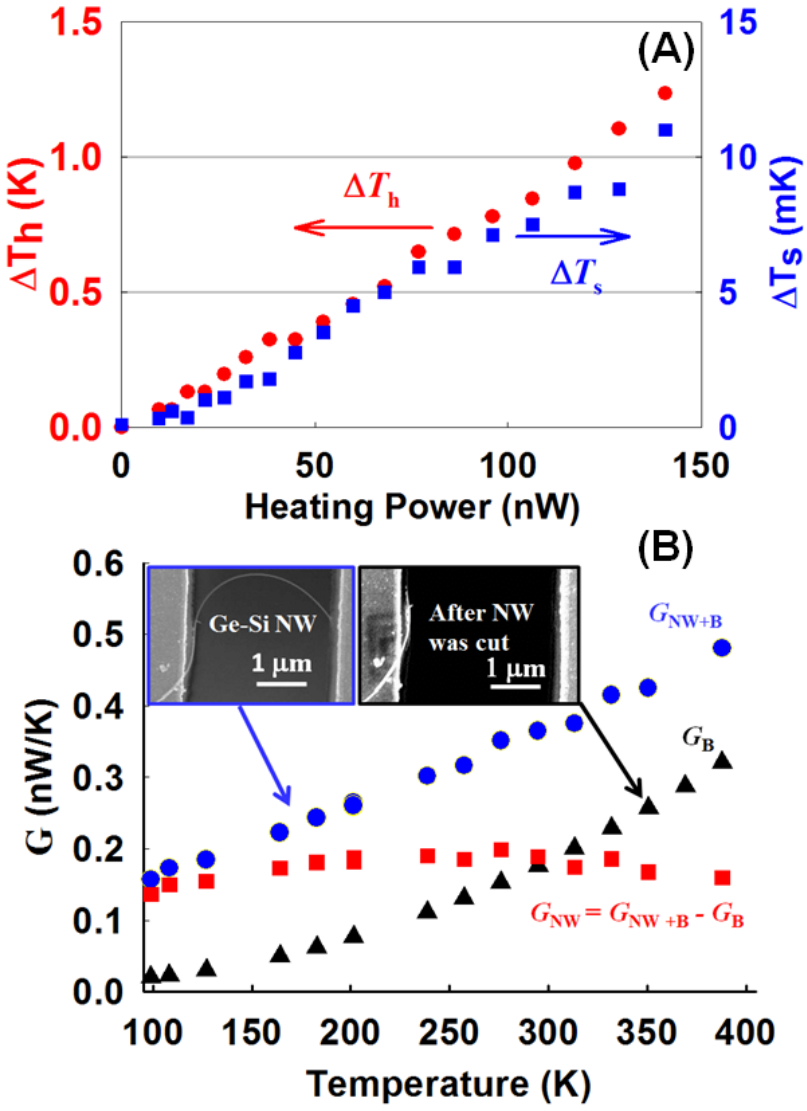


Figure 3.3: (A) Measured temperature rise on the heating and sensing sides as a function of the heating power. The bridge method has a Ts sensitivity of ~1 mK, leading to a G sensitivity of ~10 pW/K (Eq. 3.2). (B) G of the device with a ~19 nm diameter Ge-Si NW (GNW+B, blue circles) and without the NW (GB, black triangles) to extract the intrinsic G of the NW (GNW, red square). The insets in (B) show the SEM images of the same device with and without the NW respectively.

3.4 Thermal conductivity of Ge nanowires

We have measured NWs of pristine Ge and Ge-Si core-shell structures with outer diameters between 15-20 nm, within the temperature range of 108 to 388 K (178-382 K for Ge NW #2), as shown in Fig. 3.4. To elucidate the size effect and to ensure that the thermal contact resistance between the NWs and the devices is negligibly small we have also measured κ of large diameter Ge NWs (d ~ 60 - 120 nm), and the data of a representative NW (d ~ 62±2 nm, L~ 10 μm) is shown in Fig. 3.5(A). The diameter of each sample was measured by a combination of SEM and AFM and typically has an uncertainty of 1-2 nm. The range of the diameters for each NW sample is also shown in the legend of Fig. 3.4. This uncertainty in diameter causes a fairy large uncertainty in thermal conductivity because of the small NW diameters. The error bars shown in the figure are a combination of the uncertainty due to the diameter determination and the standard deviations of multiple measured data points at a given temperature (typically 3-5 points), but the latter typically leads to less than 5% uncertainly because of the highly sensitive bridge circuit employed in these measurements. Only the representative error bars at 382 or 388 K, 300 K and 108 K respectively (178 K for Ge NW #2) are shown for better clarity of the figure, however the uncertainties in κ are similar at other temperatures. As shown in Fig. 3.4, at 300 K, κ for the 15-nm and 19-nm Ge NWs are (1.54+0.59/-0.30) W/m-K and (2.26+0.60/-0.39) W/m-K respectively, which are significantly lower than that of bulk Ge (~58 W/m-K at 300 K). The measured κ are also lower than those of Si NWs with similar diameters (κ ~ 7-10 W/m-K for 18-22 nm Si NWs[12, 13]), which is a result of the larger

atomic mass and lower speed of sound of Ge. Within the entire temperature range of 108–382 K, κ of the Ge NWs increase monotonically with temperature, and are about 2.8+1.0/-0.6 W/m-K at 382 K. This significant reduction in κ, along with the absence of the *Umklapp* peak in κ, suggests that phonon boundary scattering dominates over other scattering mechanisms in the entire measured temperature range. This is in qualitative agreement with prior theoretical studies[39, 40] on smooth Ge NWs with larger diameters (d > 32 nm). However, given the small diameter (15 and 19 nm) of the NWs studied here, it is necessary to take the phonon confinement effect into account in order to understand the experimental data.

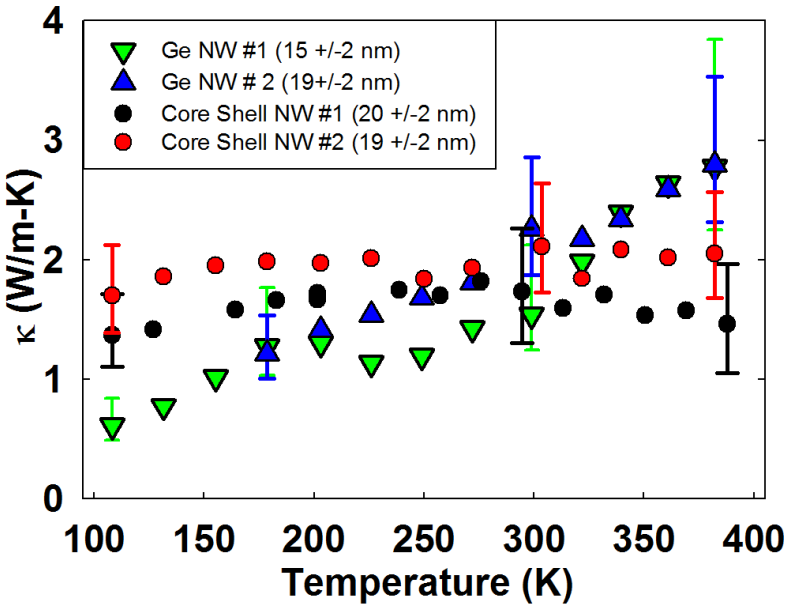


Figure 3.4: Measured thermal conductivity of pristine Ge NWs (green and blue triangles) and Ge-Si core-shell NWs (red and black circles) with diameters ranging from 15-20 nm. The error bars shown are representative errors at 388 or 383 K, 300 K and 108 K respectively (178 K for Ge NW #2). The primary error source comes from the uncertainty in the diameter determination, as the NWs are very thin and are not perfectly uniform. At 300 K, κ for the 15-nm and 19-nm Ge NWs are (1.54+0.59/-0.30) W/m-K and (2.26+0.60/-0.39) W/m-K respectively, while κ of the core shell NWs are in the range of 1.1-2.6 W/m-K and show little temperature dependence within the entire measured temperature range. κ of both Ge and Ge-Si core shell NWs is significantly lower than that of bulk SiGe alloy as well as smooth Si NWs with similar diameters.12, 13

3.5 Thermal conductivity modeling of Ge nanowires

To elucidate the effects of the spatial confinement[20] in Ge NWs, we have calculated the phonon dispersions and thermal conductivity of Ge NWs. With the NW phonon dispersions, we can calculate phonon group velocities for each mode at a specific frequency $\left(v_n(\omega) = \frac{d\omega}{dk}\right)$ where n is the index for phonon modes (The cutoff n is 800 in our calculation), by numerically differentiating the dispersion relations. Subsequently, thermal conductivity of the NWs is modeled using the Boltzmann

transport equations (BTE). The detail of the BTE modeling is only briefly described here. We followed the procedure used by Lu *et al.*[41] to derive the Boltzmann phonon transport along the axial direction of NWs. Based on this derivation, the effective phonon density of states and phonon group velocities can be defined for nanowire structures to calculate the κ_{NW}:

$$\kappa_{\mathrm{NW}} = \sum_n \frac{1}{3}\left(\frac{k_B}{\hbar}\right) k_B T \int_{\hbar\omega_{n,min}/k_B}^{\hbar\omega_{n,max}/k_B} \frac{u^2 e^u}{(e^u-1)^2} \tau_n(u) v_n(u)^2 D_n(u) du \qquad (3.3)$$

where $\omega_{n,min}$ and $\omega_{n,min}$ are the maximum and minimum phonon frequencies for mode *n*, respectively, k_B and $\hbar$ are the Boltzmann constant and reduced Plank constant respectively, T is the temperature, D_n is the phonon density of states calculated for mode *n*, τ_n is the effective relaxation time for mode *n*. In our calculation, we modeled τ_n using the Matthiessen rule: $\tau_n^{-1} = \tau_i^{-1} + \tau_b^{-1} + \tau_U^{-1} + \tau_N^{-1}$ with each term representing the scattering mechanism of phonons due to impurities, boundary, *Umklapp* and *Normal* processes respectively. In our model, we used the *same* parameters of bulk Ge to determine τ_i^{-1}, τ_U^{-1} *and* τ_N^{-1} *without* further adjustment. The only scattering term that is modified in the NW models is that of the boundary scattering, $\tau_b^{-1} = v_n(\omega)/d$, where d is the diameter of NWs. This represents the diffusive boundary scattering.

Fig. 3.5(A) shows the modeled thermal conductivity of Ge NWs. We first compare the modeling results to the experimental data of the thicker Ge NW (d ~ 62±2 nm). The model uses *bulk phonon dispersions* of Ge, as well as bulk phonon group velocities and Debye density of states. As can be seen from the figure, the calculated κ matches well with the experimental data for the 62±2 nm diameter NW, especially in

the temperature range of 108-300K. At higher temperatures, the model underestimates the κ by up to 15%. This discrepancy is possibly caused by a slightly different *Umklapp* scattering term for NWs compared to bulk. To minimize the number of fitting parameters used in the present model, we did not intend to modify the τ_U^{-1} term for better fitting with the data.

Interestingly, if we also use the same bulk phonon dispersions to model κ of 15 nm diameter Ge NWs, the calculated κ (dark dash line in Fig. 3.5A) is significantly higher than the experimental data (by more than 100% below 250 K). For example, at 179 K, the measured κ are 1.27+0.50/-0.24 W/m-K and 1.22+0.32/-0.20 W/m-K for Ge NW #1 and #2 respectively, whereas the calculated κ is 4.24 W/m-K. The disagreement for Ge NW #1 is even greater at 108 K. We showed that this large discrepancy is likely due to modified phonon dispersions in NWs caused by the confinement effect. As shown in Fig. 3.5(A), the modeling results using NW dispersions (pink dash-dot line) show good agreement with the data. The improved agreement is impressive given the fact that no any additional fitting parameters are introduced in the NW models. This result indicates that the modified phonon spectrum due to phonon confinement further reduces κ of 15-20 nm Ge NWs by a factor of 2-3 compared to the prediction that only considers the diffusive boundary scattering. This effect is especially important in the lower temperature range (100-250 K). It is also interesting to note that at higher temperatures (300-382 K), the experimental data lie between the two model curves using bulk and NW dispersions, respectively. This may indicate that the confinement effect is less pronounced at higher temperature, or it is

also possible that the model using NW dispersions is not accurately capturing the *Umklapp* scattering mechanism that is responsible for a decreasing κ at high temperature, similar to the case for the 62 nm Ge NW.

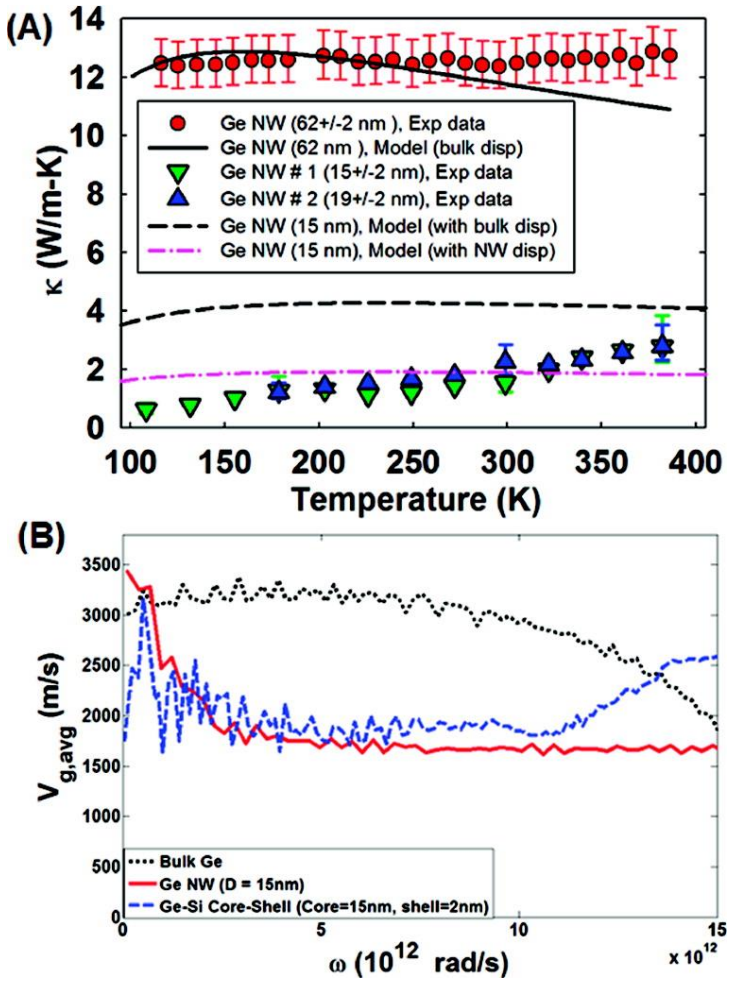


Figure 3.5: Comparisons between modeling and experimental results. (A) The calculated κ of the 62-nm Ge NW using bulk dispersions (black solid line) agree well with the experimental data (circles), whereas the calculated κ of the 15-nm Ge NW using bulk dispersions (black dashed line) is significantly higher than the experimental data (triangles), by more than 100% below 250 K. Modeling results using NW dispersions (pink dash-dot line) show good agreement with the data. This suggests the important role of phonon confinement in small diameter NWs. (B) Calculated group velocities of 15 nm Ge NWs (red) and a 19 nm Ge-Si core shell NWs (15 nm Ge core + 2 nm thick Si shell, blue) are significantly lower than that of bulk Ge (black).

To further elucidate the effect of phonon confinement, we also calculated the mode averaged phonon group velocities, $V_{g,avg}(\omega)$, by averaging the group velocities of all the computed phonon modes (~800 modes in our model) at a given frequency. As shown in Fig. 3.5(B), the 15-nm Ge NWs have significantly lower group velocities compare to bulk Ge, which is caused by the phonon confinement effect in small diameter NWs (d < 20 nm). The significantly lower group velocity is the primary reason for the lower κ in thin NWs compared to the diffusive scattering limited κ (Fig. 3.5A). Similar effects have also been observed in theoretical work by Zou *et al.* [20] on 20-nm diameter Si NWs.

3.6 Thermal conductivity of Ge-Si core-shell nanowires

Now we turn our discussion to Ge-Si core shell heterostructure NWs to understand the effect of the epitaxial interface between Ge-Si on phonon transport. The measured κ of the core-shell NWs are also shown in Fig. 3.4 along with the data for the Ge NWs: within the entire measured temperature range, κ of the core shell NWs are in the range of 1.1-2.6 W/m-K and show little temperature dependence. It is worth mentioning that κ of the core-shell NWs is much lower than that of bulk SiGe alloy (~4.5 W/m-K for $Si_{63.5}Ge_{36.5}$ at 300 K[42]) and larger diameter SiGe alloy NWs[43]. When compared to the Ge NWs, κ of the core-shell NWs is higher at lower temperature (below 250 K), but lower at room temperature and above. In particular, at 382 K, κ of the core shell NWs is 1.1-2.5 W/m-K, significantly lower than κ of Ge NWs (2.3-3.9 W/m-K). This trend can also be understood by looking at phonon

spectrum in the confinement regime. As shown in Fig. 3.5(B), the differences in phonon group velocities of Ge and Ge-Si core-shell NWs indicate that the ~2 nm Si shell influences the phonon spectra. Ge-Si core-shell NWs have higher group velocities compare to pristine Ge NWs for a wide range of frequencies, because Si has a higher speed of sound than Ge. The higher $V_{g,avg}$ can explain the higher κ in Ge-Si core-shell NWs compared to that in Ge NWs below 250 K (Fig. 3.4 and 3.5(A)). However, at high temperatures (T > 300 K), the thermal conductivity data show the opposite trend. This could be caused by a stronger scattering of phonons at the core-shell interface at higher temperatures where the dominant phonons have shorter wavelength. It is also possible that other intriguing effects may play a role in the suppressed κ in the core-shell NWs, such as the presence of non-propagating modes at the disordered surface[17] or localized low frequency modes at the core-shell interface[37]. A MD study by Hu *et al*[22] on Si-Ge core shell NWs with diameters up to 7.7 nm shows that heterostructure NWs exhibit up to 75% lower κ compared to Si wires at 300 K. Chen *et al.*[37] also observed a significant κ reduction in Ge core- Si shell structures compared to pristine Ge NWs. In both cases, the κ reduction was attributed to strong localization of low frequency vibrations as well as the suppression of high frequency modes for atoms located in proximity to the Si-Ge interface. This effect originates from the lattice mismatch and dissimilar atomic masses of Si and Ge, which causes a nontrivial phonon coherent resonance effect[37]. As our measured NWs have larger diameters and consequently a smaller percentage of atoms located proximal to the interface, the measured κ suppression is not as pronounced as in the thinner wires

studied in the MD simulations. Future experimental study with 5-10 nm diameter NWs could provide invaluable data to observe these intriguing coherent phonon effects, which is currently under investigation by us using the sensitive measurement technique developed here.

3.7 Conclusion

In summary, we have conducted a comparative experimental study on the thermal conductivity of Ge and Ge-Si core-shell NWs with diameters in the range of 15-20 nm. In order to measure thin NWs with low thermal conductivity, we have developed a highly sensitive measurement technique based on the Wheatstone bridge circuit that is able to resolve thermal conductance as low as ~10 pW/K. The measured κ of both the Ge and Ge-Si NWs is significantly lower than that of bulk Ge and SiGe alloy as well as Si NWs with comparable diameters, indicating the effects of strong phonon boundary scattering as well as the larger atomic mass of Ge. Boltzmann transport modeling also elucidates the important role of phonon confinement on further reducing κ of 15-20 nm diameter NWs in addition to the reduced MFP by diffusive phonon boundary scattering. Comparing κ of the Ge-Si core-shell NWs and Ge NWs suggests that the acoustic interfacial mismatch between the Ge-core and Si-shell suppresses phonon transport above room temperature, but facilitate heat conduction at lower temperatures. The measured κ of the Ge-Si core shell NWs are in the range of 1.1-2.6 W/m-K at 108-388 K, which is even lower than that of large diameter SiGe alloy NWs in the same temperature range[43]. The low κ, along with the

high hole mobility[8], suggests that the Ge-Si core-shell NWs are a promising new class of materials for nanostructured thermoelectrics.

Acknowledgments

This chapter is a reprint of M. C. Wingert, Z. C. Y. Chen, E. Dechaumphai, J. Moon, J. Kim, J. Xiang, R. Chen, "Thermal Conductivity of Ge and Ge-Si Core-Shell Nanowires in the Phonon Confinement Regime," *Nano Letters*, 11, 5507-5513 (2011).

References

1. L. J. Lauhon, M. S. Gudiksen, C. L. Wang and C. M. Lieber, Nature **420** (6911), 57-61 (2002).

2. F. Qian, Y. Li, S. Gradecak, D. L. Wang, C. J. Barrelet and C. M. Lieber, Nano Lett **4** (10), 1975-1979 (2004).

3. Y. Li, F. Qian, J. Xiang and C. M. Lieber, Mater Today **9** (10), 18-27 (2006).

4. F. Qian, S. Gradecak, Y. Li, C. Y. Wen and C. M. Lieber, Nano Lett **5** (11), 2287-2291 (2005).

5. B. Z. Tian, X. L. Zheng, T. J. Kempa, Y. Fang, N. F. Yu, G. H. Yu, J. L. Huang and C. M. Lieber, Nature **449** (7164), 885-U888 (2007).

6. Y. J. Dong, B. Z. Tian, T. J. Kempa and C. M. Lieber, Nano Lett **9** (5), 2183-2187 (2009).

7. X. Chen, Y. C. Wang and Y. M. Ma, J Phys Chem C **114** (19), 9096-9100 (2010).

8. J. Xiang, W. Lu, Y. J. Hu, Y. Wu, H. Yan and C. M. Lieber, Nature **441** (7092), 489-493 (2006).

9. G. Q. Zhang, W. Wang and X. G. Li, Advanced Materials **20** (19), 3654-+ (2008).

10. R. Prasher, Appl Phys Lett **89** (6), - (2006).

11. R. G. Yang, G. Chen and M. S. Dresselhaus, Nano Lett **5** (6), 1111-1115 (2005).

12. R. Chen, A. I. Hochbaum, P. Murphy, J. Moore, P. D. Yang and A. Majumdar, Phys Rev Lett **101** (10), - (2008).

13. D. Y. Li, Y. Y. Wu, P. Kim, L. Shi, P. D. Yang and A. Majumdar, Appl Phys Lett **83** (14), 2934-2936 (2003).

14. A. I. Boukai, Y. Bunimovich, J. Tahir-Kheli, J. K. Yu, W. A. Goddard and J. R. Heath, Nature **451** (7175), 168-171 (2008).

15. A. I. Hochbaum, R. K. Chen, R. D. Delgado, W. J. Liang, E. C. Garnett, M. Najarian, A. Majumdar and P. D. Yang, Nature **451** (7175), 163-167 (2008).

16. P. Martin, Z. Aksamija, E. Pop and U. Ravaioli, Phys Rev Lett **102** (12), - (2009).

17. D. Donadio and G. Galli, Phys Rev Lett **102** (19), - (2009).

18. C. Bera, N. Mingo and S. Volz, Phys Rev Lett **104** (11), - (2010).

19. A. S. Henry and G. Chen, J Comput Theor Nanos **5** (2), 141-152 (2008).

20. J. Zou and A. Balandin, J Appl Phys **89** (5), 2932-2938 (2001).

21. E. P. Pokatilov, D. L. Nika and A. A. Balandin, Phys Rev B **72** (11), - (2005).

22. M. Hu, K. P. Giapis, J. V. Goicochea, X. L. Zhang and D. Poulikakos, Nano Lett **11** (2), 618-623 (2011).

23. J. Chen, G. Zhang and B. W. Li, The Journal of Chemical Physics **135**, 104508 (2011).

24. M. Hu, X. L. Zhang, K. P. Giapis and D. Poulikakos, Phys Rev B **84** (8) (2011).

25. E. P. Pokatilov, D. L. Nika and A. A. Balandin, Appl Phys Lett **85** (5), 825-827 (2004).

26. J. H. Kang, J. W. Roh, W. Y. Shim, J. H. Ham, J. S. Noh and W. Y. Lee, Advanced Materials **DOI: 10.1002/adma.201101460** (2011).

27. L. Shi, D. Y. Li, C. H. Yu, W. Y. Jang, D. Kim, Z. Yao, P. Kim and A. Majumdar, J Heat Trans-T Asme **125** (5), 881-888 (2003).

28. J. W. Roh, K. Hippalgaonkar, J. H. Ham, R. K. Chen, M. Z. Li, P. Ercius, A. Majumdar, W. Kim and W. Lee, Acs Nano **5** (5), 3954-3960 (2011).

29. C. H. Yu, L. Shi, Z. Yao, D. Y. Li and A. Majumdar, Nano Lett **5** (9), 1842-1846 (2005).

30. K. Schwab, E. A. Henriksen, J. M. Worlock and M. L. Roukes, Nature **404** (6781), 974-977 (2000).

31. M. P. Pettes, M. T. and L. Shi, Adv Funct Mater **19** (24), 3918-3925 (2009).

32. G. Chen, S. Shen, A. Henry, J. Tong and R. T. Zheng, Nat Nanotechnol **5** (4), 251-255 (2010).

33. A. V. Savin, M. A. Mazo, I. P. Kikot, L. I. Manevitch and A. V. Onufriev, Phys Rev B **83** (24) (2011).

34. J. Chen, G. Zhang and B. W. Li, Nano Lett **10** (10), 3978-3983 (2010).

35. W. Lu, J. Xiang, B. P. Timko, Y. Wu and C. M. Lieber, P Natl Acad Sci USA **102** (29), 10046-10051 (2005).

36. J. Xiang, A. Vidan, M. Tinkham, R. M. Westervelt and C. M. Lieber, Nat Nanotechnol **1** (3), 208-213 (2006).

37. J. Chen, G. Zhang and B. Li, J. Chem. Phys. **To be published** (2011).

38. L. Shi and A. L. Moore, Meas Sci Technol **22** (1) (2011).

39. P. N. Martin, Z. Aksamija, E. Pop and U. Ravaioli, Nano Lett **10** (4), 1120-1124 (2010).

40. N. Mingo, L. Yang, D. Li and A. Majumdar, Nano Lett **3** (12), 1713-1716 (2003).

41. X. Lu, J Appl Phys **104** (5) (2008).

42. D. M. Rowe and V. S. Shukla, J Appl Phys **52** (12), 7421-7426 (1981).

43. H. Kim, I. Kim, H. J. Choi and W. Kim, Appl Phys Lett **96** (23), - (2010).

Chapter 4: Sub-amorphous thermal conductivity in ultra-thin crystalline Silicon nanotubes

4.1 Introduction

Understanding and controlling extraordinary thermal transport behavior in nanostructures has been widely pursued[1-5] because of its broad implications for a diverse range of applications, such as nanoscale transistors[6], phase change memory[7], and advanced thermoelectrics[8, 9]. In particular, nano-structuring has proven to be an effective approach to reduce the thermal conductivity[9-12] of crystalline semiconductors. This approach shortens the phonon MFP, which is limited by the characteristic size of crystalline nanostructures due to scattering at surfaces and interfaces. Crystalline thermal conductivity has been measured for nanowires as thin as ~15-20 nm[10, 13] and ~10-100 nm thick films[12, 14]. However, it is believed that the lower limit of the thermal conductivity of a material is that of its amorphous form[15], thereby setting the minimum one could achieve through nano-structuring. Here we experimentally probed thermal transport in Si NT structures at unprecedentedly small length scales of ~5 nm. We showed that the thermal conductivity of the c-Si NTs at this scale is even lower than that of a-Si NTs of similar geometries. These striking results were further supported by a drastic reduction in elastic moduli of the 5 nm c-Si NTs, measured as a 6-fold reduction compared to bulk Si and nearly half that of the a-Si NTs compared to the a-Si NTs. A convincing explanation of this sub-amorphous thermal conductivity in

the 5 nm c-Si NTs is presented based on the phonon softening effect, due to the drastically reduced mechanical stiffness.

Thermal characterization of nanostructures with an ultra-small size down to 5 nm has not been realized in the past due to the experimental challenges in both sample manipulation and accurate thermal measurements. We employed crystalline NTs of sp^3 Si with ultra-thin shells as a novel platform for probing thermal transport in this previously inaccessible regime. These NTs have thin crystalline shells ranging from 5 to 10 nm and, at the same time, large outer diameters (ODs) greater than 40 nm, facilitating sample manipulation. The Si NTs were prepared from Ge-Si core-shell nanowires (NWs) synthesized using a chemical vapor deposition (CVD) process [16], during which crystalline and amorphous Si shells were grown on Ge cores at 520 and 490 °C, respectively. The Ge core was then etched away using a H_2O_2 solution to obtain hollow Si NTs [17]. Figure 4.1a and b show TEM characterization of ~5 nm shell crystalline and amorphous NTs, respectively, and Figure 4.1c shows a representative hollow NT at low magnification in TEM. The crystallinity of the c-Si NTs is clearly demonstrated in the TEM images and their associated electron diffraction patterns. Additionally, electrical conductivity[17] and fracture strength (Figure 4.2) measurements indicate that, while the c-Si NTs are polycrystalline, they are of high growth quality with grain sizes larger than 300 nm, much larger than the NT shell thickness, similar to NTs in previous studies.[18]

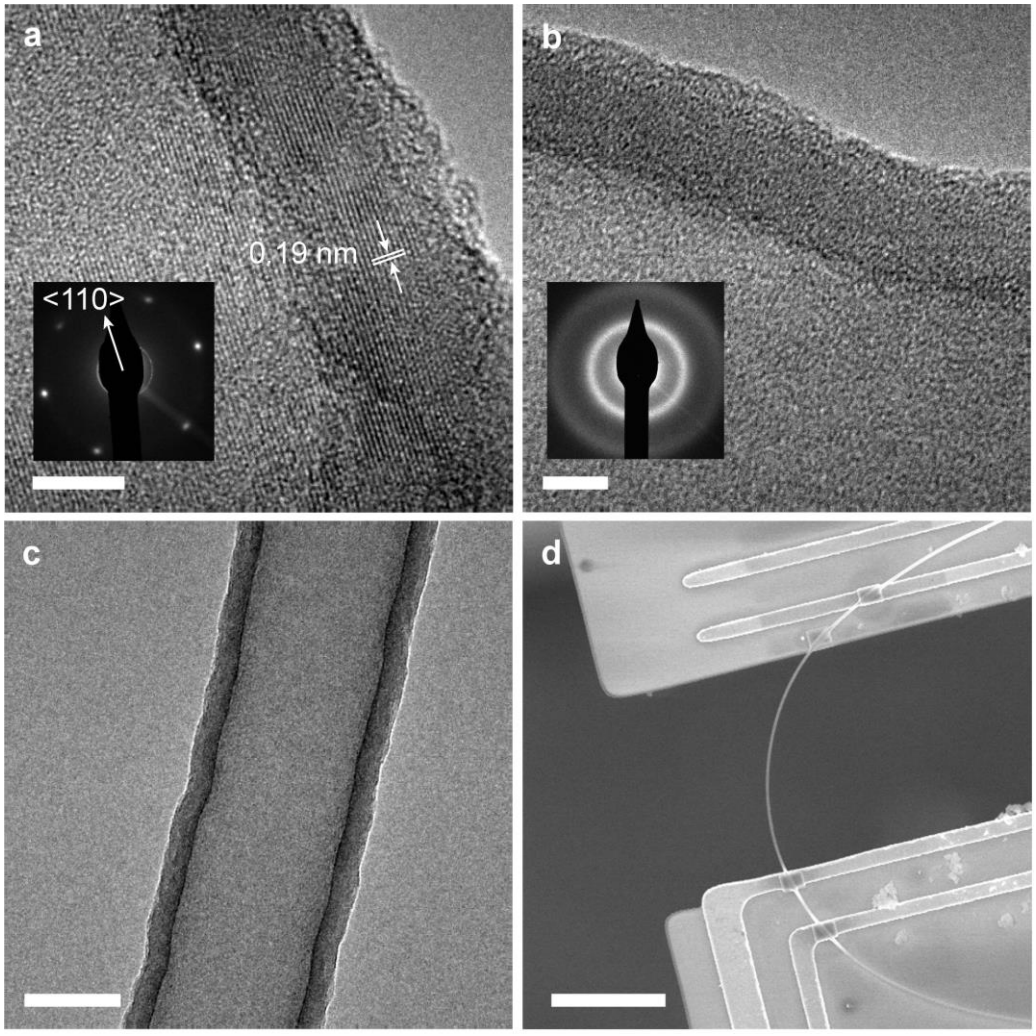


Figure 4.1: TEM images of silicon NTs: Crystalline 5 nm Si shell thickness, a, and diffraction pattern (inset a) as well as amorphous 5 nm Si shell thickness, b, and diffraction pattern (inset b). c, Low-resolution TEM image of hollow NT. d, Suspended nanotube sample used in the thermal conductivity measurement setup. TEM was performed to characterize all samples prior to thermal and tensile measurements to ensure crystalline or amorphous structure as well as geometry. Scale bars are 5 nm, 5 nm, 50 nm, and 5 μm for a, b, c, and d, respectively.

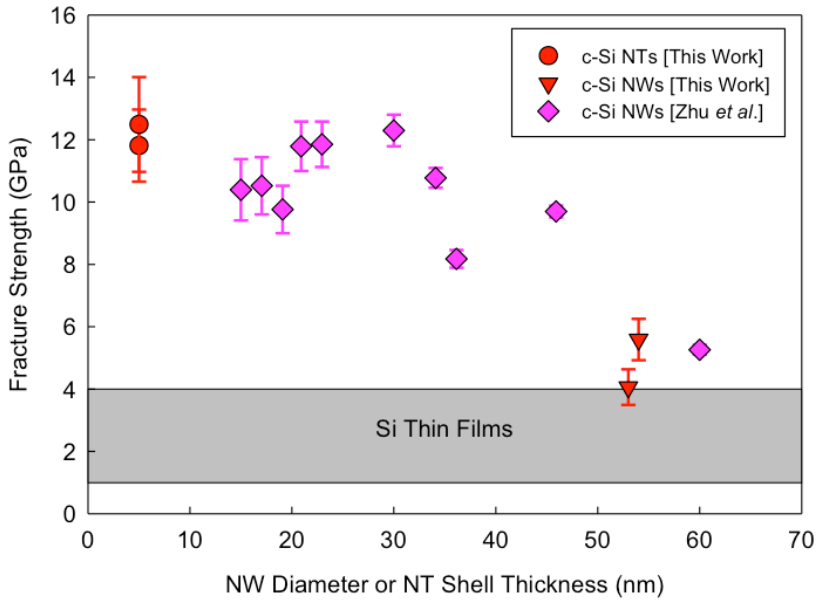


Figure 4.2: Fracture strength of crystalline silicon nanowires and nanotubes versus nanowire diameter or nanotube shell thickness. Following tensile testing of crystalline nanowires and nanotubes, the samples were stretched until breaking. The cantilever deflection is continuously measured until the nanotube/nanowire fracture point. This deflection leads to the maximum applicable stress, or fracture strength. This fracture strength is an indication of the concentration of defects in the sample, with low fracture strength indicating a higher amount of defects. From the measured data, it can be seen that the thin ~5 nm crystalline nanotubes are relatively defect free. Values of fracture strength of silicon nanowires and silicon thin films were taken from Zhu et al.[19] and Tsuchiya et al,[20] respectively.

4.2 Thermal conductivity of crystalline and amorphous Si nanotubes

After examining individual NTs in TEM, we then transferred the same NTs to suspended micro-devices for thermal conductivity (κ) measurements (Figure 4.1d). The measurement was done in a differential bridge configuration we developed [21], which possesses a low noise floor of ~10 pW K^{-1} necessary for individual NT κ measurements. We have also characterized and subtracted the parasitic background

conductance of all measured devices. Figure 4.3a shows the measured thermal conductivity of Si NTs with nominal crystalline shell thicknesses of ~5, 7, and 10 nm over a temperature range of 35-300 K. The combined structural characterization by high-resolution (HR) TEM carried out on *each* of the measured NTs allowed us to confirm crystallinity and precisely measure the dimensions of the samples, as shown in Appendix A. We used the full tubular thickness, as characterized by HRTEM for each measured NT (~5-10 nm c-Si or ~5 nm a-Si with ~1-1.5 nm inner/outer oxide coatings) to determine the thermal conductivity from the measured total thermal conductance. While we could have estimated the oxide contribution to thermal conductance and subtracted it from the total measured conductance, we elected instead to use the full NT thickness (including oxide) because there could be acoustic coupling at the interfaces between the oxide and Si. In addition, the thermal conductivity of the ~1 nm thick SiO_2 could deviate from the bulk value and is not known. We note that the native oxide thickness, which is formed during the H_2O_2 etching of the Ge cores, is usually ~1 nm, but sometimes as thick as 1.5 nm, and did not grow over the period of study. We did not see oxide layer thickness greater than 1.5 nm. This is consistent with previous Si NT growth studies.[18] Measured dimensions and thermal conductivity for all NT samples are listed in Table 4.1. Multiple samples of each type, including seven 5 nm c-Si NTs, have been measured, all with high repeatability, underpinning the accuracy and reliability of the measurement technique. Furthermore, the measured thermal conductivity shows no length dependence for lengths ranging from 4 to 8 μm (see Figure 4.4), suggesting negligible thermal contact resistance.

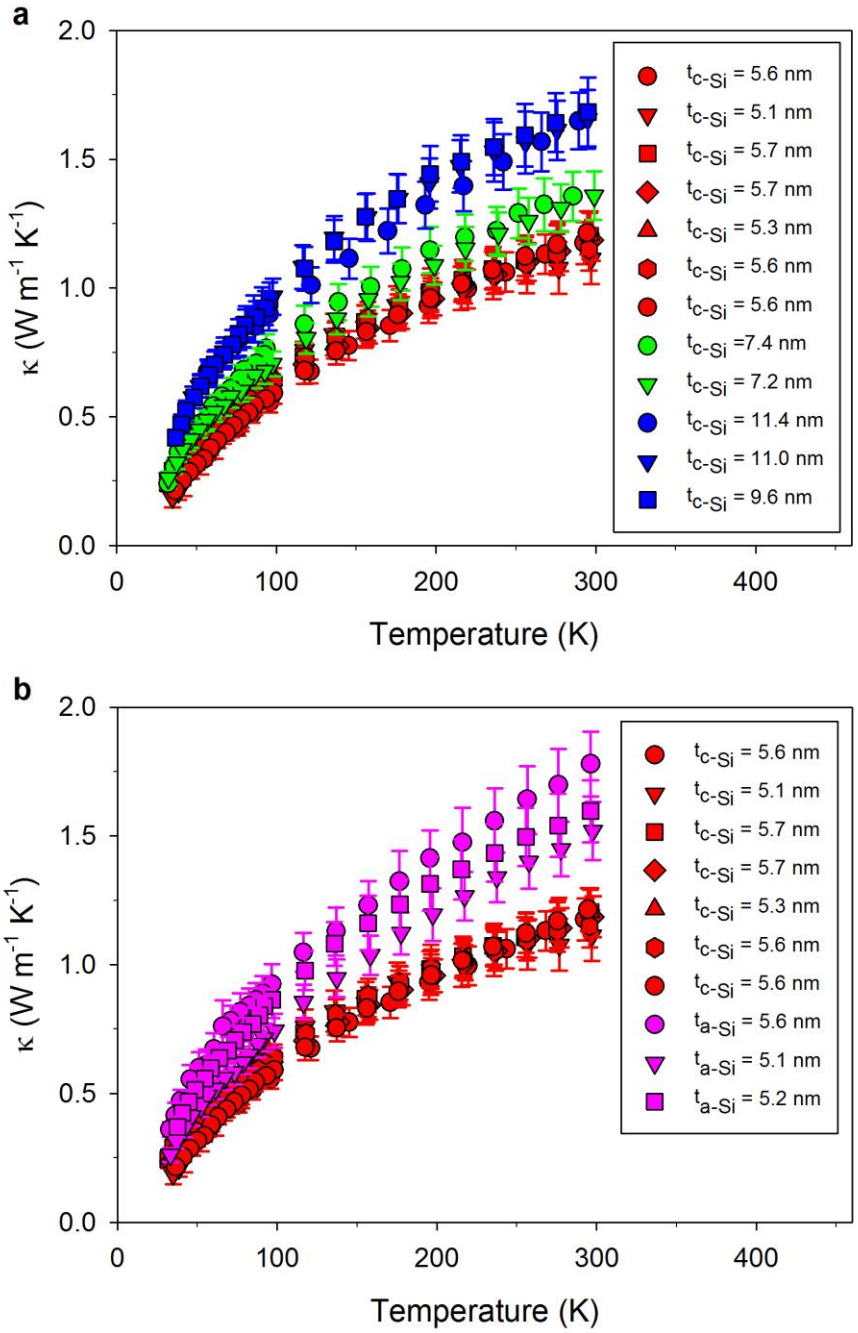


Figure 4.3: Thermal conductivity of silicon NTs: a, ~5, 7, and 10 nm c-Si NTs versus temperature and b, ~5 nm amorphous and crystalline NTs versus temperature. The dependence of thermal conductivity on shell thickness at room temperature is clearly visible in a, with a gradual decrease in thermal conductivity with decreasing thickness of the crystalline shell layer.

Table 4.1: Geometry and thermal conductivity of measured Si nanotube samples.

Sample ID	Sample Type	Shell Thickness (nm)	Outer Diameter (nm)	Sample Length (μm)	κ @ 300 K (W m^{-1} K^{-1})
C5-1	Crystalline NT	5.6	138	7.66	1.18±0.08
C5-2	Crystalline NT	5.1	48	5.75	1.11±0.10
C5-3	Crystalline NT	5.7	101	4.76	1.21±0.09
C5-4	Crystalline NT	5.7	143	4.78	1.19±0.08
C5-5	Crystalline NT	5.3	111	4.20	1.21±0.09
C5-6	Crystalline NT	5.6	91	4.21	1.15±0.08
C5-7	Crystalline NT	5.6	108	3.72	1.21±0.08
C7-1	Crystalline NT	7.4	113	10.25	1.36±0.10
C7-2	Crystalline NT	7.2	100	5.16	1.36±0.09
C10-1	Crystalline NT	11.4	109	10.60	1.65±0.11
C10-2	Crystalline NT	11.0	89	10.02	1.66±0.11
C10-3	Crystalline NT	9.6	84	7.42	1.68±0.13
A5-1	Amorphous NT	5.6	81	10.50	1.78±0.13
A5-2	Amorphous NT	5.1	88	5.67	1.52±0.11
A5-3	Amorphous NT	5.2	46	6.23	1.60±0.12

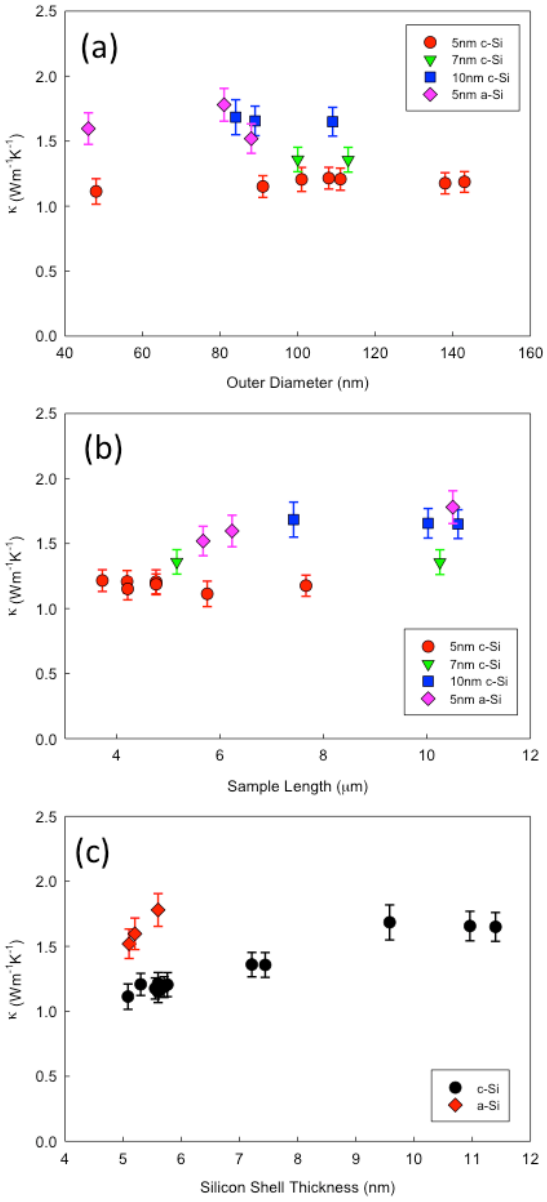


Figure 4.4: Thermal conductivity of crystalline and amorphous nanotubes versus (a) outer diameter, (b) suspended sample length, and (c) shell thickness. There is no correlation between the measured nanotube thermal conductivity and the nanotube outer diameter for any of the crystalline or amorphous samples. This leaves the shell thickness as the sole dimension that strongly affects phonon scattering. Since thermal conductivity of the Si NTs is independent of the sample length, contact resistance between the nanotubes and the measurement devices is negligible. A clear size dependence on shell thickness can be seen in (c) for c-Si NTs from 5 to 10 nm.

As shown in Figure 4.3a, the average measured thermal conductivities were 1.18±0.12, 1.36±0.10, and 1.66±0.13 W m^{-1} K^{-1} at 300 K for ~5, 7, and 10 nm shell c-Si NTs, respectively. The measured κ of the ~5 nm c-Si NTs approaches the theoretical minimum thermal conductivity (κ_{min}) for amorphous silicon (1 W m^{-1} K^{-1})[15], which is extraordinary given that these are crystalline structures, whereas the κ_{min} model is used to describe amorphous materials where phonon energy transport is limited to nearest atomic neighbors.[15] Furthermore, we compared κ of 5 nm crystalline NTs to fully amorphous Si NTs with similar shell thickness (Figure 4.3b). Surprisingly, the measured κ of the crystalline samples is even lower than that of the a-Si NTs. The difference (~30%) is substantial and clearly exceeds the measurement uncertainty. Similar sub-amorphous behavior has been observed in layered WSe_2 crystals[22], which was largely due to the interfacial thermal resistance between stacked crystal layers, whereas the low κ observed in the c-Si NTs here corresponds to heat conduction along the axial direction without interfacial resistance. While the NTs contain a small concentration of Ge (less than ~1% atomic ratio, see Figure 4.5), in line with previous NT studies[18], it would not affect thermal conductivity in the ~5 nm c-Si NTs. The small amount of Ge could only affect thermal conductivity in much larger nanostructures (>100 nm) because of the co-existence of impurity and boundary scattering.[23, 24] However, for very small nanostructures, such as the NTs studied here, boundary scattering overwhelmingly dominates impurity and even *Umklapp* scattering.[25] It has additionally been shown that thermal conductivity of a-Si is far below that of Si-Ge alloys with Ge concentrations ranging from 0.13% to 20%.[26] Therefore, impurity scattering introduced by the small amount of Ge would not be

strong enough to induce the sub-amorphous thermal conductivity in the ~5 nm c-Si NTs.

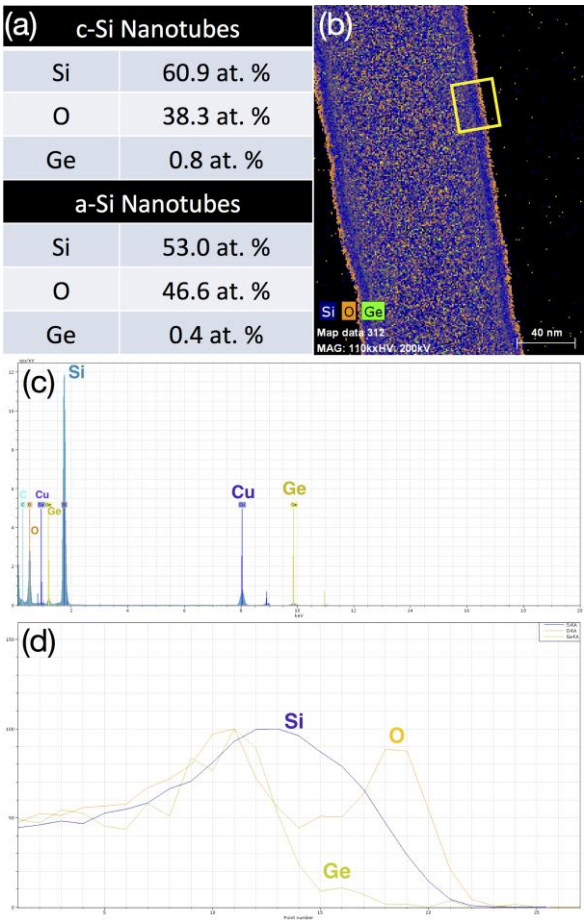


Figure 4.5: TEM EDX on Si NTs. (a) Elemental concentrations in c-Si and a-Si NTs. The Si shell (~5 nm thick) and outer/inner oxide coatings (each ~1 nm thick) account for the majority of atomic constituents while Ge impurities in the NT account for less than 1%. The higher Ge impurity concentrations observed in the c-Si versus a-Si NTs is most likely caused by larger amounts of Ge diffusion during the growth at higher temperature (c-Si is grown at 520 °C while a-Si is grown at 490 °C). (b) EDX elemental mapping of c-Si NT in TEM. (c) Element counts from EDX mapping (b). The peaks for Cu and C come from the lacy C support structure on the Cu TEM grid. (d) Cross-sectional element mapping from yellow box in (b), starting from the inner tube surface (left) to outside the NT (right). The Si shell (blue curve) has inner and outer oxide coatings (orange peaks), while the majority of Ge impurities (green curve) are close to or within the inner oxide surface. The vertical scale is a.u. and the Ge curve was scaled vertically to emphasize the spatial distribution.

To develop an understanding of the extraordinarily low thermal conductivity in the crystalline Si NTs, it is necessary to first discuss the phonon transport mechanisms that occur in their amorphous counterparts. In amorphous Si, κ can be modeled as the sum of the contributions from two distinct vibrational modes, propagons and diffusons[27]. Propagons, as their name suggests, are propagating and delocalized modes, and in the case of a-Si, could possess a broad MFP possibly ranging from ~10 to ~40 or even 100s of nm.[1, 28, 29] Diffusons, on the other hand, are non-propagating and delocalized modes, whose MFP is rather short (~0.5-10s of nm), albeit not well-defined, and contribute to thermal conductivity by coupling with other modes through atomic disorder.[28, 29] The diffuson contribution can be modeled using the Allen-Feldman theory[27] and is estimated to be ~1 W m^{-1} K^{-1} for a-Si, whereas the propagon contribution has been shown to exhibit a strong size dependence.[28] Therefore, our measurement results (Figure 4.3b) suggest that the propagon contribution is about ~0.5 W m^{-1} K^{-1} for our 5 nm thick a-Si, indicating the important size effect for propagons even down to the 5 nm regime in the >5 μm long NTs, which has not previously been probed experimentally. Our results on a-Si NTs are also qualitatively in line with previous thermal conductivity measurements on thin films of a-Si, which show values ranging from 1.1-4.0 W/m-K over film thicknesses ranging from ~50 nm to tens of microns. The wide variation is presumably caused by the dependence of the thermal conductivity on a combination of factors including film fabrication method, film thickness, growth temperature, and purity.[30, 31] The thermal conductivity of the thinnest a-Si film at ~50 nm[32] was found to be 1.4 W m^{-1} K^{-1} while ion-amorphized ~17 nm thick films[33] were 1.7 W m^{-1} K^{-1}. The thermal conductivity values measured

for a-Si NTs in this work are very similar to values measured for thin high-purity and fully-dense a-Si films.

The MFP alone, however, cannot explain the sub-amorphous values of thermal conductivity in 5 nm c-Si NTs, as one would expect that phonons in the crystalline NTs would have MFP longer than that of propagons in disordered a-Si NTs with similar geometries. In addition to MFP, the thermal conductivity can also be influenced by the phonon group velocity (v_g), which is characterized by the speed of sound in the low frequency limit, which has been proposed theoretically to decrease due to phonon confinement in NWs with diameter less than 20 nm.[34] The phonon specific heat could also increase due to excitation of low frequency phonon modes, leading to enhancement of the thermal conducitvity. However, these modes are only excited at very low temperatures. Consequently, specific heat is expected to be bulk-like even for 5 nm structures over the measured temperature range (35-300 K).[35-37] We hypothesize that phonon modes could have been altered in the ultra-thin c-Si NTs, leading to a lower speed of sound and, consequently, contributing to the sub-amorphous thermal conductivity.

4.3 Mechanical testing of crystalline and amorphous Si nanotubes

To experimentally verify this hypothesis, we indirectly measured the speed of sound (v) in single Si NTs through tensile Young's modulus (E) tests (Figure 4.6a), as v is related to $\sqrt{E/\rho}$, where ρ is the mass density. Figure 4.6b shows the measured

Young's moduli of a-Si and c-Si NTs, as well as literature data on Si NWs with larger diameters (15-60 nm)[19], bulk c-Si[19], and a-Si thin films[38]. Two c-Si NWs with diameters of 54 and 53 nm were used to calibrate the measurement and exhibited bulk-like elasticity, consistent with prior measurements on large-diameter Si NWs.[19] The averaged E of the three 5 nm crystalline NTs is 30.1±2.7 GPa, or about *six times lower* than bulk Si. This drastically reduced E is consistent with previous studies on small diameter c-Si nanostructures including sub-25 nm NWs[19] and ~6 nm nano-junctions[39], as well as the observed reduction of v_g in InSb NWs[40]. Comparatively, three ~5 nm shell a-Si NTs were found to have an average modulus of 62.7±6.5 GPa, within the range of measured elastic moduli of a-Si thin films[38] and nearly twice that of the crystalline NTs of the same size. This elastic softening in c-Si NTs stems from the growing importance of surface effects at reduced dimensions. Surface atoms have lower coordination numbers and electron densities than bulk atoms, requiring changes in bond spacing which leads to strain and surface stresses[41, 42]. Meanwhile, simulations have shown that Si surface stresses are compressive in nature and require atomic reorganization and bond lengthening to reach an equilibrium state[43, 44], leading to elastic softening. Furthermore, other surface and interfacial effects may also play a role, such as the presence of native oxide layers.[41, 45]

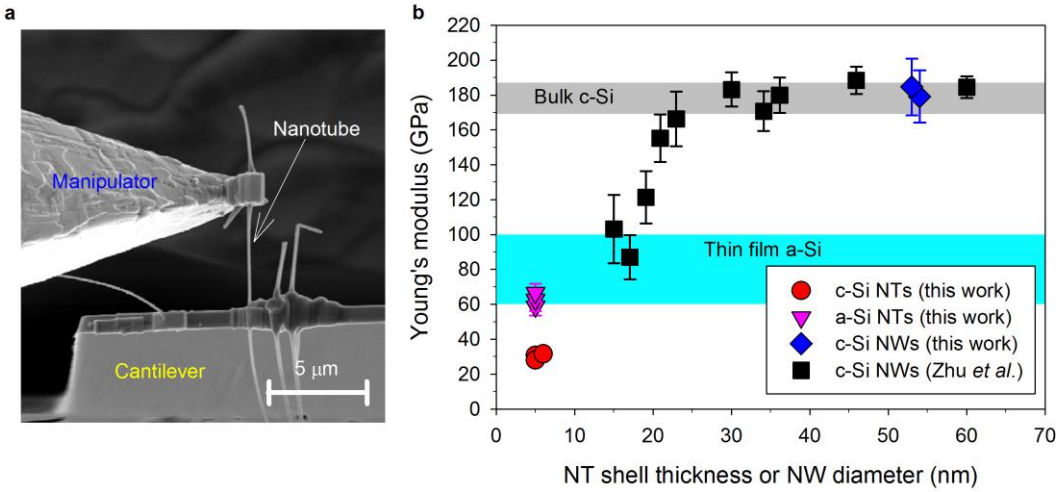


Figure 4.6: Elastic tensile tests: a, Elastic modulus tensile measurement using manipulator probe to pull NW attached to the end of an AFM cantilever. b, Elastic moduli of silicon NTs and NWs. ~5 nm amorphous NTs exhibit ~2× stiffer moduli than ~5 nm crystalline NTs. Values of elastic moduli of silicon NWs were taken from Zhu et al.[19] and expected ranges for bulk c-Si[19] and a-Si thin films[38] are shown.

The close correlation between thermal conductivity and elastic properties in Si NTs and NWs is clearly illustrated in Figure 4.7, which shows the κ^*/D^* ratio (left axis) and $\sqrt{E^*}$ (right axis), where κ^*, D^*, and E^* are κ, D, and E normalized with their respective values from ~60 nm Si NWs (all values taken at 300 K), as a function of D, the shell thickness for NTs or the diameter for NWs, whichever applicable. In the boundary scattering regime, the κ/D ratio scales with the phonon velocity ($\kappa/D \sim Cv$, where C is the phonon heat capacity), while $\sqrt{E}$ is also a measure of the speed of sound ($v = \sqrt{E/\rho}$). Figure 4.7 shows that there is an excellent match between the size effects on thermal and elastic properties within the size range considered here (5-70 nm). Above 25 nm, diffusive scattering at the NW surface dominates and κ^*/D^* and $\sqrt{E^*}$ are the same among NWs with different sizes, suggesting no change in v. This is

also known as the boundary scattering or Casimir limit[10]. However, below 25 nm, κ^*/D^* markedly drops below unity, by as much as 50% in the 5 nm c-Si NTs. The reduction in κ^*/D^* coincides exactly with the decline in $\sqrt{E^*}$. Additionally, the previously measured 22 nm c-Si NW[10], for which a theoretical explanation of the low κ has been elusive, matches very well with the observed trend of $\sqrt{E^*}$. The close correlation between elastic and thermal properties suggests that the observed ultra-low thermal conductivity in the 5 nm c-Si NTs is caused by elastic softening arising at these reduced dimensions. It is important to note that, since the NTs are softer compared to bulk Si, the actual theoretical κ_{min} will be lower, by as much as ~50% (or ~0.5 W m^{-1} K^{-1}) in our 5 nm c-Si NTs, due to its dependence on the speed of sound.[15] Therefore, the measured κ of 1.18 W m^{-1} K^{-1} is still substantially larger than what the theoretical κ_{min} could be for such a soft material. Furthermore, even though the ~5 nm NTs are very small, approaching the phonon wavelength (<6 nm at 300 K in bulk Si),[46] the transport is still largely three-dimensional, which warrants the applicability of the *same* '$\kappa \sim Cvl$' formula for all the NW and NT samples shown in Fig. 4.7. One-dimensional (1-D) behavior is predicted to occur only at low-temperature (<30 K) in structures approaching sizes comparable to half the dominant thermal wavelength.[35, 47]

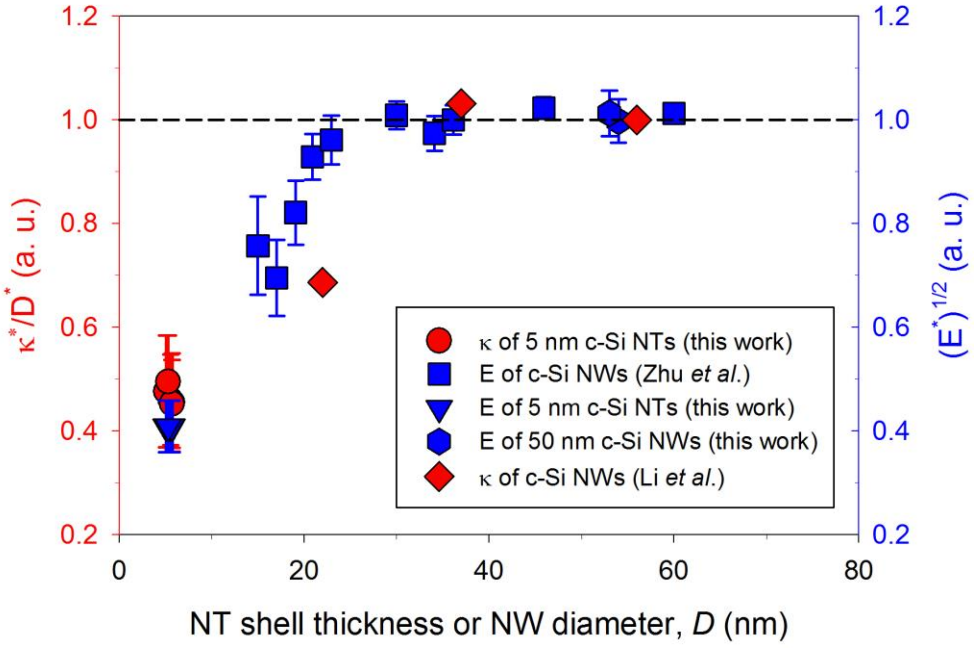


Figure 4.7: Correlation between thermal conductivity (κ) and elastic modulus (E) in crystalline NTs and NWs. κ, D, and E have been normalized with their respective values for ~60 nm Si NWs and plotted as a function of D, where D is the shell thickness for NTs or the diameter for NWs, whichever applicable. Normalized variables are labeled as κ^*, D^*, and E^*, respectively, while the dashed line represents the maximum of both κ/D and $\sqrt{E}$. Above 25 nm, the nanostructure dimensions are smaller than the phonon MFPs, which limits the thermal conductivity due to diffuse phonon-boundary scattering. Below 25 nm, elastic softening in the nanostructure alters the phonon dispersion and causes a rapid decrease in thermal conductivity beyond the expected influence of boundary scattering. The κ/D and $\sqrt{E}$ for ~5 nm thick c-Si NTs and c-Si NWs are from thermal and elastic measurements shown in Figures 4.3b and 4.6b, respectively, as well as literature values from Li et al.[10]

4.4 Molecular dynamics simulation of thermal and mechanical properties

In order to theoretically underpin and quantify the mechanisms leading to the measured ultra-low thermal conductivity of c-Si NTs, we performed equilibrium molecular dynamics (EMD) simulations of phonon transport in such structures. Figure

4.8a shows the calculated κ and E of an as-quenched c-Si NT. For all cases in Figure 4.8a, the inner diameter is 20 nm and the thickness of the amorphous layer on the inner and outer surfaces is 2 nm. The total thickness of the shell is varied from 5 to 10 nm, which is comparable to the experimental measurements. It is clear that, both the thermal conductivity and Young's modulus decrease with decreasing shell thickness, confirming the relationship between the thermal conductivity reduction and the softening of the elastic modulus, as revealed by the experiments (Figures 4.6 and 4.7). In order to imitate realistic experimental conditions, where roughness at the crystalline/amorphous interface is inevitable, for the case of inner diameter of 20 nm and total thickness of 5 nm, we also considered the presence of such roughness by randomly removing up to 80% of the interface atoms on the crystalline sides and investigated its effects on κ and E. A total thickness of 5 nm, as opposed to the smallest total shell thickness measured experimentally (~7 nm, i.e., ~5 nm Si with ~1 nm oxide on each side), was used due to computational limitations. Nevertheless, it is clearly shown in Fig. 4.8(b) that, upon interface roughening, both κ and E are reduced compared to the as-quenched interface, which again demonstrates the close correlation between κ and E, as we observed experimentally. Furthermore, the vibrational density of states (VDOS) of the amorphous layer in the high frequency regime is significantly reduced compared to the crystalline layer and the entire VDOS shifts toward low frequencies (Figure 4.9). This results in a large vibrational mismatch between the crystalline and amorphous layers thereby causing strong phonon scattering at the crystalline/amorphous interface, which leads to the ultra-low thermal conductivity in amorphous coated c-Si NTs. We would like to note that it is more informative to view

the MD simulations as a tool to illustrate possible mechanisms giving rise to the experimental observations, which, in this case, is the close correlation between thermal conductivity and elastic properties. It is difficult to quantitatively compare the MD and experimental results due to the various inherent differences, including but not limited to interatomic potential, surface roughness, native oxide, and defects.

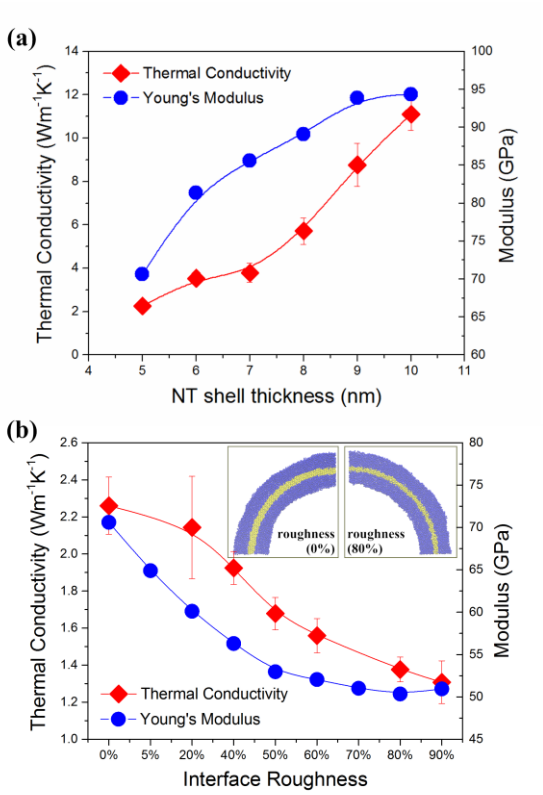


Figure 4.8: (a) EMD simulation of thermal conductivity and elastic modulus with different NT thickness. The interface between amorphous layer and crystalline part is the as-grown condition, which is quenched from the high temperature liquid phase of the amorphous region. (b) EMD simulation of thermal conductivity and elastic modulus reduction with c-Si NT interface roughness. Interface roughness is achieved through random removal of atoms on the crystalline face of the crystalline shell-amorphous coating interface. The insets show two typical atomic structures of the Si NTs with different interface roughness. Color coding: yellow: c-Si; blue: amorphous layer.

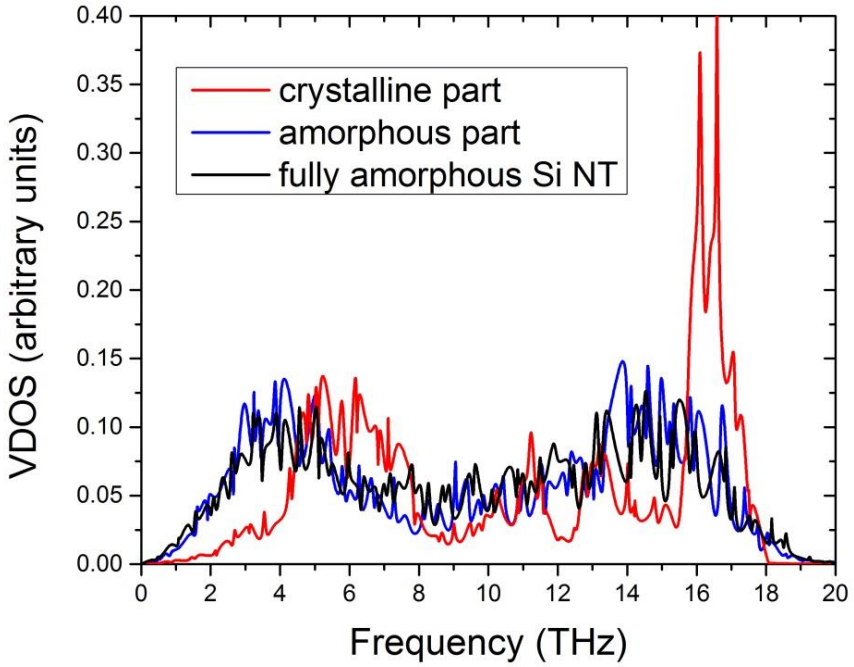


Figure 4.9: Comparison of vibrational density of states from EMD simulation in crystalline and amorphous layers in a thin Si nanotube with inner diameter of 20 nm and total thickness of 5 nm including 2 nm amorphous layer on inner and outer surfaces. The VDOS of a pure amorphous Si nanotube is also shown for comparison. The VDOS is calculated by a Fourier transform of the atomic velocity autocorrelation function.

4.5 Estimation of Thermal Contact Resistance

To estimate the thermal contact resistance between the Si NTs and the suspended devices, we can use studies on similar systems, such as for Si NWs and multi-walled carbon nanotubes (MWCNTs). Length dependent measurements (2-10 μm) on VLS synthesized c-Si NWs with diameters ranging from 70-130 nm exhibited an average contact resistance for all samples of ~4.5×10^{6} K W^{-1}.[48] These NWs were Pt-C bonded onto suspended membranes similar to those used in this study, with NWs

in contact with Pt electrodes and Pt-C bonding over ~1 μm long sections. Because of the similar OD and Pt-C contact bonding of the present Si NT samples, we can assume that the contact thermal resistance of our NT samples is of the same order of magnitude (1-10×10^6 K W^{-1}), which is two to three orders of magnitude lower than the total measured thermal resistance of the NT samples (<1 nW K^{-1}). Therefore, we can conclude that the thermal contact resistance is negligible in the present Si NT samples. This is in agreement with the length dependent measurements seen in Fig. 4.4(b).

Another way to look at the relative role of the contact resistance is by examining the areal interfacial thermal resistance, which is typically on the order of 2×10^{-8} m^2 K W^{-1} or lower for common materials. For instance, Li and coworkers studied MWCNTs with outer diameter (OD) of 10 and 66 nm in contact with 2 μm wide Pt electrodes measured both with and without electron-deposited Au bonding.[49] The 66 nm OD MWCNT had a calculated contact width of ~4 nm and an areal contact resistance of 2.2×10^{-8} m^2 K W^{-1}. If we consider a 1 μm contact length for our Si NTs with similar values for contact width and areal contact resistance as the 66 nm MWCNT, then we have a contact resistance of ~5.5×10^6 K W^{-1}, which is similar to that observed for the Si NWs previously mentioned.

4.6 Further Equilibrium Molecular Dynamics (EMD) Simulation Details

The employed molecular model system consists of a hollow c-Si NT with a-Si layers on both inner and outer shell surfaces. In order to directly compare simulations

to experimental samples, the ID is chosen to be 20 nm and total thickness is about 5 nm. For all cases the thickness of the a-Si layer on both surfaces is about 2 nm. All molecular dynamics calculations were performed using the LAMMPS package,[50] and the original Stillinger-Weber (SW) potential[51] was used to describe Si-Si interactions. A time-step of 0.25 fs was used throughout all simulations. The initial structure was cut from a perfect crystalline structure of bulk Si and the longitudinal direction of the NT was extended in the [110] direction. Next, the outer and inner surfaces with thickness pre-specified as 2 nm were heated to 5000 K and maintained at this temperature for 10 ps such that atoms in both regions melted. Subsequently, the regions were rapidly quenched down to 300 K in 0.5 ps such that the amorphous structure was formed. We then continued to relax the entire NT with an NPT (constant particles, pressure, and temperature) ensemble for 100 ps. After relaxation, the thermal conductivity of the Si NTs was computed with an NVE (constant particles and volume without thermostat) ensemble by integrating the heat flux autocorrelation function (the Green-Kubo method)

$$\kappa = \frac{1}{Vk_BT^2}\int_0^{\tau_m}\langle Q_z(t)Q_z(t+t')\rangle dt', \qquad (4.1)$$

where V is the volume of the NT which is considered a hollow cylinder, k_B is Boltzmann's constant, T is the absolute temperature, Q_z is the heat current along the longitudinal direction (z) of the NT, τ_m is the autocorrelation length, and the angular brackets denote an average over time. In our EMD simulation, τ_m is chosen to be 50 ps and the total simulation time for a single run lasts over 2.5 ns. The final thermal

conductivity results reported here were averaged over at least 5 independent runs by assigning different initial velocities in the NVE stage.

It is known that convergence can be a problem while running EMD simulations. To this end, we checked the length dependence of the thermal conductivity of Si NTs. For a selected case of total thickness 5 nm, we simulated four different lengths (11.5, 15.4, 19.2, and 23.0 nm), but did not find any noticeable change in the calculated thermal conductivity for both amorphous coated crystalline NTs and fully amorphous NTs. Therefore, in order to save computational time, we chose a length of 15.4 nm for all EMD simulations.

4.7 Growth of Silicon Nanotubes and Nanowires

Ge/Si core/shell NWs were synthesized using gold nanocluster catalysts (Ted Pella, Inc.) dispersed on Si (100) wafers using a vapor-liquid-solid (VLS) mediated low-pressure chemical-vapor-deposition process (ET-2000, CVD Corporation). On the Ge core backbone grown at 290 °C, 300 Torr, and 100 sccm flow of GeH_4 (1.8% in H_2) for 2 hours, different types of Si shell were grown using 520 °C, 40 Torr, and 40 sccm of SiH_4 (2% in H_2) for crystalline shell and 490 °C, 70 Torr, and 100 sccm of SiH_4 for their amorphous counterpart. During the transition period between Ge core and Si shell growth, a small amount of SiH_4 (0.7 Torr, 15 sccm) was added to prevent gold diffusion from the AuGe eutectic droplets at the end of the Ge cores.[52] The shell thickness was controlled by the growth time ranging from 5~25 min to deposit 5~10 nm of crystalline (growth rate 1.3 nm/min) or amorphous shell (growth rate 0.4 nm/min). Subsequent Ge core wet etching was performed in 30% hydrogen peroxide

at 60 °C for 5 hours followed by purification process using multiple centrifugal filtration (Nanosep 30K MWCO, Pall Co.) in isopropyl alcohol (IPA). For the thermal conductance study, NTs were further transferred onto 19 by 19 μm holey TEM grids (Ted Pella, G1000HS) to investigate their inner-/outer- diameters, Si/oxide thicknesses and select clean and long NTs. Final FIB process was carried out to suspend selected NTs across two membranes of micro-fabricated devices.

4.8 Preparation of Nanotube Thermal Measurement Samples

After the nanotubes were etched in solution, they were drop-cast onto TEM grids (Gilder 1000 Mesh) for sample characterization. Using TEM (FEI Tecnai Sphera), nanotube samples with the desired shell thickness and usable lengths (~15-20 μm, fully suspended) were identified. These nanotubes were then checked using both electron diffraction and lattice pattern images to identify whether tubes were crystalline or amorphous as well as accurate shell dimensions. The positions of the chosen nanotubes were carefully documented and then the TEM grids were transported to a dual-beam FIB (FEI Quanta 3D) for further processing. Using SEM, the documented positions from TEM were identified and checked to make sure identified nanotubes were undamaged. The nanotube was then attached to a tungsten probe by electron-deposited Pt-C and lifted off the TEM grid with a nano-manipulator (Omniprobe 200) after waiting for the Pt-C gas to dissipate. The nanotube was subsequently moved to a suspended membrane thermal measurement device, maneuvered into the preferred orientation, and placed into contact with the heating and sensing membranes, with ~10 μm distance between the edge of the gap between the

two membranes and the end of the nanotube attached to the tungsten probe to eliminate exposure of the suspended nanotube section to the ion beam if used to cut the probe free and reduce exposure to re-deposition effects. The nanotube was then bonded to the membranes using the electron-deposited Pt-C, with care taken to not expose the suspended portion to the electron beam. The probe was then either cut free using the ion beam or broken free after moving the probe. This process is shown in Fig. 4.10. Later, the outer diameter and suspended nanotube length were measured using a UHR SEM (FEI XL30) to calculate the thermal conductivity from the measured conductance. Several samples were checked in TEM after the fabrication and measurement procedure to ensure that the nanotubes were not amorphized during device fabrication (Fig. 4.11).

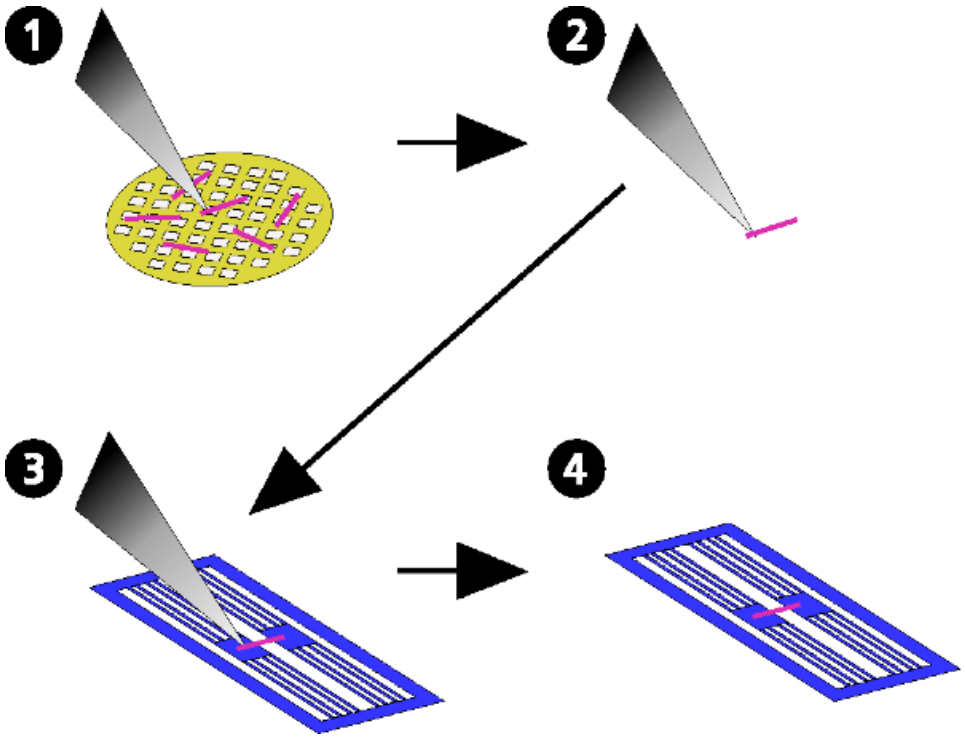


Figure 4.10: Nanotube thermal device fabrication procedure. The nanotube thermal conductivity samples are fabricated via a pick-and-place procedure. 1) Nanotubes are characterized in TEM to identify crystallinity and geometry. Furthermore, samples are mapped and then re-located in a dual-beam FIB. 2) In the FIB, the nanotubes are picked up using a tungsten manipulator probe. 3) The samples are then moved to a suspended thermal characterization device and placed between the hot and cold reservoir membranes. 4) The manipulator is then removed, leaving the suspended nanotube ready for thermal conductivity measurements.

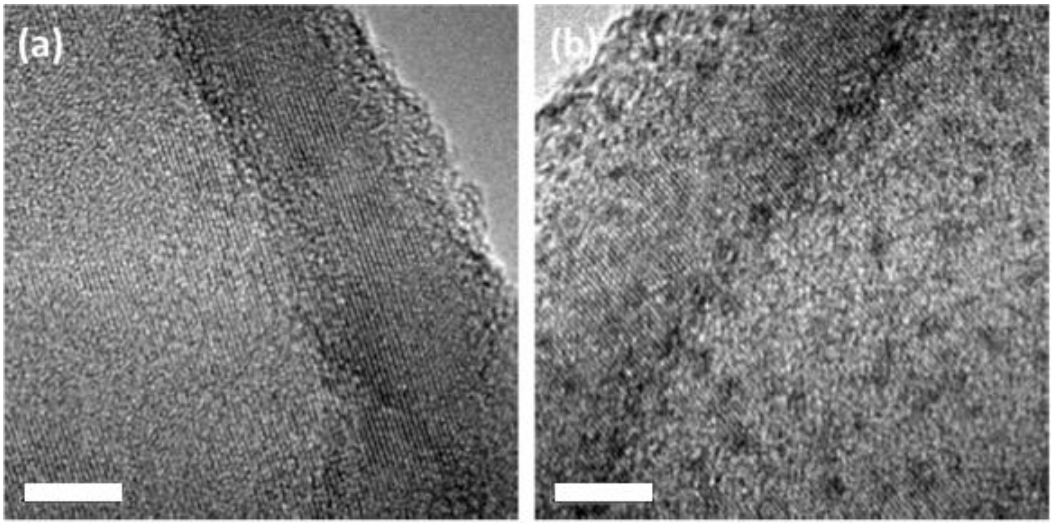


Figure 4.11: TEM of nanotube sample for thermal measurement (a) before and (b) after device fabrication. Nanotube samples were checked in TEM after device fabrication in FIB and compared to initial TEM images taken of samples. The measurement sample fabrication procedure does not damage the thin crystalline walls of the nanotubes as can be seen from the clear lattice images afterward. The small dark dots in (b) are small Pt-C deposits on the surface from the FIB bonding procedure. Scale bars are 5 nm.

4.9 Thermal Conductivity Measurement

The thermal conductance of nanotube samples was measured using the suspended micro-device technique,[10, 53] where two SiN_x membranes patterned with Pt resistive thermometer (PRT) coils are each suspended by six SiN_x beams. One of the membranes is used as a heater by passing DC current through the PRT, inducing a temperature rise by Joule heating, while the other is used solely as a sensor. Subsequently, the temperature rise is measured on both membranes, with knowledge of the temperature coefficient of resistance (TCR), by passing small AC currents through both PRTs and measuring the change in resistance. The TCR is directly found by fitting the measured base resistance as a function of sample temperature to the Bloch-Gruneisen equation. Sample temperatures were measured using a K-type

thermocouple directly attached to the micro-device being measured. The nanotube to be measured is placed bridging the two membranes and the applied Joule heating is varied. By measuring the resulting temperature rise on both heating and sensing membranes, the heat flux through the suspended nanowire sample can be found and the thermal conductivity calculated. The measurement is conducted in a closed cycle He cryostat used to vary the global temperature of the sample from 35-300 K. The system is also held in vacuum pressure of less than ~10^{-5} Torr to reduce conductive and convective heat transfer by residual gas molecules in the chamber. Radiative heat losses along the suspending SiN_x beams are also negligible as it accounts for <1% of the systematic measurement error over the measurement temperature range.[54] Due to the low thermal conductance of the nanotubes (<1 nW K^{-1}), a variation on the measurement employing a Wheatstone bridge based circuit to measure the resistance change of the sensing membrane was used to increase sensitivity, enabling measurements of thermal conductance as low as ~0.1 nW K^{-1}.[13, 21] At such sensitivities, however, there is an intrinsic background thermal conductance in addition to the nanotube thermal conductance, which has a value of ~0.2 nW K^{-1} at 300 K for device with a 5 μm gap between the membranes and decreasing with the system temperature. In order to eliminate this background conductance, a canceling scheme is used, with the sensing membrane of an identical blank pair device with no nanotube present as the other branch of the Wheatstone bridge.[55, 56] The heating membrane of this pair device is Joule heated with applied power equal to that of the heating power applied to the nanotube device. The bridge then measures the difference between the temperature rises of the nanotube and pair sensing devices, effectively subtracting the background

conductance and leaving only the nanotube thermal conductance which is used to calculate the thermal conductivity. Error in the measured thermal conductivity comes from error in the measured TCR, standard deviations of multiple measurements to account for random errors, and uncertainties in the geometry measurements from TEM and SEM.

The measured thermal conductance was then converted to the reported thermal conductivity values using cross sectional area based on the total shell thickness including the Si shell and 1-1.5 nm native oxide layers on both inner and outer surfaces. The thermal conductance of the native oxide layers was not subtracted from the total conductance because thermal conductivity of ~1 nm thick SiO_2 is unknown. Therefore, the reported thermal conductivity values can be viewed as the effective ones for the Si and SiO_2 composite nanotubes, which is also consistent with the values extracted from the MD simulations in this work. Nevertheless, it should be noted that since the thermal conductivity of the SiO_2 is on the order of 1 W m^{-1} K^{-1}, similar to the measured thermal conductivity value of the NT samples, the thermal conductivity of the 'pure' Si shells would only be altered slightly if the oxide layer contribution was subtracted.

4.10 AFM Cantilever Calibration for Tensile Measurements

The elastic modulus tensile testing was done using an AFM cantilever as force transducer by measuring its deflection in SEM. For this reason, accurate knowledge of the cantilever spring constant is required to convert the deflection distance into an applied force. Before any tensile measurements were performed, we calibrated the

AFM cantilever spring constant using the Sader method[57, 58]. The spring constant of a rectangular cantilever is dependent on the cantilever geometry, material, and the fundamental radial resonant frequency in a vacuum. This can be calculated without knowledge of the density and thickness when the length (100 μm) is longer than the width (40 μm) which is longer than the thickness (1-2 μm), which is the case for our cantilevers (Bruker ORC8). The fundamental vacuum frequency shifts in the presence of a fluid, such as air, and can be calculated from the resonant frequency in the fluid with knowledge of the fluid properties, cantilever width, hydrodynamic function, and quality factor in the fluid (which should be $\gg 1$). Using an AFM (Veeco Scanning Probe Microscope), we measured the resonance spectrum of the cantilever through a frequency sweep and narrowed the sweep band to capture both the fluid resonance frequency and the quality factor. The measured AFM cantilever resonant frequency and quality factor was 67.5 kHz and ~104, respectively. These parameters were used to calculate the static spring constant (as opposed to the dynamic spring constant) necessary for the tensile tests, which was found to be 0.64 N m^{-1}. This proved very similar to the vibrometer test results supplied by Bruker (resonant frequency: 67.9 kHz, spring constant: 0.66 N m^{-1}).

4.11 Elastic Modulus Measurement Details

To measure the elastic modulus of nanotubes and nanowires, samples were first identified and characterized in a TEM, their positions were documented, and then they were moved to a FIB, similar to the sample fabrication process previously described. Then, in a process similar to previous tensile measurements on single

nanowires,[19] the samples were picked up with a tungsten probe in a dual-beam FIB (FEI Quanta 3D) and attached to the end of an AFM cantilever (Bruker ORC8) using electron beam deposited Pt-C. The nanotube was then pulled using the probe while both the deflection of the cantilever and the length of the nanotube were measured (schematic in Fig. 4.6(a) and SEM measurement pictures in Fig. 4.12), providing both the applied force (stress) due to the cantilever deflection and strain from measurements of the nanotube length. Spring constants for the AFM cantilevers were independently calculated using the Sader method[57, 58] and were found to be approximately the same as the vibrometer calibrated spring constant values from manufacturer (see previous section). The linear fit to the stress-strain slope is the Young's modulus of the nanostructure (Fig. 4.13). In addition to the calibration measurements on large diameter (~50 nm) c-Si NWs, for which we measured bulk-like elastic modulus similar to Zhu *et al*.[19], we measured the modulus of soft Nylon-11 polymer fibers. We measured two fibers of diameter approximately 615 and 713 nm with moduli of 706±92 and 614±92 MPa, respectively, within the range of values for bulk Nylon-11 (612-860 MPa)[59-61]. Error in the measured elastic modulus came from uncertainty in the slope of the stress-strain curve do to errors in the measured nanotube lengths, uncertainties in the measured cantilever deflection and uncertainties in the calculated cantilever spring constant.

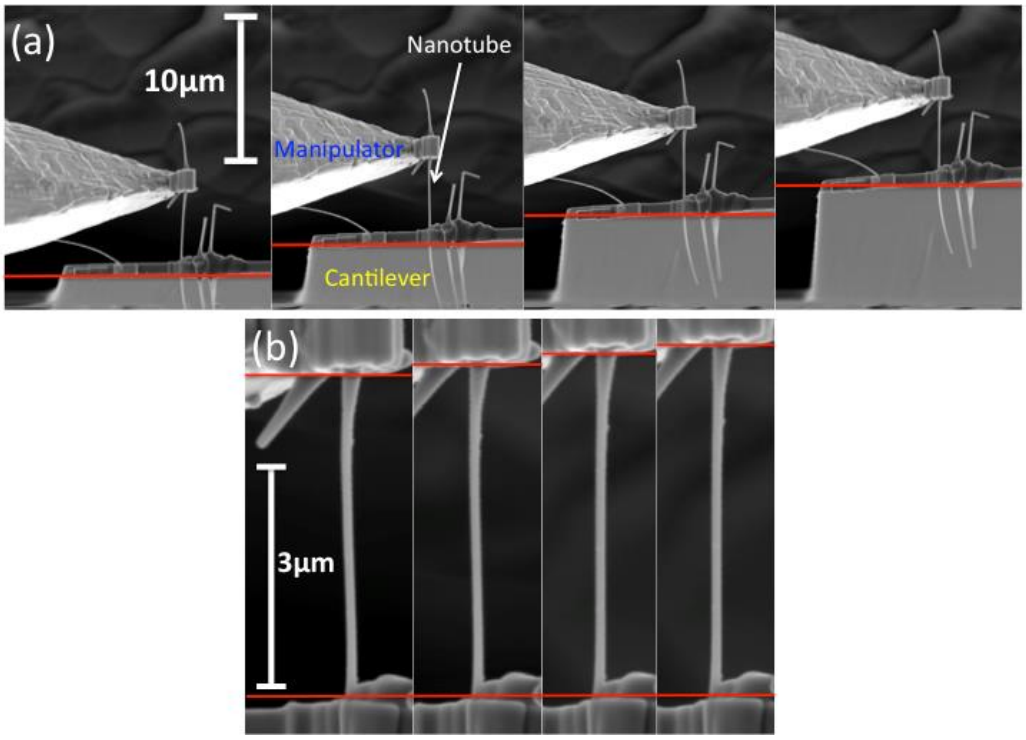


Figure 4.12: SEM of elastic tensile testing. (a) AFM cantilever deflection measurements for applied stress. The nanotube sample being tested is bonded to a tungsten probe manipulator with electron beam deposited Pt-C and is then attached to the end of an AFM cantilever. Moving the tungsten manipulator perpendicular to the cantilever direction then stretches the nanotube. (b) The nanotube strain is measured from increases in the nanotube length. At each cantilever deflection step, the length of the nanotube is measured.

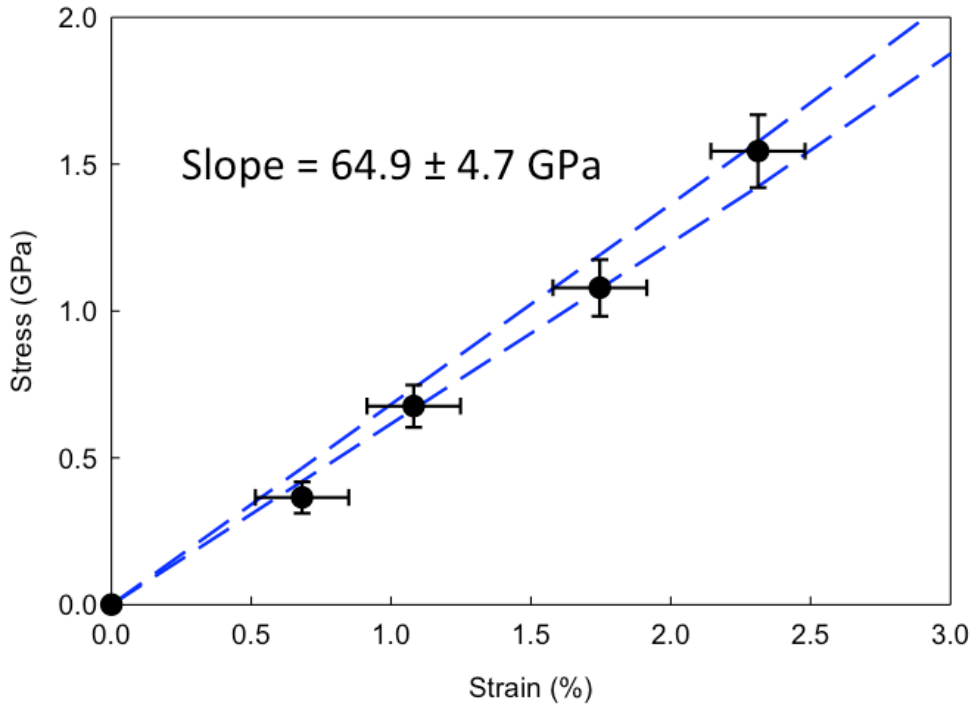


Figure 4.13: Stress-strain curve from nanotube tensile test. Applied stress to nanotubes during tensile tests is calculated from the nanotube geometry, as measured by TEM and SEM, and AFM cantilever force. The force is calculated from the cantilever deflection and spring constant. The nanotube strain is measured from increases in length during cantilever deflections. The dashed blue lines represent upper and lower bounds of the linear stress-strain slope fitting.

4.12 Conclusion

The close link between thermal and elastic properties discovered from the ultrathin c-Si NTs reveals that one can engineer the thermal properties of crystalline nanostructures beyond the phonon boundary scattering limit via the phonon softening effect, and consequently achieve thermal conductivities in crystalline structures below their amorphous analogues. This finding paves the way for new approaches to reduce thermal conductivity in nanostructures, which has been a key obstacle and the topic of voluminous research, such as in the field of thermoelectrics[9], over the past decade.

Moreover, understanding the thermal and mechanical behavior of materials with ultra-small length scale is critical for the design and performance prediction of a diverse range of technologies including flexible nanowire electronics[62], nano-electrode materials for batteries[63], and nano-electromechanical systems[64].

Since the observed elastic softening is strongly size dependence, it is most likely a surface induced phenomenon, similar to effects predicted with core-shell models. Whether the phenomenon is due to the native oxide coating, large number of surface bonding defects, or strain/defects at the native oxide/Si shell interface, understanding the dynamics of the surface or near-surface layer may elucidate some of the sources of the elastic softening. To that effect, the following chapter will cover time- and size- dependent mechanical tests on the amorphous and crystalline nanotube structures covered in this chapter. Probing the dynamics of the structures with and without interfaces and with varying surface to volume ratios will allow us to gather a new set of data to better understand the physics of the surface/interface.

Acknowledgments

This chapter is a reprint of M. C. Wingert, S. Kwon, M. Hu, D. Poulikakos, J. Xiang, R. Chen, "Sub-Amorphous Thermal Conductivity in Ultra-Thin Crystalline Silicon Nanotubes," *Nano Letters*, 15, 2605-2611 (2015).

References

1. K. T. Regner, D. P. Sellan, Z. H. Su, C. H. Amon, A. J. H. McGaughey and J. A. Malen, Nat Commun **4**, 1640 (2013).

2. M. N. Luckyanova, J. Garg, K. Esfarjani, A. Jandl, M. T. Bulsara, A. J. Schmidt, A. J. Minnich, S. Chen, M. S. Dresselhaus, Z. F. Ren, E. A. Fitzgerald and G. Chen, Science **338** (6109), 936-939 (2012).

3. J. Ravichandran, A. K. Yadav, R. Cheaito, P. B. Rossen, A. Soukiassian, S. J. Suresha, J. C. Duda, B. M. Foley, C. H. Lee, Y. Zhu, A. W. Lichtenberger, J. E. Moore, D. A. Muller, D. G. Schlom, P. E. Hopkins, A. Majumdar, R. Ramesh and M. A. Zurbuchen, Nat Mater **13** (2), 168-172 (2014).

4. J. K. Yang, Y. Yang, S. W. Waltermire, X. X. Wu, H. T. Zhang, T. Gutu, Y. F. Jiang, Y. F. Chen, A. A. Zinn, R. Prasher, T. T. Xu and D. Y. Li, Nat Nanotechnol **7** (2), 91-95 (2012).

5. N. B. Li, J. Ren, L. Wang, G. Zhang, P. Hanggi and B. W. Li, Rev Mod Phys **84** (3), 1045-1066 (2012).

6. E. Pop, S. Sinha and K. E. Goodson, P Ieee **94** (8), 1587-1601 (2006).

7. F. Xiong, A. D. Liao, D. Estrada and E. Pop, Science **332** (6029), 568-570 (2011).

8. A. Majumdar, Science **303** (5659), 777-778 (2004).

9. A. I. Hochbaum, R. K. Chen, R. D. Delgado, W. J. Liang, E. C. Garnett, M. Najarian, A. Majumdar and P. D. Yang, Nature **451** (7175), 163-167 (2008).

10. D. Y. Li, Y. Y. Wu, P. Kim, L. Shi, P. D. Yang and A. Majumdar, Appl Phys Lett **83** (14), 2934-2936 (2003).

11. B. Poudel, Q. Hao, Y. Ma, Y. C. Lan, A. Minnich, B. Yu, X. A. Yan, D. Z. Wang, A. Muto, D. Vashaee, X. Y. Chen, J. M. Liu, M. S. Dresselhaus, G. Chen and Z. F. Ren, Science **320** (5876), 634-638 (2008).

12. Y. S. Ju and K. E. Goodson, Appl Phys Lett **74** (20), 3005-3007 (1999).

13. M. C. Wingert, Z. C. Y. Chen, E. Dechaumphai, J. Moon, J. H. Kim, J. Xiang and R. K. Chen, Nano Lett **11** (12), 5507-5513 (2011).

14. E. Chávez-Ángel, J. S. Reparaz, J. Gomis-Bresco, M. R. Wagner, J. Cuffe, B. Graczykowski, A. Shchepetov, H. Jiang, M. Prunnila, J. Ahopelto, F. Alzina and C. M. Sotomayor Torres, APL Materials **2** (1), 012113 (2014).

15. D. G. Cahill, S. K. Watson and R. O. Pohl, Phys Rev B **46** (10), 6131-6140 (1992).

16. L. J. Lauhon, M. S. Gudiksen, C. L. Wang and C. M. Lieber, Nature **420** (6911), 57-61 (2002).

17. S. Kwon, Z. C. Y. Chen, H. Noh, J. H. Lee, H. Liu, J. N. Cha and J. Xiang, Nanoscale **6** (14), 7847-7852 (2014).

18. M. B. Ishai and F. Patolsky, J Am Chem Soc **131** (10), 3679-3689 (2009).

19. Y. Zhu, F. Xu, Q. Q. Qin, W. Y. Fung and W. Lu, Nano Lett **9** (11), 3934-3939 (2009).

20. T. Tsuchiya, M. Hirata, N. Chiba, R. Udo, Y. Yoshitomi, T. Ando, K. Sato, K. Takashima, Y. Higo, Y. Saotome, H. Ogawa and K. Ozaki, Journal of Microelectromechanical Systems **14** (5), 1178-1186 (2005).

21. M. C. Wingert, Z. C. Y. Chen, S. Kwon, J. Xiang and R. K. Chen, Review of Scientific Instruments **83** (2), 024901 (2012).

22. C. Chiritescu, D. G. Cahill, N. Nguyen, D. Johnson, A. Bodapati, P. Keblinski and P. Zschack, Science **315** (5810), 351-353 (2007).

23. D. G. Cahill, F. Watanabe, A. Rockett and C. B. Vining, Phys Rev B **71** (23), 235202 (2005).

24. H. Kim, I. Kim, H.-j. Choi and W. Kim, Appl Phys Lett **96** (23), 233106 (2010).

25. Z. Wang and N. Mingo, Appl Phys Lett **97** (10), 101903 (2010).

26. R. Cheaito, J. C. Duda, T. E. Beechem, K. Hattar, J. F. Ihlefeld, D. L. Medlin, M. A. Rodriguez, M. J. Campion, E. S. Piekos and P. E. Hopkins, Phys Rev Lett **109** (19), 195901 (2012).

27. J. L. Feldman, M. D. Kluge, P. B. Allen and F. Wooten, Phys Rev B **48** (17), 12589-12602 (1993).

28. J. M. Larkin and A. J. H. McGaughey, Phys Rev B **89** (14), 144303 (2014).

29. Y. P. He, D. Donadio and G. Galli, Appl Phys Lett **98** (14), 144101 (2011).

30. H. S. Yang, D. G. Cahill, X. Liu, J. L. Feldman, R. S. Crandall, B. A. Sperling and J. R. Abelson, Phys Rev B **81** (10), 104203 (2010).

31. B. S. W. Kuo, J. C. M. Li and A. W. Schmid, Appl Phys a-Mater **55** (3), 289-296 (1992).

32. S. Moon, M. Hatano, M. Lee and C. P. Grigoropoulos, International Journal of Heat and Mass Transfer **45** (12), 2439-2447 (2002).

33. P. Ferrando-Villalba, A. F. Lopeandia, L. Abad, J. Llobet, M. Molina-Ruiz, G. Garcia, M. Gerboles, F. X. Alvarez, A. R. Goni, F. J. Munoz-Pascual and J. Rodriguez-Viejo, Nanotechnology **25** (18), 185402 (2014).

34. J. Zou and A. Balandin, J Appl Phys **89** (5), 2932-2938 (2001).

35. R. Prasher, T. Tong and A. Majumdar, Nano Lett **8** (1), 99-103 (2008).

36. J. A. Pascual-Gutierrez, J. Y. Murthy and R. Viskanta, J Appl Phys **102** (3), 034315 (2007).

37. Y. Zhang, J. X. Cao, Y. Xiao and X. H. Yan, J Appl Phys **102** (10), 104303 (2007).

38. L. B. Freund and S. Suresh, *Thin film materials : stress, defect formation, and surface evolution*, 1st pbk. ed. (Cambridge University Press, Cambridge, England ; New York, 2009).

39. T. Kizuka, Y. Takatani, K. Asaka and R. Yoshizaki, Phys Rev B **72** (3), 035333 (2005).

40. A. Jurgilaitis, H. Enquist, B. P. Andreasson, A. I. H. Persson, B. M. Borg, P. Caroff, K. A. Dick, M. Harb, H. Linke, R. Nuske, L. E. Wernersson and J. Larsson, Nano Lett **14** (2), 541-546 (2014).

41. H. Sadeghian, C. K. Yang, J. F. L. Goosen, A. Bossche, U. Staufer, P. J. French and F. van Keulen, J Micromech Microeng **20** (6), 064012 (2010).

42. C. Q. Sun, B. K. Tay, X. T. Zeng, S. Li, T. P. Chen, J. Zhou, H. L. Bai and E. Y. Jiang, J Phys-Condens Mat **14** (34), 7781-7795 (2002).

43. H. W. Shim, L. G. Zhou, H. C. Huang and T. S. Cale, Appl Phys Lett **86** (15), 151912 (2005).

44. R. E. Miller and V. B. Shenoy, Nanotechnology **11** (3), 139-147 (2000).

45. M. J. Gordon, T. Baron, F. Dhalluin, P. Gentile and P. Ferret, Nano Lett **9** (2), 525-529 (2009).

46. K. Esfarjani, G. Chen and H. T. Stokes, Phys Rev B **84** (8), 085204 (2011).

47. K. Schwab, E. A. Henriksen, J. M. Worlock and M. L. Roukes, Nature **404** (6781), 974-977 (2000).

48. J. W. Lim, K. Hippalgaonkar, S. C. Andrews, A. Majumdar and P. D. Yang, Nano Lett **12** (5), 2475-2482 (2012).

49. J. K. Yang, Y. Yang, S. W. Waltermire, T. Gutu, A. A. Zinn, T. T. Xu, Y. F. Chen and D. Y. Li, Small **7** (16), 2334-2340 (2011).

50. S. Plimpton, Journal of Computational Physics **117** (1), 1-19 (1995).

51. F. H. Stillinger and T. A. Weber, Phys Rev B **31** (8), 5262-5271 (1985).

52. M. I. den Hertog, J. L. Rouviere, F. Dhalluin, P. J. Desre, P. Gentile, P. Ferret, F. Oehler and T. Baron, Nano Lett **8** (5), 1544-1550 (2008).

53. L. Shi, D. Li, C. Yu, W. Jang, D. Kim, Z. Yao, P. Kim and A. Majumdar, Journal of Heat Transfer **125** (5), 881-888 (2003).

54. Z. Zhong, M. C. Wingert, J. Strzalka, H.-H. Wang, T. Sun, J. Wang, R. Chen and Z. Jiang, Nanoscale **6** (14), 8283-8291 (2014).

55. J. L. Zheng, M. C. Wingert, E. Dechaumphai and R. K. Chen, Review of Scientific Instruments **84** (11), 114901 (2013).

56. A. Weathers, K. D. Bi, M. T. Pettes and L. Shi, Review of Scientific Instruments **84** (8), 084903 (2013).

57. J. E. Sader, J. W. M. Chon and P. Mulvaney, Rev Sci Instrum **70** (10), 3967-3969 (1999).

58. J. E. Sader, J. A. Sanelli, B. D. Adamson, J. P. Monty, X. Z. Wei, S. A. Crawford, J. R. Friend, I. Marusic, P. Mulvaney and E. J. Bieske, Rev Sci Instrum **83** (10), 103705 (2012).

59. Y. C. Hu, L. Shen, H. Yang, M. Wang, T. X. Liu, T. Liang and J. Zhang, Polym Test **25** (4), 492-497 (2006).

60. E. Petrovicova, R. Knight, L. S. Schadler and T. E. Twardowski, J Appl Polym Sci **78** (13), 2272-2289 (2000).

61. H. Chung and S. Das, Mat Sci Eng a-Struct **437** (2), 226-234 (2006).

62. K. Takei, T. Takahashi, J. C. Ho, H. Ko, A. G. Gillies, P. W. Leu, R. S. Fearing and A. Javey, Nat Mater **9** (10), 821-826 (2010).

63. H. Wu, G. Chan, J. W. Choi, I. Ryu, Y. Yao, M. T. McDowell, S. W. Lee, A. Jackson, Y. Yang, L. B. Hu and Y. Cui, Nat Nanotechnol **7** (5), 309-314 (2012).

64. M. Li, H. X. Tang and M. L. Roukes, Nat Nanotechnol **2** (2), 114-120 (2007).

Chapter 5: Fluid-like surface layer and its dynamics in glassy nanotubes

5.1 Introduction

Nanoscale glassy films are ubiquitous and critical components for a variety of electronic and energy devices such as optical coatings[1-3], amorphous oxide transistors[4, 5] and gate dielectrics[6-8], non-volatile solid state memory[9, 10], memristors[11-13], solid-electrolyte interphase layers[14] and anodes[15, 16] in batteries, and amorphous Si solar cells[17, 18]. The mechanical properties of such amorphous materials is practically important in system design and issues can arise when shrinking them down to nanoscale dimensions. For instance, in glassy polymers extensive studies have shown the presence of a highly mobile surface layer on the order of tens of nanometers thick.[19-26] In the case of glassy (or amorphous) inorganic materials, whether or not a similar surface layer exists, however, is largely unexplored. A prior study has indicated such a possibility through imaging the motion of surface atoms in ultrathin SiO_2 films[27, 28], but its effect on the dynamic mechanical properties is not known. On the other hand, it is well known that inorganic nanostructures, in both amorphous and crystalline forms, can exhibit unusual mechanical phenomena, such as electron beam induced deformation[29-31], brittle-plastic transition[32-34], and strong anelasticity (atomic diffusion)[35]. It is, therefore, expected that if a mobile surface layer does exist, the mechanical behavior of nanostructured glass could be different from its bulk form. One of the challenges of directly probing the dynamic mechanical response of this

surface layer lies in creating and measuring ultra-thin samples, as the mobile surface layer, if it exists, would be on the scale of several nanometers, much smaller than that in polymers.

Herein, we systematically studied the dynamic mechanical behavior of novel amorphous SiO_2 (a-SiO_2) and Si (a-Si) nanotube (NT) structures with exceedingly thin shells down to 7 nm (Figure 5.1), unambiguously showing the presence of highly mobile surface layers in inorganic glasses. The thin shells and high aspect-ratio of the tubular structure, having increased surface atom fraction, allow us to apply large stresses (10^9 Pa) and examine the mechanical behavior. Exponentially increasing creep deformation at room temperature is observed as the NT shell thickness is reduced, with strain increases up to 60% greater than the initial strain (< 5.5%) for the thinnest tubes. We also observed that creep deformation occurs only in the amorphous samples we studied (a-SiO_2 and a-Si NTs) and not in crystalline Si (c-Si) NTs of similar geometry. Furthermore, we performed temperature dependent creep tests and found a low diffusion-like activation energy associated with the creep.

5.2 Nanotube fabrication and characterization

The ultrathin NTs in this study were fabricated by etching the Ge cores in Ge-Si core-shell nanowires (NWs)[36] as we previously reported, where crystalline and amorphous NTs were fabricated by controlling the temperature during epitaxial deposition of the Si shells on the Ge cores.[37] Amorphous SiO_2 NTs were synthesized by oxidizing c-Si NTs in air at 950 °C for 3 hours and are completely oxidized with no internal interfaces while the a-Si and c-Si NTs have 1-2 nm thick inner and outer

native oxide coatings encompassing the Si shells. NT shell thicknesses ranged from ~7.5, 12, and 20 nm for a-SiO_2, ~9, 12, 20, and 150 nm for a-Si, and ~10 nm for c-Si, ±2 nm each, with deviations of < 1 nm along the NT length. The outer diameters (ODs) of the NTs range from ~70-150 nm. Each NT was characterized by high-resolution (HR) TEM (representative images in Figure 5.1a, b, and c, with larger NTs shown in Fig. 5.2) prior to tensile testing in order to confirm the crystallinity of the sample and to precisely measure its dimensions (OD, shell thickness, and native oxide thickness for the a-Si and c-Si NTs).

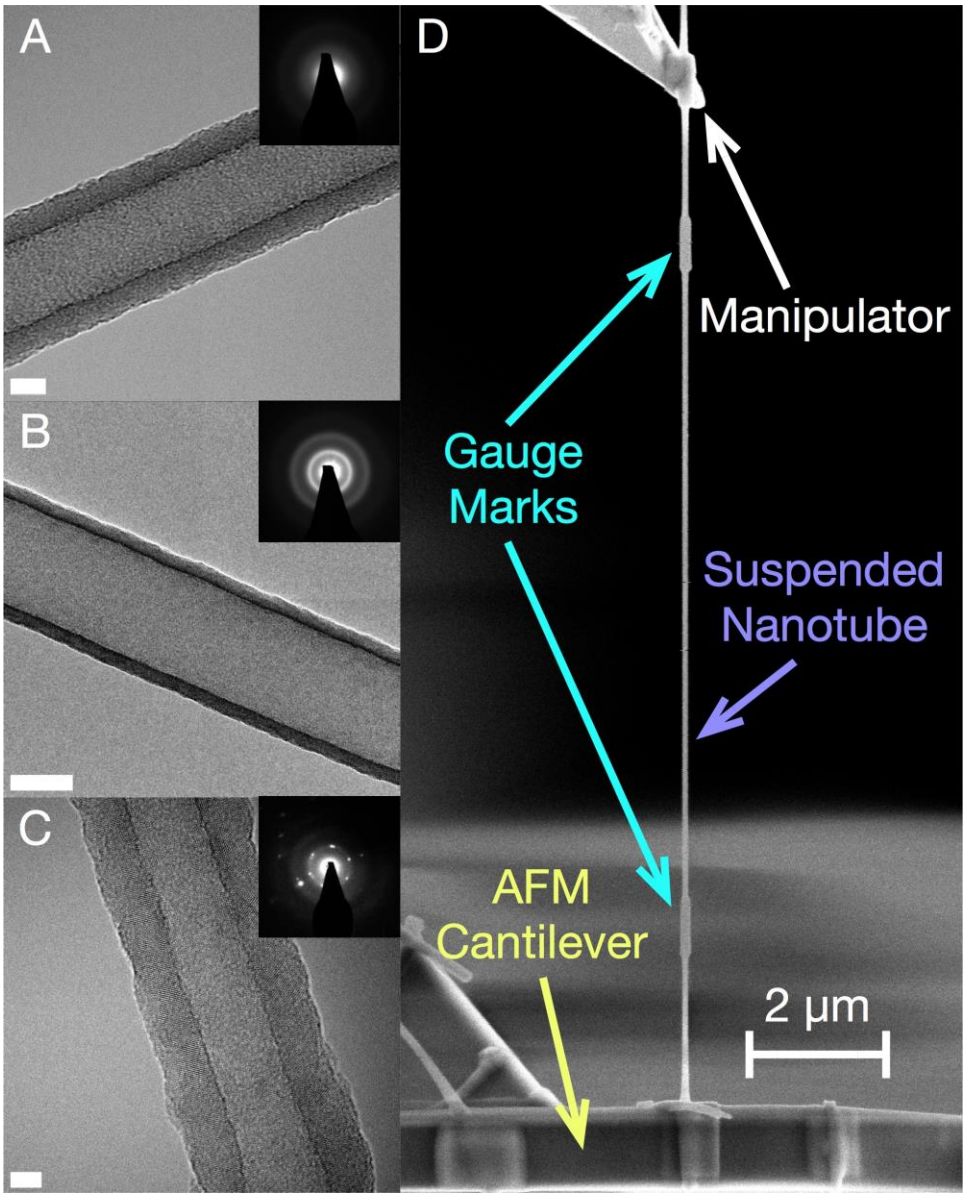


Figure 5.1: TEM images of individual ultrathin (a) amorphous SiO2, (b) amorphous Si, and (c) crystalline Si nanotube (NT) samples and (d) SEM of tensile creep experimental setup. Scale bars are (a) 10 nm, (b) 50 nm, and (c) 5 nm.

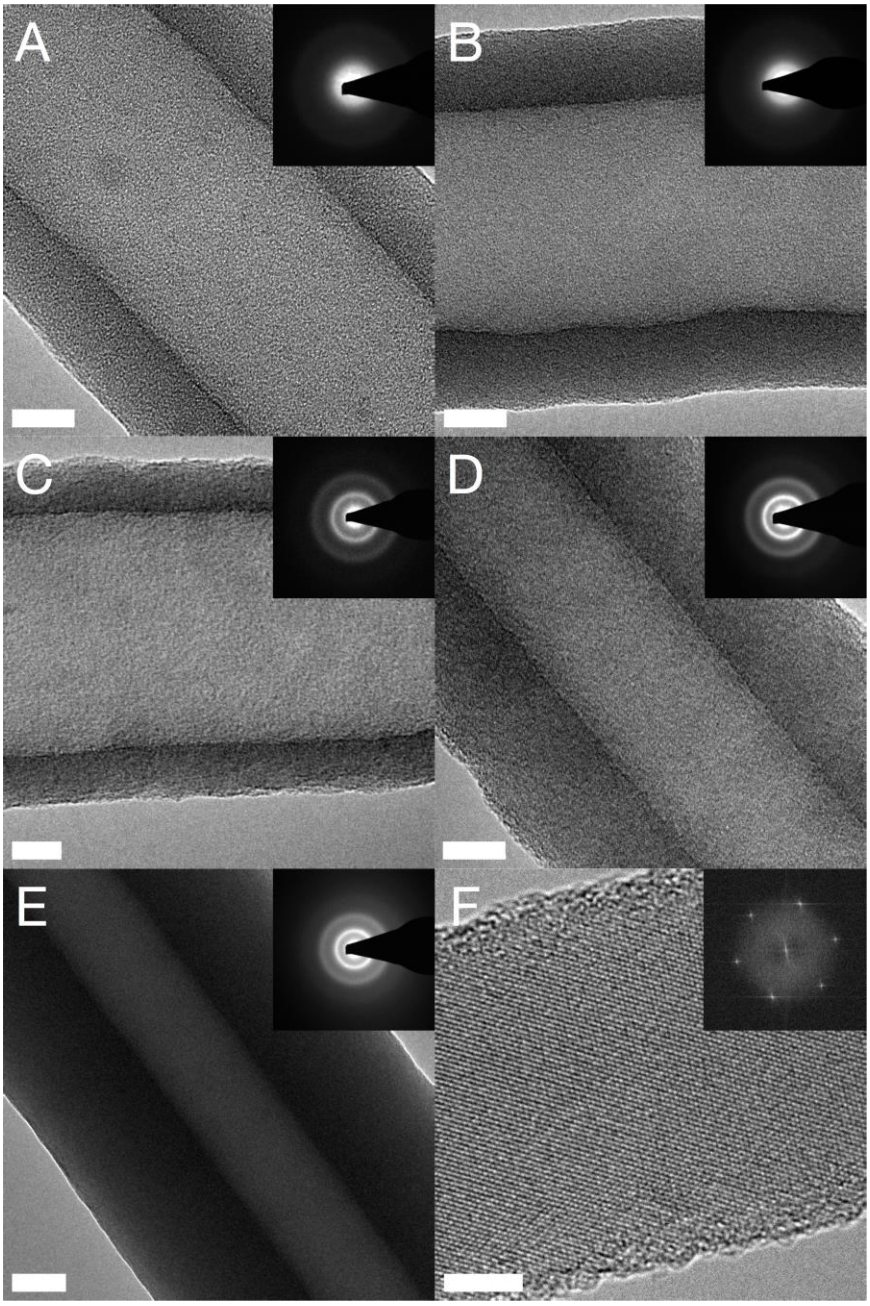


Figure 5.2: TEM images of (a) 14 and (b) 25 nm thick a-SiO2 and (c) 12, (d) 20, and (e) 150 nm thick a-Si NTs, and (f) representative c-Si NW. Scale bars are (a) 10, (b) 20, (c) 10, (d) 10, (e) 50, and (f) 5 nm.

5.3 Tensile setup and measurement

After TEM characterization, the *same* exact NTs were then transferred to a dual (electron and ion) beam chamber where a micromanipulator probe was used to pick up and attach each NT to the free end of an AFM cantilever. Tensile measurements were then performed according to an established procedure[37, 38] using the setup shown in Figure 5.1d. During the initial loading stress-strain measurements were performed to calculate instantaneous tensile moduli (Figure 5.3), which were consistent with those of SiO_2,[39-41] a-Si,[42] and c-Si nanostructures,[43] including our previously measured NTs[37]. Each of these initial measurements only took 2-3 minutes and were performed in the linear-elastic regime, with strains and stresses up to 1.5-5.5% and 0.8-5 GPa, respectively (Table 5.1). Such large stresses can only be sustained when the nanostructure has a low volumetric concentration of defects to avoid fracturing, as shown by the high fracture strength of our NTs (Figure 5.4). Transient creep was then monitored with the NT at the maximum loaded stress by measuring changes in length every 5 to 10 minutes over a period of up to two hours, blanking the electron beam between measurements. Several samples had gauge marks deposited *via* e-beam induced Pt (seen in Figure 5.1d) and strain was measured using both the gauge marks and the entire NT length to ensure no slippage occurred. Temperature dependent creep tests were also performed *in-situ* in the same chamber, where a heater implanted in the sample stage was used to control the temperature above 300 K and the sample temperature was measured with a thermometer.

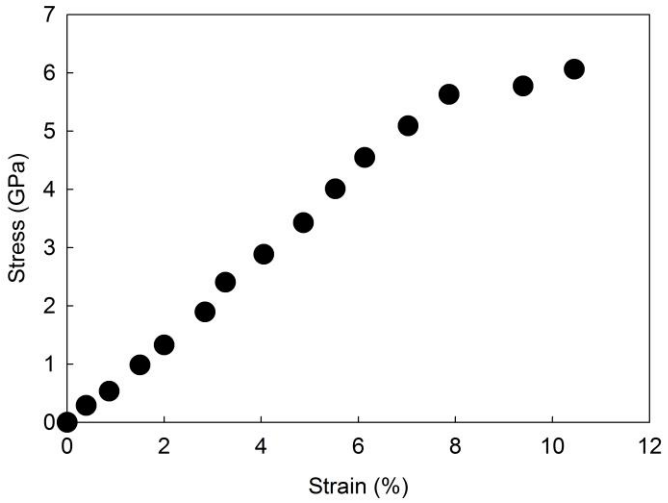


Figure 5.3: Nanotube stress-strain measurement exhibiting linear elastic regime up to 8% strain.

Table 5.1: Nanotube information for samples used in creep tests.

Material	Nominal Thickness (nm)	Sample #	Shell Thickness (nm)	Native Oxide Thickness (nm)	Outer Diameter (nm)	Initial Length (μm)	Initial Strain (%)
a-SiO_2	7.5	SiO_2-7-1	7.5	N/A	108	2.69	2.68
a-SiO_2	7.5	SiO_2-7-2	7.5	N/A	104	10.00	3.50
a-SiO_2	7.5	SiO_2-7-3	7.5	N/A	134	11.90	3.03
a-SiO_2	7.5	SiO_2-7-4	7.5	N/A	126	7.45	2.75
a-SiO_2	14	SiO_2-14-1	14	N/A	134	8.04	2.14
a-SiO_2	14	SiO_2-14-2	14	N/A	136	11.94	2.60
a-SiO_2	14	SiO_2-14-3	14	N/A	129	7.42	3.74
a-SiO_2	20	SiO_2-20-1	23	N/A	131	9.41	3.27
a-SiO_2	20	SiO_2-20-2	25	N/A	148	11.78	2.89
a-Si	9	aSi-9-1	9.4	1.5	72	12.1	3.87
a-Si	9	aSi-9-2	10.3	1.5	77	13.35	3.52
a-Si	9	aSi-9-3	9.8	1.5	82	10.38	3.59
a-Si	9	aSi-9-4	9.8	1.5	79	8.52	4.14
a-Si	9	aSi-9-5	9.1	1.5	84	5.67	2.68
a-Si	12	aSi-12-1	11.7	1.5	100	13.3	3.16
a-Si	12	aSi-12-2	13	1.5	75	21.5	5.49
a-Si	12	aSi-12-3	11.5	1.5	71	10.46	2.87
a-Si	20	aSi-20-1	20.1	1.5	114	19.7	1.73
a-Si	20	aSi-20-2	21.4	1.5	93	11.9	3.78
a-Si	20	aSi-20-3	19.6	1.5	74	23.8	2.10
a-Si	150	aSi-150-1	145	1.5	316	17.4	1.58
c-Si	10	cSi-10-1	9.2	1.5	80	14.61	3.97
c-Si	10	cSi-10-2	11.0	1.5	75	6.05	3.27
c-Si	10	cSi-10-3	11.6	1.5	109	4.24	7.59

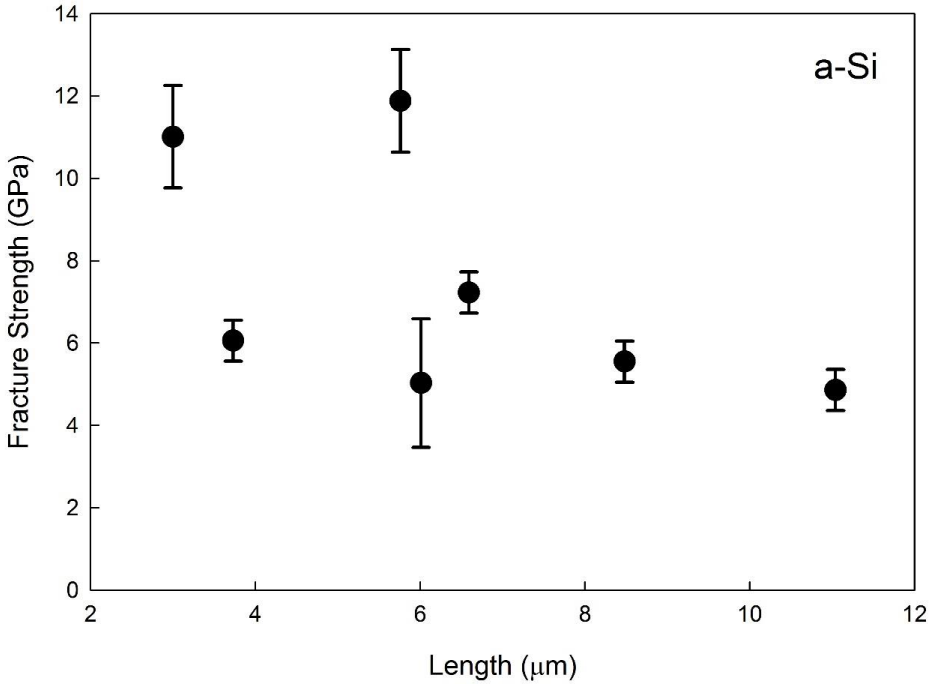


Figure 5.4: Measured fracture strength of a-Si NTs versus suspended NT length.

5.4 Creep measurement

The creep strain measured in the a-SiO_2 NTs is shown in Figure 5.5a, where the strain increase due to creep, $\Delta\varepsilon$, is normalized by the initial strain, ε_o. The majority of the creep occurred within the first 20-30 minutes and saturated thereafter. The creep is clearly related to the a-SiO_2 NT shell thickness (δ), where $\Delta\varepsilon/\varepsilon_o$ only reaches 10% for NTs with δ>10 nm but is as high as 60% when δ<10 nm. The a-Si NTs exhibit a similar amount of creep in terms of overall strain increase and size-dependence, shown in Figure 5.5b. This similarity between the ultrathin a-SiO_2 and a-Si NTs indicates that a-Si indeed exhibits glass-like behavior, as has been previously suggested.[44, 45] The creep saturation in the a-Si NTs, however, took longer than in the a-SiO_2 NTs.

Negligible creep was observed in a 145 nm thick a-Si NT, as expected for bulk-like behavior. Interestingly, no creep was observed in ~10 nm thick crystalline Si NTs (Figure 5.5c), just like in our control experiment on a 50 nm diameter c-Si NW. After one of the creep tests on a 7.5 nm SiO_2 NT (loaded state), the stress was removed from the sample (un-loaded state) and most of the creep strain recovered over the next 30 minutes (Figure 5.5d), indicating that the creep deformation in this study is viscoelastic, as opposed to previously observed[34] enhanced plastic deformation which occurred above a threshold yield-stress and with larger strain (typically ~10%).

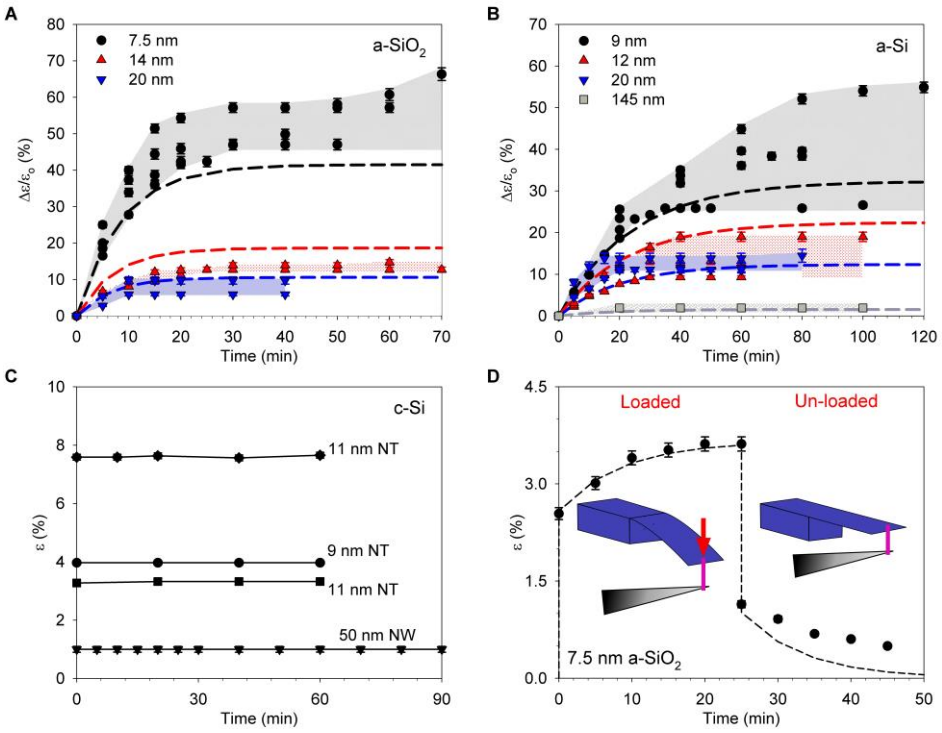


Figure 5.5: Creep strain measured for (a) amorphous SiO2 (a-SiO2), (b) amorphous Si, and (c) crystalline Si nanotubes (NTs), and (d) viscoelastic behavior of a 7.5 nm shell a-SiO2 NT. Colored bands in (a) and (b) represent the range of the experimental data for similar shell thickness NTs. The insets of (d) show schematics of the loading and unloading of the NT with the AFM cantilever. The dashed lines in (a), (b), and (d) represent fittings based on the core-shell model shown in Figure 5.6a.

The size-dependent creep observed in Figure 5.5a, b, and d is presumably due to the growing influence of a fluid-like surface layer on the amorphous nanostructures, similar to that of the thin mobile surface layers in amorphous polymer films. As such, we used a core-shell model, similar to a Maxwell-solid spring-dashpot system (Figure 5.6a), to understand the observed behavior, where the NT shell is comprised of mobile surfaces surrounding a stiff center layer. Here, the time dependent mechanical response of the NT under the influence of a tensile force, $F(t)$, is

$$F(t) = E_1 \varepsilon(t) A_{core} + E_2 \varepsilon'(t) A_{surf} \tag{5.1}$$

where the stiff middle layer has a modulus, E_1, cross-sectional area, A_{core}, and experiences a strain, $\varepsilon(t)$, while the fluid-like surface layers have elastic moduli, E_2, total cross-sectional area, A_{surf}, and experience a strain, $\varepsilon'(t)$. The average stress over the entire cross-section of the NT, with a total shell thickness of δ, and inner/outer surface layers, each of thickness c, is

$$\bar{\sigma}(t) = E_1 \varepsilon(t)\left(1 - \frac{2c}{\delta}\right) + E_2 \varepsilon'(t)\left(\frac{2c}{\delta}\right) \tag{5.2}$$

and the elastic and viscous contributions in the inner/outer surface layers are related by

$$E_2 \varepsilon'(t) = \eta \dot{\varepsilon}''(t) \tag{5.3}$$

where η is the viscosity of the surface layer and $\varepsilon''(t)$ is the viscous strain. Using Eqs. 5.2 and 5.3 and the condition of constant average stress, the time-dependent creep strain in the NT, normalized by the initial strain, can be found to be

$$\frac{\varepsilon(t)}{\varepsilon_o}=1+\frac{E_2\left(\frac{2c}{\delta}\right)}{E_1\left(1-\frac{2c}{\delta}\right)}-\left[\frac{E_2\left(\frac{2c}{\delta}\right)}{E_1\left(1-\frac{2c}{\delta}\right)}\right]\cdot\exp\left[-\frac{E_1\left(1-\frac{2c}{\delta}\right)}{E_1\left(1-\frac{2c}{\delta}\right)+E_2\left(\frac{2c}{\delta}\right)}\left(\frac{t}{\tau}\right)\right] \quad (5.4)$$

where the time constant is defined as $\tau=\eta/E_2$ and the normalized maximum creep strain is

$$\frac{\Delta\varepsilon_{\max}}{\varepsilon_o}=\frac{E_2}{E_1}\left(\frac{2c}{\delta-2c}\right). \quad (5.5)$$

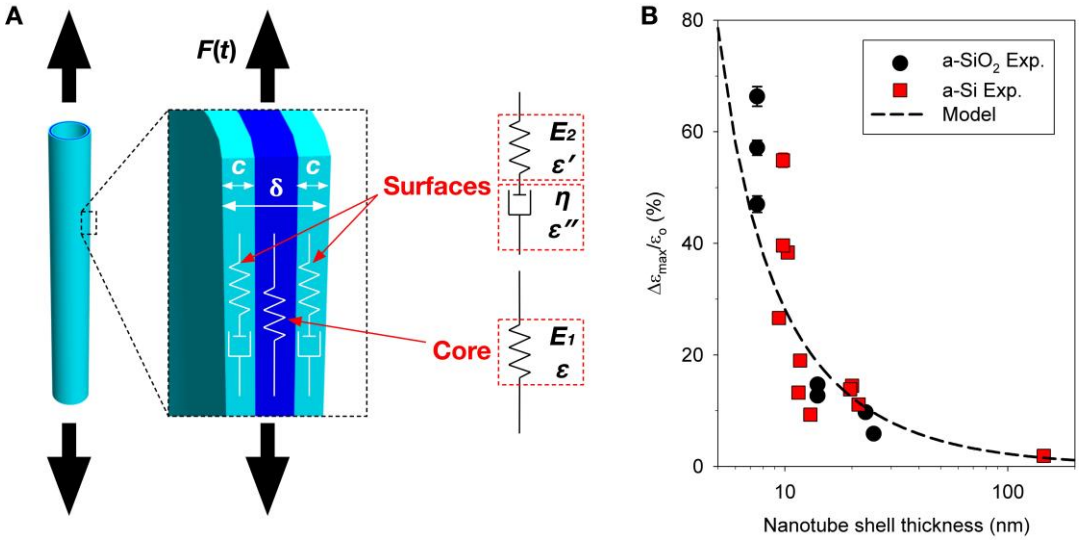


Figure 5.6: (a) Core-shell model describing the dynamic and size-dependent behavior of the amorphous nanotubes and (b) the experimental (circles and squares) and modeled (dashed line) size-dependent normalized saturated creep.

We assumed that $E_1 \approx E_2$ based on the lack of a clear size-dependent instantaneous modulus (Figure 5.7) in the amorphous NTs and found that a surface layer thicknesses, c, of 1.1 nm best fit the experimental data for both amorphous NT materials, which is reasonable considering that the mobile surface layers should be on the order of nanometers. The creep calculated from Eq. 5.4, and represented by the dashed lines in Figure 5.5a and b, matches the measured time-dependence trends of the creep fairly well. The initial creep shown in Figure 5.5d also fits well to Eq. 5.4, where the initial starting strain was calculated as the ratio of the initial stress and elastic modulus, $\varepsilon_o = \sigma_o / E_1$. The creep recovery after stress removal is simply

$$\varepsilon_{\text{recovery}}(t) = \Delta\varepsilon_{\max} \cdot \exp\left[-\frac{E_1\left(1-\frac{2c}{\delta}\right)}{E_1\left(1-\frac{2c}{\delta}\right)+E_2\left(\frac{2c}{\delta}\right)}\left(\frac{t-t_c}{\tau}\right) \right] \tag{5.6}$$

where $\Delta\varepsilon_{max}$ is defined from Eq. 5.5 and t_c is the time at which the stress was removed. Here, the time constant that best fit the a-SiO_2 and a-Si NTs was 6 and 18 minutes, respectively. The corresponding viscosity of the soft outer/inner layers can be estimated from $\eta = \tau \cdot E_2$ and was ≈10-20 TPa·s for the a-SiO_2 NTs, equivalent to the viscosity of glass measured[46, 47] between 1250-1500 K, and ≈ 60-90 TPa·s for the a-Si NTs.

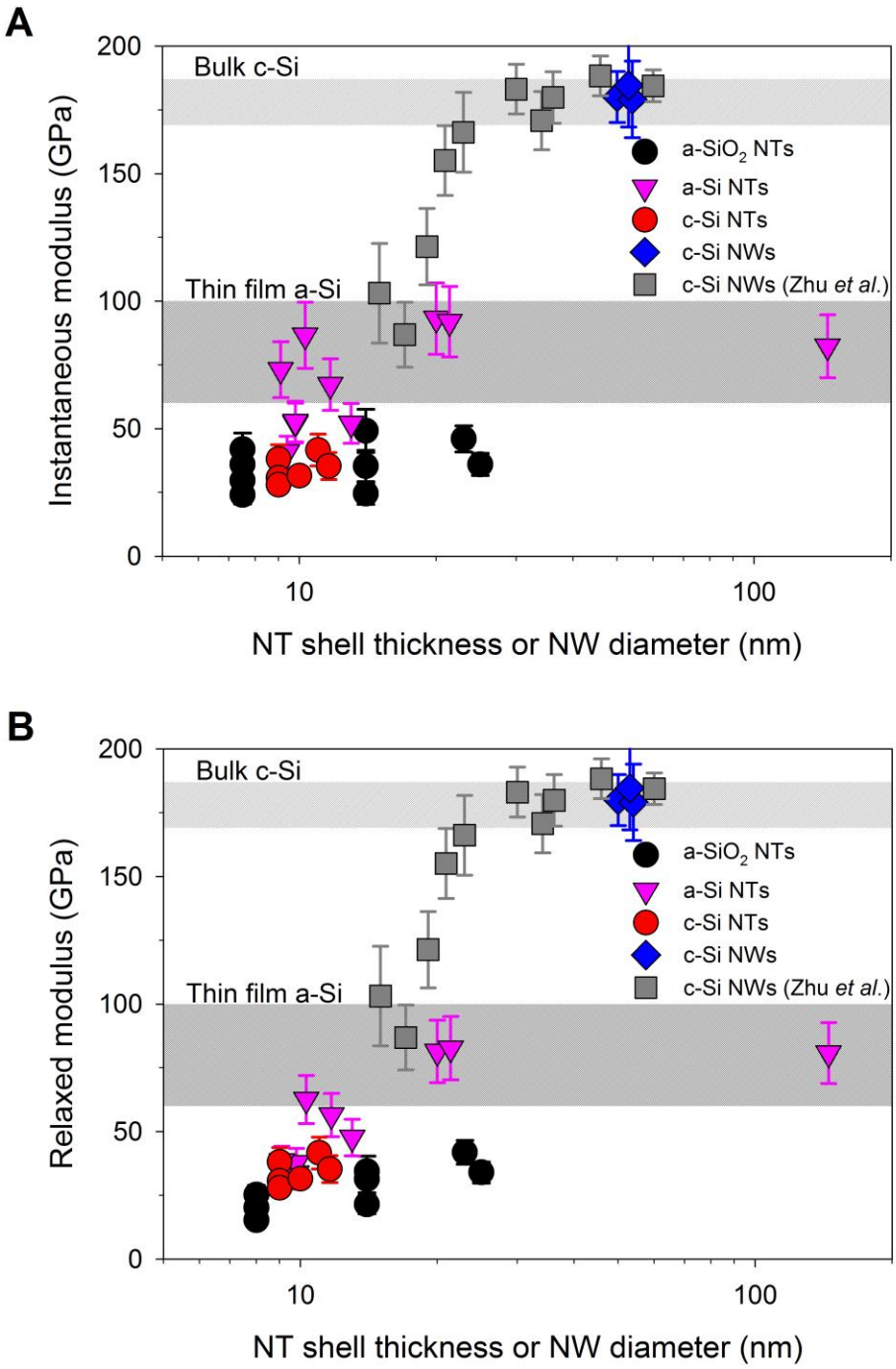


Figure 5.7: Size-dependent (a) instantaneous and (b) relaxed moduli of a-SiO2, a-Si, c-Si NTs, and c-Si NWs measured by us and also by Zhu et al.38.

The size-dependence of the creep deformation is more clearly evident in Figure 5.6b, where $\Delta\varepsilon_{max}/\varepsilon_o$ is plotted against NT shell thickness. The a-SiO_2 and a-Si NTs follow strikingly similar size-dependent trajectories, with the maximum creep exponentially increasing as the NT shell thickness decreases. The observed creep trends only with the NT thickness and is independent of testing parameters such as the initial strain and stress (Figure 5.8). The dashed lines represent the modeled saturation creep strain based on Eq. 5.5 using the same constants previously mentioned and shows good agreement with the experimental data. Interestingly, if we calculate the *relaxed* tensile modulus using the saturated total strain (Figure 5.7), we find that it decreases as δ falls below 30 nm for a-Si, similar to the size-dependent moduli of c-Si NTs[37] and NWs[38].

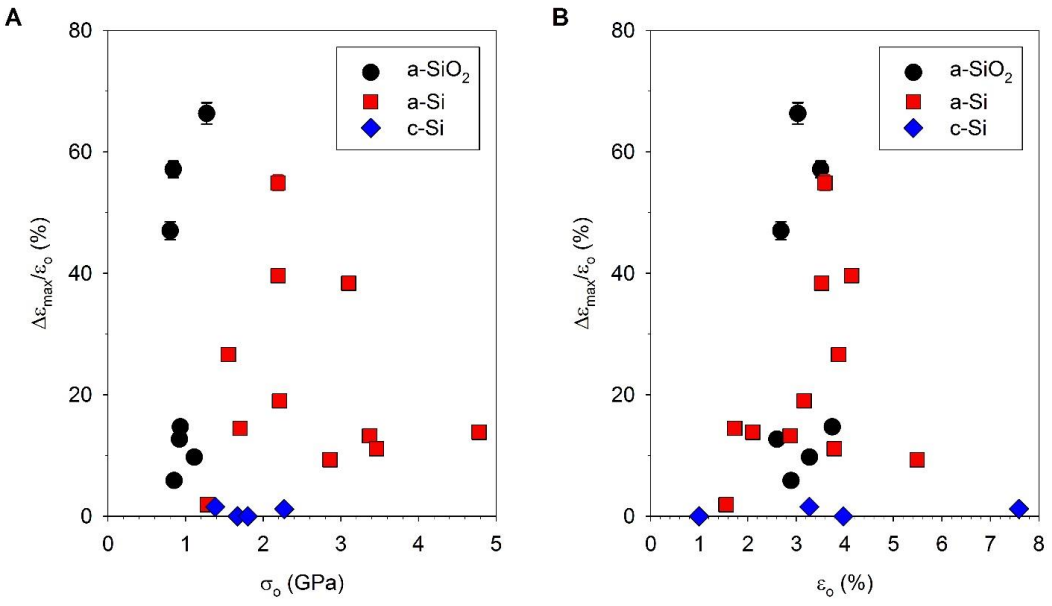


Figure 5.8: Dependence of normalized maximum creep strain increase versus (a) initial applied stress and (b) initial applied strain.

Differences in the saturation time between the a-SiO_2 and a-Si NTs, however, may stem from a difference in atomic species mobility in either material. It is also possible that the a-SiO_2/a-Si interface, present in the a-Si NTs and a source of atomic defects and roughness[37], may frustrate overall atomic mobility, increasing the time required for the atoms to reorganize. Furthermore, the lack of any creep in the c-Si NTs, even with similar geometry as the a-Si NTs and with native surface oxides, also highlights the importance of the exact nature of this interface. This could be caused by the presence of a higher density layer at the c-Si-SiO_2 interface (~1 nm thick)[48], or atoms in the native surface oxide, near to the interface with the ordered crystalline surface, could be more ordered, confining and inhibiting their movement.[49] However, understanding the exact role of the interfaces among the a-SiO2, a-Si and c-Si NTs warrants further investigation.

5.5 Creep activation energy

To understand the mechanism behind the surface-based creep, we performed temperature dependent creep tests on 20 nm thick SiO_2 NTs (Figure 5.9a), and found that the amount of creep significantly increased with temperature, however τ remained constant. The resulting creep viscosity was found to fit well to an Arrhenius temperature dependence[50] (Figure 5.9b),

$$\eta = E_2\tau \propto \exp\left(\frac{E_A}{k_B T}\right) \tag{5.7}$$

where k_B is the Boltzmann constant and T is absolute temperature. The activation energy of the deformation processes, E_A, was found to be 0.1 eV, of similar order as

low values for diffusion and defect relaxation (~0.2 eV) in a-Si[51-53] and a-SiO_2[54]. Furthermore, activation energies could be lower for the fluid-like surface, similar to values simulated for SiO_2 surfaces[55, 56]. These energies are consistent with analysis[57] showing deformation at room temperature requires activation energies less than 0.3 eV and indicate that bond motion, not bond breaking[58], is the source of the measured creep.

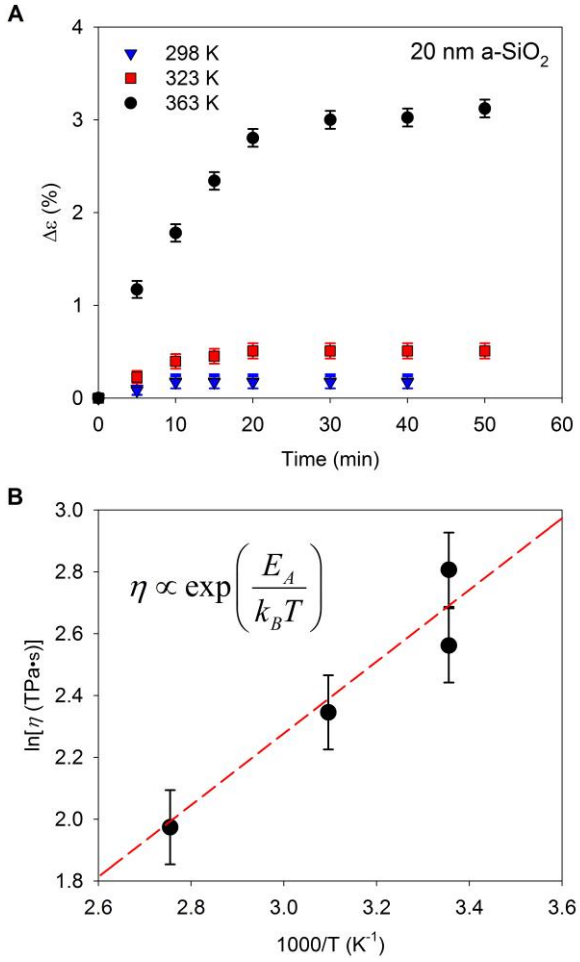


Figure 5.9: (a) Creep strain observed for 20 nm shell amorphous SiO2 nanotubes at various temperatures. (b) Creep viscosity versus temperature, fitted to an Arrhenius temperature dependence (red dashed line).

Based on our low observed activation energy the creep deformation in the amorphous NTs is most likely due to multiple defected bond relaxation events which result in the migration of atomic clusters[59, 60]. Such reorganizations will alter coordinated bonding groups, rings of Si-O molecules in a-SiO_2 or Si-Si in a-Si, such as transforming five- and six- fold coordinated group rings into three-, four-, and eight- member coordinated groups[61] and migration of non-bridging atoms leading changes in bond angles[59]. This atomic re-ordering is particularly concentrated at surfaces, where natural defects such as dangling bonds allow atomic processes to circumvent the higher energy barriers present among the bulk atoms, leading to the high mobility of the surface layers. Since our NTs are made up of a significant fraction of surface atoms, they will increasingly govern the mechanical response of the entire nanostructure, as observed in in our experiments.

Deformation in prior studies on SiO_2 and Si nanostructures was investigated using constant strain rates[33, 34] or high energy electron beams[29-31] which break atomic bonds and dislocate atoms. One such recent study[34] found that sub-20 nm diameter a-SiO_2 nanofibers show ductile behavior and enhanced plastic elongation above a threshold yield-stress. Our results, however, were performed in the elastic range, and while we show similar strong size-dependent deformation, it occurs significantly below the yield-stress and is viscoelastic, recovering the majority of the creep upon removal of the tensile load. Also in this study, the 5 kV electron beam will only transfer <0.4-0.7 eV to atoms our nanostructures[62], which is much lower than the energy required to break Si-O or Si-Si bonds (~2-5 eV)[63], but could have some influence on our measurement due to our measured E_A=0.1 eV. TEM irradiation in

previous studies is much stronger, 100-300 kV beams can transfer ~9-33 eV,[62] strong enough to continuously create defects. We took further precaution by blanking the beam between measurements. Heating of the nanostructure should be negligible under a periodically scanning 5 kV beam. Stresses on the order of 10^9 Pa, as applied in our experiments, are also large enough to initiate defect bond rearrangements, providing >0.4 eV compared to our 0.1 eV.

5.6 Electron beam exposure

In order to reduce the effect of exposure to the electron beam, the beam was blanked in between length measurements and a relatively low beam energy of only 5 kV was used during imaging, however, measurements were also performed without blanking the beam, but showed similar results. This is likely because the low incident beam energy is not sufficient to initiate or enhance bond breaking, unlike several hundred kV used in the experiments conducted in a TEM in prior studies.[29, 30]. Temperature rises in the suspended NTs should be negligible, or very close to room temperature, with rises less than a few Kelvin at worst.[29, 31] One 50 nm diameter c-Si NW was used to calibrate the measurement and exhibited bulk-like elasticity (~180 GPa), consistent with prior measurements on large-diameter Si NWs,[38] with no observable creep over a measurement period of two hours. Similarly, we did not observe creep in c-Si NTs with dimensions similar to those of the a-Si and a-SiO_2 NTs. All of these control experiments suggest that the observed size-dependent creep in the a-Si and a-SiO_2 NTs is indeed an intrinsic property of the NTs and not due to the electron beam exposure or other experimental artifacts.

5.7 Conclusion

We observed strongly size-dependent creep deformation in ultrathin amorphous nanostructures, which was viscoelastic and not solely plastic in nature, nor limited by a threshold yield-stress. This same time- and size- dependent behavior did not occur in crystalline structures with similar geometry and native surface oxide. Furthermore, a core-shell model shows that a ~1 nm thick fluid-like surface layer has a significant effect on mechanical behavior and matches well with our experimental results. Additionally, a low activation energy extracted from temperature dependent creep measurements indicates that the deformation is due to bond motion, not bond breaking. These findings show that the mobility of surfaces must be accounted for in nanoscale amorphous systems. Such behavior could have major implications for the design and functionalities of future electronic and energy devices.

Acknowledgments

This chapter is a reprint of material which has been submitted for publication by Matthew C. Wingert, Soonshin Kwon, Shengqiang Cai, and Renkun Chen. The dissertation author was the primary investigator and author of this material.

References

1. Y. Du, L. E. Luna, W. S. Tan, M. F. Rubner and R. E. Cohen, ACS Nano **4** (7), 4308-4316 (2010).

2. M. A. Kats, R. Blanchard, P. Genevet and F. Capasso, Nat Mater **12** (1), 20-24 (2013).

3. L. C. Klein, *Sol-gel optics: processing and applications*. (Springer Science & Business Media, 2013).

4. K. Nomura, H. Ohta, A. Takagi, T. Kamiya, M. Hirano and H. Hosono, Nature **432** (7016), 488-492 (2004).

5. T. Kamiya, K. Nomura and H. Hosono, Science and Technology of Advanced Materials **11** (4), 044305 (2010).

6. B. N. Pal, B. M. Dhar, K. C. See and H. E. Katz, Nat Mater **8** (11), 898-903 (2009).

7. J. Liu, D. B. Buchholz, J. W. Hennek, R. P. H. Chang, A. Facchetti and T. J. Marks, Journal of the American Chemical Society **132** (34), 11934-11942 (2010).

8. H. Wong and H. Iwai, Microelectronic Engineering **83** (10), 1867-1904 (2006).

9. S. Raoux, F. Xiong, M. Wuttig and E. Pop, MRS Bulletin **39** (08), 703-710 (2014).

10. F. Yoshihisa, Japanese Journal of Applied Physics **52** (4R), 040001 (2013).

11. F. Miao, J. P. Strachan, J. J. Yang, M.-X. Zhang, I. Goldfarb, A. C. Torrezan, P. Eschbach, R. D. Kelley, G. Medeiros-Ribeiro and R. S. Williams, Advanced Materials **23** (47), 5633-5640 (2011).

12. D. Liu, H. Cheng, X. Zhu, G. Wang and N. Wang, ACS Applied Materials & Interfaces **5** (21), 11258-11264 (2013).

13. Z. Q. Wang, H. Y. Xu, X. H. Li, H. Yu, Y. C. Liu and X. J. Zhu, Advanced Functional Materials **22** (13), 2759-2765 (2012).

14. D. Zhou, R. Liu, Y.-B. He, F. Li, M. Liu, B. Li, Q.-H. Yang, Q. Cai and F. Kang, Advanced Energy Materials, n/a-n/a (2016).

15. H. Wu, G. Chan, J. W. Choi, I. Ryu, Y. Yao, M. T. McDowell, S. W. Lee, A. Jackson, Y. Yang, L. Hu and Y. Cui, Nat Nano **7** (5), 310-315 (2012).

16. Y. Yao, M. T. McDowell, I. Ryu, H. Wu, N. Liu, L. Hu, W. D. Nix and Y. Cui, Nano Lett **11** (7), 2949-2954 (2011).

17. M. Kondo, T. Matsui, Y. Nasuno, H. Sonobe and S. Shimizu, Thin Solid Films **501** (1–2), 243-246 (2006).

18. A. Shah, P. Torres, R. Tscharner, N. Wyrsch and H. Keppner, Science **285** (5428), 692-698 (1999).

19. Z. Fakhraai and J. A. Forrest, Science **319** (5863), 600-604 (2008).

20. Y. Chai, T. Salez, J. D. McGraw, M. Benzaquen, K. Dalnoki-Veress, E. Raphaël and J. A. Forrest, Science **343** (6174), 994-999 (2014).

21. Y. Gueguen, J. C. Sangleboeuf, V. Keryvin, E. Lepine, Z. O. Yang, T. Rouxel, C. Point, B. Bureau, X. H. Zhang and P. Lucas, Phys Rev B **82** (13) (2010).

22. H. Yin, S. Madkour and A. Schönhals, Macromolecules **48** (14), 4936-4941 (2015).

23. C. J. Ellison and J. M. Torkelson, Nat Mater **2** (10), 695-700 (2003).

24. L. Zhu, C. W. Brian, S. F. Swallen, P. T. Straus, M. D. Ediger and L. Yu, Physical Review Letters **106** (25), 256103 (2011).

25. C. W. Brian and L. Yu, The Journal of Physical Chemistry A **117** (50), 13303-13309 (2013).

26. J. A. Forrest and K. Dalnoki-Veress, ACS Macro Letters **3** (4), 310-314 (2014).

27. P. Y. Huang, S. Kurasch, J. S. Alden, A. Shekhawat, A. A. Alemi, P. L. McEuen, J. P. Sethna, U. Kaiser and D. A. Muller, Science **342** (6155), 224-227 (2013).

28. M. Heyde, Science **342** (6155), 201-202 (2013).

29. K. Zheng, C. Wang, Y.-Q. Cheng, Y. Yue, X. Han, Z. Zhang, Z. Shan, S. X. Mao, M. Ye, Y. Yin and E. Ma, Nat Commun **1**, 24 (2010).

30. X. Zhu, J. Su, Y. Wu, L. Wang and Z. Wang, Nanoscale **6** (3), 1499-1507 (2014).

31. S. Dai, J. Zhao, L. Xie, Y. Cai, N. Wang and J. Zhu, Nano Lett **12** (5), 2379-2385 (2012).

32. Y.-J. Kim, W. W. Lee, I.-C. Choi, B.-G. Yoo, S. M. Han, H.-G. Park, W. I. Park and J.-i. Jang, Acta Materialia **61** (19), 7180-7188 (2013).

33. Y. Yue and K. Zheng, Appl Phys Lett **104** (23), 231906 (2014).

34. J. Luo, J. Wang, E. Bitzek, J. Y. Huang, H. Zheng, L. Tong, Q. Yang, J. Li and S. X. Mao, Nano Lett **16** (1), 105-113 (2016).

35. G. Cheng, C. Miao, Q. Qin, J. Li, F. Xu, H. Haftbaradaran, E. C. Dickey, H. Gao and Y. Zhu, Nat Nano **10** (8), 687-691 (2015).

36. M. C. Wingert, Z. C. Y. Chen, E. Dechaumphai, J. Moon, J.-H. Kim, J. Xiang and R. Chen, Nano Lett **11** (12), 5507-5513 (2011).

37. M. C. Wingert, S. Kwon, M. Hu, D. Poulikakos, J. Xiang and R. Chen, Nano Lett **15** (4), 2605-2611 (2015).

38. Y. Zhu, F. Xu, Q. Q. Qin, W. Y. Fung and W. Lu, Nano Lett **9** (11), 3934-3939 (2009).

39. Z. L. Wang, R. P. Gao, P. Poncharal, W. A. de Heer, Z. R. Dai and Z. W. Pan, Materials Science and Engineering: C **16** (1–2), 3-10 (2001).

40. D. A. Dikin, X. Chen, W. Ding, G. Wagner and R. S. Ruoff, Journal of Applied Physics **93** (1), 226-230 (2003).

41. B. Polyakov, M. Antsov, S. Vlassov, L. M. Dorogin, M. Vahtrus, R. Zabels, S. Lange and R. Lõhmus, Beilstein Journal of Nanotechnology **5**, 1808-1814 (2014).

42. L. B. Freund and S. Suresh, *Thin film materials : stress, defect formation, and surface evolution*, 1st pbk. ed. (Cambridge University Press, Cambridge, England ; New York, 2009).

43. T. Kizuka, Y. Takatani, K. Asaka and R. Yoshizaki, Phys Rev B **72** (3), 035333 (2005).

44. A. Hedler, S. L. Klaumunzer and W. Wesch, Nat Mater **3** (11), 804-809 (2004).

45. S. Ashtekar, G. Scott, J. Lyding and M. Gruebele, Physical Review Letters **106** (23), 235501 (2011).

46. E. P. EerNisse, Appl Phys Lett **30** (6), 290-293 (1977).

47. R. H. Doremus, Journal of Applied Physics **92** (12), 7619-7629 (2002).

48. A. Naoki, O. Satoshi, N. Toshiro, S. Yoshihiro, T. Kanetake and K. Satoshi, Japanese Journal of Applied Physics **35** (1B), L67 (1996).

49. K. Watanabe, T. Kawasaki and H. Tanaka, Nat Mater **10** (7), 512-520 (2011).

50. V. N. Novikov and A. P. Sokolov, Nature **431** (7011), 961-963 (2004).

51. L. Brambilla, L. Colombo, V. Rosato and F. Cleri, Appl Phys Lett **77** (15), 2337-2339 (2000).

52. J. H. Shin and H. A. Atwater, Phys Rev B **48** (9), 5964-5972 (1993).

53. S. Coffa, F. Priolo and A. Battaglia, Physical Review Letters **70** (24), 3756-3759 (1993).

54. D. L. Griscom, Journal of Non-Crystalline Solids **68** (2–3), 301-325 (1984).

55. J. M. Stallons and E. Iglesia, Chemical Engineering Science **56** (14), 4205-4216 (2001).

56. A. Hemeryck, N. Richard, A. Estève and M. D. Rouhani, Journal of Non-Crystalline Solids **353** (5–7), 594-598 (2007).

57. C. A. Volkert, Journal of Applied Physics **70** (7), 3521-3527 (1991).

58. F. Strauß, L. Dörrer, T. Geue, J. Stahn, A. Koutsioubas, S. Mattauch and H. Schmidt, Physical Review Letters **116** (2), 025901 (2016).

59. Y.-C. Chen, Z. Lu, K.-i. Nomura, W. Wang, R. K. Kalia, A. Nakano and P. Vashishta, Physical Review Letters **99** (15), 155506 (2007).

60. N. Pradeep, D.-I. Kim, J. Grobelny, T. Hawa, B. Henz and M. R. Zachariah, Appl Phys Lett **91** (20), 203114 (2007).

61. C. Tang and L. P. Dávila, Journal of Applied Physics **118** (9), 094302 (2015).

62. R. F. Egerton, P. Li and M. Malac, Micron **35** (6), 399-409 (2004).

63. B. d. B. Darwent, National Bureau of Standards (31) (1970).

Chapter 6: Structure-induced enhancement of thermal conductivities in electrospun polymer nanofibers

6.1 Introduction

Recent progress in polymeric material engineering, especially in the synthesis and processing of materials with structure on nanometer-length scales, has created very promising opportunities for designing and fabricating a new class of nanostructured thermal transport materials with high thermal conductivity and compliant mechanical properties.[1,2] It has been discovered that, in addition to enhanced mechanical performance,[3,4] polymer materials under tension also exhibit increased thermal conductivity along the tensile direction.[3,5-9] Polymeric materials, which are nearly insulating in bulk forms,[10-12] exhibit increased thermal conductivity when they are stretched to high draw ratios. For instance, the thermal conductivity (κ) of micron-sized polyethylene (PE) fibers was found to increase from 0.2 W/m-K in bulk forms to 50 W/m-K after drawing, accompanied by an increase in Young's modulus.[3] More recently, Shen *et al.*[1] observed thermal conductivity as high as ~100 W/m-K for a single PE nanofiber (drawn from a gel to a diameter of ~100 nm). Polymer nanofibers therefore represent a new class of materials potentially suited to thermal applications and related technologies that require good thermal conductivity, electric insulation, mechanical flexibility, chemical stability, and other attributes uniquely related to polymers.

Heat transport mechanisms in polymers have been studied quite extensively. As an intrinsically low-dimensional system, isolated individual polymer chains can, in principle, have very high thermal conductivity.[13] However, a macroscopic ensemble of polymer chains is often a thermal insulator because of the twisted random orientations of the polymer chains and the weak coupling between the chains, in addition to inherent defects such as voids, impurities, polymer chain ends, and entanglements. These imperfections and defects generate high interfacial thermal resistance between conducting crystalline domains because high-frequency phonon modes within the crystalline domains must transfer to low-frequency modes across the domains. In highly stressed nanofibers, however, voids and entanglements are less likely to exist and polymer chains tend to form highly oriented structures as a result of transverse axial confinement and large surface aspect ratio. Molecular dynamic simulations have shown that κ of PE polymer nanofibers may achieve ~350 W/m-K,[14-16] and is ever diverging with length.[14,17,18]

These prior experimental and computational studies suggest a correlation between structures (e.g., crystalline domain size and orientation) and thermal conductivities in polymeric materials. In mechanical drawing experiments,[1,3,5,8,19] it was believed that stress imposed during the fiber drawing re-orients the crystallites along the draw direction. These crystallites are connected by tie-molecules that originate in the unfolding polymer chains. Upon further drawing, the number of fully extended tie-molecules increases, producing oriented and stretched polymer chains as well as increased crystal sizes, thereby enhancing mechanical strength and thermal conductivity. Much effort has therefore gone into developing advanced fabrication

techniques, for example, direct proximal probe-based drawing[1] and nanoporous template wetting,[20] as well as into uniaxially stretching bulk polymers into nanofibers of aligned chains in order to produce high modulus and high thermal conductivity.

Despite these recent advancements in thermal conductivity enhancement via drawing, there is still a lack of fundamental understanding of the relationship between the structures and attained thermal transport properties in polymer nanofibers. For instance, there is no study revealing how the size and anisotropic alignment of polymer crystallites is correlated with thermal transport. To that end, we used high-resolution in situ wide-angle X-ray scattering (WAXS) to systematically determine the structures of Nylon-11 nanofibers fabricated by electrospinning, which is a simple and versatile method to produce polymer nanofibers with controlled fiber diameters from tens of microns to tens of nanometers.[21] Nylon-11 is a widely used polymer material in high-performance applications, and it is relatively easier to produce highly aligned Nylon-11 nanofibers through electrospinning. A highly sensitive micro-device platform was employed to measure the thermal conductivities of corresponding individual nanofibers. Using electrospun Nylon-11 as a model system, we established a close correlation between the axial thermal conductivity and crystalline structures (e.g., the orientational distribution and dimension of the crystallites). The methodology in the current study can be readily extended to other commonly investigated polymer materials, such PVDF (polyvinylidene fluorid), PE, PEO (polyethylene glycol), and etc.

6.2 Sample preparation

Nylon-11 pellets (Sigma-Aldrich) with a density of 1.026 g/mL (melting temperature T_m=198°C) were dissolved in 1,1,1,3,3,3-Hexafluoro-2-propanol (HFIP, from Sigma-Aldrich). Solution concentration varied from 2 wt% to 12.5 wt% for the control of nanofiber diameters. The nanofibers were spun on a vertical electrospinning apparatus (Fig. S3) with an electric potential of 6-7 kV. In order to produce uniaxially aligned nanofibers, two parallel collecting electrodes were placed 20-30 cm below the spinneret.[54] The electrospinning jet then stretched itself across the gap as the electric field lines are attracted towards the edges of the electrode. The electrostatic repulsion between the deposited charged fibers further facilitated the parallel and relatively even distribution of fibers.[55,56] The highly oriented nanofibers were then carefully transferred either onto micro-devices for thermal property measurement or to an X-ray-compatible vacuum chamber for internal structure characterization. The diameters of nanofibers were determined on an FEI Quanta 400F environmental scanning electron microscope (SEM).

6.3 Structure measurement

The internal crystalline structures of the nanofibers, in terms of lattice dimension, crystalline size, and orientational order, etc., were quantitatively characterized using wide-angle X-ray scattering (WAXS) at beamline 8-ID at the Advanced Photon Source with an X-ray energy of 7.35 keV. The aligned nanofibers were placed under tension between two parallel posts that can be individually

translated axially in order to stretch the nanofibers. Controlled thermal annealing of the nanofibers was achieved via homogenous infrared radiation from an in-vacuum IR heater (200 W, 120 V, Mor Electric Heating Assoc., Inc., USA). *In situ* hot-stretching was performed by ramping to and maintaining the desired annealing temperature until fibers reached structural equilibrium, followed by uniaxial stretching at a rate of 5 μm/s. The temperature was measured with a platinum resistance thermometer placed in close proximity to the nanofiber sample. To protect the polymer nanofibers from radiation damage, the samples as well as the entire hot-stretching instrument are enclosed in an X-ray compatible vacuum chamber. WAXS patterns were recorded by a single-photon-counting pixel array detector (Pilatus 1M, Dectris) located 194 mm downstream from the sample. Routine WAXS data processing was performed for air gap scattering, efficiency, polarization, and solid angle before the 2D WAXS data were finally reduced to 1D data for further data analysis.

6.4 Structural characterization

During the fast electrospinning, long filaments of Nylon-11 chains are wound up at an extremely high speed to form crystalline lamellar domains whose orientation and crystallization occur in line with the elongation flow along the extrusion direction. In each domain, the extended parallel chains are connected by hydrogen bonds forming a layered structure.[22,23] These oriented crystallites are connected by random networks of tie molecules or chain segments that represent the amorphous constituent of the internal structure. The mixed phase, consisting of co-existing amorphous and oriented crystalline regions and schematically shown in Fig. 6.1a, is confirmed by the

WAXS pattern from uniaxially aligned as-spun Nylon-11 nanofibers where Bragg diffractions appear as broken arcs while the isotropic amorphous phase scatters X-rays to form a broader circular ring of uniform angular intensities (Fig. 6.1b and 6.1c).

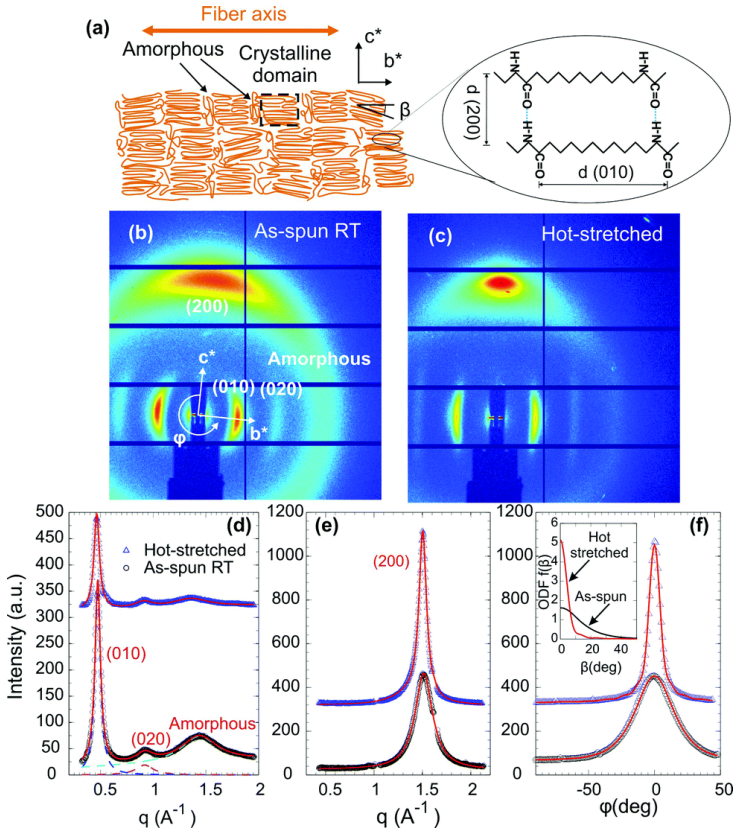


Figure 6.1: (a) Schematic of the molecular arrangement in Nylon-11 nanofibers. WAXS patterns from uniaxially aligned nanofibers of an initial diameter of ~200 nm are shown for (b) as-spun at room temperature (RT) and (c) after hot-stretching to a 1.5× draw ratio at 120 °C, respectively. The long axes of the nanofibers are laid along the b* axis, and the X-ray is incident perpendicular to the fibers (into the page). (d), (e) and (f) correspond to the intensity line cuts along the (010) direction (b* axis), (200) direction (c* axis), and the polar angle φ across the (200) diffraction peak, respectively. Solid red lines are fits to the models described in the text. Hot-stretched data are shifted vertically for clarity. Dashed blue, violet, and cyan curves displayed in (d) are best fits to the (010), (020), and amorphous peaks for the RT data, respectively. The inset in (f) shows corresponding orientational distribution functions of the crystalline domains as a function of inclination angle β of the crystalline domain with respect to the nanofiber axis.

Detailed information about the internal structure can be obtained by quantitative analysis of the line shapes of the Bragg diffractions. The longitudinal (axial) line cut along the fiber c* axis is excellently described by the superposition of the (010), (020) and the diffuse peak from the amorphous regions, which is modeled by three Lorentzian functions (Fig. 6.1d). The lattice spacing along the fiber axis can then be determined from the peak position, and the size of the crystalline domain is estimated from the peak width via the Scherrer equation.[24] The shape factor of the amorphous phase obtained from the axial line cut is then used as the background scattering to extract the lattice spacing and crystalline domain dimension along the fiber perpendicular direction a* (Fig. 6.1e). The degree of the uniaxial orientational order of the crystalline domains is described by the orientational distribution function (ODF) $f(\beta)$, where β denotes the inclination angle between the long molecular chain axis and the fiber axis. The ODF can be obtained from the angular intensity distribution[25,26] across the (200) Bragg peak, as shown in Fig. 6.1f. Knowing the ODF, any averaged orientational property $\langle X \rangle$ can be numerically calculated by

$$\langle X \rangle = \frac{\int_0^{\pi/2} X f(\beta) \sin\beta d\beta}{\int_0^{\pi/2} f(\beta) \sin\beta d\beta} . \qquad (6.1)$$

In particular, the average inclination angle of the crystalline domains $\langle \beta \rangle$ and the 2nd-order orientational order parameter $\langle P_2 \rangle$ with respect to the fiber axis are determined by substituting X by β and $(3\cos^2\beta - 1)/2$, respectively. It should be noticed that the orientation due to the inter-fiber alignment in a bundle also contributes to the overall orientational WAXS analysis as a convolution with the intrinsic orientation arising from the molecular alignment.[27] Analysis on the scanning electron microscope

(SEM) images, however, revealed that nanofibers are highly aligned so that the effect due to fiber alignment is very small in comparison to that from the intrinsic internal crystalline orientation. Quantitative structure information about the internal structures is summarized in Figure 6.2 for as-spun and hot-stretched nanofibers as a function of nanofiber diameter, and will be discussed along with their thermal properties. It is known that Nylon-11 possesses five different polymorphs and that thermal annealing and stretching may induce transitions among these phases.[28,29] However, during the entire hot-stretching process the (010) and (200) diffractions are always orthogonal to each other, their lattice parameters are consistent with literature bulk values for monoclinic β form of Nylon-11,[22,23] and they do not show much dependence on nanofiber diameter or drawing ratio (Fig. 6.2c and 6.2e). The d-spacing effect on thermal conductivity, therefore, will be ignored in the following discussions.

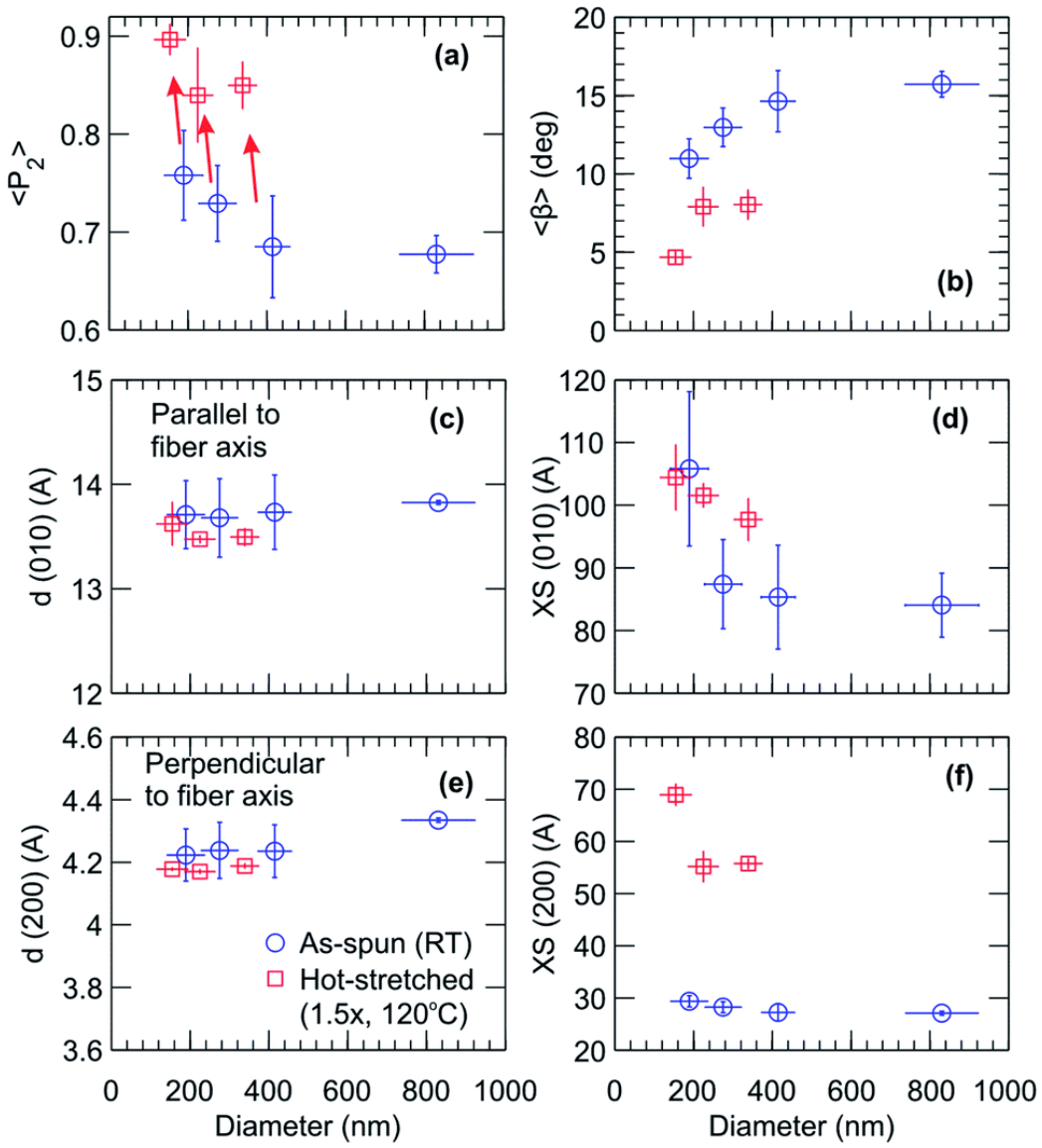


Figure 6.2: Structural data of the crystalline domains as a function of diameter for nanofibers as-spun at room temperature (blue circles) and hot-stretched at 120 °C to a 1.5× draw ratio (red squares). (a) and (b) are the orientational order parameter and average inclination angle, respectively; (c) and (e) are lattice parameters along the (010) direction (nanofiber axis) and the (200) direction (perpendicular to nanofiber axis), respectively; (d) and (f) are the average crystalline domain sizes along the (010) and (200) directions, respectively. Error bars are standard deviations from measurements on multiple and identical nanofiber samples.

6.5 Thermal measurement

The thermal conductivity of the Nylon-11 nanofibers was measured using the well-established suspended micro-device method[58,59] over a wide temperature range. Pt resistance thermometer coils patterned onto suspended SiN_x membranes allow for heating and temperature sensing, where one coil acts as a heater to create a temperature differential across the individual nanofibers, and both coils simultaneously act as thermometers to measure the temperature rise of each suspended membrane. Measurements were performed in a vacuum chamber evacuated to better than ~10^{-5} Torr to reduce the conduction and convection heat transfer due to residual air molecules. Heat loss along the suspending beams supporting the heating and sensing membranes as well as along the nanofiber was found to be within the systematic error of the nanofiber thermal property measurement and thereby can be negligible.

Excess nanofibers on the micro-devices were cut using focused ion beam (FIB) with care taken to avoid accidental Ga ion or electron beam damage[60] to the nanofiber of interest (Fig. 6.3b and 6.3c). Platinum deposition for enhanced thermal contact between nanofibers and SiN_x membranes was not applied as it was found to damage the fibers and reduce measured thermal conductivity values. The conductivity reported here therefore includes the thermal contact resistance, thereby representing the lower bound of the intrinsic value of the nanofibers. The contact resistance, however, is estimated to be very small compared to the fiber conduction resistance based on previous investigations on suspended nanowire/fiber systems.[61]

Since the thermal conductance of thin polymer nanofibers herein is rather low compared to wires made of most inorganic materials, we employed a sensitive measurement technique based on the Wheatstone bridge, which can resolve a thermal conductance as low as ~0.1 nW/K.[62] Our measurements suggested that the contribution from the background conductance is not negligible due to the low conductance of the nanofibers. Therefore, a 'canceling' scheme[63,64] was applied so that the background is directly subtracted by measuring the conductance difference between a nanofiber device and a neighboring identical blank device with no nanofiber.

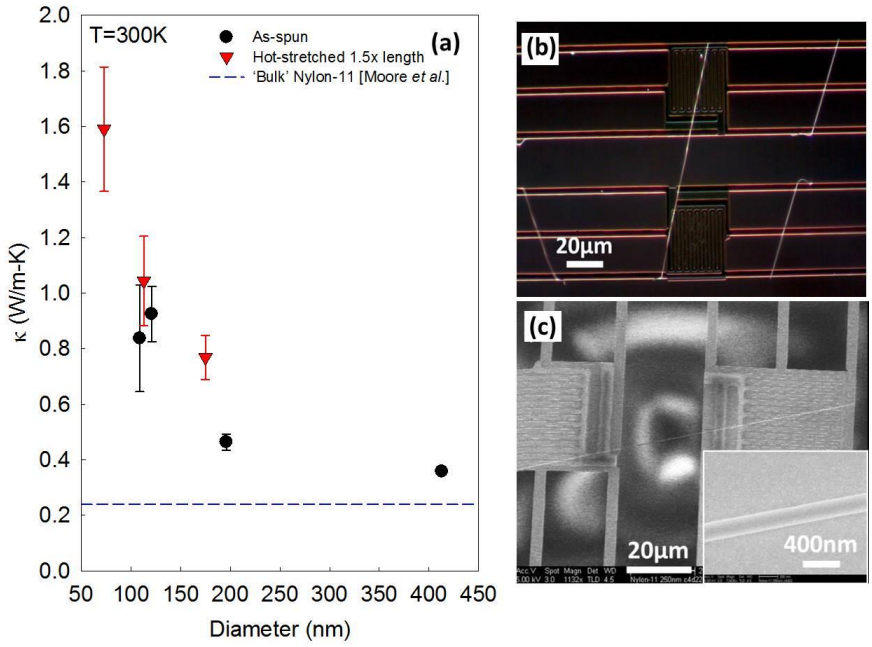


Figure 6.3: (a) Thermal conductivity versus nanofiber diameter at 300 K. Black circles represent as-spun nanofibers and red triangles represent nanofibers hot-stretched to 1.5× original length. Thermal conductivity of all samples increases as diameter decreases, with larger increases among hot-stretched fibers. Blue dashed line represents bulk Nylon-11 values.[10] (b) Dark-field optical image of nanofibers on a suspended micro-device for thermal measurement. (c) SEM of the same fiber in (b) with inset of a close-up of the fiber segment on the supporting pad.

6.6 Size dependence of thermal conductivity

Stretching crystalline polymer films and fibers has been reported in both computer simulations and experiments to be capable of modifying crystalline structures or inducing crystal transitions, which subsequently can lead to enhanced or even new performance in mechanical and thermal properties.[1,30,31] Although the statistics in our WAXS data cannot tell if drawing may improve the orientational distribution of the amorphous chains, it is commonly believed that drawing stretches the loose chains between crystal domains and yields increased tension in these chains and larger crystal size; on the other hand, the entangled polymer chains are restricted and the molecules orient themselves along the fiber axis direction, resulting in improved orientation. In the case of lamellar-structured Nylon-11, drawing can also enable the hydrogen-bonded polyamide sheets to slip past each other and form a more oriented structure.[32] The as-spun nanofibers are intrinsically highly stretched with an extremely high draw-ratio of 10^4-10^5 from the electrospinning process.[33] By uniaxially drawing the as-spun nanofibers at elevated temperatures below Nylon-11's melting point (T_m=198°C), we succeeded in obtaining an extra draw ratio of up to 2× original length. Data with a draw ratio of 1.5× were demonstrated in this study as the 1.5× ratio is applicable for all fibers. The structural improvements and the tension along the polymer chains are expected to increase the axial thermal conductivity, which was indeed observed in the present study.

Fig. 6.3a shows the increasing axial thermal conductivity κ measured at room temperature on as-spun and hot-stretched Nylon-11 nanofibers as a function of fiber diameter. As-spun nanofibers, even the one with 413-nm diameter, displayed a higher

thermal conductivity than the literature values (0.216-0.24 W/m-K) of bulk Nylon-11,[10,34,35] and the thermal conductivity increased as fiber diameter was further reduced to 196 nm, 121 nm, and 109 nm. Hot-stretched nanofibers (175 nm, 113 nm, and 73 nm) had even higher thermal conductivity values than those of similarly sized as-spun samples. Due to the challenging nature of the thermal conductivity measurements of individual nanofibers, it was prohibitively time-consuming to carry out these measurements with a broad sampling to probe possible variations of thermal properties of fibers with the same diameter. Such a study with large sampling size would be useful to establish a stronger diameter-dependence correlation, which warrants more systematic experimental study in the future.

6.7 As-spun nanofibers

The increase in thermal conductivity with decreasing diameter for as-spun nanofibers is strongly correlated with the structural trend revealed by the WAXS data (Figure 6.2). The perpendicular crystal size, i.e., along the (200) direction, does not vary as the fiber diameter reduces from the micron scale to ~200 nm (Figure 6.2f), while the longitudinal crystal size grows by ~25% (Figure 6.2d), implying a longer phonon mean free path (MFP) along the aligned molecular chains before phonons are scattered at crystal boundaries. Moreover, the population fraction of crystals whose extended chains are parallel to the fiber axis is higher as the fiber diameter decreases, which has been verified by the higher orientational order parameter $\langle P_2 \rangle$ and smaller averaged crystal inclination angle $\langle \beta \rangle$ (Figures 6.2a and 3b). This further facilitates phonon propagation along the fiber axis. On the other hand, the crystallinity analysis[36]

reveals a nearly constant degree of crystallinity of 36% for all the studied nanofibers, consistent with 35-45% determined by X-ray diffraction and differential scanning calorimetry on electrospun Nylon nanofibers[11,37] and bulk Nylon samples.[38,39] In addition, WAXS from bulk Nylon-11 samples does not reveal preferred orientations. Therefore, it is the improved crystallite orientation and polymer chain alignment arising from the confinement of diameter reduction rather than the fraction of crystallinity that contributes to the enhanced thermal performance.

6.8 Hot-stretched nanofibers

As the diameter reduces below a critical value of ~200 nm, regardless of as-spun or hot-stretched nanofibers, κ increases in an accelerated trend (Figure 6.3a), consistent with previous studies on PE nanofibers,[1,3] albeit with lower κ for the stretched Nylon fibers studied herein. In addition, hot-stretched nanofibers show higher κ values than as-spun fibers with comparable diameters. This enhancement is highly correlated with the *in situ* hot-stretching WAXS data, which reveal a significantly narrower orientational distribution of the crystals, i.e., $\langle P_2 \rangle$ increased from 0.75 for as-spun 190-nm nanofiber to 0.9 after hot-stretching (Fig. 6.2a), and the averaged crystal inclination angle reduced from 11° to 4.4° (Fig. 6.2b). In contrast to a very small change in the longitudinal crystal size, the transverse crystal size after hot-stretching expanded to more than twice that of the as-spun fibers, which implies a much lower phonon scattering probability at the crystal boundaries and hence an increase in thermal conductivity along the crystal axis. For the smallest hot-stretched

nanofiber in the present study (73 nm in diameter), the thermal conductivity is about 1.6±0.2 W/m-K, more than 6× that of bulk Nylon.

It is also worth pointing out that the conductivities of the hot-stretched fibers, regardless of the size, are consistently slightly higher than those of the as-spun fibers. As can be seen from Fig. 6.3a, the hot-stretched 113 nm fiber has a higher thermal conductivity than the 121 nm and 109 nm as-spun fibers. This observation indicates that the (hot-) stretching leads to higher orientation order, which is in addition to the effect of the diameter reduction.

6.9 Temperature dependence of thermal conductivity

To further understand phonon scattering mechanisms in nanofibers, we investigated the temperature dependence of κ over a temperature range of 30-300 K (Fig. 6.4). Bulk Nylon exhibits three temperature regimes: 1) below the Debye temperature T_D, 2) above the Debye temperature but below the brittleness temperature T_b, and 3) above the brittleness temperature up to room temperature. The temperature dependence of thermal conductivity can be understood from the relation, $\kappa \propto Cvl$, where C is the heat capacity, v is the phonon speed of sound, and l is the phonon MFP. In the first regime, the temperature dependence is due to the increase in heat capacity with increasing temperature which saturates approaching the Debye temperature. In the second regime, the heat capacity is constant, but there is still a slight increase in κ, up to the brittleness temperature (~188 K[40]). Above T_b, in the third regime, κ is nearly constant. This provides a baseline for comparison with the measured nanofibers.

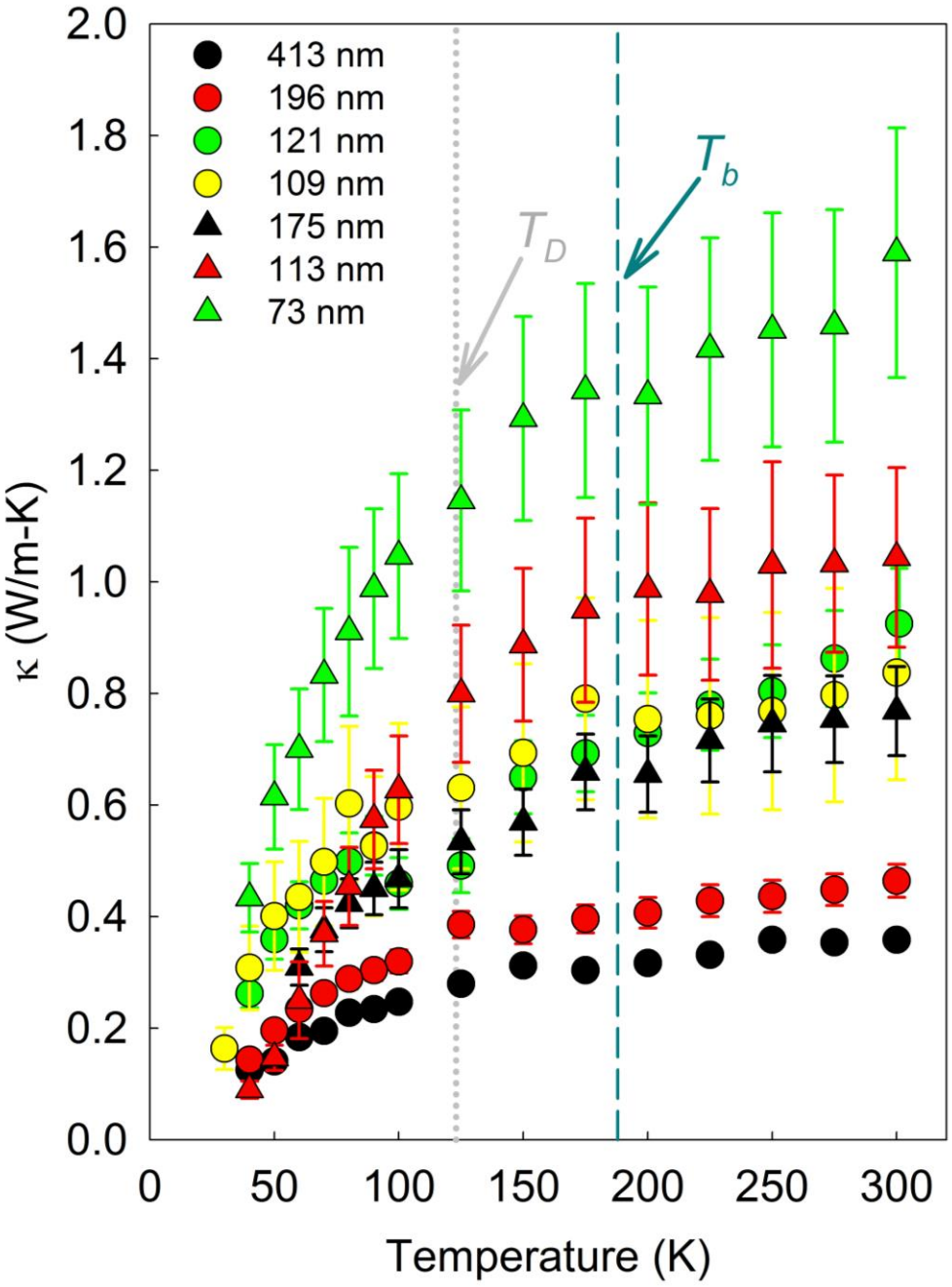


Figure 6.4: Thermal conductivity versus temperature for all measured nanofiber samples. Nanofiber diameters ranged from the largest at 413 nm down to the smallest at 73 nm. Fibers of diameters 413, 196, 121, and 109 nm (circles) were as-spun, whereas the 175, 113, and 73 nm diameter fibers (triangles) were hot-stretched to 1.5× original length. Vertical lines denote Debye (T_D) and brittleness (T_b) temperatures for bulk Nylon.

In the first regime, below T_D (~123 K for bulk Nylon-11[41]), the temperature dependence is again due to the heat capacity, however, the κ increase is scaled higher at smaller diameters due to longer phonon MFPs from the increased crystal size and orientation. The thermal conductivity, however, increases above the bulk Debye temperature, which becomes more pronounced for smaller diameter fibers. This is possibly due to the relationship between the Debye temperature and the elastic modulus, E, ($T_D \propto \sqrt{E}$),[42] where increasing E with decreasing diameter[2] leads to increases in T_D for smaller nanofibers. This could be the reason there is no discernable plateau or maximum in the thermal conductivity over the measured temperature range.

Impurity and inter-chain scattering dominates thermal transport in bulk and amorphous Nylon.[11] Similar scattering mechanisms also exist in the nanofibers in the present study, but with reduced impurity and inter-chain scattering leading to the higher κ. Moreover, a recent study[43] on the thermal conductivity of polymers has seen $1/T$ temperature dependence above the peak in κ due to Umklapp scattering. However, these polymers had a crystallinity of ~80%, whereas the Nylon in this study is comparatively low at ~36%, leaving much of the polymer amorphous. This large amorphous component could reduce the peak thermal conductivity and mask the *1/T* behavior in the measured κ data.

6.10 High temperature measurement and annealing effect

The thermal properties were also examined on an as-spun nanofiber sample (196 nm in diameter) above room temperature before and after annealing at 500 K

(Fig. 6.5). In the heating cycle before the annealing, κ maximizes at ~330 K, around Nylon's glass transition temperature (325-335 K),[44,45] and declines again upon further temperature increase. Similar behavior has been previously observed in some other polymers.[43,46] As the temperature rises above the glass transition temperature, structural changes[46] cause a decrease in κ.[43] The nanofiber was then annealed at 500 K (slightly above the T_m of 471 K) for about one hour without breaking the fiber and then allowed to cool to room temperature; its conductivity was found to be significantly depressed from 0.48 to 0.19 W/m-K at ~330 K. This may be accounted for by a few possible changes of the internal structures which were challenging in the current study to identify on single free-standing fibers: the degree of crystallinity substantially decreased; crystal size and morphology may be significantly affected; or more probably, preferred molecular orientation of the crystallites with respect to the fiber axis was lost with the thermal history.

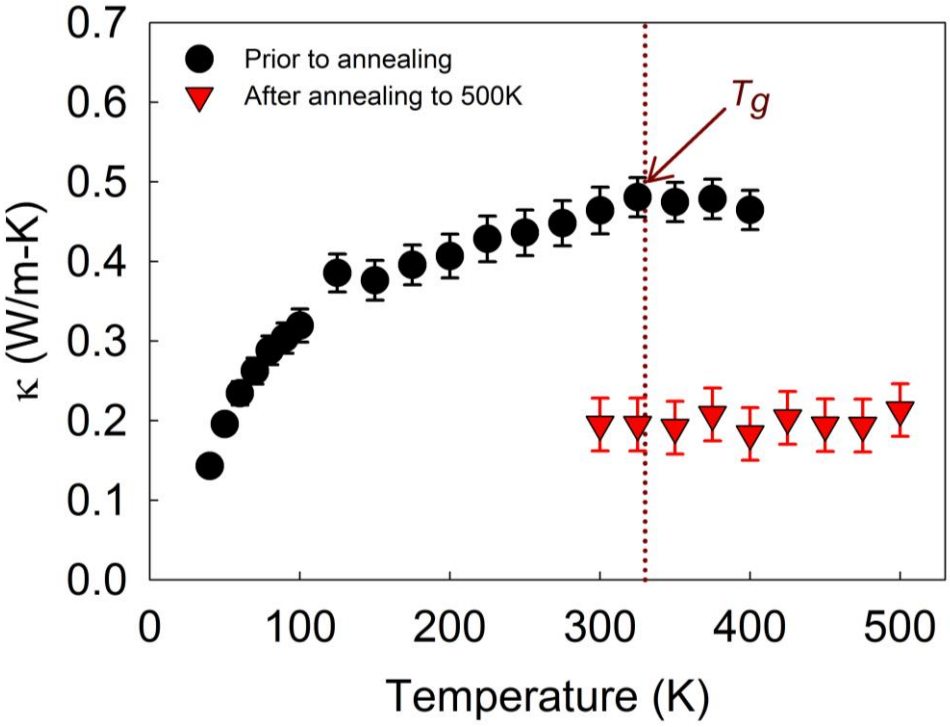


Figure 6.5: Thermal conductivity versus temperature for annealed nanofiber sample NF2 (196 nm diameter as-spun). Nanofiber thermal conductivity was measured from 30 K to 400 K (black circles) and further annealed to 500 K. The thermal data above room temperature shows a peak at ~330 K, which is approximately the glass transition temperature for Nylon (vertical dotted line). After holding at 500 K for ~1 hr, the sample was cooled to room temperature and the thermal conductivity was re-measured from 300 K to 500 K (red triangles) and found to be significantly reduced.

6.11 Effect of structural defects

The close correlation between structural and thermal properties in electrospun nanofibers was also clearly demonstrated in a nanofiber with intentionally induced defects, namely, a beaded nanofiber (Fig. 6.6). The capillary instability squeezes the fluid electrospinning jet into droplets that are still connected by the entangled polymer chains, thereby forming a beaded structure.[47] Previous orientation analysis along single-beaded fibers via electron diffraction has revealed a bulk-like structure in the

beads with randomly oriented crystallites,[48] which can account for the measured bulk-like κ (~0.28 W/m-K) for the beaded nanofiber in the present study.

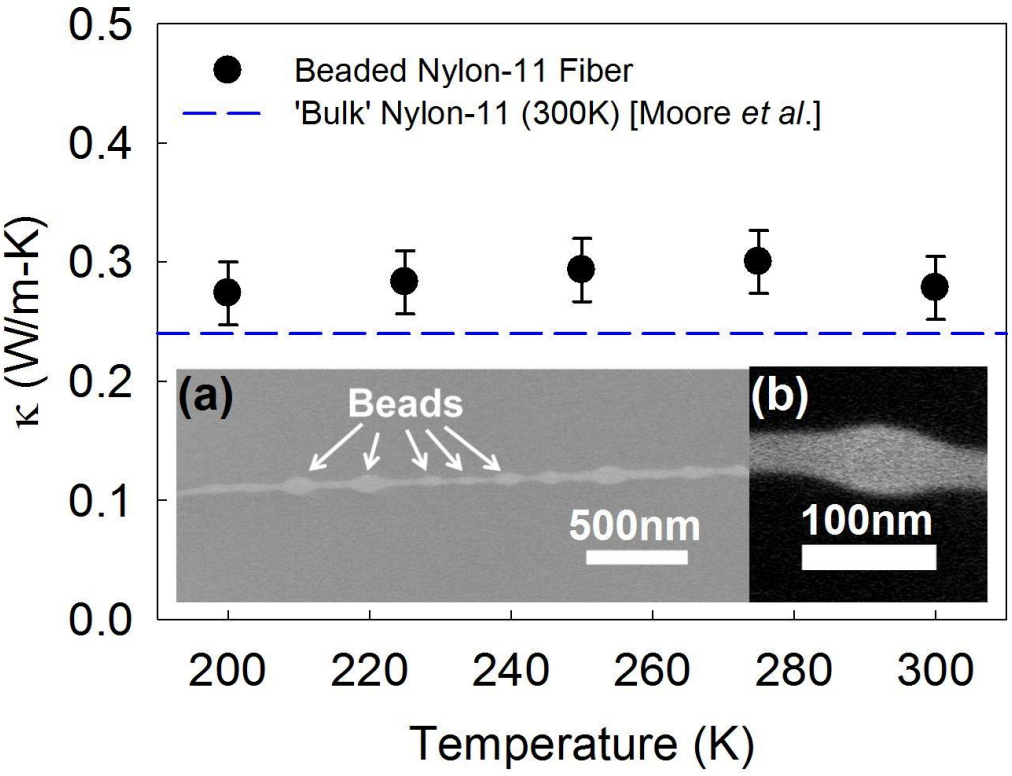


Figure 6.6: Thermal conductivity of a beaded nanofiber. Bulk Nylon-1110 (blue dashed line) shown for comparison purposes. Inset (a) shows an SEM image of a beaded nanofiber segment with several beaded structures marked. Inset (b) shows an individual bead structure from the beaded fiber.

6.12 Comparison with other nanofibers

In agreement with Shen *et al.*,[1] our results showed a significant structural-induced increase in thermal conductivity in small diameter nanofibers. The lower absolute κ observed in the Nylon-11 nanofibers as compared to PE, is attributed to the intrinsic difference in the molecular structure and the lower crystallinity. In addition,

the macroscopic conductivity of an ensemble of polymer chains drastically depends on the manner in which the chains are folded. Linear high-density PE has the simplest molecular structure with chains that can fold to form almost entirely crystalline domains (80-90% crystallinity)[3] with a much higher packing density than its amorphous counterpart. In contrast, the degree of crystallinity of Nylon-11 is only 35-40%, leaving most of the polymer in non-crystalline phase with very high thermal resistance. Furthermore, both experimental studies on PE mats[5] and molecular simulations on individual polymer chains[18,49,50] have shown that polymers of high mechanical strength also have superior thermal performance. Given Nylon's intrinsically lower Young's modulus (~25 GPa) of the crystalline lattice compared to PE (~240 GPa),[51] it is expected to possess a much lower thermal conductivity.

The structural properties and corresponding enhanced thermal conductivities of the Nylon nanofibers in the present study correlate well with their mechanical properties previously studied. As the electrospun nanofiber diameter reduces to 200-500 nm, it has been shown to exhibit rapidly rising Young's modulus and ultimate tensile strength along the fiber axis.[4] The fast electrospinning induces tensile strains on polymer chains even in the amorphous region. This lowers the phonon-phonon scattering and improves energy transport along the polymer backbones.[31]

6.13 Conclusion

We have established a relationship between the internal crystalline structures of electrospun Nylon-11 nanofibers with high as-spun draw ratio and their axial thermal properties. In consistence with previous experimental studies,[1,3,6] we found

that although the thermal conductivity starts deviating from the bulk value when the fibers reach as thick as several hundred nanometers (e.g. ~400 nm), this further accelerates only when the nanofiber diameter decreases to about two hundred nanometers, where crystallites start to show a significantly higher degree of preferred orientation with respect to the fiber axis. The combination of crystal size growth and improved orientational order (along with the narrowing of crystalline domain inclination distribution) increases the intermediate-range order and the phonon MFP, resulting in an enhanced thermal conductivity. Additional axial hot-stretching improved the orientation distribution and the crystallite size, thereby further reducing phonon scattering at crystal boundaries and facilitating heat transport along the fibers. Subsequently, thermal conductivity six times greater than bulk was achieved on the thinnest Nylon nanofibers in the present study.

Temperature-dependent tests showed some deviation from bulk behavior below room temperature. The larger crystal size increased thermal conductivity over the entire temperature range. This would plateau near the Debye temperature, which could shift to higher temperature with decreasing fiber diameter. On the other hand, increasing temperature above T_g led to a maximum thermal conductivity around T_g. It was also found from the beaded fibers that the disordering in crystallite orientations as well as nanofiber defects can significantly reduce the thermal conductivity to close to bulk-like values.

Nylon-11 is a ferroelectric polymer[52] and the dipole interactions can help improve the crystallite orientations during the electrospinning, as have been observed in other ferroelectric polymers such as PVDF.[53] The effect of the ferroelectricity of

polymer nanofibers on their thermal behavior is certainly of great interest for future investigations, yet there is no direct evidence on their correlations. Since the main set of thermal measurements were conducted below the glass transition temperature of Nylon-11 (between 40-70°C),[45] ferroelectric effects should be negligible. In addition, for measurements above the transition temperature, electronic contributions to the thermal conductivity are negligible and dominated by phonon transport.

In summary, our findings from the Nylon-11 nanofibers unambiguously provided very important experimental evidence of the strong dependence of the thermal performance on the crystalline morphology of the polymer nanofibers. Therefore, these studies will not only shed light on further understanding of phonon transport mechanisms in low-dimensional polymer systems, but also lay out a possible path to achieve full control of the design and fabrication of nanostructured polymer nanofibers endowed with high thermal conductivity and other desired properties.

Still, the results of this work do not conclusively state that the size-dependent properties are due to the crystal morphology itself. Since the overall crystallinity of the Nylon-11 fibers is practically constant, the mechanism for the thermal conductivity increase is not identical to that of polyethylene, where stretching fibers to smaller diameter leads to increased crystallinity[1]. Arguments that the amorphous content are the source of the behavior[2,65] is still possible. In fact, the crystal morphology measured in this chapter may lead to confinement of the amorphous polymer chains in between crystallites, which could lead to increased amorphous chain alignment, etc. In order to test for this, the following chapter details time- and size- dependent mechanical tests of the Nylon-11 fibers studied in this chapter. Time-dependent stress relaxation

measurements should be able to confirm if there are size-dependent phenomena resulting from increasingly confined amorphous chain regions in the fibers.

Acknowledgments

This chapter is a reprint of Z. Zhong*, M. C. Wingert*, J. Strzalka, H. H. Wang, T. Sun, J. Wang, R. Chen, Z. Jiang, "Structure-induced Enhancement of Thermal Conductivities in Electrospun Polymer Nanofibers," *Nanoscale*, 6, 8283-8291 (2014). *These authors contributed equally to this work.

References

1. S. Shen, A. Henry, J. Tong, R. T. Zheng and G. Chen, *Nat. Nanotechnol.*, 2010, **5**, 251.

2. A. Arinstein, M. Burman, O. Gendelman and E. Zussman, *Nat. Nanotechnol.*, 2007, **2**, 59.

3. C. L. Choy, Y. W. Wong, G. W. Yang and T. Kanamoto, *J. Polym. Sci. Pol. Phys.*, 1999, **37**, 3359.

4. C. T. Lim, E. P. S. Tan, S. Y. Ng, *Appl Phys Lett* **2008**, 92, 141908.

5. T. Kanamoto, A. Tsuruta, K. Tanaka, M. Takeda and R. S. Porter, *Macromolecules*, 1988, **21**, 470.

6. D. B. Mergenthaler, M. Pietralla, S. Roy and H. G. Kilian, *Macromolecules*, 1992, **25**, 3500.

7. B. Poulaert, J. C. Chielens, C. Vandenhende, J. P. Issi and R. Legras, *Polym. Commun.*, 1990, **31**, 148.

8. P. Smith and P. J. Lemstra, *J. Mater. Sci.* 1980, **15**, 505.

9. C. L. Choy, Y. Fei and T. G. Xi, *J. Polym. Sci. Pol. Phys.*, 1993, **31**, 365.

10. A. L. Moore, A. T. Cummings, J. M. Jensen, L. Shi and J. H. Koo, *J. Heat Trans.-T. Asme*, 2009, **131**, 091602.

11. C. L. Choy, E. L. Ong and F. C. Chen, *J. Appl. Polym. Sci.*, 1981, **26**, 2325.

12. G. DeCarvalho, E. Frollini and W. N. DosSantos, *J. Appl. Polym. Sci.*, 1996, **62**, 2281.

13. S. Lepri, R. Livi and A. Politi, *Phys. Rep.*, 2003, **377**, 1.

14. A. Henry and G. Chen, *Phys. Rev. Lett.*, 2008, **101**, 235502.

15. A. Henry, G. Chen, S. J. Plimpton and A. Thompson, *Phys. Rev. B*, 2010, **82**, 144308.

16. T. Zhang and T. Luo, *ACS Nano*, 2013, **7**, 7592.

17. A. Henry and G. Chen, *Phys. Rev. B*, 2009, **79**, 144305.

18. J. W. Jiang, J. H. Zhao, K. Zhou and T. Rabczuk, *J. Appl. Phys.*, 2012, **111**, 124304.

19. G. Capaccio and I. M. Ward, *Polym. Eng. Sci.*, 1975, **15**, 219.

20. B. Y. Cao, Y. W. Li, J. Kong, H. Chen, Y. Xu, K. L. Yung and A. Cai, *Polymer*, 2011, **52**, 1711.

21. D. H. Reneker and A. L. Yarin, *Polymer*, 2008, **49**, 2387.

22. S. Rhee and J. L. White, *J. Polym. Sci. Pol. Phys.*, 2002, **40**, 2624.

23. A. Kawaguchi, T. Ikawa, Y. Fujiwara, M. Tabuchi and K. Monobe, *J. Macromol. Sci. Phys.*, 1981, **B20**, 1.

24. J. I. Langford and A. J. C. Wilson, *J. Appl. Crystallogr.*, 1978, **11**, 102.

25. P. Davidson, D. Petermann and A. M. Levelut, *J. Phys. Ii.*, 1995, **5**, 113.

26. F. Giesselmann, R. Germer and A. Saipa, *J. Chem. Phys.*, 2005, **123**, 034906.

27. M. D. Edwards, G. R. Mitchell, S. D. Mohan and R. H. Olley, *Eur. Polym. J.*, 2010, **46**, 1175.

28. Q. Zhang, Z. Mo, H. Zhang, S. Liu and S. Z. D. Cheng, *Polymer*, 2001, **42**, 5543.

29. M. Richard-Lacroix and C. Pellerin, *Macromolecules*, 2013, **46**, 9473.

30. J. Liu and R. G. Yang, *Phys. Rev. B*, 2010, **81**, 174122.

31. S. Pal, G. Balasubramanian and I. K. Puri, *J. Chem. Phys.*, 2012, **136**, 044901.

32. J. W. S. Hearle and R. H. Peters, *Fibre structure*. Textile Institute: 1963.

33. A. L. Yarin, S. Koombhongse and D. H. Reneker, *J. Appl. Phys.*, 2001, **89**, 3018.

34. J. E. Mark, *Physical properties of polymers handbook*. 2nd ed.; Springer: New York, 2007.

35. J. F. Shackelford and W. Alexander, *CRC materials science and engineering handbook*. 3rd ed.; CRC Press: Boca Raton, FL, 2001.

36. N. S. Murthy and H. Minor, *Polymer*, 1990, **31**, 996.

37. C. Carrizales, S. Pelfrey, R. Rincon, T. M. Eubanks, A. X. Kuang, M. J. McClure, G. L. Bowlin and J. Macossay, *Polym. Advan. Technol.*, 2008, **19**, 124.

38. G. W. Ehrenstein and R. P. Theriault, *Polymeric materials: structure, properties, applications*. Hanser: Munich, 2001.

39. P. Ricou, E. Pinel and N. Juhasz, *Advances in X-ray Analysis* 2005, **48**, 170.

40. H. W. Starkweather and R. E. Brooks, *J. Appl. Polym. Sci.*, 1959, **1**, 236.

41. A. Xenopoulos and B. Wunderlich, *Polymer*, 1990, **31**, 1260.

42. M. X. Gu, C. Q. Sun, Z. Chen, T. C. Au Yeung, S. Li, C. M. Tan and V. Nosik, *Phys. Rev. B*, 2007, **75**, 125403.

43. X. J. Wang, V. Ho, R. A. Segalman and D. G. Cahill, *Macromolecules*, 2013, **46**, 4937.

44. T. Ashworth, L. R. Johnson, C. Y. Hsiung and M. M. Kreitman, *Cryogenics*, 1973, **13**, 34.

45. R. M. Neagu, E. Neagu, N. Bonanos and P. Pissis, *J. Appl. Phys.*, 2000, **88**, 6669.

46. P. Dashora and G. Gupta, *Polymer*, 1996, **37**, 231.

47. H. Fong, I. Chun and D. H. Reneker, *Polymer*, 1999, **40**, 4585.

48. T. Yoshioka, R. Dersch, M. Tsuji and A. K. Schaper, *Polymer*, 2010, **51**, 2383.

49. T. F. Luo, K. Esfarjani, J. Shiomi, A. Henry and G. Chen, *J. Appl. Phys.*, 2011, **109**, 074321.

50. T. F. Luo and J. R. Lloyd, *Adv. Funct. Mater.*, 2012, **22**, 2495.

51. I. Sakurada, T. Ito and K. Nakamae, *J. Polym. Sci. Pol. Sym.*, 1967, **15**, 75.

52. J. I. Scheinbeim, J. W. Lee and B. A. Newman, *Macromolecules*, 1992, **25**, 3729.

53. C.-C. Tsai, P. Mikes, T. Andrukh, E. White, D. Monaenkova, O. Burtovyy, R. Burtovyy, B. Rubin, D. Lukas, I. Luzinov, J. R. Owens and K. G. Kornev, *Nanoscale*, 2011, **3**, 4685.

54. C. Lai, G. Zhong, Z. Yue, G. Chen, L. Zhang, A. Vakili, Y. Wang, L. Zhu, J. Liu and H. Fong, *Polymer*, 2011, **52**, 519.

55. D. Li, Y. L. Wang and Y. N. Xia, *Nano Lett.*, 2003, **3**, 1167.

56. S. Ramakrishna, *An introduction to electrospinning and nanofibers*. World Scientific: Hackensack, NJ, 2005.

57. Z. Jiang, X. Li, J. Strzalka, T. Sun, M. Sprung, A. Sandy, S. Narayanan, D. R. Lee and J. Wang. *J. Synchrotron Radiat.*, 2012, **19**, 627.

58. L. Shi, D. Y. Li, C. H. Yu, W. Y. Jang, D. Kim, Z. Yao, P. Kim and A. Majumdar, *J. Heat Trans.-T. Asme*, 2003, **125**, 881.

59. D. Y. Li, Y. Y. Wu, P. Kim, L. Shi, P. D. Yang and A. Majumdar, *Appl. Phys. Lett.*, 2003, **83**, 2934.

60. D. L. Vezie, E. L. Thomas and W. W. Adams, *Polymer*, 1995, **36**, 1761.

61. C. H. Yu, S. Saha, J. H. Zhou, L. Shi, A. M. Cassell, B. A. Cruden, Q. Ngo and J. Li, *J. Heat Trans.-T. Asme*, 2006, **128**, 234.

62. M. C. Wingert, Z. C. Y. Chen, S. Kwon, J. Xiang and R. K. Chen, *Rev. Sci. Instrum.*, 2012, **83**, 024901.

63. J. Zheng, M. C. Wingert, E. Dechaumphai and R. Chen, *Rev. Sci. Instrum.*, 2013, **84**, 114901.

64. A. Weathers, K. Bi, M. T. Pettes and L. Shi, *Rev. Sci. Instrum.*, 2013, **84**, 084903.

65. V. Singh, T. L. Bougher, A. Weathers, Y. Cai, K. D. Bi, M. T. Pettes, S. A. McMenamin, W. Lv, D. P. Resler, T. R. Gattuso, D. H. Altman, K. H. Sandhage, L. Shi, A. Henry and B. A. Cola, *Nat. Nanotechnol.*, 2014, **9** 384.

Chapter 7: Strong size-dependent stress relaxation in polymer nanofibers

7.1 Introduction

One striking feature of electrospun[1-4] polymer nanofibers is their strong size-dependent material properties, which can change many times that of their bulk values. Widespread interest in polymer nanofibers stems from studies showing that the moduli[5] and thermal conductivities[6] of semi-crystalline polymer nanofibers are strongly dependent on the fiber diameter, specifically in the range of several hundred nanometers.[1, 5, 7-14] Further studies have expanded our understanding of the mechanical and thermal properties in these nanoscale fibers, such as strength, toughness, and glass transition and melting temperatures. These various observed mechanical and thermal behaviors are closely associated with the dynamics of polymer chains within the nanofiber. Quite recently it was found that along with the modulus, the yield strength and toughness of individual semi-crystalline nanofibers also increases significantly as diameter decreased.[13] This increase in toughness was unexpected as it opposes the classical tradeoff between strength and toughness present in bulk materials,[15] such as in bulk polymers and metals. As such, diverse applications of polymer nanofibers have been proposed, such as for military protective clothing[16], nanosensors[3, 17], tissue engineering scaffolding[18-20], and as thermal packaging[21].

The toughness of polymers mainly comes from two molecular scale contributions: breaking of polymer chains and sliding between polymer chains.

Macroscopically, the sliding between polymer chains usually manifests as viscoelasticity. In electrospun fibers, this tough behavior was attributed to originate in the amorphous polymer chain content, which was a considerable portion of the fiber. Furthermore, temperature based studies on nanofibers have observed similar size-dependent dissipative effects, such as reduction of the modulus upon heating[22] and decreased glass transition[23] and melting[24] temperatures with diameter reduction. The thermal responses of fibers have pointed to the significant amorphous content in these fibers as the leading cause of size-dependent behavior, without identifying specific mechanisms. From these disparate observations, it is not directly shown but can be inferred that a size-dependence should be associated with any mechanical relaxation in single electrospun polymer nanofibers, which has not been shown in previous studies on the elastic modulus.

Herein, we report for the first time significant size-dependent stress relaxation in electrospun Nylon-11 nanofibers (with a low diameter independent crystallinity of only 36%)[14], where diameter reduction leads to increasing amounts of stress relaxation. We also find that the relaxation time constant initially decreases, but saturates for fibers with diameters below 200 nm. This further means that the viscosity of the relaxing components, which is independent of size above ~200 nm, increases with diameter reduction below ~200 nm. Furthermore, the strong size-dependent stress relaxation in combination with exponentially increasing stiffness with decreasing diameter leads to nanomaterials with size-tunable properties capable of exhibiting high metal-like stiffness and near state-of-the-art mechanical energy dissipation.

7.2 Mechanics measurement

Individual Nylon-11 nanofibers were picked up with a micromanipulator in SEM and attached to the free end of an AFM cantilever with electron beam deposited Pt (Figure 7.1a) to conduct tensile measurements. The fiber was then pulled, causing the AFM cantilever to deflect and stress the fiber, where the applied force is directly related to the cantilever deflection and spring constant. The induced strain was found by measuring the fiber length (Figure 7.2), with care taken to use low beam energies (1-1.5 kV) as to not damage[25] the fiber. The instantaneous tensile modulus, E_{inst}, of the fiber was measured based on the slope of consecutive stress and strain measurements (measured in ~1 minute) and well within the linear extent of the stress-strain curve (Figure 7.3). Two different AFM cantilevers were used to measure E_{inst} of the fibers, with one cantilever having ~10× stiffer spring constant, and the resulting moduli were in good agreement with one another. Fibers tested using the stiffer cantilever were also used for time-dependent mechanical testing since changes in force manifest as small changes in cantilever deflection compared to that of the fiber elongation (initial strains ranging from 1.5 to 7% for fiber lengths of ~20-30 μm). Stress relaxation was monitored, after measuring E_{inst}, by measuring decreases in the cantilever deflection every five to ten minutes over a period of two hours. Relaxed tensile moduli, E_e, were calculated based on the final applied stress after relaxation ceased.

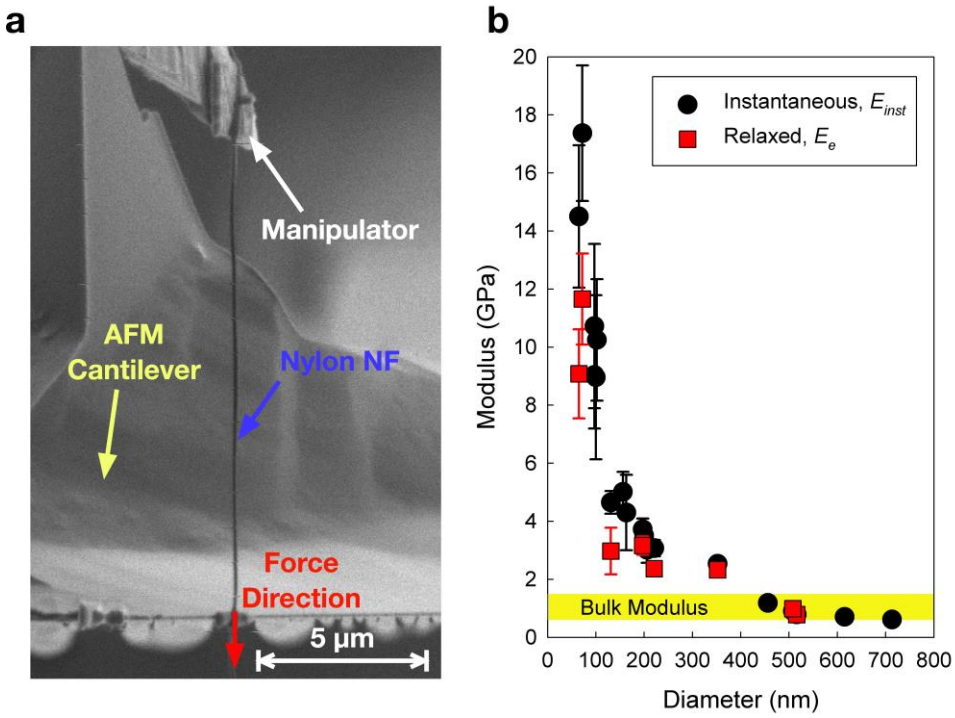


Figure 7.1: (a) Single nanofiber tensile relaxation measurement setup and (b) diameter dependence of instantaneous and relaxed moduli. (a) Individual nanofibers were attached to AFM cantilevers via a tungsten manipulator in a dual-beam FIB. The fibers were pulled with the manipulator and both cantilever deflection and fiber length were monitored to measure applied stress and fiber strain. (b) While the elastic modulus of fibers with diameter >400 nm are bulk-like[26-28], a dramatic exponential increase occurs as diameter drops below ~200 nm. The smallest nanofibers measured here, 65 and 72 nm, have instantaneous elastic moduli ~20 times larger than the bulk modulus. The relaxed moduli show two interesting phenomena: the degree of relaxation increases as diameter decreases, but not down to bulk-like values, and it is exponentially increasing as the diameter is reduced, similar to that of the instantaneous moduli.

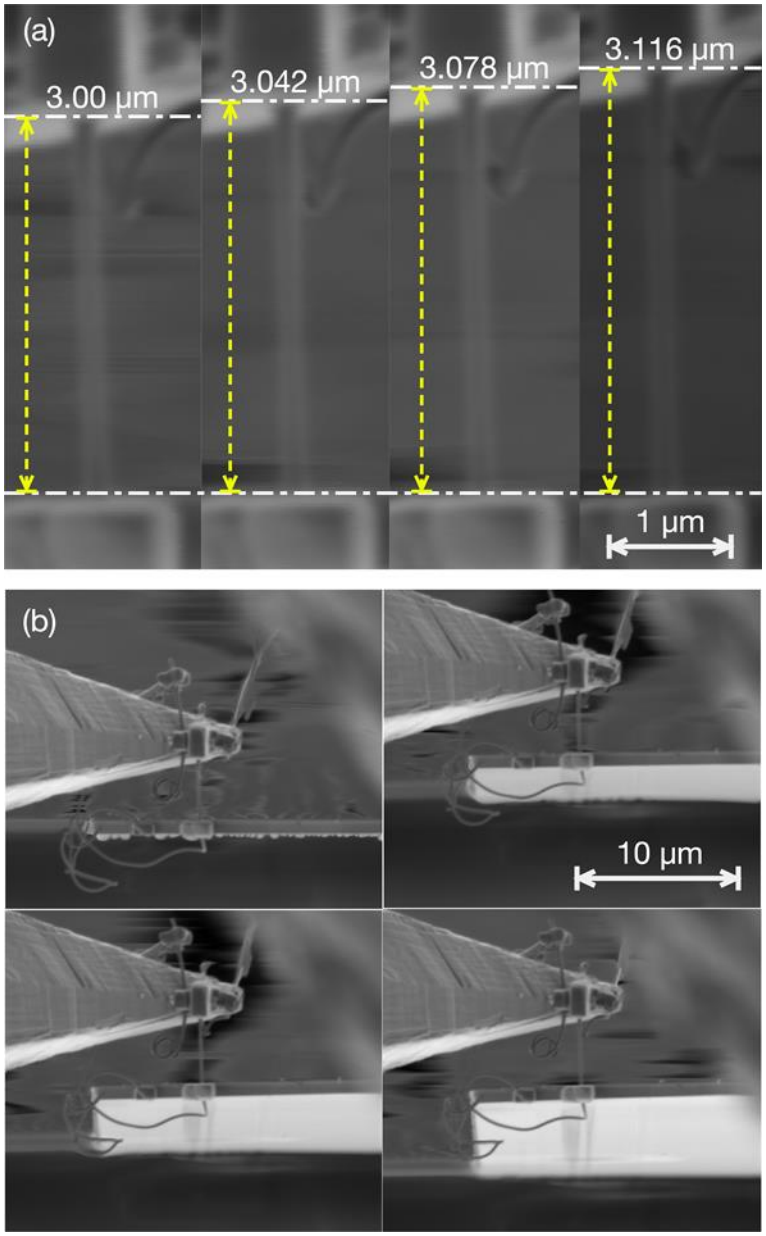


Figure 7.2: (a) Nanofiber strain measurement. During each loading, in addition to the cantilever deflection, the fiber length is measured and converted to applied strain. (b) Cantilever deflection during elastic modulus measurement. The nanofiber is attached to the edge of an AFM cantilever and pulled. The deflection measured is converted to stress applied to the fiber for each loading step.

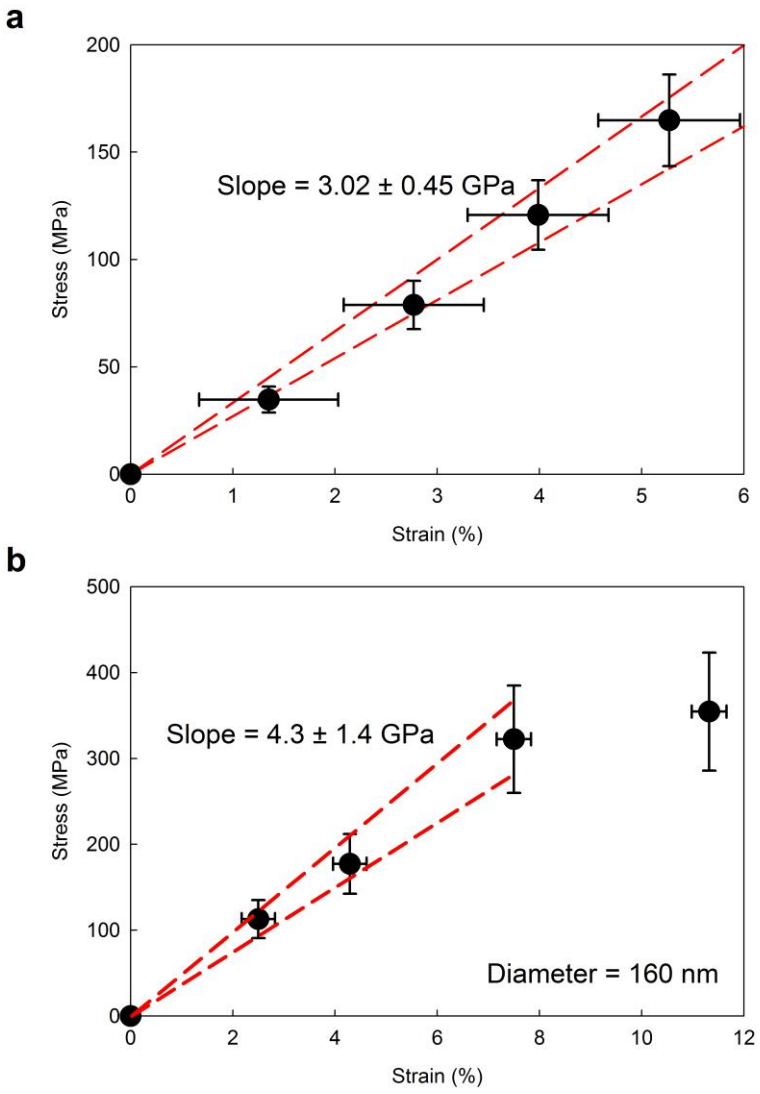


Figure 7.3: Stress-strain curve for single ~200 nm diameter nanofiber. The measured cantilever deflection and fiber length are converted to stress and strain on each fiber. The slope of the linear portion of the stress-strain curve is the nanofiber elastic modulus. Since the measurement is done quickly (within ~1 minute), the modulus can be considered instantaneous. Dashed red lines represent upper and lower bounds of the linear portion of the stress-strain curve.

7.3 Measured modulus and stress relaxation

Instantaneous and relaxed tensile moduli were measured for nanofibers of diameters ranging from 713 to 65 nm (Figure 7.1b), and were found to both exponentially increase as fiber diameter decreased. This observed dramatic increase is similar to moduli previously measured in other polymer nanofibers upon size reduction[5, 12, 13, 24, 29-32] as well as in drawn polymer mats[33]. Fibers with diameters larger than ~400 nm exhibit moduli consistent with that of bulk Nylon-11[26-28], ~0.6-1.5 GPa, whereas the thinnest nanofiber, with diameters of 65 and 72 nm, had E_{inst} as high as 14.5±2.5 and 17.4±2.3 GPa, respectively, which is a ~20-fold increase over the bulk value. A critical diameter of ~200 nm is observed for the onset of the exponential increase in the tensile modulus which is similar to the ~500 nm observed for Nylon-6,6[34, 35], compared to the lower ~50 nm for polypyrrole nanotubes[29] and higher ~800 nm for electro-spun polystyrene[36]. Interestingly, the relaxed moduli, E_e, exhibit a similar, albeit suppressed, exponential increase, indicating that some non-relaxing portion of the fiber (from the elastic or crystalline content) contributes to the increased tensile modulus. The deviation between E_{inst} and E_e, which also increases as the diameter is reduced, indicates that the relaxing (amorphous) component of the fiber still accounts for an appreciable amount of the enhanced stiffness, at least initially.

The relaxation which led to the eventual stiffness reduction was examined by measuring stress relaxation in fibers of diameters ranging from 516 to 65 nm over two hours. The supported stress over time was found to significantly correlate with fiber diameter, as seen in Figure 7.4 where the stress supported by the fiber was normalized by the initial stress, σ/σ_0. No stress relaxation was detected for ~500 nm diameter

nanofibers, however, the relaxation steadily increased as diameter decreased with the total stress supported by the 65 and 72 nm diameter fibers reduced to ~60% of the starting stress after only 20 minutes. Such stress relaxation is a well-known viscoelastic property of polymers, though the relaxation we have observed in the smaller diameter fibers is very fast comparatively. We must note that though no relaxation was seen in the largest diameter nanofibers, it is possible that they would follow a bulk-like relaxation process which may take much longer time scales to observe than allowed in the current experimental setup. This, however, indicates that the fast relaxation process is a symptom of the size reduction, most likely from increasingly confined amorphous regions present between the crystallites.

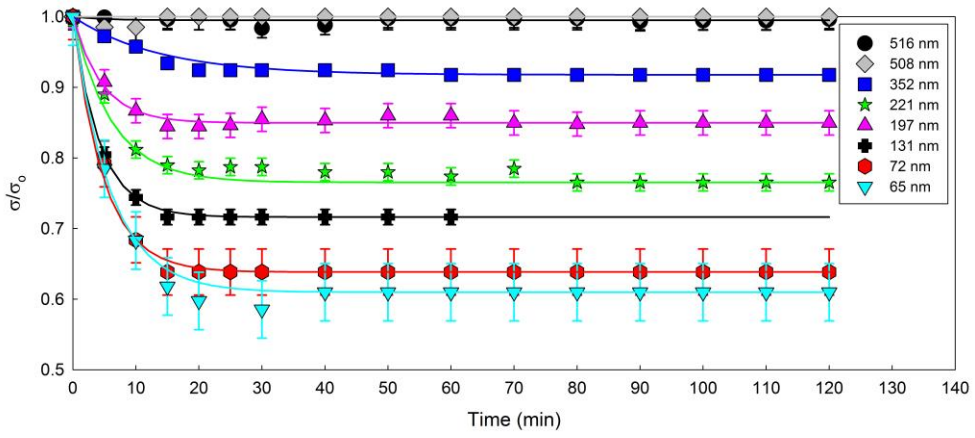


Figure 7.4: Stress relaxation in individual Nylon-11 nanofibers. The time-dependent stress normalized by the initial stress, σ/σ_0, was measured over a two-hour period, with measurements taken every five to ten minutes. Fibers of diameter ~500 nm show no relaxation over the measured time period, however, as diameter is reduced, stress relaxation increases, with stresses reduced to ~60% of the initial stress in the thinnest fibers. Legend lists nanofiber diameter for each relaxation measurement. Solid lines are fittings to the data based on a viscoelastic standard linear solid model.

7.4 Size-dependent relaxation in other polymers

This is similar to other size-dependent properties of polymer nanofibers which are believed to stem from confinement of polymer chains near surfaces and in amorphous regions[5, 10, 23, 30] and reduced polymer chain entanglement[24, 37]. Confinement induced orientation of polymer chains and chain dis-entanglement, specifically in the amorphous regions of fibers are ideal for enabling molecular relaxation processes. It has been observed that while large diameter fibers are comprised of densely packed, misaligned lamellar structures connected by relaxed amorphous tie molecules, smaller diameter fibers consist of a fibrillar structure with alternating crystallites and extended amorphous tie molecules.[12] This is somewhat similar to the structure of the Nylon-11 nanofibers in this study, which were found to have increased crystallite orientation and size as well as increased orientation and confinement of connecting amorphous tie molecule regions. Many recent studies have also observed the formation of a core-shell structure in electrospun fibers caused by quick solvent evaporation at the fiber surface during formation, which leads the polymer matrix to solidify in a non-equilibrium state.[24, 32, 38, 39] It has also been found that the process creates a preferred orientation for polymer chains in the shell layer, whose thickness is independent of fiber diameter[32], and prevents polymer chain relaxation, leaving them in a partially disentangled state.[31, 38, 39] These structural observations clearly show that as fiber diameter is reduced, the exponential increase in polymer chain orientational alignment and increasing volume fraction of partially disentangled chains will increase molecular mobility, which should manifest as strongly size-dependent mechanical relaxation, similar to what we have observed here.

7.5 Viscoelastic model of stress relaxation

To better understand the implications of this size-dependent viscoelastic behavior, we analyzed the measured stress relaxation as the behavior of a viscoelastic standard linear solid (SLS). In this model the modulus is time dependent and follows $E = E_e + E_r \cdot \exp(-t/\tau)$, where E_e and E_r are the elastic and relaxing contributions to the modulus, t is time, and τ is the relaxation time constant associated with the dissipative process. Since $E_{inst} = E_e + E_r = \sigma_0/\varepsilon$ and ε is approximately constant, we can relate the normalized stress and modulus as $\sigma/\sigma_0 = E/E_{inst}$. Furthermore, we can define a parameter, β, relating our measured saturated stress relaxation to the moduli components as $\beta = \lim_{t\to\infty} \sigma/\sigma_0 = E_e/(E_e + E_r)$. The stress relaxation for the SLS model then follows $\sigma/\sigma_0 = \beta + (1-\beta) \cdot \exp(-t/\tau)$, which has been fit to each set of nanofiber relaxation data sets (shown as the solid lines in Figure 7.4). From this we can define the amount of relaxation as for each nanofiber as $1-\beta$ (Figure 7.5a), where the relaxation is linearly correlated with the fiber diameter, compared to only a weak correlation with the initial applied stress (Figure 7.6).

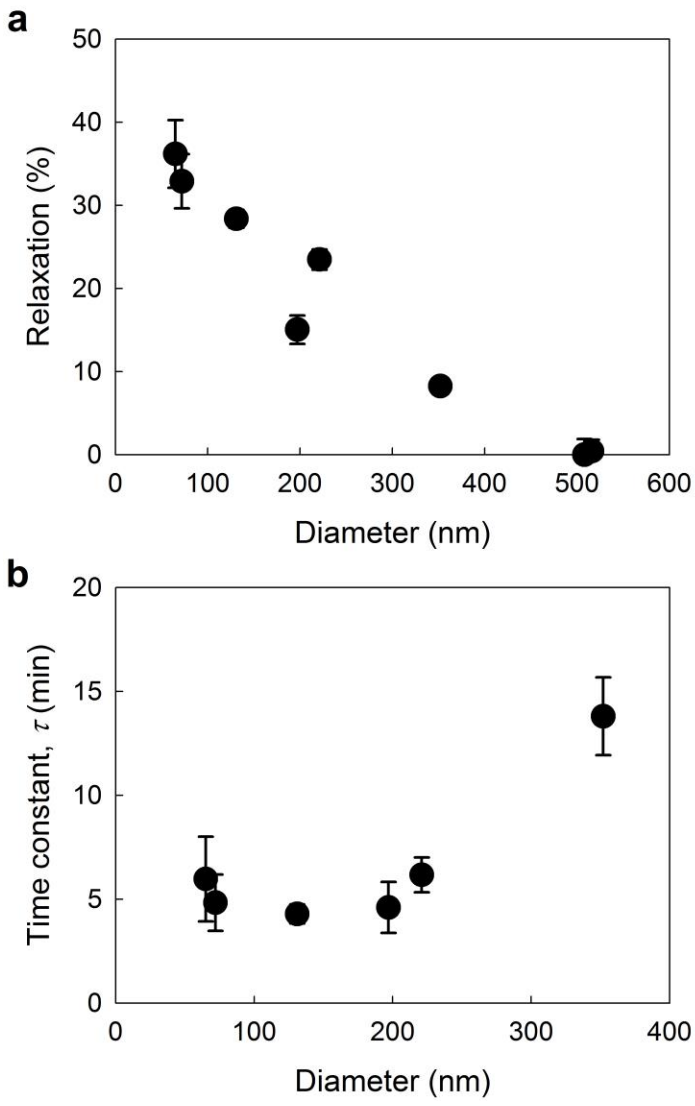


Figure 7.5: Diameter dependent (a) stress relaxation and (b) relaxation time constant. The relaxation and time constants were calculated based on fittings of the measured stress relaxation in Figure 7.4 to the viscoelastic standard linear solid model. (a) The degree of relaxation increases almost linearly with diameter reduction, starting from fibers of ~500 nm, for which no relaxation is observed, up to ~40% for the thinnest fibers measured. (b) The relaxation time constant initially decreases with decreasing diameter down to ~200nm, below which it saturates at ~5 minutes for all smaller diameters. Time constants could not be extracted from the ~500 nm diameter fibers as no relaxation was observed. The viscosity associated with the relaxing mechanisms of the fiber is initially constant down to ~200 nm and then, based on the saturated time constant and increasing relaxing component of the modulus, increases as the fiber diameter further decreases.

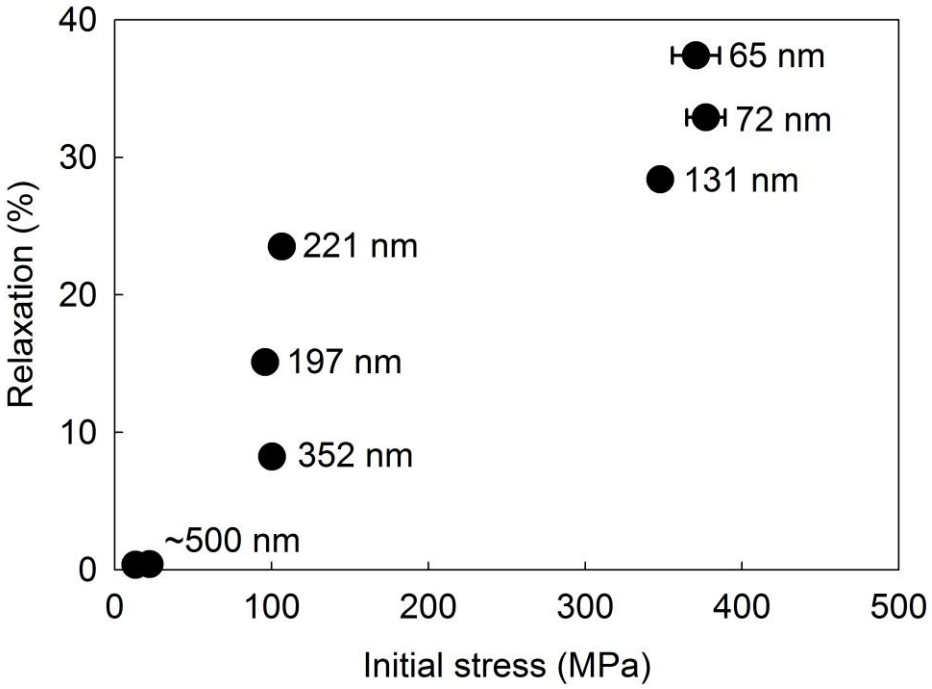


Figure 7.6: Full stress relaxation versus initial applied stress. The amount of relaxation is strongly dependent on the diameter of the nanofiber and not on the initial applied stress or induced strain. Data points are labeled by fiber diameter.

This stress relaxation fitting also allows us to extract the time constant (τ) related to the relaxation process for each measured fiber. Since no relaxation is observed for the ~500 nm diameter fibers, no time constant could be extracted, however, we do observe a decrease in $_{\tau}$ as the diameter decreases and saturates below ~200 nm (Figure 7.5b), from ~14 minutes for the 352 nm fiber to ~5 minutes for the remaining 65-221 nm diameter fibers. Based on these time constants, the viscosity (η) of the relaxing region of the fiber, related as $\eta = E_r \cdot \tau$, is initially constant down to ~200 nm. However, since $_{\tau}$ saturates for fibers below this size while the relaxing portion of the modulus (E_r) only continues to increase, η should increase as diameter

is further reduced. This indicates that as the nanofibers are reduced in size, they will display a unique combination of high stiffness and large mechanical energy dissipation not present their bulk form.

7.6 Size-dependent stiffness and damping

Where high stiffness is required metals are usually used and polymers are left to applications that require stress damping. This comes from the internal relaxation processes that occur in polymers due to their complex molecular structure. These processes involve the time dependent molecular motion that occurs within and around a polymer's internal structures, such as unraveling of tie-molecules and sliding of long molecular chains within amorphous regions. This high damping, consequently leads to the low stiffness of polymers compared to metals, ceramics, and single crystal materials, which have low damping. However, based on the increasingly stiff moduli and large size-dependent degree of relaxation observed in our polymer nanofibers at the nanoscale, this material property tradeoff can be avoided.

From our viscoelastic stress relaxation model, we can define the ratio of the relaxing and elastic moduli components as $\Delta = E_r/E_e = (1-\beta)/\beta$ and define a dissipation capacity, $\Delta/\left(2\sqrt{1+\Delta}\right)$, which represents the ability of the material to dissipate mechanical energy.[40] As the diameters of the Nylon-11 nanofibers are reduced, the dissipation capacity significantly increases by a factor of ~20 (Figure 7.7) and while the dissipation is initially small, similar to metals, it increases even beyond that of other polymeric materials to levels comparable to the best recently developed

composite materials[41]. It is important to note that the damping in the polymer nanofibers was measured at room temperature, whereas the high performance of the composites is achieved at elevated temperature and performance drops as the operation temperature falls from 57°C to 40°C. The specific modulus also increases from polymer-like to near metallic levels due to the higher strength to density ratios. This propels the nanofibers towards simultaneously high stiffness and dissipation as compared to most materials, which is uncommon and highly suitable for applications involving vibration damping[40]. This is the first observation that nanoscaling of polymers, specifically fibers, could produce a new set of materials, tunable *via* size alone, with simultaneously high stiffness and large mechanical energy dissipation which would be highly desirable and useful.

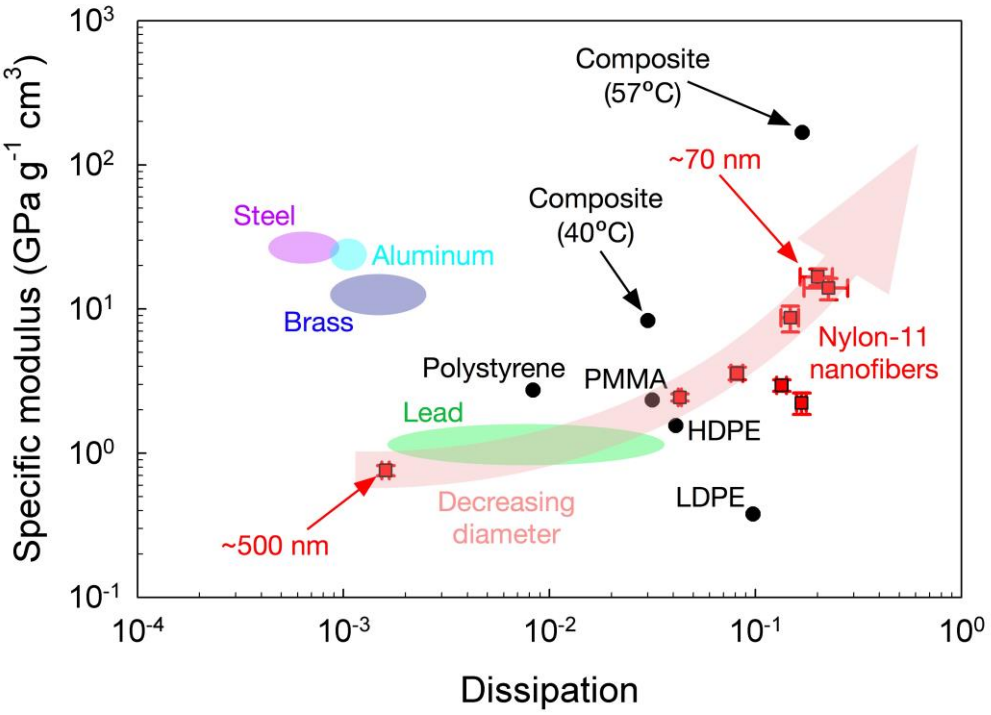


Figure 7.7: Specific modulus versus maximum dissipation capacity. The specific modulus and dissipation capacity of the Nylon-11 nanofibers, calculated based on the measured tensile modulus and stress relaxation, is compared to other polymeric and metallic materials,[40] as well as a state-of-the-art composite[41] material. The dissipation capacity and specific modulus significantly increase by over an order of magnitude as fiber diameter is reduced, rising from low polymeric damping levels for ~500 nm diameter fibers to an impressive combination of specific modulus, comparable to the best structural metals, and dissipation capacity above that of many other polymers as fiber diameters are reduced below 100 nm. The thinnest fibers are even comparable to a state-of-the-art composite material[41]. The nanofibers, however, are operational at room temperature, whereas the composite performs best at elevated temperature and its performance quickly degrades as temperature drops.

7.7 Conclusion

While size-dependent behavior of nanofibers has been previously studied for a number of polymer systems, time-dependent mechanical properties of individual nanofibers have little to no attention even though they are important aspects of

polymer mechanics due to their viscoelastic nature. Here we performed size-dependent tensile elastic and relaxation test on semi-crystalline Nylon-11 nanofibers and found that stress relaxation in individual fibers is highly size-dependent, increasing significantly as diameter is reduced. The observed strong relaxation of ~40% occurs rapidly, saturating within ~30 minutes for the smallest nanofibers, which emphasizes the importance of considering the relaxed modulus when designing mechanical systems incorporating nanofibers, such as piezoelectric based devices[42] and nano-generators[43-45]. Furthermore, we found that the combination of significant increasing relaxation and exponentially increasing modulus upon size reduction leads to nanofibers with exceptionally high stiffness and mechanical energy damping properties, comparable to state-of-the-art composite materials, but operational at room temperature. This suggests that thin nanofibers could be ideal candidates and provide substantially enhanced performance for applications which involve vibration damping, require tough and flexible materials, as artificial tissues such as skin, or in protective garments.

Acknowledgements

This chapter is a reprint of material currently being prepared for submission for publication by Matthew C. Wingert, Zhang Jiang, Shengqiang Cai, and Renkun Chen. The dissertation author was the primary investigator and author of this material.

References

1. Z. M. Huang, Y. Z. Zhang, M. Kotaki and S. Ramakrishna, Compos Sci Technol **63** (15), 2223-2253 (2003).

2. Y. Dzenis, Science **304** (5679), 1917-1919 (2004).

3. D. Aussawasathien, J. H. Dong and L. Dai, Synthetic Met **154** (1-3), 37-40 (2005).

4. A. Frenot and I. S. Chronakis, Curr Opin Colloid In **8** (1), 64-75 (2003).

5. A. Arinstein, M. Burman, O. Gendelman and E. Zussman, Nat Nanotechnol **2** (1), 59-62 (2007).

6. S. Shen, A. Henry, J. Tong, R. T. Zheng and G. Chen, Nat Nanotechnol **5** (4), 251-255 (2010).

7. S. Y. Chew, T. C. Hufnagel, C. T. Lim and K. W. Leong, Nanotechnology **17** (15), 3880-3891 (2006).

8. M. Richard-Lacroix and C. Pellerin, Macromolecules **46** (24), 9473-9493 (2013).

9. M. Naraghi, P. V. Kolluru and I. Chasiotis, J Mech Phys Solids **62**, 257-275 (2014).

10. A. Arinstein, J Polym Sci Pol Phys **51** (9), 756-763 (2013).

11. A. Baji, Y. W. Mai, S. C. Wong, M. Abtahi and P. Chen, Compos Sci Technol **70** (5), 703-718 (2010).

12. C. T. Lim, E. P. S. Tan and S. Y. Ng, Appl Phys Lett **92** (14) (2008).

13. D. Papkov, Y. Zou, M. N. Andalib, A. Goponenko, S. Z. D. Cheng and Y. A. Dzenis, Acs Nano **7** (4), 3324-3331 (2013).

14. Z. Zhong, M. C. Wingert, J. Strzalka, H.-H. Wang, T. Sun, J. Wang, R. Chen and Z. Jiang, Nanoscale **6** (14), 8283-8291 (2014).

15. R. O. Ritchie, Nat Mater **10** (11), 817-822 (2011).

16. H. Schreuder-Gibson, P. Gibson, K. Senecal, M. Sennett, J. Walker, W. Yeomans, D. Ziegler and P. P. Tsai, J Adv Mater-Covina **34** (3), 44-55 (2002).

17. S. J. Kwoun, R. M. Lec, B. H. Han and F. K. Ko, P Ieee Int Freq Cont, 52-57 (2000).

18. Q. P. Pham, U. Sharma and A. G. Mikos, Tissue Eng **12** (5), 1197-1211 (2006).

19. B. K. Gu, M. S. Kim, C. M. Kang, J. I. Kim, S. J. Park and C. H. Kim, J Nanosci Nanotechno **14** (10), 7621-7626 (2014).

20. V. Beachley, E. Katsanevakis, N. Zhang and X. J. Wen, Adv Polym Sci **246**, 171-212 (2012).

21. V. Singh, T. L. Bougher, A. Weathers, Y. Cai, K. D. Bi, M. T. Pettes, S. A. McMenamin, W. Lv, D. P. Resler, T. R. Gattuso, D. H. Altman, K. H. Sandhage, L. Shi, A. Henry and B. A. Cola, Nat Nanotechnol **9** (5), 384-390 (2014).

22. W. Wang, A. J. Bushby and A. H. Barber, Appl Phys Lett **93** (20), 201907 (2008).

23. W. Wang and A. H. Barber, Journal of Polymer Science Part B: Polymer Physics **50** (8), 546-551 (2012).

24. Y. Liu, S. Chen, E. Zussman, C. S. Korach, W. Zhao and M. Rafailovich, Macromolecules **44** (11), 4439-4444 (2011).

25. D. L. Vezie, E. L. Thomas and W. W. Adams, Polymer **36** (9), 1761-1779 (1995).

26. Y. C. Hu, L. Shen, H. Yang, M. Wang, T. X. Liu, T. Liang and J. Zhang, Polym Test **25** (4), 492-497 (2006).

27. E. Petrovicova, R. Knight, L. S. Schadler and T. E. Twardowski, J Appl Polym Sci **78** (13), 2272-2289 (2000).

28. H. Chung and S. Das, Mat Sci Eng a-Struct **437** (2), 226-234 (2006).

29. S. Cuenot, S. Demoustier-Champagne and B. Nysten, Phys. Rev. Lett. **85**, 1690-1693 (2000).

30. M. Burman, A. Arinstein and E. Zussman, EPL (Europhysics Letters) **96** (1), 16006 (2011).

31. Y. Ji, C. Li, G. Wang, J. Koo, S. Ge, B. Li, J. Jiang, B. Herzberg, T. Klein, S. Chen, J. C. Sokolov and M. H. Rafailovich, EPL (Europhysics Letters) **84** (5), 56002 (2008).

32. U. Stachewicz, R. J. Bailey, W. Wang and A. H. Barber, Polymer **53** (22), 5132-5137 (2012).

33. C. L. Choy, Y. W. Wong, G. W. Yang and T. Kanamoto, J Polym Sci Pol Phys **37** (23), 3359-3367 (1999).

34. E. Zussman, M. Burman, A. L. Yarin, R. Khalfin and Y. Cohen, J. Polym. Sci. B **44**, 1482-1489 (2006).

35. M. Burman, A. Arinstein and E. Zussman, Appl Phys Lett **93** (19), 193118 (2008).

36. Y. Ji, B. Li, S. Ge, J. C. Sokolov and M. H. Rafailovich, Langmuir **22**, 1321-1328 (2006).

37. A. Arinstein, Y. Liu, M. Rafailovich and E. Zussman, EPL (Europhysics Letters) **93** (4), 46001 (2011).

38. M. Richard-Lacroix and C. Pellerin, Macromolecules **48** (13), 4511-4519 (2015).

39. M. Richard-Lacroix and C. Pellerin, Macromolecules **48** (1), 37-42 (2015).

40. R. Lakes, *Viscoelastic Materials*. (Cambridge University Press, 2009).

41. T. Jaglinski, D. Kochmann, D. Stone and R. S. Lakes, Science **315** (5812), 620-622 (2007).

42. L. Persano, C. Dagdeviren, Y. Su, Y. Zhang, S. Girardo, D. Pisignano, Y. Huang and J. A. Rogers, Nat Commun **4**, 1633 (2013).

43. J. Chang, M. Dommer, C. Chang and L. Lin, Nano Energy **1** (3), 356-371 (2012).

44. C. Chang, V. H. Tran, J. Wang, Y.-K. Fuh and L. Lin, Nano Lett **10** (2), 726-731 (2010).

45. B. J. Hansen, Y. Liu, R. Yang and Z. L. Wang, Acs Nano **4** (7), 3647-3652 (2010).

Chapter 8: Conclusions and future work

The first studies of nanoscale size effects on thermal conduction in nanostructures were performed almost two decades ago. However, while experiments on structure size in the boundary scattering regime have been successful at developing our understanding of the effect of reducing the phonon MFP on thermal conductivity, little work has been done on structures approaching the phonon wavelength, or so-called the "phonon confinement" regime. In this regime, nanomaterial properties are almost entirely dictated by surface effects, which can greatly alter the physical properties of the material from bulk behavior. Yet only recently, in the last several years, have measurements on ultra-thin structures (<30 nm) gained renewed interest. Thanks to the extension of previous measurement techniques as well as the development of new ones, thermal conductivity measurements on structures of this size, specifically one-dimensional structures such as NWs and NTs, are finally achievable with sufficient accuracy.

In this sub-30 nm size regime, many questions regarding thermal transport behavior remain. As structure size approaches the size of a few nanometers, the same scale as the phonon wavelength, surface and interface atoms will dominate the physical properties. Studying different materials at this range can extend our understanding of thermal transport, specifically at the atomic scale and possibly elucidate new physical phenomena, such as the observed sub-amorphous and elastic softening behaviors. For thin films, while thermal conductivity can be theoretically predicted, explanations for the experimentally measured reductions in flexural mode velocities are still required, as well as the effect of surface oxides and roughness on

elastic constants. For NWs, the behavior at sub-30 nm diameters proved difficult to explain, yet in conjunction with recent results of thin films and thin-shelled NTs, some common phenomena are present, such as reduced elastic modulus and the increasing importance of surface quality, through oxidation and roughness.

Currently, more experimental effort is needed to understand thermal properties at sub-30 nm length scales and the effects of interfaces, surfaces, and coatings. Specific areas that should prove useful toward answering many questions include studies of: 1) core-shell NWs, specifically with ultra-thin NWs and varied coating thicknesses; 2) thinner NWs, in the 1-20 nm range, and of varying materials (Si, Ge, etc.); and 3) understanding how other nanoscale phenomena develop, such as elastic softening and altered heat capacity, and how these affect thermal transport.

Specific work which should be done to answer these questions include measuring thermal conductivity of sub-10 nm diameter nanowires of various semiconductor materials. Such tests should aim to achieve one-dimensional conductance and measure ballistic and near-room temperature quantum of thermal conductance in these structures over a variety of materials. To better understand the effects of coatings, thermal conductivity measurements should be performed while varying the thickness of shell materials deposited on sub-10 nm nanowires, preferably with atomic precision so that the influence of the shell can be accurately measured. The effect of soft versus hard shells, as compared to the nanowire core material (*via* acoustic impedance), is also important and should be checked by adding ultrathin heavier element shells and polymer coatings to the nanowire.

Other sub-30 nm semiconductors materials, such as Ge, should also be studies for ‘sub-amorphous’ thermal conductivity, both to see if the effect is universal and/or at what size the effect manifests. Checking to see if the effect is still present after removing oxide coatings is important to understand its origin. Studying the effect of elastic softening on thermoelectric properties could also lead to enhanced thermoelectric materials (highly reduced thermal conductivity while retaining crystalline electric conductivity). It is also interesting to see if this phenomenon could be combined with other thermal conductivity reduction mechanisms, such as increasing surface roughness, to further reduce thermal transport. For practical applications, these ultrathin soft nanostructure materials could be used in flexible electronics, therefore studying how to incorporate them in real devices could be very useful. Furthermore, since the ultrathin amorphous Si nanotubes do not exhibit the minimum thermal conductivity, this raises the question of whether the thermal conductivity of amorphous Si is size-dependent, as has been recently proposed theoretically. This can be studied by varying the size of materials like the shell of the thin amorphous nanotube structures measured in this thesis.

In light of the presence of a fluid-like surface in the amorphous nanotubes, there are a number of future studies of interest. How relaxation of the amorphous nanotubes (like the observed reduced modulus which decreased as size reduced below 30 nm, similar to the crystalline nanostructures) affects the thermal conductivity, either increasing or decreasing it, could add to our understanding of the elastic softening. Since the creep appears to be influenced by interfaces present in the nanotubes, performing mechanics test on the amorphous and crystalline Si nanotubes

with the oxide coating removed would help elucidate the interfacial influence. Furthermore, temperature dependent creep testing on a-SiO_2, a-Si, and c-Si nanotubes should be performed while also varying the nanotube shell thickness along with the temperature. This will clearly relate the affect temperature has on the modulus and thickness of the fluid-like surface. Finally, it is important to study how this creep in ultrathin structures affects the performance of flexible micro/nano-electronics and other ultrathin nanoscale devices.

In terms of polymers, more work needs to be done to identify the sources of the increased thermal conductivity and elastic modulus upon size reduction such that rational engineering of fiber properties can be achieved. This will require understanding size-dependence of the structure-property relationship of thermal and mechanical properties (thermal conductivity, heat capacity, elastic modulus, etc.) for many different polymers under varying processing conditions. Specifically, a variety of crystalline (polyethylene), other semi-crystalline (Nylon 6,6), and amorphous polymers should be investigated as well as for various electrospinning conditions. Size-dependent stress relaxation behavior should also be studied for other polymers and under more testing conditions, such as frequency and temperature dependent responses, in order to find optimal materials and conditions under which performance is acceptable. Theses optimized polymer nanofibers can then be used to engineer functional fabric materials with combined high stiffness and toughness, tuned to operate under a variety of conditions. Other related properties which could be of interest include thermal contraction for investigating nanofiber use in applications such as artificial muscles.

Appendix A

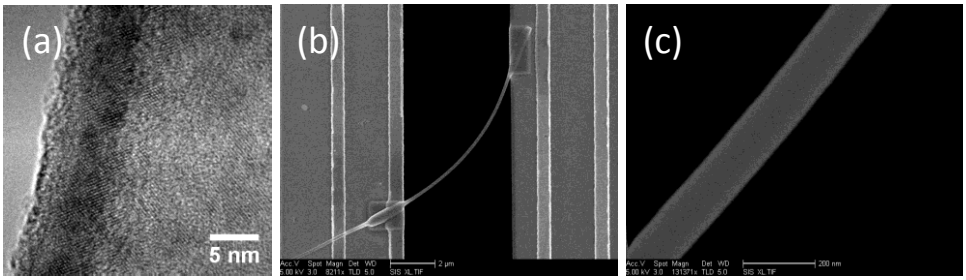


Figure A1: TEM and SEM images of measured ~5 nm thick crystalline nanotube (sample ID: C5-1): (a) shell thickness from TEM, (b) suspended sample length on thermal measurement device from SEM, and (c) suspended nanotube outer diameter from SEM. Specific geometric and thermal measurements for each sample can be found listed in Table 4.1.

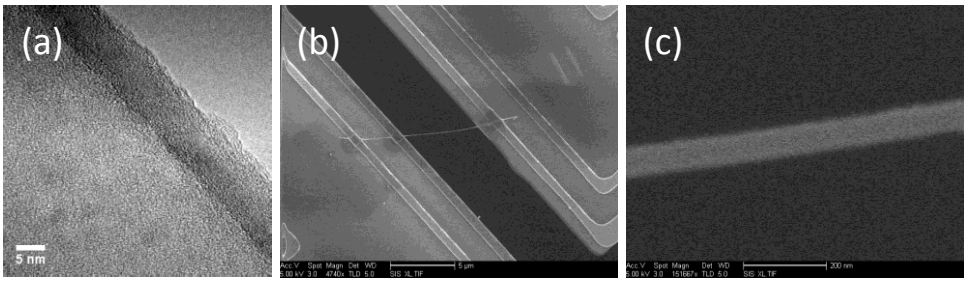


Figure A2: TEM and SEM images of measured ~5 nm thick crystalline nanotube sample (sample ID: C5-2): (a) shell thickness from TEM, (b) suspended sample length on thermal measurement device from SEM, and (c) suspended nanotube outer diameter from SEM. Specific geometric and thermal measurements for each sample can be found listed in Table 4.1.

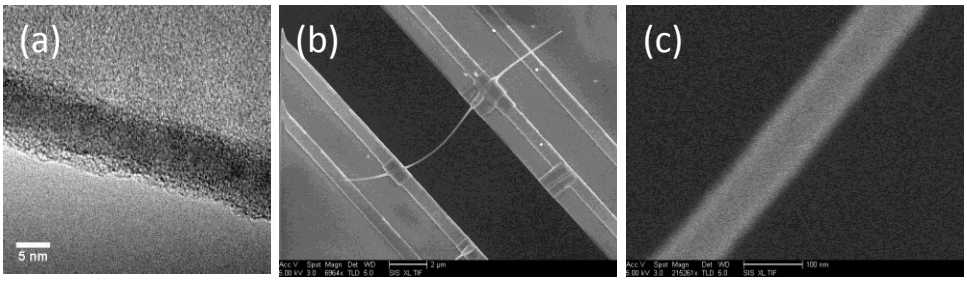


Figure A3: TEM and SEM images of measured ~5 nm thick crystalline nanotube sample (sample ID: C5-3): (a) shell thickness from TEM, (b) suspended sample length on thermal measurement device from SEM, and (c) suspended nanotube outer diameter from SEM. Specific geometric and thermal measurements for each sample can be found listed in Table 4.1.

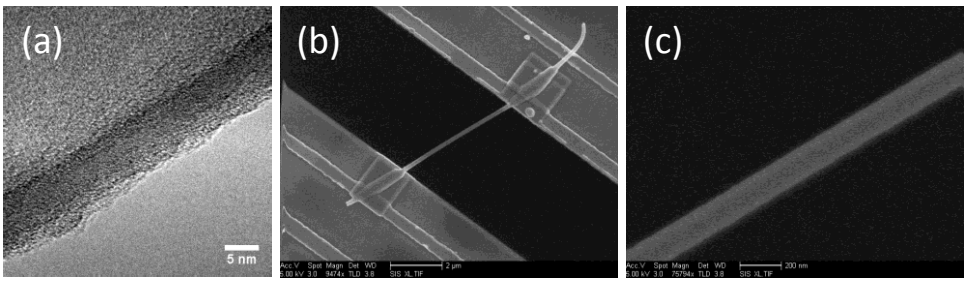


Figure A4: TEM and SEM images of measured ~5 nm thick crystalline nanotube sample (sample ID: C5-4): (a) shell thickness from TEM, (b) suspended sample length on thermal measurement device from SEM, and (c) suspended nanotube outer diameter from SEM. Specific geometric and thermal measurements for each sample can be found listed in Table 4.1.

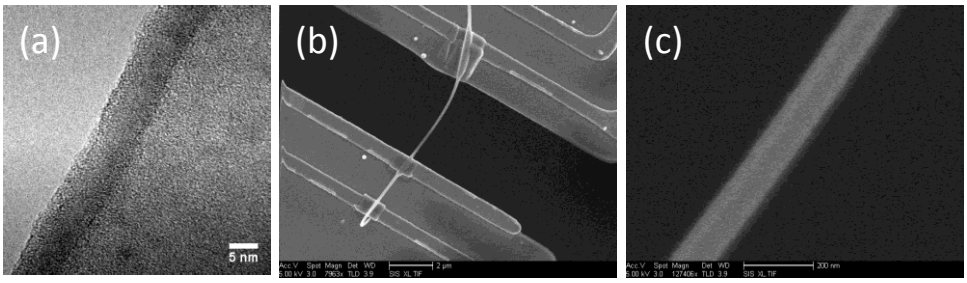


Figure A5: TEM and SEM images of measured ~5 nm thick crystalline nanotube sample (sample ID: C5-5): (a) shell thickness from TEM, (b) suspended sample length on thermal measurement device from SEM, and (c) suspended nanotube outer diameter from SEM. Specific geometric and thermal measurements for each sample can be found listed in Table 4.1.

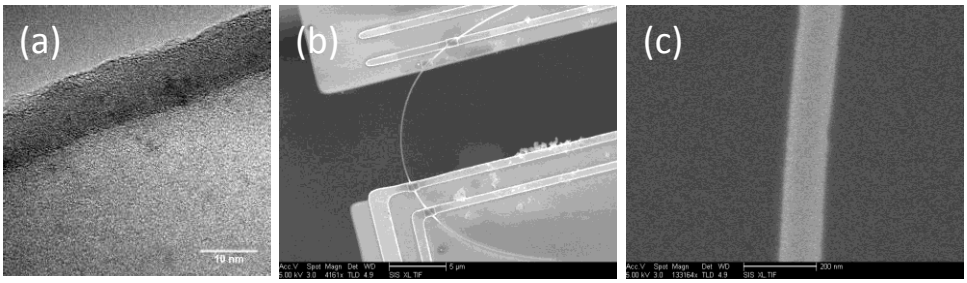


Figure A6: TEM and SEM images of measured ~7 nm thick crystalline nanotube sample (sample ID: C7-1): (a) shell thickness from TEM, (b) suspended sample length on thermal measurement device from SEM, and (c) suspended nanotube outer diameter from SEM. Specific geometric and thermal measurements for each sample can be found listed in Table 4.1.

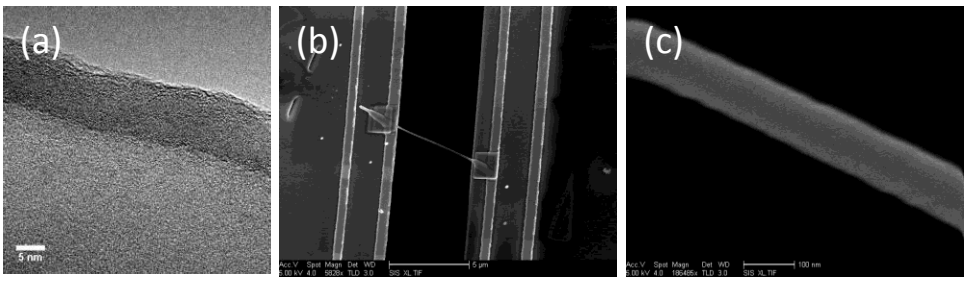


Figure A7: TEM and SEM images of measured ~7 nm thick crystalline nanotube sample (sample ID: C7-2): (a) shell thickness from TEM, (b) suspended sample length on thermal measurement device from SEM, and (c) suspended nanotube outer diameter from SEM. Specific geometric and thermal measurements for each sample can be found listed in Table 4.1.

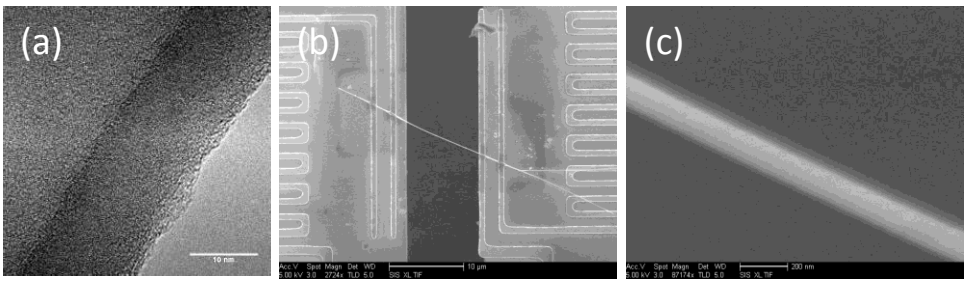


Figure A8: TEM and SEM images of measured ~10 nm thick crystalline nanotube sample (sample ID: C10-1): (a) shell thickness from TEM, (b) suspended sample length on thermal measurement device from SEM, and (c) suspended nanotube outer diameter from SEM. Specific geometric and thermal measurements for each sample can be found listed in Table 4.1.

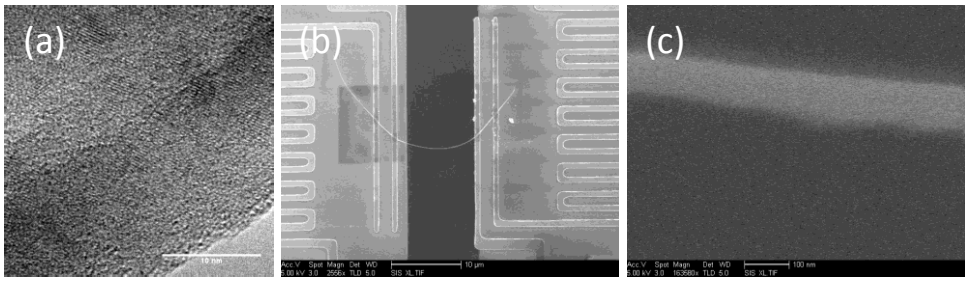


Figure A9: TEM and SEM images of measured ~10 nm thick crystalline nanotube sample (sample ID: C10-2): (a) shell thickness from TEM, (b) suspended sample length on thermal measurement device from SEM, and (c) suspended nanotube outer diameter from SEM. Specific geometric and thermal measurements for each sample can be found listed in Table 4.1.

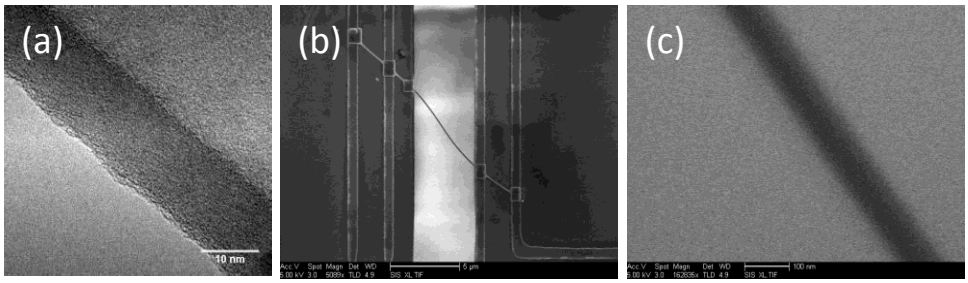


Figure A10: TEM and SEM images of measured ~10 nm thick crystalline nanotube sample (sample ID: C10-3): (a) shell thickness from TEM, (b) suspended sample length on thermal measurement device from SEM, and (c) suspended nanotube outer diameter from SEM. Specific geometric and thermal measurements for each sample can be found listed in Table 4.1.

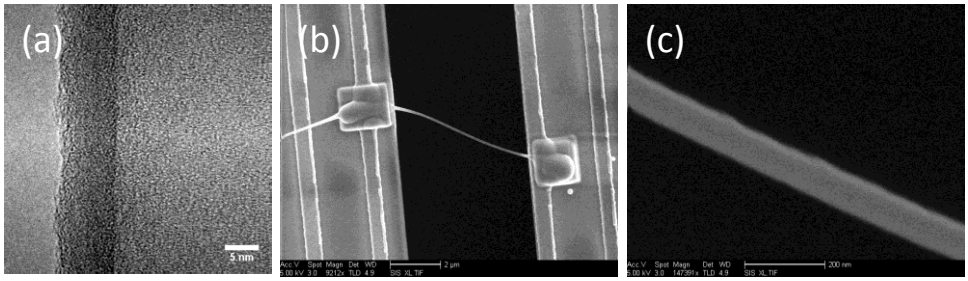


Figure A11: TEM and SEM images of measured ~5 nm thick amorphous nanotube sample (sample ID: A5-1): (a) shell thickness from TEM, (b) suspended sample length on thermal measurement device from SEM, and (c) suspended nanotube outer diameter from SEM. Specific geometric and thermal measurements for each sample can be found listed in Table 4.1.

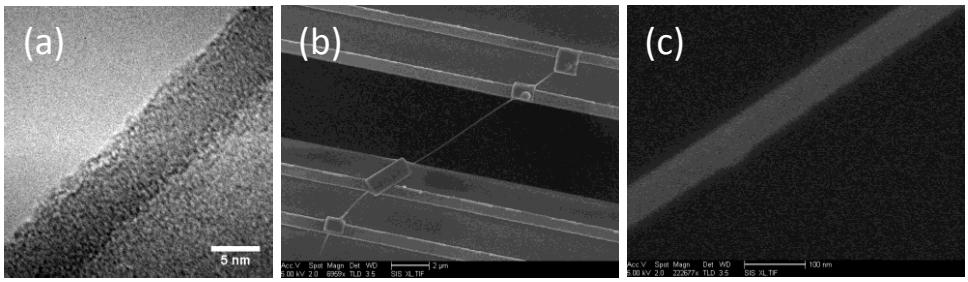


Figure A12: TEM and SEM images of measured ~5 nm thick amorphous nanotube sample (sample ID: A5-2): (a) shell thickness from TEM, (b) suspended sample length on thermal measurement device from SEM, and (c) suspended nanotube outer diameter from SEM. Specific geometric and thermal measurements for each sample can be found listed in Table 4.1.

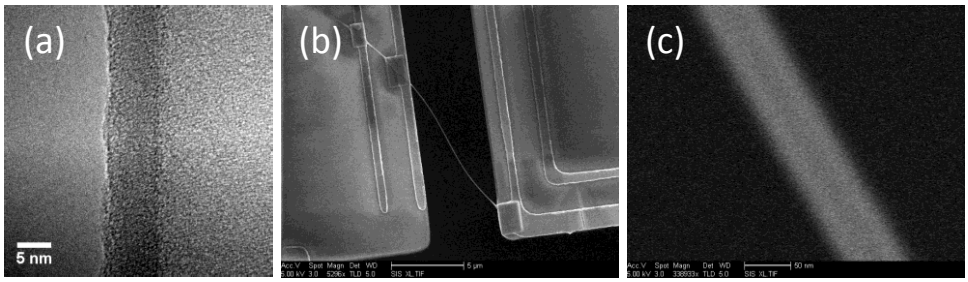


Figure A13: TEM and SEM images of measured ~5 nm thick amorphous nanotube sample (sample ID: A5-3): (a) shell thickness from TEM, (b) suspended sample length on thermal measurement device from SEM, and (c) suspended nanotube outer diameter from SEM. Specific geometric and thermal measurements for each sample can be found listed in Table 4.1.